Autonomous Landing of a Tethered Multi-Rotor Unmanned Aerial Vehicle on a Stationary Platform

by

Joshua Tatenda Mfiri

Thesis presented in partial fulfilment of the requirements for the degree
Master of Science in Engineering
in the Faculty of Engineering at Stellenbosch University.

Supervisor:
Mr J Treurnicht

Co-supervisor:
Dr J.A.A Engelbrecht

Department of Electrical and Electronic Engineering

April 2019

Acknowledgements

This project has presented life-changing experiences and challenges both in my professional career as an engineer and also as a human being. Throughout the course of the project I have been lucky to rub shoulders with extraordinary individuals whose support and contributions have been instrumental in the successful completion of this project. Without their input in various forms and at various times, a project of such complexity and wide scope would be impossible to undertake. Even though a mere thank you doesn't do justice to their contributions, it is the least that they deserve.

1. Firstly to my supervisor Mr Johann Treurnicht for offering me the opportunity to undertake research under his supervision. His immense experience, knowledge and insight which he freely shared even into his retirement have been a pillar of technical soundness for this project.

2. To my supervisor Dr Japie Engelbrecht whose knowledge of aerospace systems and his extraordinary aptitude to communicate complex technical ideas in simple terms are unparalleled. Together with Mr Treurnicht, they have gone above and beyond what a student is entitled to from his/her supervisors; sourcing supplementary funding where necessary and assisting with transport and moral support during flight tests.

3. To Piero Ioppo who designed and built the quad-rotor UAV platform used for this project and handed it over in one piece. He pioneered tethered UAV research in the Electronics Systems Laboratory (ESL) and his work served as a strong foundation for this project.

4. To former ESL engineers Christopher Fourie and Cornelus Le Roux for facilitating the initial flight tests.

5. To Mr Wessel Croukamp from the mechanical workshop who was instrumental in the assembling of the winch. His insights have been invaluable in the design and selection of components for the winch system.

6. To Mr Pietro Petzer who always found a way to avail the departmental truck for flight tests, even on short notice.

7. To Mr Hilton Johnson and Mr Ashley Cupido for going out of their way to source electronic components for the winch hardware design.

8. To Mr Wynand van Eeden for printing PCBs for the winch electronics and Mr Johan Arendse for soldering surface mount components.

9. To our skilled safety pilot Michael Basson for his outstanding job in flying the quad-rotor UAV and ensuring its safety.

10. To my many colleagues in the ESL who gladly stepped in to help with flight tests including Gerju Goosen, Bongani Maseko, Izaak van Zyl, Jurgen and Aaron Buyse.

11. To the various lecturers in the Electrical and Electronics Engineering Department whom I consulted regarding post-graduate study opportunities. This research opportunity was made possible by their guidance and counsel. They are Prof Petrie Meyer, Prof Thomas Jones, Dr Cornè Van Daalen, Prof Thomas Niesler, Dr Japie Engelbrecht and finally Mr Johann Treurnicht.

12. To my friend Sylvester for his selfless support through the good and challenging times, willing to step out into the cold winter mornings and help with flight tests.

13. To my cousins Bridget and Linda and my brother Desire for providing financial support when the going got tough.

14. To my friend Sylvester and my brother Desire for proof-reading this thesis.

15. To my family and friends who have been a source of moral support. They include Desire, Alford, Ruth, Unathi, Bianca, Sylvester and Thomas.

16. Finally, to my dear mother Winnie who has instilled in me the principles of hard work and the spirit to persist through hardships and to never give up. To her this thesis is dedicated.

Declaration

By submitting this thesis electronically, I declare that the entirety of the work contained herein is my own, original work, that I am the sole author thereof (save to the extent explicitly otherwise stated), that reproduction and publication thereof by Stellenbosch University will not infringe any third party rights and that I have not previously in its entirety or in part submitted it for obtaining any qualification.

April 2019

Abstract

This thesis contributes to the research of persistent tethered aerial vehicles by presenting a strategy to autonomously land a tethered multi-rotor UAV. A flight control system is developed for a quad-rotor UAV which was inherited from a previous project. A winch system is also added and a control system is designed to winch the tethered quad-rotor. A novel point-mass model of the tethered UAV is formulated and utilised to design a tethered landing strategy which is robust against inaccuracies in aircraft position measurement. The work culminates in the demonstration of autonomous landings of a tethered quad-rotor UAV on a 2.4 m $\times$ 2.4 m stationary platform.

The flight control system is designed by using successive loops of Proportional-Integral-Derivative (PID) controllers. Flight control loops are designed based on an untethered quad-rotor model and integral control laws are implemented to aid the rejection of tether disturbances. A spring-damper model proved to be sufficient in modelling tether dynamics. A novel point-mass model of the tethered UAV is utilised in deriving closed-form analytical expressions for the tethered system poles both in the radial and angular directions as functions of quad-rotor and tether parameters.

Flight control systems are designed and simulated in a software-in-the-loop environment. Control loops that are critical to the landing strategy are also simulated in a hardware-in-the-loop environment. Practical results show satisfactory performance in horizontal control in wind speeds of up to 2 m.s^{-1} while the vertical control system exhibits relative immunity to an increase in wind speed.

Uittreksel

Hierdie tesis dra by tot die navorsing van aanhoudendevlug lugvoertuie deur 'n strategie aan te bied om outonoom 'n vasgehegde multi-rotor onbemande lugvoertuig (OLV) te laat land. 'n Vlugbeheerstelsel is ontwikkel vir 'n vier-rotor OLV wat beskikbaar was vanuit 'n vorige projek. 'n Katroltoestel is ook ontwerp met 'n beheerstelsel om die lugvoertuig in te katrol. 'n Nuwe puntmassamodel van die vasgehegde OLV is ontwikkel en gebruik om 'n strategie vir 'n vasgehegde landing te ontwerp. Die werk word afgerond met 'n demonstrasie van outome landings van die vasgehegde OLV op 'n 2.4 m $\times$ 2.4 m stilstaande platform.

Die vlugbeheerstelsel is ontwerp deur van opeenvolgende lusse met PID beheerders gebruik te maak. Die vlugbeheer ontwerp is 'n multi-lus tipe gebaseerd op die vrye vier-rotor model met integraalbeheer om steuringinsette te verwerp. 'n Veer-demper model blyk genoegsaam te wees vir die modellering van die vashegdinamika. 'n Nuwe puntmassamodel van die vasgehegde OLV word gebruik om die geslotelus analitiese uitdrukkings van die vasgehegde stelselpole vir beide radiale en hoekrigtings as funksies van vier-rotor en vashegparameters te onttrek.

Vlugbeheerstelsels is ontwerp en gesimuleer in 'n sagteware-in-die-lus omgewing. Beheerlusse wat krities is vir die landing word ook in 'n hardeware in-die-lus omgewing gesimuleer. Praktiese resultate wys aanvaarbare prestasie in horisontalebeheer vir windsnelhede tot 2 m.s^{-1} terwyl die vertikale beheerstelsel redelik immuun is vir windspoed.

Table of Contents

List of Figures

List of Tables

Chapter 1

Introduction

This chapter serves to introduce the research problem and place the research in the context of the existing body of knowledge. The chapter begins by outlining the project background in Section 1.1. The research question is formulated in Section 1.2 and thereafter the research aims and objectives are set out in Section 1.3 . Section 1.4 discusses the available literature on multi-rotors and tethered UAVs in general. The chapter concludes by providing a roadmap of the chapters to come and explaining the organisation of this thesis in Section 1.5.

1.1 Project Background

This project is part of a series of projects commissioned in the Electronic Systems Laboratory (ESL) at Stellenbosch University. This section outlines the emergence of the project in the context of research work in the ESL. The relevance of the project in the broader UAV research field is presented in Section 1.4.

The Electronic Systems Laboratory and the Institute for Maritime Technology embarked on a joint research and development program in 2007 with the goal of developing a countermeasure system capable of diverting anti-ship missiles away from naval ships [1]. It was decided that the countermeasure system be implemented in the form of an Unmanned Aerial Vehicle (UAV). The first iteration of the countermeasure UAV was implemented using a ducted fan concept, consisting of two counter-rotating propellers housed in a cylindrical fuselage [1]. According to Möller, the ducted fan UAV was seen to be quite limited in agility and payload-carrying capacity leading to its replacement by a quad-rotor (i.e. a multi-rotor with four rotors) [1]. The quad-rotor

UAV became known as SLADe, which is an abbreviation for Surface Launched Aerial Decoy electric. The term SLADe is also used to refer the research program aimed at the development of the countermeasure UAV.

To fulfil its intended purpose of diverting anti-ship missiles away from naval ships, the SLADe quad-rotor system was designed to have four flight phases namely take-off, decoy, return and landing [1]. A series of research projects was set out in the ESL in order to sequentially demonstrate each of the quad-rotor's flight phases. By early 2013, autonomous take-off and landing (ATOL) on a stationary platform was demonstrated using the SLADe quad-rotor. Möller extended SLADe's flight envelope and successfully demonstrated SLADe's autonomous landing on a translating platform for platform speeds of up to 30 km.h^{-1} [1].

Lithium-ion Polymer (LiPo) batteries are usually used to power multi-rotor UAVs due to their light weight and high energy density [2]. Even with the extensive research that has been conducted on UAVs in general, the use of LiPo batteries has always limited the achievable flight durations [3]. While LiPo batteries suffice for the intended application of the SLADe quad-rotor, other applications of quad-rotors would benefit immensely from extended flight durations [4]. Tethered power was proposed as a way to render the quad-rotor persistent and capable of indefinite flight durations. A tether can be used to transmit power from a power source such as from a ship's deck. The ability to design persistent multi-rotor UAVs would benefit a host of other multi-rotor applications including photography, communications, surveillance, etc. The literature review in Section 1.4 gives a more detailed coverage of the applications of multi-rotor UAVs.

Although tethered power makes persistent aerial vehicles a possibility, tethering introduces complexity to multi-rotor UAV control. The tether is an additional component to the UAV system and conventional multi-rotor control strategies documented in Section 1.4 have to be adapted to cater for the tether. Based on the control complexity introduced by tethering, it is imperative to research the control of a tethered multi-rotor UAV. To understand the dynamics of tethered multi-rotors, a project was completed in the ESL by Ioppo, which culminated in the design of a tethered quad-rotor and its control in hover [4].

This project uses the hardware from the existing tethered quad-rotor system and seeks to add more subsystems necessary to demonstrate a tethered landing. Section 2.5

clearly highlights the additional subsystems that were added to the existing system. The existing quad-rotor UAV system is shown in Figure 1.1.

Figure 1.1: Existing untethered quad-rotor (left) and tethered quad-rotor in hover (right).

1.2 Problem Statement

The available battery technologies continue to limit the flight times and payload carrying capacities of multi-rotor UAVs. Tethered power is a possible solution to alleviate these limitations and realise persistent multi-rotor platforms with indefinite flight times. Tethering introduces an additional layer of complexity to the vehicle control system due to tether dynamics. A series of projects was commissioned in the ESL, with each project focussing on a specific phase of tethered multi-rotor flight.

A recently completed project culminated in the demonstration of the autonomous flight of a tethered quad-rotor in hover [4]. The project documented in this thesis seeks to explore techniques for executing the landing phase in the flight of a tethered multi-rotor UAV. The current research utilises the existing quad-rotor hardware and implements a flight control system and a state machine to demonstrate the autonomous

landing of a tethered quad-rotor on a stationary platform. A winch was also developed as part of the tethered landing system.

There is very limited literature on tethered landings and this research seeks to fill this gap in the existing body of knowledge by proposing a landing strategy for a tethered multi-rotor. Equally important, the research contributes a novel point-mass model of a tethered quad-rotor which has been used to accurately predict the dynamic response of the tethered system. The point-mass model is an invaluable tool in the designing and analysing of the dynamic behaviour of tethered multi-rotors during the landing phase of their flight.

1.3 Research Aims and Objectives

The primary objective of this research is to design a tethered multi-rotor system and demonstrate the autonomous landing of a tethered quad-rotor UAV on a 2.4 m $\times$ 2.4 m stationary platform. The following aims, when achieved, will culminate in the consequent achievement of the primary objective:

(i) To analyse the existing flight control system and make necessary improvements for use during tethered landing

(ii) To design a winch system and a winch control system as part of the tethered landing system.

(iii) To design a strategy to autonomously land a tethered quad-rotor on a stationary platform.

(iv) To demonstrate simulated autonomous landing of a tethered quad-rotor as a way of validating the flight control system and the landing strategy.

(v) To demonstrate autonomous landing of a tethered quad-rotor through practical flight tests.

The secondary objective of this project is to determine and validate the dynamics of a tethered multi-rotor UAV during the landing phase of its flight. The dynamics shall be presented in a form that is applicable not only to the particular vehicle used in this project, but to tethered multi-rotor UAVs in general. The secondary objective is further broken down in to the following aims:

(a) To formulate a simplified model of a tethered multi-rotor UAV, from which the dynamics of the vehicle during its landing phase can be obtained.

(b) To use the simplified model to determine the dynamics of a tethered multi-rotor UAV during its landing phase.

(c) To validate the derived dynamics using data from simulated landings of the quad-rotor UAV used in this project.

1.4 Literature Study

This section details a review of the literature available on multi-rotors and tethered UAVs. Section 1.4.1 addresses the applications of multi-rotors in general while tethered multi-rotors are discussed in Section 1.4.2. Strategies for the control and autonomous landing of UAVs are explored in Section 1.4.3.

1.4.1 Multi-Rotor Systems

Research and development of small UAVs is on the rise due to their ever-increasing demand in civilian applications [5], [1], [4]. Within the UAV fraternity, rotary wing vehicles further constitute a special class of UAVs capable of Vertical Take-Off and Landing (VTOL). Helicopters are a subclass of rotary wing vehicles and have been favoured in applications requiring significant payload lifting capabilities. Helicopters however have complex rotor heads consisting of swashplates thereby rendering helicopters difficult to maintain [6]. Multi-rotors on the other hand have a simpler mechanical structure comprising of at least three fixed-pitch rotors situated at the ends of a cross structure.

In addition to their simple mechanical structure, multi-rotors can be controlled through simple control algorithms. Multi-rotor configurations are differentiated by numerically prefixed names to indicate the number of rotors on a specific multi-rotor (e.g. quad-rotor) [4]. The control of multi-rotors is achieved by varying the thrust commands to each of the rotors. With the availability of variable speed drives and an increase in microprocessor computing power, the control of multi-rotors is far simpler than that of helicopters. The simpler control strategy and mechanical structure of quad-rotors comes at the cost of reduced efficiencies compared to helicopters due to reduced rotor size [7], [6]. Multi-rotors however still remain the preferred configuration for relatively small rotary wing UAVs whose applications do not require high payload carrying capabilities [8], [5].

The physics of multi-rotor flight is dominated by the inertial and aerodynamic properties of the vehicle. The aerodynamic and inertial properties were determined

through a system identification campaign conducted in Section 3.3 of [4]. Chapter 3 of this thesis gives a brief overview of the vehicle properties as well how they affect the dynamics of the quad-rotor.

UAV research and development started off as a primarily military activity due to the high capital which was needed to implement the appropriate technology. UAV technology has however been increasingly available for civilian applications due to advances in integrated avionic systems [4], [5]. When coupled with camera technology, multi-rotor UAVs find military applications in surveillance, reconnaissance, situational awareness, battle information fusion and counter-measurement [9]. With the increased accessibility of multi-rotors, the private and public safety sector has began applying multi-rotors for fire detection, emergency communications and surveillance [10].

The telecommunications industry enhances coverage and connectivity in remote areas by using multi-rotors as airborne relays to establish temporary ad-hoc networks for cellular, wifi or 3G/4G signals [9]. Multi-rotors are also used in traffic monitoring applications including trajectory extraction and analysis, car park optimisation, vehicle type and speed sampling as well as daily traffic enhancement [11]. Multi-rotors are sometimes furnished with cameras for applications in photography, public event observation, accident scene monitoring, and search and rescue missions [12].

For a long time, multi-rotors have been powered using Lithium-ion Polymer (LiPo) batteries. The flight times and payload carrying capabilities of battery-powered multi-rotors are limited by the available battery technologies, with typical flight times in the region of 10 to 20 minutes [13], [4]. Of late, research has been conducted in an attempt to develop replenishable power sources for UAVs thereby achieving extended or indefinite flight times. One solution was proposed by LaserMotive where laser transmitters are used for wireless transmission of power to the UAV [14]. The solution is however inhibited by high capital cost and low power transfer efficiencies. Tethered power offers a more cost effective potential solution. The disadvantages of tethering multi-rotors include limitation of vehicle mobility. The tether dynamics also add a layer of complexity to the vehicle control system design.

1.4.2 Tethered Multi-Rotor Systems

As mentioned in Section 1.4.1, battery technology imposes limitations on flight times for multi-rotor UAVs. Flight times of less than 20 minutes are typical for reserach

multi-rotor prototypes [13], [4]. Researchers and corporations have in the past few years started to investigate tethered power as a way to render UAV platforms persistent and thereby providing indefinite flight durations [12], [15], [16], [11] [17], [10], [9]. Tethered power research is still in its infancy as indicated by limited literature available in the public domain.

The University of Southamptom has developed a tethered unmanned aircraft equipped with cameras to perform persistent stare on a target for military and civilian applications [15]. By the year 2016, the aircraft had not yet been released as a commercial product, indicating that tethered power is a fairly new area of research. Companies have also recently began releasing commercial tethered UAVs on to the market. Figure 1.2 shows a tethered UAV by The ECA Group company [12] and a tethered quad-rotor by Hoverfly [16].

Figure 1.2: Tethered UAV by ECA Group in flight (left) and tethered quad-rotor by Hoverfly on landing deck (right).

Transmitting power through a tether has been shown to be more efficient than alternative methods like wireless laser power transmission [14], [18], [19]. In addition to power transmission, some UAV platforms also utilise the tether for reliable communications [12].

1.4.3 Existing Control and Landing Strategies for UAVs

The literature outlines various multi-rotor control strategies including classical PID [20], state space [21], Linear Quadratic Regulator (LQR) [22] and fuzzy logic controllers [23]. By inspecting errors and error rates, fuzzy logic implements control decisions in a human-like fashion, therefore fuzzy logic controllers with satisfactory performance can be designed even in the absence of an accurate knowledge of the system dynamics. LQR and state space controllers are most suited when the multi-rotor vehicle is being modelled as a Multiple-Input Multiple-Output (MIMO) system. Classical PID control

methods are however the most commonly used in the literature [20] since their design is well understood by researchers. Moreover classical PID controllers are easy to tune.

Recent work on quad-rotors employed classical PID controllers implemented in a successive loop closure fashion. This control architecture comprises of inner rate and angle loops and outer velocity and position loops [1], [4]. Integral control is often used for disturbance rejection and steady state tracking performance. The flight control system in this project will be implemented using classical PID controllers in successive loop closure fashion as is the case for the existing system and all quad-rotor control systems in the Electronic Systems Laboratory [4], [1].

State machines are the trade standard for executing autonomous landings of UAVs [24], [25]. Saripalli implemented a state machine to autonomously land a model helicopter on a stationary platform in 2003 [24]. Later in 2007, Saripalli adapted his initial state machine and demonstrated the autonomous landing of a model helicopter on a moving target [25]. Swart [26] and Möller [1] from the Electronic Systems Laboratory employed state machine strategies to land a helicopter on a moving deck and to land a quad-rotor on a translating platform respectively.

State machine implementations found in the literature are based on a series of states in which the vehicle tracks the landing target and then aligns with the heading of the target, in no particular order. Thereafter, the vehicle begins descending towards the target with safety checks to ensure satisfactory tracking performance throughout the descent. If unsatisfactory tracking performance is observed, the vehicle is usually reverted back to a previous state and the descent phase is retried [1], [24], [25]. The landing strategy used in this project includes an adaptation of Möller's state machine as described in Chapter 6 [1].

The state machine designed by Möller was furnished with a more comprehensive emergency abort strategy as necessitated by the risk that comes with having a tether attached to the vehicle. When unsatisfactory tracking performance is observed, the tether is automatically detached from the vehicle, the current landing attempt is aborted, and the vehicle hovers at the current position. The safety pilot then brings the vehicle to land. Another landing is attempted only after the cause of the unsatisfactory tracking performance has been investigated and rectified. The state machine design is indicative of the high risk that tethering poses on the vehicle flight.

While Global Position Systems (GPS) are sufficient for autonomous flight of UAVs, autonomous landings are usually attempted using Differential GPS (DGPS) systems which provide more accurate position sensing [1], [27], [28], [29]. DGPS systems are very costly compared to GPS systems. Due to their high cost, DGPS systems have been mainly used in military applications [29].

An alternative way to obtain accurate position measurements during landings is to use a vision-based sensor system [26]. Vision systems, however, require computationally expensive algorithms to identify the target and estimate the pose of the vehicle. The autonomous landing in this project is attempted with the GPS inherited from the exisiting system [4]. The challenge is undertaken to design a strategy that enables a successful landing even in the absence of accurate position sensing. As explained in Chapter 6, the strategy depends on the tether's natural tendency to pull the vehicle towards the landing target.

1.5 Thesis Layout

The layout of this thesis is shown in Figure 1.3. The thesis began with this introductory chapter which focusses on unpacking the research background and research problem as well as the discussion of literature relevant to the research. Chapter 2 follows with a high-level overview of the tethered unmanned aerial system. The roles played by the various hardware, software and human components in the implementation of the system are explained.

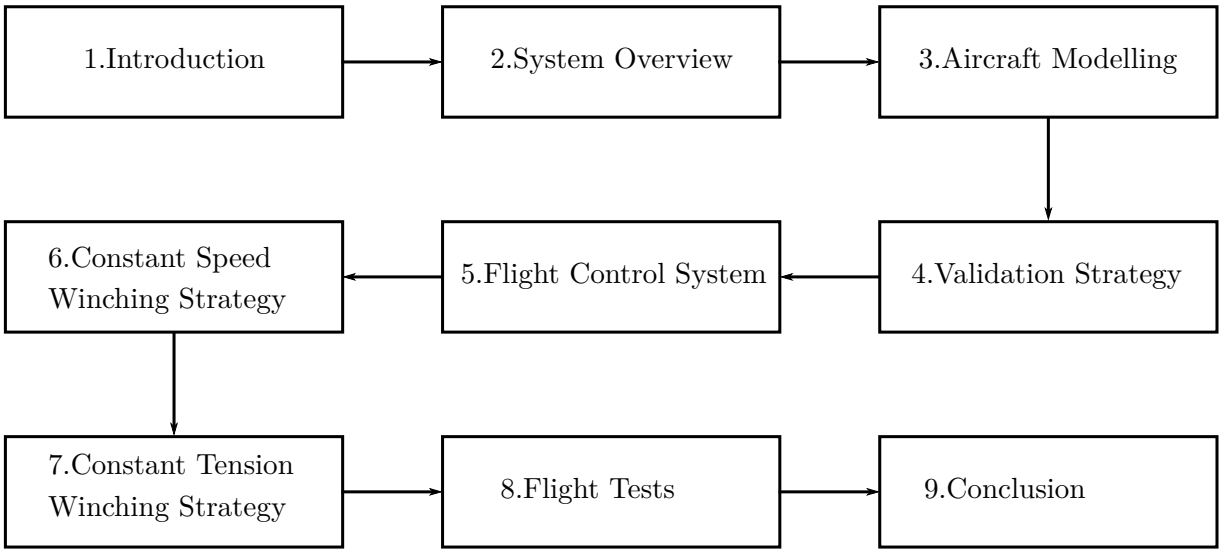

Figure 1.3: Thesis layout.

Chapter 3 will present the non-linear mathematical model derived for the tethered system. This chapter is one of the most mathematically-intense chapters, including axis system definitions, kinematic equations and kinetic equations. The forces and moments due to the UAV's rotors, gravity, aerodynamic drag and the tether are also modelled.

Chapter 4 is a high-level account of the strategy employed to incrementally build confidence in the designed system from control system design through Software-In-the-Loop (SIL) simulations and Hardware-In-the-Loop (HIL) simulations to the ultimate system validation through practical flights. The chapter also gives an overview of the flight control system architecture.

Chapter 5 is an in-depth and detailed account of the flight control system design. The design of the decoupled vertical, horizontal and yaw control systems is presented. Control system designs are supported by Bode plots, root loci and linear and non-linear step responses.

Chapter 6 and 7 propose two different strategies for the autonomous landing of a tethered quad-rotor vehicle. Chapter 6 presents a tethered landing strategy based on a constant winching speed, and Chapter 7 presents a tethered landing strategy based on a constant winching force. A novel point-mass model for the tethered quad-rotor is also developed and exploited to obtain the poles of the tethering radius system and the tethering angle system of the tethered quad-rotor.

In Chapter 8, key results from practical flight tests are presented. Chapter 9 concludes the thesis with a summary of the research performed. The contributions of the research to the body of knowledge is outlined, and its limitations are identified. Finally, some recommendations for future research are made.

Chapter 2

Overview of the Tethered Quad-Rotor Unmanned Aerial System

This chapter presents an overview of the tethered quad-rotor unmanned aerial system. Without delving into low-level technical detail, the chapter paints a high-level picture of how the various components complement each other to realise a functional system capable of landing a tethered quad-rotor UAV autonomously. Such a high-level picture is required in order to appreciate the context of the in-depth technical details which will be presented in later chapters. The unmanned aerial system consists of four major subsystems, namely the quad-rotor aircraft, the ground station, the winch and the safety pilot. The interaction of the four subsystems is illustrated by the command structure shown in Figure 2.1.

Section 2.1 outlines the roles played by each of the subsystems. In addition, a picture of the practical setup of the system and the command structure of the quad-rotor vehicle is painted. Thereafter, the low-level details of the individual subsystems are discussed. The quad-rotor mechanical structure, avionics and software are presented in section 2.2. Section 2.3 discusses the ground station and the winch is presented in Section 2.4. Section 2.5 gives an overview of the work undertaken in this project and how it blends into the existing system.

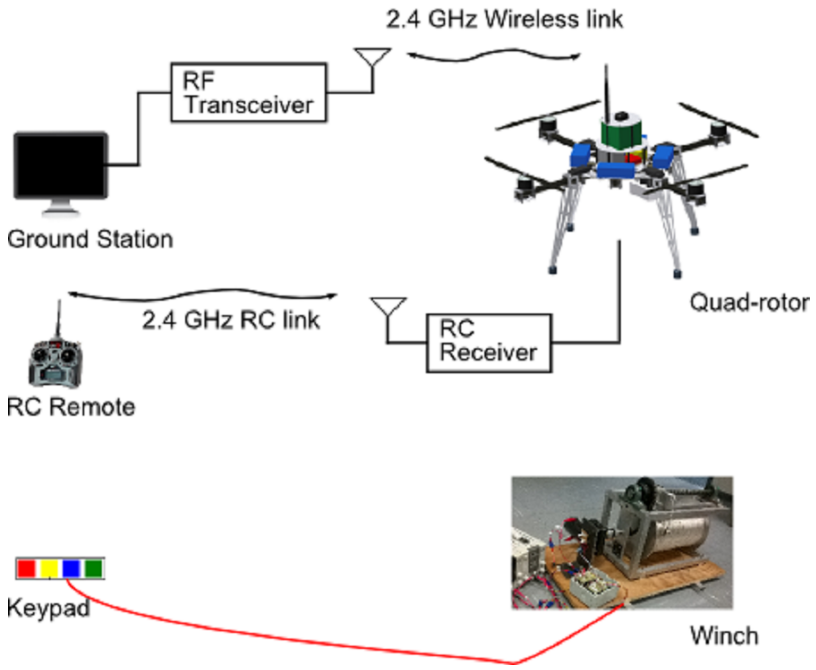

Figure 2.1: Command structure for the tethered quad-rotor unmanned aerial system.

2.1 The Tethered Quad-Rotor Unmanned Aerial System

The project makes use of the quad-rotor unmanned aerial vehicle shown in Figure 2.2. The quad-rotor configuration comprises of four identical rotors mounted to the ends of a symmetrical cross. By manipulating the common and differential thrust commands to the four rotors, the quad-rotor can be steered to a desired location in three-dimensional space. The quad-rotor is furnished with a radio frequency (RF) transceiver to communicate with the ground station.

Figure 2.2: The quad-rotor aircraft.

Figure 2.3 shows the tethered quad-rotor UAV moments before touch-down during autonomous landing. The aim of the autonomous tethered landing mission is to bring the aircraft to land while simultaneously winching the tether to keep it tight and prevent it from getting tangled into the rotors. The thrust capacity of the rotors determines the payload carrying capacity of the quad-rotor. Each of the rotors has a thrust capacity of 32 N. With the quad-rotor weighing 5.8 kg, the vehicle is capable of carrying a payload equivalent to its own weight. A high payload carrying capacity is desired to cater for the downward pulling force exerted by the tether on the quad-rotor during landing.

Figure 2.3: The tethered quad-rotor during autonomous descent.

The winch is shown in Figure 2.4 and is responsible for winching the tether during landing. The winch is powered by two laboratory DC power supplies and is driven by a geared DC motor. The winch can be manually controlled by an operator through a keypad. The design of the winch is outlined in more detail in Appendix A.

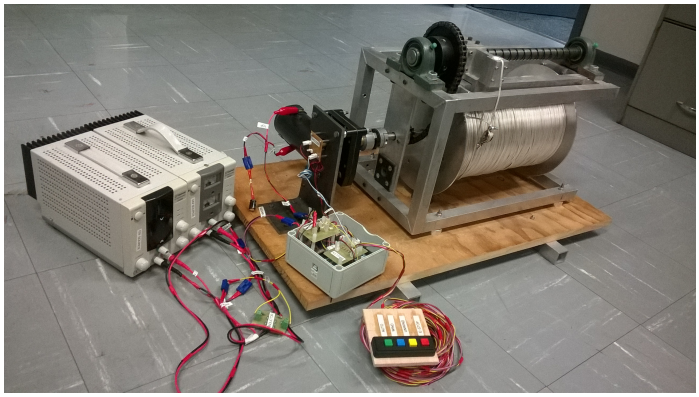

Figure 2.4: The winch system.

The ground station consists of a desktop computer and an RF transceiver. A 2.4

GHz wireless link is established between the quad-rotor and the ground station. An operator can send control commands from the ground station over the wireless link to the quad-rotor to perform autonomous missions. The quad-rotor reports telemetry data back to the ground station.

The aircraft can fly in autonomous mode in response to ground station commands or in manual mode under the control of the safety pilot. When in manual mode, the safety pilot controls the aircraft through a standard radio control (RC) remote. A typical flight procedure commences with a manual take-off by the safety pilot. Autonomous mode is enable in mid-air causing the quad-rotor to fly under the control of the ground station while the safety pilot stands by, ready to take over control in the event of unexpected aircraft behaviour.

2.2 The Quad-Rotor

A more detailed look into the quad-rotor vehicle airframe, avionics and software is taken in this section. Figure 2.5 shows a picture of the quad-rotor aircraft with annotations to show its different hardware components.

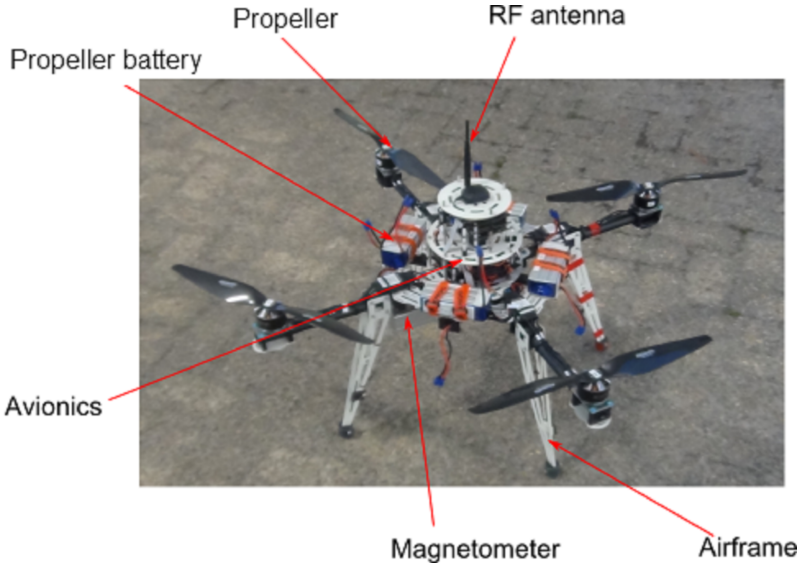

Figure 2.5: Quad-rotor components.

2.2.1 Quad-Rotor Airframe and Propulsion system

The quad-rotor used in this project is based on the Syn-X4 airframe by Syndrones shown in Figure 2.6 [4].

Figure 2.6: Syn-X4 airframe.

The airframe has a rotor to rotor span of 0.764 m and is furnished with four propulsion units. Each propulsion unit comprises of a rotor, a brushless DC motor (BLDC), an electronic speed controller (ESC) and a battery. Figure 2.7 shows one of the four propulsion units used. Fixed pitch 16x5.5" carbon fibre propellers are used as the rotor blades. The carbon fibre propellers exhibit high stiffness and and low inertia. High propeller stiffness reduces blade-flapping effects while low propeller inertia results in fast response [4]. Each propeller can output a maximum thrust output of 32 N. With the vehicle weighing 5.8 kg, the quad-rotor vehicle has a thrust to weight ratio of roughly 2.25. A thrust to weight ratio of approximately 2 has been found to be optimal for large quad-rotor applications in photography [4].

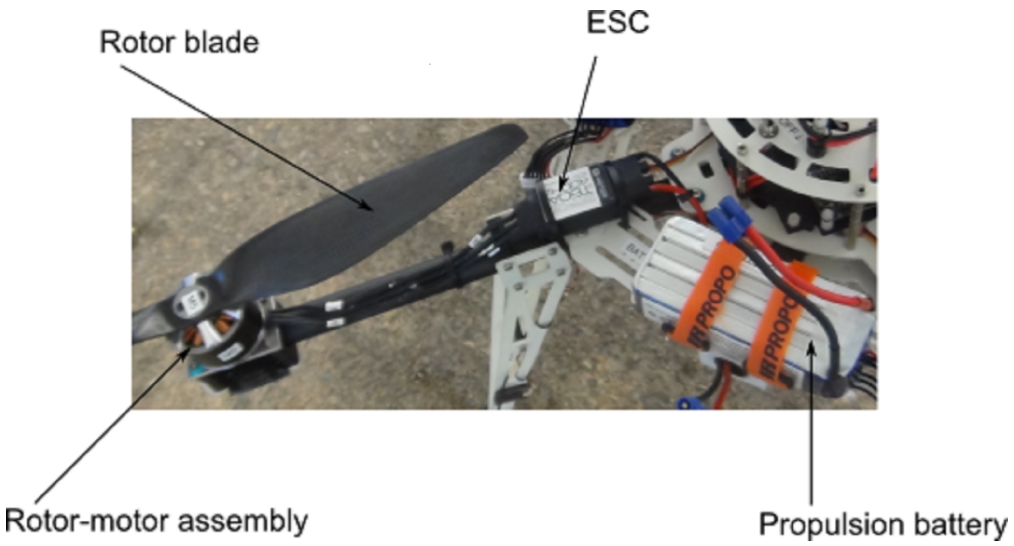

Figure 2.7: Quad-rotor aircraft propulsion unit.

Each rotor is driven by an MN4120 BLDC motor manufactured by T-motor. The motor has a 400 kV rating and is specially designed for large multirotor applica-

tions [30]. Each motor is controlled by a 60 A ESC manufactured by T-motor. The rotors, motors and ESCs are manufactured by the same manufacturer and are designed to be highly compatible [30]. Each propulsion unit is powered by a 6-cell, 2600 mAh, 22.2 V Lithium-ion polymer (LiPo) battery. The batteries are manufactured by X-Power RC. LiPo batteries have high energy densities and are rated at 35 C continuous discharged capacity [31]. When fully charged, the batteries allow for roughly 8 minutes of untethered flight or at most 4 minutes of tethered flight. As mentioned earlier, the limitation of flight duration due to battery life is the major motivation behind exploring tethered quad-rotors as a step towards the implementation of tethered power. The batteries also serve as an electronic payload and have a total mass of 1.7 kg.

Given that the quad-rotor vehicle is part of a tethered system, the airframe incorporates a tether attachment unit with a tether release mechanism as shown in Figure 2.8. The tether attachment unit is located underneath the central hub of the vehicle and consists of the tether attachment plate, the attachment bracket a servo and a pin. The tether release mechanism consists of a JR NES 591 servo linked to a pin. The end of the tether is bolted on to a steel swivel with a circular ring. To attach and lock the tether on to the aircraft, the servo pushes the pin through the swivel ring and the pin holes on the bracket as shown in Figure 2.9b. To detach/release the tether, the servo retracts the pin, leaving the swivel free from the bracket as shown in Figure 2.9a. Servo signals to attach or detach the tether can be issued by the safety pilot flicking a switch on the RC remote or by an operator clicking a button on the ground station graphical user interface (GUI).

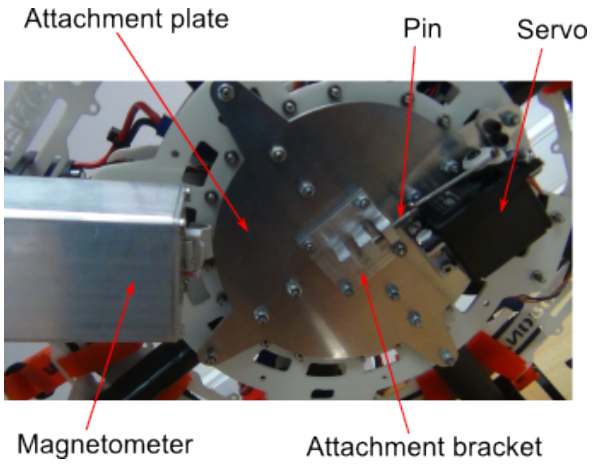

Figure 2.8: Tether attachment unit.

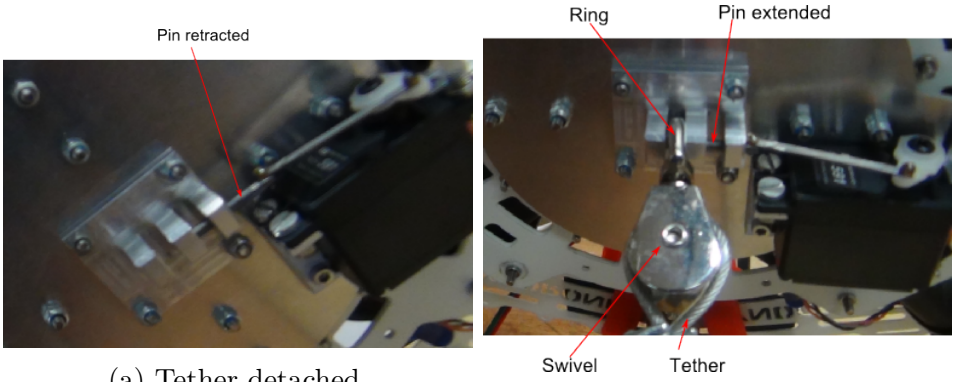

(a) Tether detached.

(b) Tether attached

Figure 2.9: Tether attachment mechanism.

The tether attachment plate and bracket are made from 6082 T6 aluminium [4]. Aluminium has a low density and therefore the design makes for a desirably low vehicle weight. Aluminium is also locally available, easily machinable and paramagnetic. The paramagnetic properties minimise the influence of the tether attachment unit on the magnetic field measured by the magnetometer.

2.2.2 Quad-Rotor Avionics and Software

The vehicle avionics hardware includes the On-Board Computer (OBC), sensors, an RF transceiver, an RC receiver, and a servo board. The architecture of the avionics is shown in Figure 2.10. The avionics stack was developed in-house in previous projects in the ESL. The design is modular and can be deployed on different platforms including fixed-wing UAVs and helicopters [32]. The quad-rotor avionics stack consists of the following sensors:

- GPS receiver
- Magnetometer
- Inertial Measurement Unit
- Status sensors

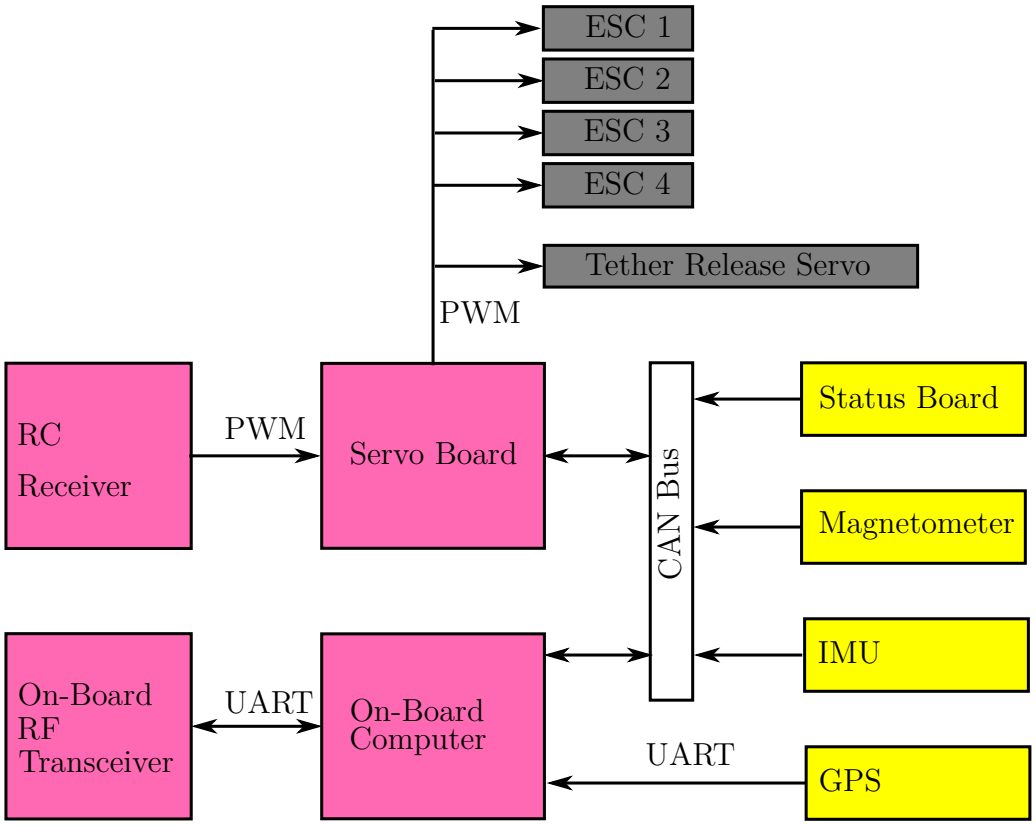

Figure 2.10: Avionics architecture.

The GPS receiver is a NEO-7P module manufactured by uBlox. The module is a stand-alone, single frequency GPS receiver. Sub-meter horizontal accuracy is achieved using *Precise Point Positioning* (PPP) technology. The NEO-7P is relatively low cost compared to its Real-Time Kinematic (RTK) and Differential GPS (DGPS) technology-based counterparts.

The HMC2003 magnetometer by Honeywell is used in the avionics stack. The magnetometer updates measurements of the geomagnetic field vector in body axes at a frequency of 50 Hz. The geomagnetic field vector is used by the OBC kinematic state estimator software and compared to the geomagnetic field vector of the flight location to obtain the vehicle's measured attitude.

The Inertial Measurement Unit (IMU) used is the ADIS16255 by Analog devices and it consists of a 3-axis gyroscope and a 3-axis accelerometer. Angular rate and specific acceleration measurements are obtained from the IMU at 100 Hz.

The currents and voltages of the propeller batteries and the avionics battery are

monitored by an ensemble of hall-effect sensors termed the status sensors. Status sensors are mounted onto the status board. Voltage and current readings are transmitted to the ground station over the RF link at a frequency of 2 Hz. An operator monitors status sensor readings displayed on the ground station during flight.

Sensor are mounted onto separate boards designed to perform analogue-to-digital conversion of sensor measurements [4]. Digitised sensor measurements are transmitted to the OBC via a Control Area Network (CAN) bus except for GPS measurements which are transmitted via a Universal Asynchronous Receiver-Transmitter (UART). The OBC contains two dsPIC30F microcontrollers (MCUs) manufactured by Microchip Technology Inc. One MCU is dedicated to parsing GPS data while the second MCU is responsible for executing control, state estimation, data logging and communication between the OBC and the ground station. A kinematic state estimator runs on the OBC and is responsible for generating optimal state estimates by utilising measurements from the aeronautical sensors (GPS, magnetometer and IMU). Figure 2.11 shows the state estimation scheme implemented by the OBC firmware.

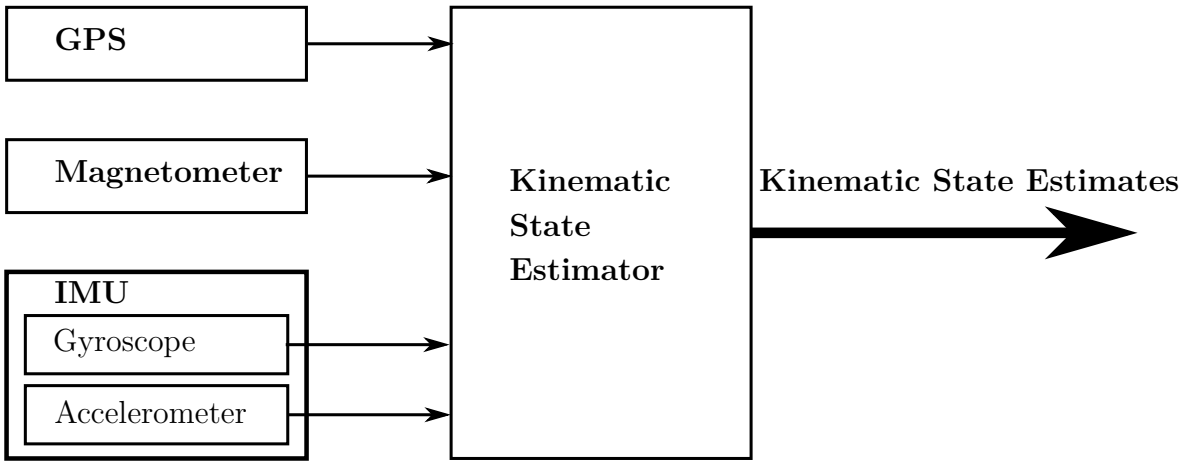

Figure 2.11: State estimation scheme.

The servo board serves to perform analogue-to-digital conversions as well as digital-to-analogue conversions [4]. The RC receiver receives safety pilot commands from the remote sticks as PWM (analogue) pulses. The servo board digitises the commands and transmits the digitised commands to the OBC via the CAN bus. The control algorithm running on the OBC computes actuator commands in digital form. The actuator commands are sent via the CAN bus to the servo board where they are converted to PWM pulses and transmitted to the ESCs. The avionics are powered by a single 3-cell, 12.6 V, 1200 mAh LiPo battery. Vibration mounts are used to mount the avion-

ics onto the airframe. The vibration mounts were designed by Ioppo to have a cut-off frequency of 50 Hz to reject the 65 - 125 Hz frequency range of the propeller motors [4].

The OBC communicates using an on-board XStream RF transceiver manufactured by Digi International. An identical RF transceiver on the ground station completes a 2.4 GHz wireless communication link between the ground station and the vehicle. Telemetry data is reported to the ground station over the wireless link and is displayed on the ground station GUI for monitoring by an operator. Control commands are also sent from the ground station to the vehicle via the wireless link. Control commands include, but are not limited to, commands to arm or disarm selected control loops.

2.3 The Ground Station Hardware and Software

The ground station hardware consists of a desktop computer and an RF transceiver. Figure 2.12 shows the ground station architecture. The ground station application (GSA) runs on the desktop computer and is written in a variation of the C++ programming language called Qt Creator. Qt Creator is designed for efficient and simple implementation of graphical user interface (GUI) type of applications. The computer communicates to the RF transceiver via USB. Vehicle commands are sent from the GSA by an operator and are transmitted to the quad-rotor's RF transceiver over the wireless communication link. The quad-rotor also reports telemetry data to the GSA over the wireless link.

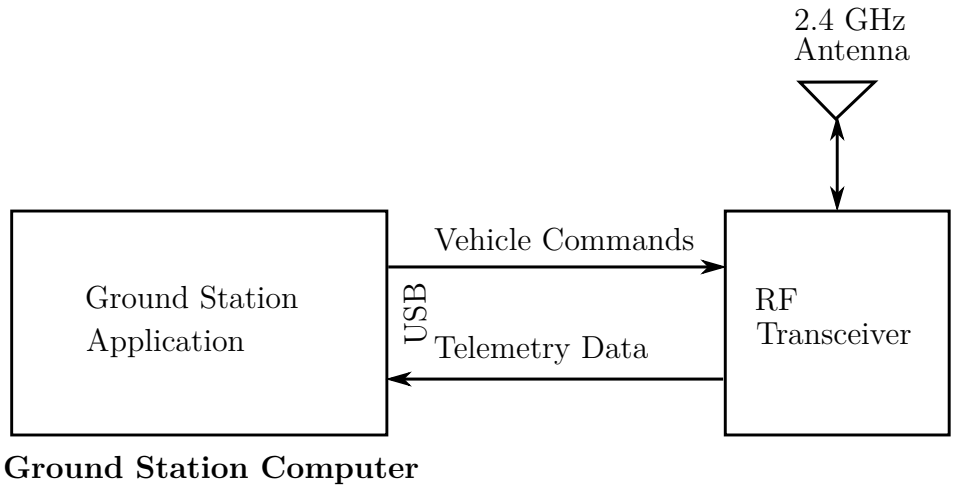

Figure 2.12: Ground station architecture.

Figure 2.13 shows a screenshot of the Ground Station Application GUI. The GSA comprises of a number of tabs including, but not limited to, the controller tab, sensors tab and estimator tab. Sensor measurements are displayed on the sensors tab in real time. The estimator tab displays kinematic state estimates. The controller tab is furnished with buttons for the arming and disarming of control loops. Outer loop control references can also be issued. The GSA also has buttons for enabling and initialising the kinematic state estimator and for starting and stopping the logging of flight data onto the on-board SD card.

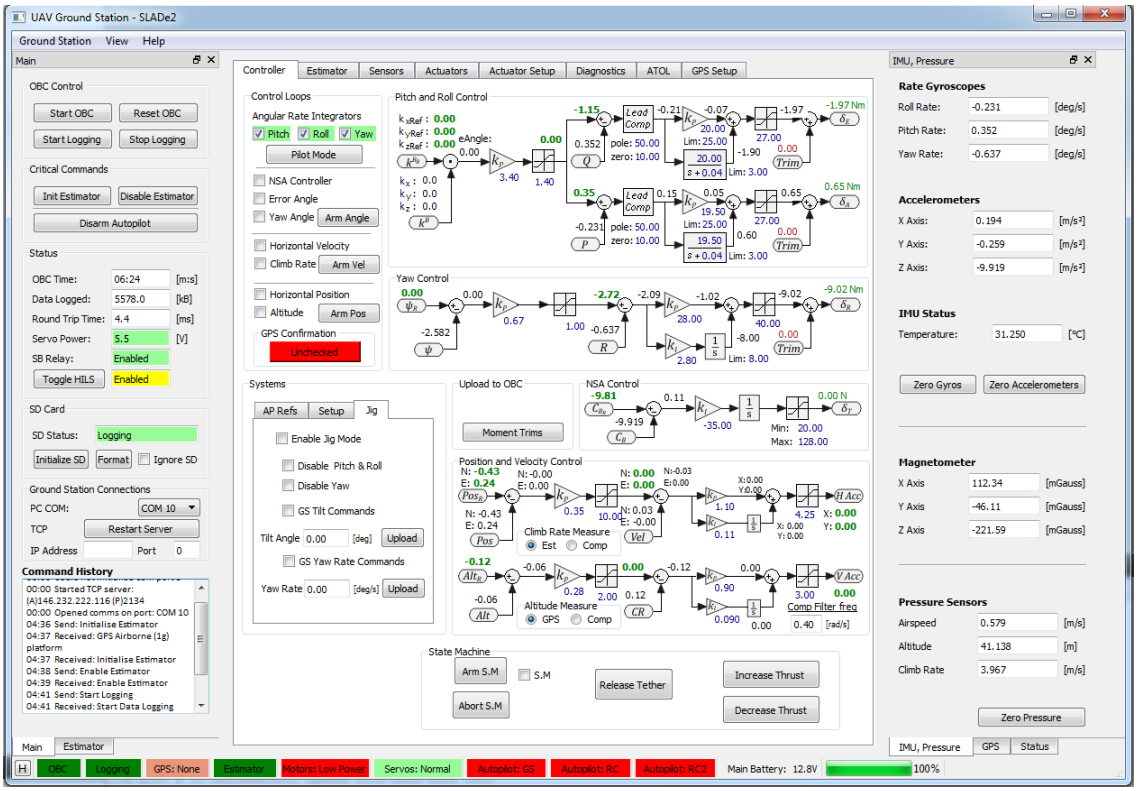

Figure 2.13: Screenshot of ground station application GUI.

2.4 The Winch

The winch is a complete subsystem whose hardware and software were developed in this project as detailed in Appendix A. The winch is responsible for winching the tethered quad-rotor during the landing phase of autonomous flight. Figure 2.14 is a picture of the winch with its different components labelled.

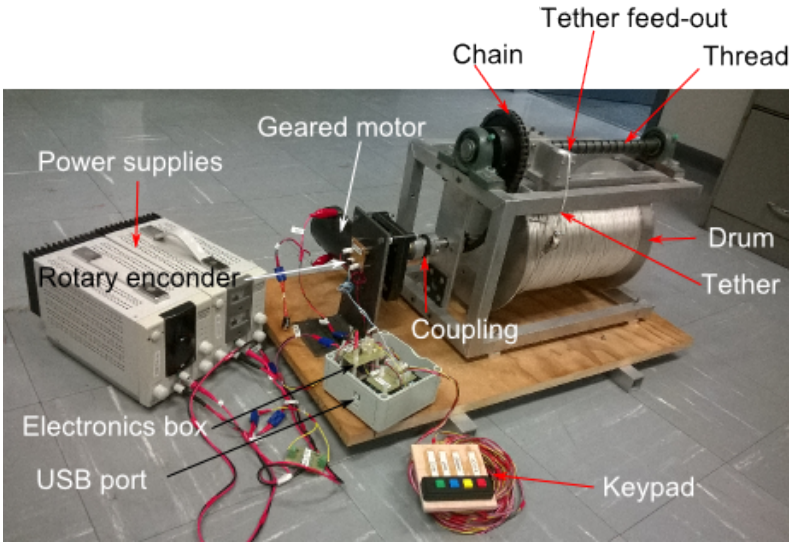

Figure 2.14: Picture of winch.

The winch is driven by a DC motor. Manual user commands are given to the winch by an operator through a keypad. During landing, the winch is controlled by the constant winching speed controller presented in Section 6.2. The winch firmware is implemented in the form of a finite state machine as detailed in Section A.3.2. Winch speed is estimated by calculating the rate of change of winch angular position as measured by a rotary encoder. The winch electronics also include a current transducer to measure armature current and an Arduino Mega 2560 board to execute the firmware. Complete details of the winch system design are given in Appendix A.

2.5 Project Overview

This section gives a brief indication of the components of the tethered quad-rotor system that were inherited from the previous project and those that constitute new work.

Components of the system that were inherited from the previous project are:

- The quad-rotor hardware.
- The kinematic state estimator portion of the flight control firmware.
- The HIL simulation environment.

The following aspects of the project include a mixture of previous work and new work:

(i) The flight control system was largely developed in this project. One control loop (NSA controller) was however inherited while one loop (Pitch/Roll rate controller)

was adapted. Such adaptations are documented when discussing the relevant loop in Chapter 5.

(ii) The ground station GUI application was largely inherited as part of the existing system. However, the components of the application that relate to the landing phase of the flight were added as new work.

(iii) Similarly, the RF communication portion of the flight firmware was also inherited, with components relating to the landing phase added as new work.

(iv) The landing platform was inherited from previous landing projects and was fitted with legs to allow for landing over the winch.

The current project contributed the following components to the system in entirety:

(a) The spring-damper tether model in Section 3.3.4 was conceptualised and developed.

(b) The software simulation environment used in the project.

(c) The formulation and validation of the point-mass model in Section 6.3.

(d) The automated landing state machines in Sections 7.1 and 6.1.

(e) The entire winch system documented in Appendix A, including hardware and firmware.

2.6 Chapter Summary

This chapter presented a high-level overview of the tethered quad-rotor unmanned aerial system. The various subsystems constituting the unmanned aerial system were presented as well as the system command structure. A more detailed discussion of the quad-rotor aircraft was presented in Section 2.2 while the ground station was handled in Section 2.3. The winch was discussed in Section 2.4. Section 2.5 presented an overview of the work that was inherited from the previous project and that which was developed in the current project. The high-level overview in this chapter gives a grasp on how the various components of the project complement each other and sets the stage for in-depth discussions of the components in the chapters to come.

Chapter 3

Mathematical Aircraft Modelling

In this chapter, a mathematical model for the quad-rotor aircraft is presented. The tether is modelled as a disturbance force and disturbance moment acting on the quad-rotor. Section 3.1 outlines the different axis systems utilised and the notation adopted for the kinetic and kinematic states of the tethered vehicle. The kinetics and kinematics of the vehicle are then presented in Section 3.2. Thereafter, the constituent forces and moments acting on the tethered quad-rotor UAV are presented in Section 3.3. The mathematical model presented in this chapter is linearised and used in flight control system design and simulation in Chapter 5.

3.1 Axis Systems and Notation

To fully represent the motion of the tethered quad-rotor throughout the landing mission, two axis systems are used. The inertial axis system is described in Section 3.1.1. Section 3.1.2 covers the aircraft body axis system. The symbols used to denote the components of forces, moments and velocities of the vehicle in the vehicle body axes are presented in section 3.1.3.

3.1.1 Inertial Axis System

Newton's equations of motion are powerful in modelling the motion of particles, rigid bodies and UAV's. However, Newton's equations can only be applied in an inertial axis system. To take advantage of Newton's equations, a North-East-Down (NED) inertial co-ordinate system is adopted as shown in Figure 3.1. An inertial axis system is also the most intuitive axis system to use when specifying performance indicators e.g. position error upon touch-down. The inertial x-axis X_I points towards North while the y-axis Y_I points towards East. The z-axis Z_I points down [33]. The origin of the

inertial axis system is chosen at a convenient location such as the take-off point on the runway or the tether feed-out point on the winch. The NED axis system is modelled as if the earth is locally flat and non-rotating.

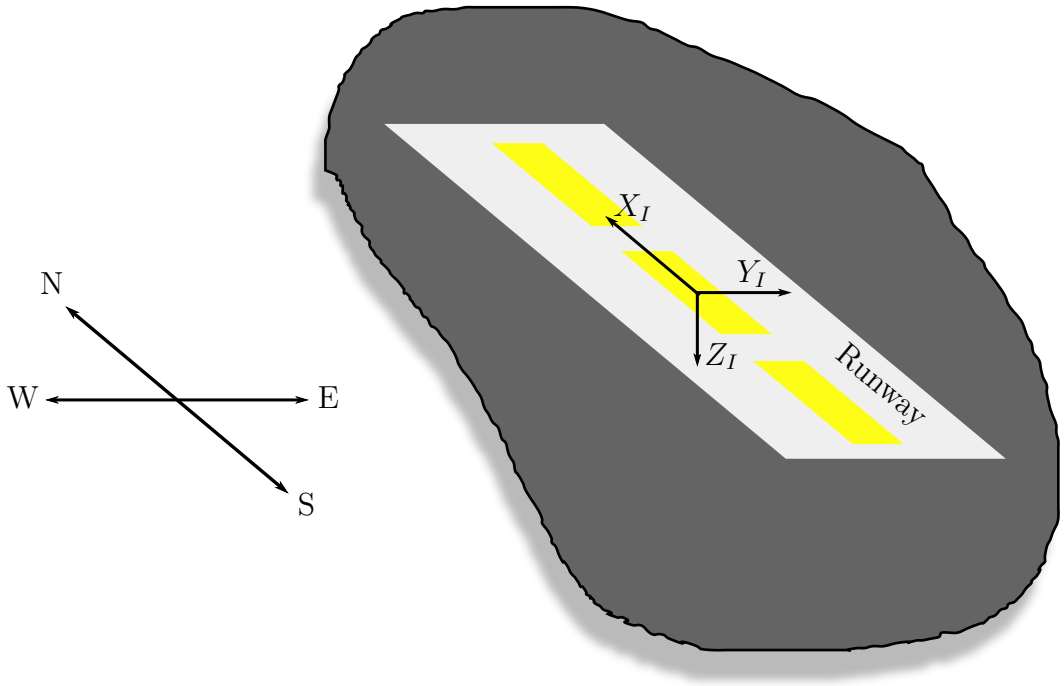

Figure 3.1: The inertial axis system.

3.1.2 Body Axis System

The aeronautical sensors and actuators are mounted on the aircraft frame. It is therefore convenient to define an aircraft body axis system in which sensor measurements and actuator forces and moments are coordinated. The body axis system has its origin at the vehicle's centre of mass. The body x-axis X_B coincides with one of the moment arms, and extends towards the front of the vehicle. The body y-axis Y_B is perpendicular to the X_B-axis, coinciding with the starboard (right) moment arm of the quad-rotor. The body z-axis is perpendicular to the plane containing the moment arms and points downwards from the aircraft's centre of mass. The body axes translate and rotate with the vehicle and are illustrated in Figure 3.2.

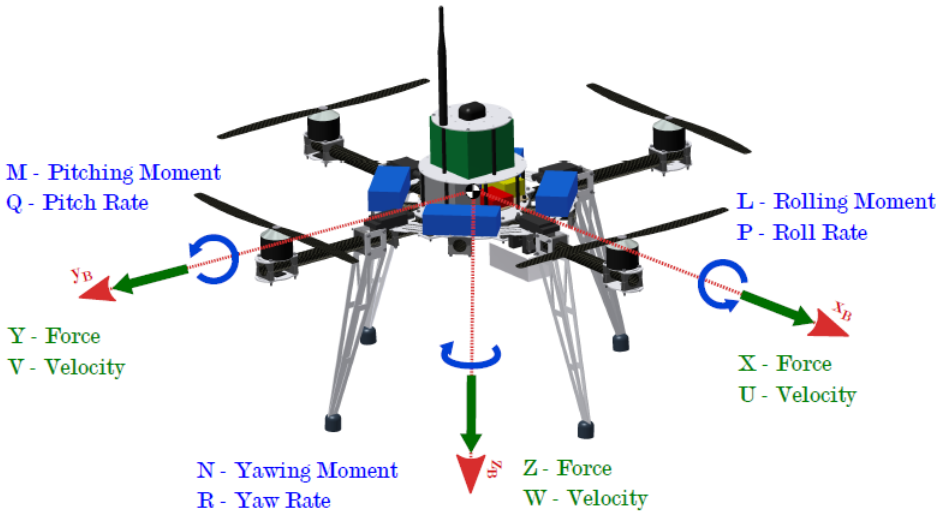

Figure 3.2: The body axis system (Adapted from [4]).

3.1.3 Notation

In addition to illustrating the body axis system, Figure 3.2 also shows the positive senses and the interpretation of forces along and moments around each of the body axes. Moreover, the linear and angular velocity components for each of the axes are also depicted in Figure 3.2. The forces, moments and velocities along the X_B, Y_B and Z_B axes are denoted as follows:

- X, Y, Z - Force components along the respective body axes.
- L, M, N - Moment components around the respective body axes.
- U, V, W - Linear velocity components along the respective body axes.
- P, Q, R - Angular velocity components around the respective body axes.

The linear velocity can alternatively be expressed in polar coordinates as a vehicle speed $\bar{\mathbf{V}}$, an angle of attack α and a side slip angle β. Figure 3.3 illustrates the relationship between the Cartesian and polar forms of the velocity vector. Equations 3.1, 3.2 and 3.3 are used to obtain polar coordinates of the velocity from the Cartesian coordinates. Inversely, Equations 3.4, 3.5 and 3.6 are used to convert velocity back to Cartesian coordinates in the body axis system [33].

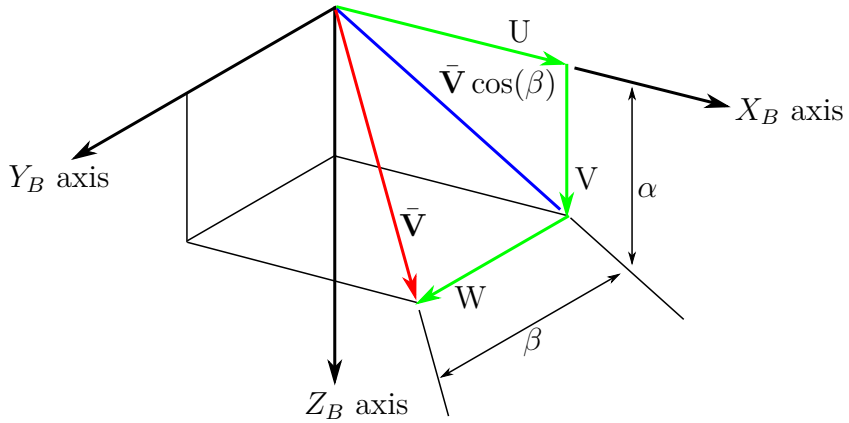

Figure 3.3: Velocity components in cartesian and polar coordinates.

$$\bar{\mathbf{V}} = \sqrt{U^2 + V^2 + W^2} \tag{3.1}$$

$$\alpha = \tan^{-1}\left(\frac{W}{U}\right) \tag{3.2}$$

$$\beta = \sin^{-1}\left(\frac{V}{\bar{\mathbf{V}}}\right) \tag{3.3}$$

$$U = \bar{\mathbf{V}}\cos(\alpha)\cos(\beta) \tag{3.4}$$

$$V = \bar{\mathbf{V}}\sin(\beta) \tag{3.5}$$

$$W = \bar{\mathbf{V}}\sin(\alpha)\cos(\beta) \tag{3.6}$$

3.2 Kinetics and Kinematics

With the tether isolated and treated as a disturbance acting on the quad-rotor UAV, the quad-rotor is modelled as a rigid body with six degrees of freedom. The disturbance forces and moments experienced by the quad-rotor due to the tether are modelled in Section 3.3.4. The vehicle's translation contributes three degrees of freedom and the vehicle's rotation contributes the remaining three degrees of freedom. Small UAVs like the one used in this project can be modelled as rigid bodies because of negligible deformation. For large UAVs however, the deformations and perturbations have to be accounted for in the modelling. In this section, rigid body dynamic equations are applied to the quad-rotor. The kinetic equations are presented in Section 3.2.1 and the kinematics are presented in Section 3.2.2.

3.2.1 Kinetics

Kinetic equations relate the forces and moments acting on the vehicle to its kinematic states such position, velocity and acceleration. With the notation shown in Figure 3.2, Cook showed that the kinetic equations of the vehicles are as shown in Equations 3.7 to 3.12 [33].

$$X = m(\dot{U} - VR + WQ) \tag{3.7}$$
$$Y = m(\dot{V} + UR - WP) \tag{3.8}$$
$$Z = m(\dot{W} - UQ + VP) \tag{3.9}$$
$$L = \dot{P}I_{xx} + QR(I_{zz} - I_{yy}) \tag{3.10}$$
$$M = \dot{Q}I_{yy} + PR(I_{xx} - I_{zz}) \tag{3.11}$$
$$N = \dot{R}I_{zz} + PQ(I_{yy} - I_{xx}) \tag{3.12}$$

Equations 3.7 to 3.12 arise from applying Newton's laws of motion to the quad-rotor vehicle in the body axis system. In the equations, m is the mass of the quad-rotor and I_{xx}, I_{yy} and I_{zz} are the quad-rotor's moments of inertia around the X_B, Y_B and Z_B axes respectively. The following assumptions are made in the derivation of Equations 3.7 to 3.12 [33]

- The quad-rotor aircraft is a rigid body.
- The quad-rotor has a constant mass.
- I_{xz} is negligibly small.
- The X_B and Z_B axes lie in the quad-rotor's plane of symmetry and therefore I_{xy} and I_{yz} are zero.

The aircraft used in this project satisfies the assumptions.

3.2.2 Kinematics

Kinematic equations describe how the vehicle's position and attitude are determined from linear and angular velocities. The transformation matrix to convert kinematic state vectors from body axes to inertial axes and vice versa also forms part of kinematic analysis.

3.2.2.1 Euler Angles

The attitude of the vehicle is specified using Euler parametrisation. A roll angle ϕ, a pitch angle θ and a yaw angle ψ are used to express the orientation of the body axis system relative to the inertial axis system. The three angles are known as Euler angles and are shown in Figure 3.4.

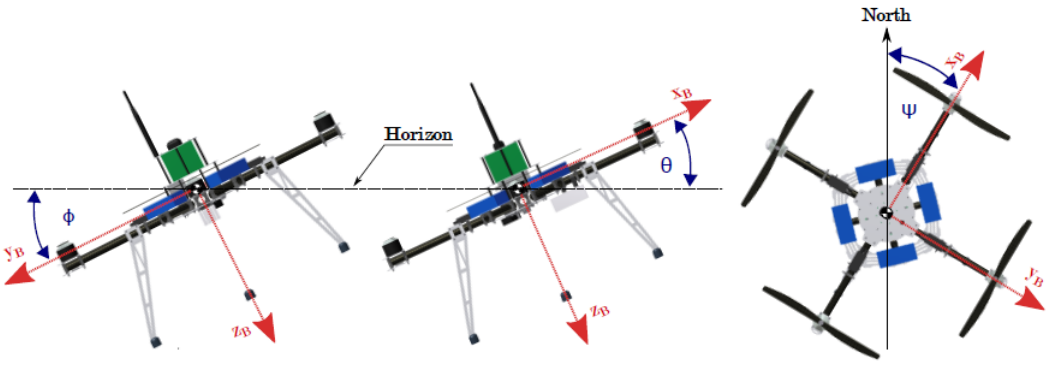

Figure 3.4: Euler angles(Adapted from [4]).

The three Euler angles can be applied in many different orders and each order yields a unique Euler angle parametrisation. For this project, the Euler 3-2-1 parametrisation is used for which the Euler angles are applied in the following sequence:

1. Begin with the body axes aligned with the inertial axes.
2. Yaw the original body axis system through a heading angle ψ.
3. Pitch the resulting body axis through a pitch angle θ.
4. Finally roll the resulting body axis through a roll angle ϕ.

3.2.2.2 Attitude Dynamics

The rates of change of the Euler angles can be expressed in terms of the instantaneous Euler angles and the angular rates in body axes [33]. For the Euler 3-2-1 parametrisation, Equation 3.13 is the expression for the rates of change of the Euler angles [33]. As seen from Equation 3.13, when the Euler 3-2-1 parametrisation is used, the pitch angle of the aircraft must always be less than $\frac{\pi}{2}$ radians. All the manoeuvres executed by the UAV in this project conform to this condition.

$$\begin{bmatrix} \dot{\phi} \\ \dot{\theta} \\ \dot{\psi} \end{bmatrix} = \begin{bmatrix} 1 & \sin\phi\tan\theta & \cos\phi\tan\theta \\ 0 & \cos\phi & -\sin\phi \\ 0 & \sin\phi\sec\theta & \cos\phi\sec\theta \end{bmatrix} \begin{bmatrix} P \\ Q \\ R \end{bmatrix}, \qquad |\theta| \neq \frac{\pi}{2} \tag{3.13}$$

3.2.2.3 Position Dynamics

Yet another important component of the kinematic analysis is the conversion of the aircraft's velocity vector from body axes to inertial axes. Transformation matrices are an effective way to transform vectors from one coordinate system to another. A transformation matrix is desired to transform a velocity vector in inertial axes through yaw, pitch and roll to body axes. Once such a transformation matrix is obtained, its inverse can then be used to transform kinematic states from body axes to inertial axes.

Consider a general vector $\mathbf{V}$ as shown in Figure 3.5 in the original x_0-y_0-z_0 axis system. The coordinates of the vector in the original axis system are given by Equation 3.14. A new x_1-y_1-z_1 system is obtained by yawing the original axes through a yaw angle ψ. Through simple geometry, the coordinates of the vector in the new axis system are determined by Equation 3.15.

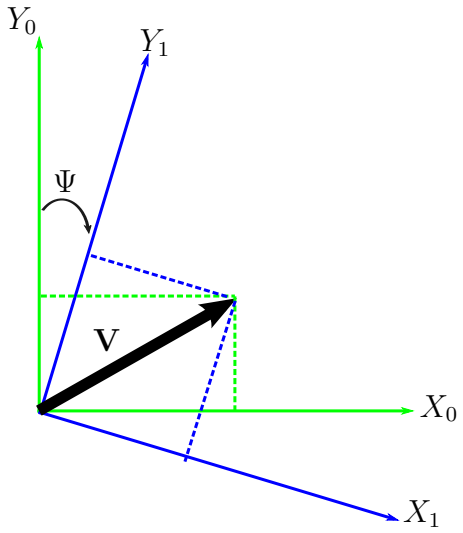

Figure 3.5: Single axis yaw rotation.

$$\mathbf{V} = \begin{bmatrix} x_0 \\ y_0 \\ z_0 \end{bmatrix} \tag{3.14}$$

$$\begin{bmatrix} x_1 \\ y_1 \\ z_1 \end{bmatrix} = \begin{bmatrix} \cos\psi & \sin\psi & 0 \\ -\sin\psi & \cos\psi & 0 \\ 0 & 0 & 1 \end{bmatrix} \begin{bmatrix} x_0 \\ y_0 \\ z_0 \end{bmatrix} \tag{3.15}$$

The x_1-y_1-z_1 axis system can be pitched by an angle θ to obtain a new x_2-y_2-z_2 axis system. The coordinates of the vector in the x_2-y_2-z_2 axis system is given by Equation 3.16.

$$\begin{bmatrix} x_2 \\ y_2 \\ z_2 \end{bmatrix} = \begin{bmatrix} \cos\theta & 0 & -\sin\theta \\ 0 & 1 & 0 \\ \sin\psi & 0 & \cos\theta \end{bmatrix} \begin{bmatrix} x_1 \\ y_1 \\ z_1 \end{bmatrix} \tag{3.16}$$

Finally, the x_2-y_2-z_2 axis system can be rolled through an angle ϕ to obtain a new x_3-y_3-z_3 axis system. Equation 3.17 gives the coordinates of the vector in the new x_3-y_3-z_3 axis system.

$$\begin{bmatrix} x_3 \\ y_3 \\ z_3 \end{bmatrix} = \begin{bmatrix} 1 & 0 & 0 \\ 0 & \cos\phi & \sin\phi \\ 0 & -\sin\phi & \cos\phi \end{bmatrix} \begin{bmatrix} x_2 \\ y_2 \\ z_2 \end{bmatrix} \tag{3.17}$$

The overall transformation matrix from the x_0-y_0-z_0 axis system to the x_1-y_1-z_1 axis system is given by Equation 3.18.

$$\begin{aligned} \begin{bmatrix} x_3 \\ y_3 \\ z_3 \end{bmatrix} &= \begin{bmatrix} \cos\psi & \sin\psi & 0 \\ -\sin\psi & \cos\psi & 0 \\ 0 & 0 & 1 \end{bmatrix} \begin{bmatrix} \cos\theta & 0 & -\sin\theta \\ 0 & 1 & 0 \\ \sin\psi & 0 & \cos\theta \end{bmatrix} \begin{bmatrix} 1 & 0 & 0 \\ 0 & \cos\phi & \sin\phi \\ 0 & -\sin\phi & \cos\phi \end{bmatrix} \begin{bmatrix} x_0 \\ y_0 \\ z_0 \end{bmatrix} \\ &= \begin{bmatrix} C_\psi C_\theta & S_\psi C_\theta & -S_\theta \\ C_\psi S_\theta S_\phi - S_\psi C_\phi & S_\psi S_\theta S_\phi + C_\psi C_\phi & C_\theta S_\phi \\ C_\psi S_\theta C_\phi + S_\psi S_\phi & S_\psi S_\theta C_\phi - C_\psi S_\phi & C_\theta C_\phi \end{bmatrix} \begin{bmatrix} x_0 \\ y_0 \\ z_0 \end{bmatrix} \end{aligned} \tag{3.18}$$

Where:

$$C_\# = \cos(\#) \tag{3.19}$$

$$S_\# = \sin(\#) \tag{3.20}$$

When aircraft attitude is expressed in terms of Euler 3-2-1 parameters, the transformation matrix in Equation 3.18 is exactly the matrix required to transform a velocity vector from inertial axes to body axes. The transformation matrix is known as the Direction Cosine Matrix (DCM) and is used to convert *all* kinematic state vectors from inertial axes to body axes. As an example, Equation 3.21 utilises the DCM to convert the aircraft's velocity vector from inertial axes to body axes.

$$\begin{bmatrix} U \\ V \\ W \end{bmatrix} = \begin{bmatrix} C_\psi C_\theta & S_\psi C_\theta & -S_\theta \\ C_\psi S_\theta S_\phi - S_\psi C_\phi & S_\psi S_\theta S_\phi + C_\psi C_\phi & C_\theta S_\phi \\ C_\psi S_\theta C_\phi + S_\psi S_\phi & S_\psi S_\theta C_\phi - C_\psi S_\phi & C_\theta C_\phi \end{bmatrix} \begin{bmatrix} \dot{N} \\ \dot{E} \\ \dot{D} \end{bmatrix} \tag{3.21}$$

The inverse of the DCM is known as the Inverse Direction Cosine Matrix (IDCM) and is used to convert *all* kinematic state vectors from body axes to inertial axes. The DCM is an orthogonal vector and therefore its inverse can be computed by simply taking its transpose [37]. Equation 3.22 shows how the IDCM is used to convert the quad-rotor's velocity vector from body axes to inertial axes. The DCM and IDCM are captured in Equations 3.23 and Equation 3.24 for future reference.

$$\begin{bmatrix} \dot{N} \\ \dot{E} \\ \dot{D} \end{bmatrix} = \begin{bmatrix} C_\psi C_\theta & C_\psi S_\theta S_\phi - S_\psi C_\phi & C_\psi S_\theta C_\phi + S_\psi S_\phi \\ S_\psi C_\theta & S_\psi S_\theta S_\phi + C_\psi C_\phi & S_\psi S_\theta C_\phi - C_\psi S_\phi \\ -S_\theta & C_\theta S_\phi & C_\theta C_\phi \end{bmatrix} \begin{bmatrix} U \\ V \\ W \end{bmatrix} \tag{3.22}$$

$$\Big[\mathbf{DCM}\Big] = \begin{bmatrix} C_\psi C_\theta & S_\psi C_\theta & -S_\theta \\ C_\psi S_\theta S_\phi - S_\psi C_\phi & S_\psi S_\theta S_\phi + C_\psi C_\phi & C_\theta S_\phi \\ C_\psi S_\theta C_\phi + S_\psi S_\phi & S_\psi S_\theta C_\phi - C_\psi S_\phi & C_\theta C_\phi \end{bmatrix} \tag{3.23}$$

$$\Big[\mathbf{IDCM}\Big] = \begin{bmatrix} C_\psi C_\theta & C_\psi S_\theta S_\phi - S_\psi C_\phi & C_\psi S_\theta C_\phi + S_\psi S_\phi \\ S_\psi C_\theta & S_\psi S_\theta S_\phi + C_\psi C_\phi & S_\psi S_\theta C_\phi - C_\psi S_\phi \\ -S_\theta & C_\theta S_\phi & C_\theta C_\phi \end{bmatrix} \tag{3.24}$$

3.3 Forces and Moments

This section presents the forces and moments acting on the tethered quad-rotor UAV. The UAV experiences forces and moments from its actuators, aerodynamic drag, gravity and the tether. All forces and moments are coordinated in the body axis system.

3.3.1 Actuators

The principle of operation of quad-rotors has been explained in Chapter 1. Quad-rotors are steered by controlling the thrusts of the four rotors. The rotors on a quad-rotor are simple in design and do not include complex swash plates and rotor-head mechanics found on helicopters [1]. In this section, the rotor thrust response model is presented.

For each of the four rotors, the relationship between the rotor thrust commanded by the flight control system T_R and the instantaneous rotor thrust T is modelled by the first order lag dynamics in Equation 3.25. The time constant τ determines the bandwidth and hence the responsiveness of the vehicle. Ioppo determined the rotor time constant by connecting a motor and propeller to a load cell [4]. A step thrust command was issued and the thrust exerted by the motor on the load cell was measured to determine the rotor time constant. The rotor time constant was determined to be 0.25 seconds [4].

$$\frac{T(s)}{T_R(s)} = \frac{1}{1 + s\tau} \tag{3.25}$$

To simplify the control system design and implementation, virtual actuators are defined. Adopting traditional names used for fixed-wing aircraft control surfaces, a virtual aileron δA was defined as the instantaneous rolling moment of the quad-rotor. A virtual elevator δE was defined as the instantaneous pitching moment of the vehicle and a virtual thrust δT defined as the total rotor thrust along the $-Z_B$ axis. Finally, the virtual rudder δR was defined as the yawing moment exerted on the vehicle.

Figure 3.6 shows the positive senses of the virtual aileron, elevator and rudder [4]. The virtual thrust is simply the sum of the thrusts from the four rotors. The relationships between the virtual actuators and the rotor thrusts are given by Equations 3.26 to 3.29. The rotor moment arm is denoted by d_m, the rotor's chord length by r_D and the rotor's lift to drag ratio by R_{LD}. The chord length is the distance from the rotor axis to where the resultant rotor drag force acts [1]. Equations 3.26 to 3.29 can be arranged in the form of a mixing matrix which converts a four-element vector of individual rotor thrusts to a four-element vector of virtual actuators as shown in Equation 3.30. For simplicity, the flight control system issues virtual actuator commands which are then resolved to individual rotor thrust commands through the inverse mixing matrix. The flight control system is presented in detail in Chapter 5.

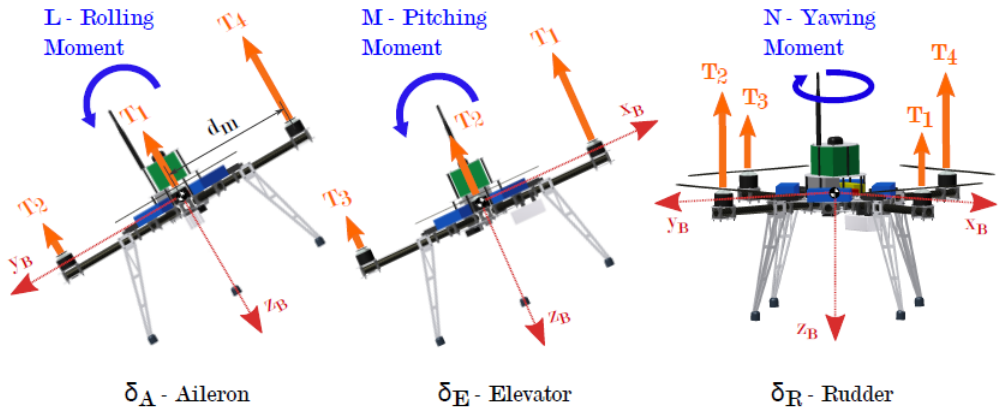

Figure 3.6: Virtual actuator definitons(Adapted from [4]).

$$\delta T = T_{R1} + T_{R2} + T_{R3} + T_{R4} \tag{3.26}$$

$$\delta A = d_m(T_{R4} - T_{R2}) \tag{3.27}$$

$$\delta E = d_m(T_{R1} - T_{R3}) \tag{3.28}$$

$$\delta R = \frac{r_D}{R_{LD}}(-T_{R1} + T_{R2} - T_{R3} + T_{R4}) \tag{3.29}$$

$$\begin{bmatrix} \delta T \\ \delta A \\ \delta E \\ \delta R \end{bmatrix} = \begin{bmatrix} 1 & 1 & 1 & 1 \\ 0 & -d_m & 0 & d_m \\ d_m & 0 & -d_m & 0 \\ -\frac{r_D}{R_{LD}} & \frac{r_D}{R_{LD}} & -\frac{r_D}{R_{LD}} & \frac{r_D}{R_{LD}} \end{bmatrix} \begin{bmatrix} T_{R1} \\ T_{R2} \\ T_{R3} \\ T_{R4} \end{bmatrix} \tag{3.30}$$

3.3.2 Aerodynamic Drag

The aerodynamic drag model used in this project quantifies the aerodynamic drag resulting from the velocity of the aircraft relative to the air. Wind is represented by a wind speed $\bar{\mathbf{V}}_{wind}$), a wind elevation angle α_{wind} and a wind azimuth angle β_{wind}. Figure 3.7 shows the wind vector representation. Equation 3.31 is used to express the wind in inertial axes. The DCM is used in Equation 3.32 to convert the wind vector from inertial to body axes. With the aircraft velocity vector and the wind velocity vector available in body axes, aerodynamic equations can now be applied to quantify the aerodynamic forces and moments acting on the aircraft.

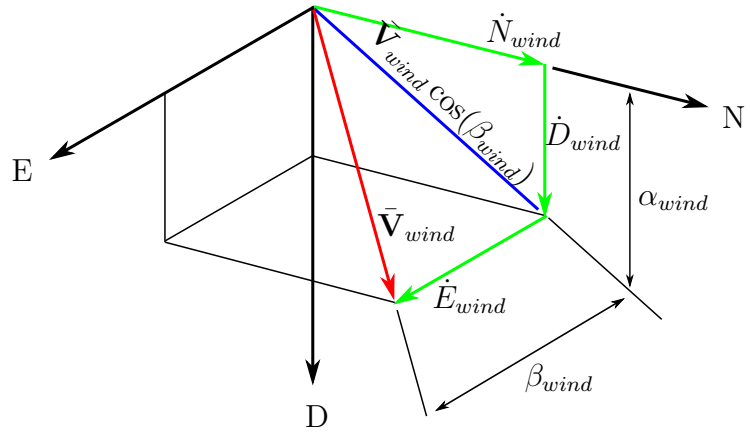

Figure 3.7: Wind components.

$$\begin{bmatrix} \dot{N}_{wind} \\ \dot{E}_{wind} \\ \dot{D}_{wind} \end{bmatrix} = \begin{bmatrix} \bar{\mathbf{V}}_{wind}\cos(\alpha_{wind})\cos(\beta_{wind}) \\ \bar{\mathbf{V}}_{wind}\sin(\beta_{wind}) \\ \bar{\mathbf{V}}_{wind}\sin(\alpha_{wind})\cos(\beta_{wind}) \end{bmatrix} \tag{3.31}$$

$$\begin{bmatrix} U_{wind} \\ V_{wind} \\ W_{wind} \end{bmatrix} = \begin{bmatrix} \mathbf{DCM} \end{bmatrix} \begin{bmatrix} \dot{N}_{wind} \\ \dot{E}_{wind} \\ \dot{D}_{wind} \end{bmatrix} \tag{3.32}$$

When an object with surface area A travels with a speed v_o through a stationary fluid of density ρ_f, the drag force opposing the motion of the object is given by Equation 3.33. The coefficient of aerodynamic drag is denoted by C_D.

$$F_d = \frac{1}{2}\rho_f C_D A {v_o}^2 \tag{3.33}$$

Equation 3.33 can modified to include the effect of the wind velocity vector in all the three body axes. The aerodynamic forces in the respective body axes are given by Equation 3.34. The terms CD_{Ax}, CD_{Ay} and CD_{Az} are the products of the drag coefficient and the respective surface area when facing each of the body axes. The terms are experimentally determined. To determine the value of CD_{Az}, the vehicle is flown at constant climb rate and constant horizontal position under no wind conditions. The total thrust exerted by the rotors and the climb rate are logged. With the air density known to be 1.225 kg.m^{-3}, Equation 3.33 is used to calculate CD_{Az}. To determine CD_{Ax} and CD_{Ay}, the vehicle is flown at constant tilt angle and constant altitude.

The thrust and velocity data logged under these conditions are used to determined CD_{Ax} and CD_{Ay}. These experiments were carried out on the vehicle by Ioppo and the determined values of the aerodynamic constants are documented in Table 3.1 [4].

Aerodynamic constant	Value (m^2)
CD_{Ax}	0.08
CD_{Ay}	0.08
CD_{Az}	0.102

Table 3.1: Experimentally determined aerodynamic constants [4].

$$\begin{bmatrix} X_D \\ Y_D \\ Z_D \end{bmatrix} = \frac{1}{2}\rho \begin{bmatrix} CD_{Ax}(U_{wind} - U)^2 \\ CD_{Ay}(V_{wind} - V)^2 \\ CD_{Az}(W_{wind} - W)^2 \end{bmatrix} \tag{3.34}$$

The moments exerted by the drag forces on the UAV result from the fact that the vehicle's Centre of Gravity (CoG) and Centre of Pressure (CoP) do not necessarily coincide. The resultant drag force acts through the CoP. The volumetric centre of the aircraft was used as an approximation for the CoP [33]. From the Autodesk Inventor CAD drawings of the quad-rotor, the vehicle's volumetric centre was found to be displaced by 0.03 m from the CoG on the Z_B-axis [4]. When the displacement between the CoP down on the Z_B from the CoG is denoted by p, the position vector in body axes from the CoG to the CoP is given Equation 3.35.

$$\mathbf{r}_D = \begin{bmatrix} 0 \\ 0 \\ p \end{bmatrix} \tag{3.35}$$

The moments due to aerodynamic drag are given by the cross product in Equation 3.36.

$$\begin{bmatrix} L_D \\ M_D \\ N_D \end{bmatrix} = \mathbf{r}_D \times \mathbf{F}_D$$
$$= \begin{bmatrix} 0 \\ 0 \\ p \end{bmatrix} \times \begin{bmatrix} X_D \\ Y_D \\ Z_D \end{bmatrix} \tag{3.36}$$

3.3.3 Gravity

Assuming a flat and non-rotating earth's surface, the vehicles CoG and Centre of Mass (CoM) are assumed to coincide [33]. The vehicle's gravitational force is modelled as acting through the vehicle's CoM and directed purely in the Z_I-axis. The forces due to gravity are presented in Equation 3.37 where g is the acceleration due to gravity with an approximate value of 9.81 m.s^{-2} and m is the mass of the quad-rotor.

$$\begin{bmatrix} X_G \\ Y_G \\ Z_G \end{bmatrix} = \begin{bmatrix} \mathbf{DCM} \end{bmatrix} \begin{bmatrix} 0 \\ 0 \\ mg \end{bmatrix}$$
$$= \begin{bmatrix} -\sin\theta \\ \cos\theta\sin\phi \\ \cos\theta\cos\phi \end{bmatrix} mg \tag{3.37}$$

Since the gravitational force acts through the CoM, gravity does not contribute any moments as shown in Equation 3.38.

$$\begin{bmatrix} L_G \\ M_G \\ N_G \end{bmatrix} = \begin{bmatrix} \mathbf{0} \end{bmatrix} \tag{3.38}$$

3.3.4 Tether

The tether is treated as a disturbance acting on the quad-rotor. For the aims of this project the UAV will fly at low altitudes with significant tether tension. The tether is therefore modelled as being straight throughout the landing phase of flight. To determine the tether force and moment vectors, the tether force direction is determined first in Section 3.3.4.1. Thereafter the tether force magnitude model is presented in

Section 3.3.4.2.

3.3.4.1 Tether Force Direction

In this section, only the tether force direction is modelled. For now, a tether force magnitude T_{tether} is assumed. The tether force magnitude is then modelled in section 3.3.4.2. Figure 3.8 illustrates the geometry of the quad-rotor, the tether and the winch. With the tether attachment point displaced by a distance r below the CoG, the position vector of the tether attachment point from the CoG is given by Equation 3.39. This vector can be transformed to the inertial system through Equation 3.40 to obtain Equation 3.41.

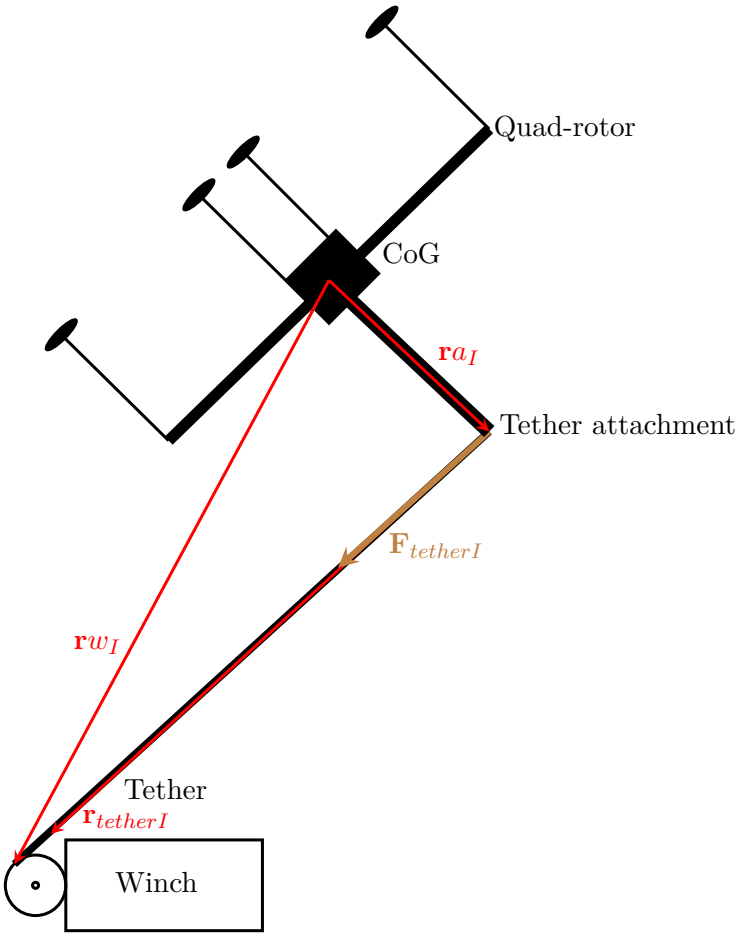

Figure 3.8: Tether force and moment vector diagram.

$$\mathbf{r}a_B = \begin{bmatrix} 0 \\ 0 \\ r \end{bmatrix} \tag{3.39}$$

$$\mathbf{r}a_I = \begin{bmatrix} \mathbf{IDCM} \end{bmatrix} \begin{bmatrix} 0 \\ 0 \\ r \end{bmatrix} \tag{3.40}$$

$$= \begin{bmatrix} \cos\psi \sin\theta \cos\phi + \sin\psi \sin\phi \\ \sin\psi \sin\theta \cos\phi - \cos\psi \sin\phi \\ \cos\theta \cos\phi \end{bmatrix} r \tag{3.41}$$

The position vector, in the inertial axis system, from the CoG to the tether feed-out point on the winch is given by Equation 3.42 where the subscript w denotes winch position. Equation 3.43 expresses the position vector from the tether attachment point to the tether feed-out point in inertial axis system. When normalised, this vector yields the unit vector pointing from the aircraft to the winch in the direction of the tether as presented in Equation 3.44.

$$\mathbf{r}w_I = \begin{bmatrix} N_w - N \\ E_w - E \\ D_w - D \end{bmatrix} \tag{3.42}$$

$$\mathbf{r}_{tetherI} = \mathbf{r}w_I - \mathbf{r}a_I \tag{3.43}$$

$$\mathbf{u}_{tetherI} = \frac{\mathbf{r}_{tetherI}}{|\mathbf{r}_{tetherI}|} \tag{3.44}$$

The tether force vector in the inertial axis system is given by Equation 3.45. The DCM is used, as indicated in Equation 3.46, to convert the inertial tether force vector into body axes. Finally, the moments due to the tether are computed through the cross product in Equation 3.47.

$$\mathbf{F}_{tetherI} = T_{tether}\mathbf{u}_{tetherI} \tag{3.45}$$

$$\begin{bmatrix} X_T \\ Y_T \\ Z_T \end{bmatrix} = \begin{bmatrix} \mathbf{DCM} \end{bmatrix} \begin{bmatrix} \mathbf{F}_{tetherI} \end{bmatrix} \tag{3.46}$$

$$\begin{bmatrix} L_T \\ M_T \\ N_T \end{bmatrix} = \mathbf{r}a_B \times \begin{bmatrix} X_T \\ Y_T \\ Z_T \end{bmatrix} \tag{3.47}$$

3.3.4.2 Tether Force Magnitude

To determine the tether force magnitude, the tether is modelled as a spring-damper composite capable of exhibiting tensile forces but not compressive forces. The spring model generates a component of tether tension proportional to the tether extension. The damper model generates a tether tension component proportional to the rate of change of the tether extension. The overall spring-damper force is given by Equation 3.48, where k_t is the tether stiffness, b_t is the tether damping coefficient and L_{ext} is the tether extension. The approximation of the tether stiffness and the damping coefficient is documented in Appendix F.2. Applying the Laplace Transform to Equation 3.48 yields Equation 3.49. The input-output relationship from tether extension to tether force is given by the transfer function in Equation 3.50. What remains is determine the value of L_{ext}.

$$T_{tether}(t) = k_t L_{ext}(t) + b_t \dot{L}_{ext}(t) \tag{3.48}$$

$$\begin{aligned} T_{tether}(s) &= k_t L_{ext}(s) + b_t s L_{ext}(s) \\ &= L_{ext}(s)\left[k_t + s b_t\right] \end{aligned} \tag{3.49}$$

$$\begin{aligned} \frac{L_{ext}(s)}{T_{tether}(s)} &= \frac{1}{s b_t + k_t} \\ &= \frac{\left(\frac{1}{k_t}\right)}{1 + s\left(\frac{b_t}{k_t}\right)} \end{aligned} \tag{3.50}$$

The tether force magnitude model is shown in Figure 3.9. The symbols appearing in the diagram denote tether variables as follows:

- L_t - instantaneous unstretched length of tether.

- L_{t0} - initial unstretched length of tether.
- L_{wound} - unstretched length of tether already wound.
- L_{ext} - instantaneous tether extension.
- v_w - linear winching speed.

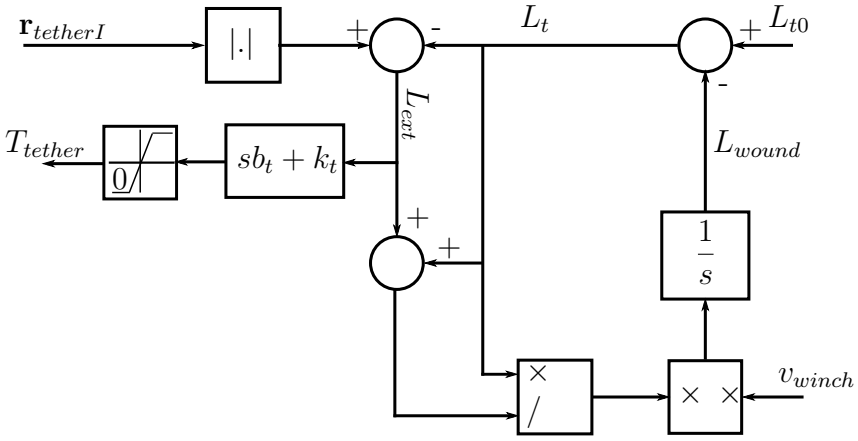

Figure 3.9: Tether force magnitude model.

With reference to Figure 3.9, the tether force is modelled by Equation 3.48 with a lower limit of 0 N. We recall from Section 3.3.4.1 that $\mathbf{r}_{tetherI}$ is the position vector in inertial axes from the tether attachment point to the tether feed-out point on the winch. Equation 3.51 is an expansion of Equation 3.43 to represent this vector. With the tether modelled as being straight, the magnitude of the vector represents the stretched tether length. The instantaneous tether extension is therefore given by Equation 3.52.

$$\begin{aligned}\mathbf{r}_{tetherI} &= \mathbf{r}w_I - \mathbf{r}a_I \\ &= \begin{bmatrix} N_w - N_{quad} - r(\cos\psi\sin\theta\cos\phi + \sin\psi\sin\phi) \\ E_w - E_{quad} - r(\sin\psi\sin\theta\cos\phi - \cos\psi\sin\phi) \\ D_w - D_{quad} - r(\cos\theta\cos\phi) \end{bmatrix}\end{aligned} \tag{3.51}$$

$$L_{ext} = |\mathbf{r}_{tetherI}| - L_t \tag{3.52}$$

Assuming an initial unstretched tether length L_{t0}, the instantaneous unstretched tether length still to be wound L_t is given by Equation 3.53. The variable L_{wound} is the unstretched length of tether already wound. It is assumed that there is no tether

wound at the beginning of the landing mission. It is also assumed that the wound portion of the tether does not participate in stretching or compression.

$$L_t = L_{t0} - L_{wound} \tag{3.53}$$

What remains is an expression for the unstretched tether length wound as a function of time. For near-vertical tether orientations the winching speed is approximately equal to the product of the winch angular rate ω_w and the winch drum radius r_w as shown in Equation 3.54.

$$v_w \approx \omega_w r_w \tag{3.54}$$

For a perfectly non-elastic tether, the wound tether length is the integral of the winching speed. For an elastic tether, the integral needs to be scaled to account for the stretch of the tether during winding. The unstretched length of the wound tether as a function of time is given by Equation 3.55.

$$L_{wound}(t) \approx \int_{t0}^{t} \frac{L_t(x)}{L_{ext}(x) + L_t(x)} v_w(x) dx \tag{3.55}$$

3.4 Chapter Summary

This chapter presented the non-linear model of the tethered quad-rotor UAV system. Section 3.1 outlined the different axis systems and the notation adopted for the vehicle's kinematic states. Kinetic and kinematic equations based on Newton's laws of motion, as well as the attitude parameterisation used in the project, were presented in Section 3.2. The forces and moments exerted on the quad-rotor vehicle by actuators, aerodynamic drag, gravity and the tether were modelled in Section 3.3. A high level coverage of the strategy and simulation environment employed in simulating flight control systems and validation through practical flights is presented in Chapter 4. Thereafter, the quad-rotor non-linear model derived in this chapter will be linearised around a working point and utilised in flight control system design in Chapter 5. The control system design presented in Chapter 5 includes simulation results obtained from the environment outlined in Chapter 4.

Chapter 4

Control, Simulation and Validation Strategy

The overview of the tethered quad-rotor unmanned aerial system has been outlined in Chapter 2. A systematic approach was adopted in developing an autonomous system to land the tethered quad-rotor UAV on a stationary platform. This chapter outlines the architecture of the flight control system and the strategy taken in simulating and validating the tethered system. Figure 4.1 shows the progression of the design and validation process up to the demonstration of the system through practical flight tests.

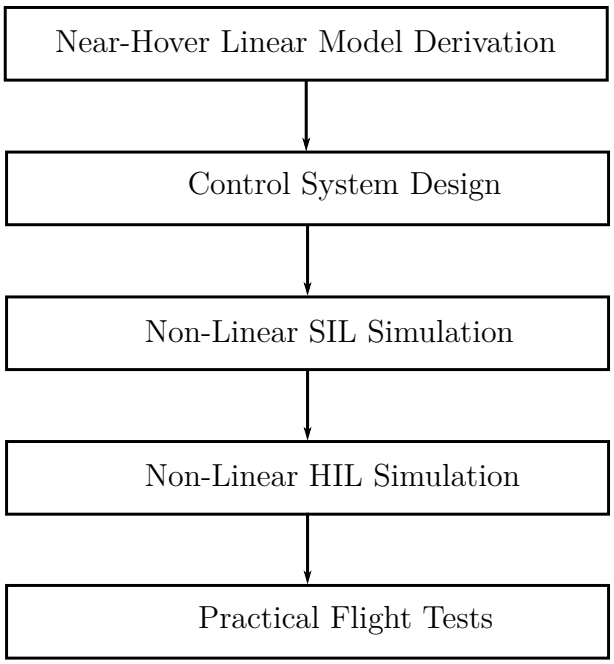

Figure 4.1: System validation progression.

The derivation of a near-hover linearised model for the tethered quad-rotor lays the foundation for the flight control system design. The derivation of the near-hover model and the detailed design of flight control loops are the subjects of Chapter 5. The architecture of the flight control system is described in Section 4.1. A non-linear Software-In-the-Loop (SIL) simulation of the system is performed in Simulink to build initial confidence in the flight control system.

The Hardware-In-the-Loop (HIL) simulation environment consists of the models of the tethered vehicle and aeronautical sensors in Simulink linked to the actual OBC hardware through serial communications. In a HIL simulation, the flight control algorithms are executed on the OBC on the aircraft and the control signals are transmitted to the Simulink model. The kinematic states of the Simulink vehicle model with simulated sensor noise are parsed and transmitted to the control system on the OBC.

The HIL simulation provides confidence that the control algorithms have been correctly coded in the OBC firmware and it presents initial insight into the influence of sensor noise on autonomous flight accuracy. Furthermore the HIL simulation verifies the performance of the OBC hardware in executing the control strategy in real time. The final stage of validation is the demonstration of the autonomous system through practical flight tests.

4.1 Quad-Rotor Flight Control System Architecture

The flight control system was designed using a successive loop closure technique based on the work by Peddle [32]. The tether dynamics are not included when designing the quad-rotor flight control system and are treated as an "unknown" external disturbance. The control system is designed based on a tether-less vehicle model, but with strong disturbance rejection characteristics. Thereafter, the performance of the control system when the tether dynamics are included is verified through non-linear simulation. This non-linear simulation is therefore used to validate the assumption that the tether dynamics may be neglected in the control system design.

The flight control system architecture is shown in Figure 4.2 and consists of high-bandwidth rate and angle controllers and low-bandwidth velocity and position control loops. Each loop in the flight control system suite implements a variation of

Proportional-Integral-Derivative (PID) control. This strategy has been applied extensively in quad-rotor flight control systems with impressive robustness [1], [4]. The layered nature of the control architecture allows for individual control loops to be armed separately thereby presenting flexibility in the design of automated landing strategies.

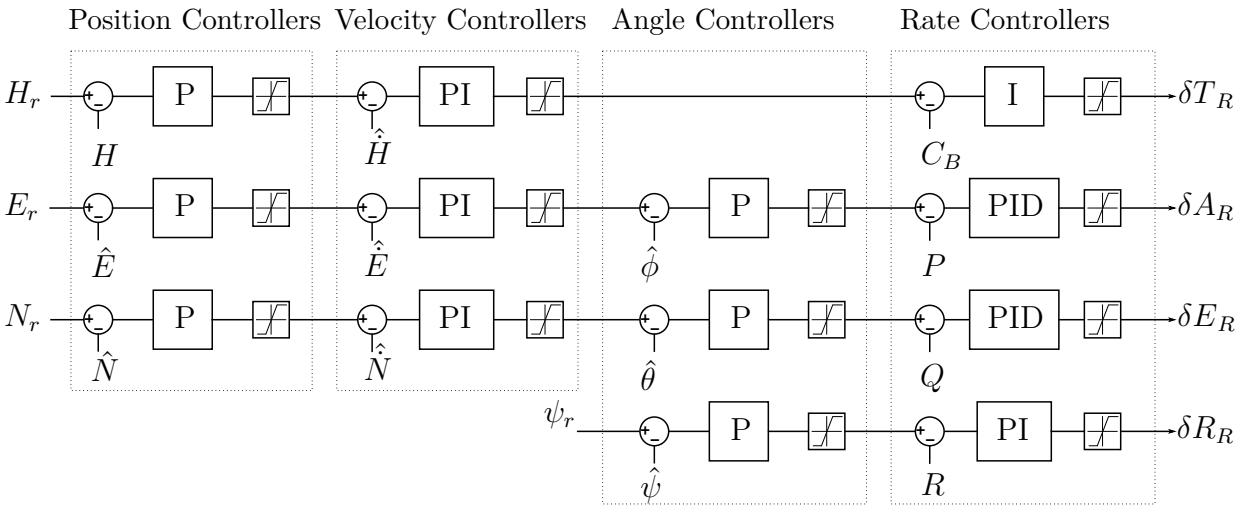

Figure 4.2: Architecture of the flight control system.

The inner rate controllers are always armed regardless of whether the vehicle is being steered by the autonomous control system or manually controlled by the safety pilot. Rate references are received from the RC remote when in manual flight mode and from the angle controllers when in autonomous flight mode. In both flight modes, the rate controllers issue virtual actuator commands. As mentioned in Section 3.3.1, the virtual actuators are related to the four rotor thrusts through the mixing matrix as shown in Equation 3.30. In the control system implementation, the inverse mixing matrix is used to compute individual rotor thrusts from virtual actuator commands. The inverse mixing matrix is obtained by passing the mixing matrix to the *inv* function in Matlab.

An Extended Kalman Filter (EKF) estimator is used to estimate the quad-rotor's attitude $(\hat{\phi}, \hat{\theta}, \hat{\psi})$, inertial position $(\hat{N}, \hat{E}, \hat{D})$ and inertial velocity $(\hat{\dot{N}}, \hat{\dot{E}}, \hat{\dot{D}})$. The estimator is vehicle-independent and was developed in the ESL to accommodate a variety of research UAV vehicles [33]. A detailed account of the EKF algorithm is documented in [33]. The EKF propagates the state estimate of the quad-rotor's attitude, velocity and position by propagating a kinematic model based on accelerometer and gyroscope measurements. Thereafter, measurements from the Inertial Measurement Unit (IMU) and the GPS sensor are used to correct the propagated state estimate [1], [4], [33]. The

vehicle's angular rates (P, Q, R) and specific forces (a_x, a_y, a_z) are supplied directly by the IMU and are not estimated by the EKF.

The EKF and the three outermost layers of the flight control system are updated at a frequency of 50 Hz. The inner rate loops are updated at an increased frequency of 100 Hz to increase disturbance rejection and enhance the stability of the vehicle [4]. The rate loops also have the highest bandwidth of the order of 10 rad.s^{-1}, also to enhance vehicle stability and disturbance rejection. A detailed analysis of the flight control system is presented in Chapter 5.

4.2 Software-In-the-Loop Simulation

The SIL simulation is a non-linear simulation of the system. The design of the flight control system using linear feedback control theory requires a linearised model of the system. The non-linear aircraft model derived in Chapter 3 is therefore linearised around a hover equilibrium/trim condition before performing the control system design. The SIL simulation serves to verify the performance of the non-linear quad-rotor system across its entire flight envelope, other than just the trim condition.

SIL simulations are performed in the Simulink environment. For SIL simulations, it is assumed that noiseless kinematic state measurements are available. Consequently the SIL environment simulates neither sensor noise nor the EKF kinematic state estimator. The SIL simulation is used mostly to check that the feedback control systems that were designed on Single-Input-Single-Output (SISO) linear models still work when applied to the full non-linear Multiple-Input-Multiple-Output (MIMO) system. Numerical approximations for continuous control operations like differentiation and integration are implemented using Simulink embedded functions.

4.3 Hardware-In-the-Loop Simulation

Once the flight control system has been validated in SIL simulation, the control system is ported into the HIL environment. The HIL environment is a hybrid set-up consisting of Simulink, the OBC and a HIL interface board. The HIL avionics architecture is shown in Figure 4.3 and is an adaptation of the flight avionics architecture shown in Figure 2.10. HIL simulation allows the control firmware on the OBC to fly a Simulink model of the tethered aircraft. Aircraft, wind and sensor models are implemented in

Simulink while the EKF kinematic state estimator and control strategy are executed on the OBC.

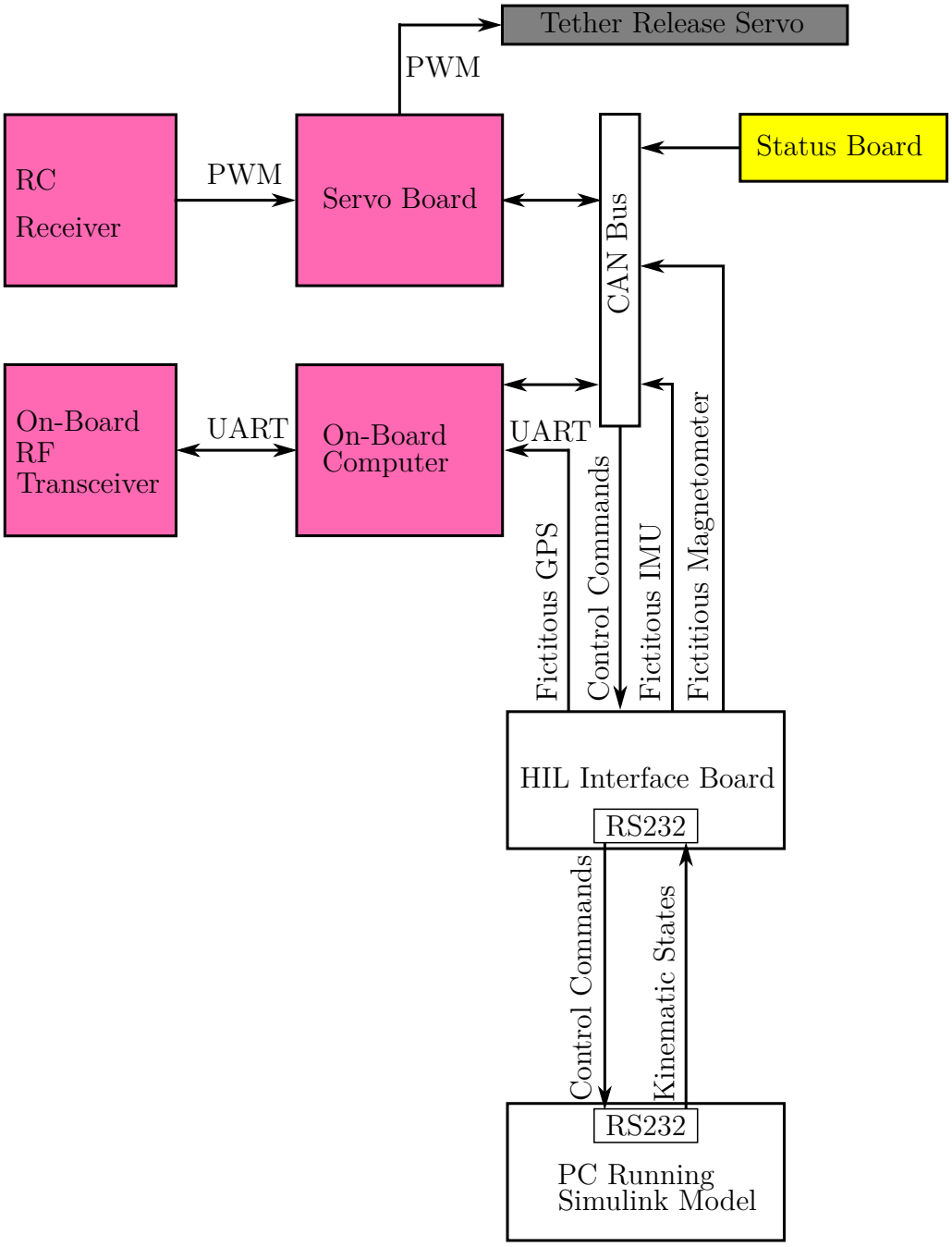

Figure 4.3: HIL simulation architecture.

Kinematic state measurements in the Simulink environment are parsed into the format of raw sensor measurements. The flight test location is specified in the HIL simulation environment in terms of latitude, longitude and altitude. Based on the

flight test location, a simulated earth's magnetic field vector is generated and is in turn used to simulate magnetometer measurements. Sensor noise signals on accelerometer, magnetometer, gyroscope and GPS position and speed measurements are simulated as band-limited white noise (BLWN) using Simulink BLWN blocks. Band-limited white noise is also added to the simulated wind velocity vector. The BLWN blocks are populated with Power Spectral Density heights and sample times as determined by sensor characterisation experiments already carried out in the ESL on the same sensors but for use on different UAV platforms [1], [4]. The GPS north, east, and down position measurements are further low-pass filtered to simulate GPS drift. Finally, high frequency noise is added to the GPS down position measurement [1]. The simulated sensor measurements containing sensor noise are transmitted serially to the HIL interface board via an RS232 link.

With reference to Figure 4.3, the HIL interface board transmits simulated sensor measurements to the OBC. Simulated GPS measurements are sent to the OBC through UART communications whereas simulated IMU and magnetometer measurements are sent over the CAN bus. The OBC executes the control algorithms and transmits actuator commands back to the CAN bus. The HIL interface board retrieves the commands and conveys them to the Simulink vehicle model via RS232 communications.

HIL simulations are used to verify that the control algorithms have been correctly coded in the OBC firmware. Researchers in the Electronic Systems Laboratory (ESL) traditionally also use HIL simulation results to predict landing accuracy in the presence of simulated sensor noise for projects involving autonomous landings of unmanned aircraft [29], [1], [27], [28].

As later discussed in Section 6.1, the landing state machine used for landing involves Safety Pilot Takes Off and Pilot Hovers Vehicle phases where the safety pilot flies the quad-rotor on a slack tether. These phases of the flight are difficult to implement in HIL simulation for two reasons. Firstly, the tether model developed is only applicable to a taut tether and is therefore not applicable to these phases of the flight. Secondly the author does not have the skill to fly the quad-rotor with only inner rate loops armed, as the safety pilot would during these two flight phases.

SIL and HIL simulation results from [4] indicate that when the inner rate loops are executed at a frequency of 100 Hz and the remainder of the loops are executed at a frequency of 50 Hz, SIL simulation results agree very closely with HIL simulation results.

Due to the afore-mentioned challenges associated with performing HIL simulations for the tethered vehicle as well as the close agreement between SIL and HIL simulation data from the previous project, HIL simulations for the tethered vehicle were excluded from the project scope. In order to take advantage of the accuracy of SIL simulations, the dynamics of the tethered vehicle are investigated using SIL simulations and by analysing system poles obtained from the point-mass model presented in Section 6.3.

To confirm that the control system has been ported correctly from the SIL environment into the OBC fimware, HIL simulations are performed on an untethered vehicle model in the HIL environment inherited from the previous project [4]. When performing HIL simulations for the untethered vehicle, all control loops are armed before take-off and take off is achieved by issuing an altitude step command from the ground station. This effectively bypasses the Safety Pilot Takes Off and the Pilot Hovers states of the landing state machine. Even though these HIL simulation results do not represent the dynamics of the tethered vehicle, the results verify that the vehicle transitions correctly through the different landing states in response to ground station commands. Specifically, the HIL simulation results verify that the correct control loops are armed and are executed with the correct references during the landing procedure.

The behaviour of the untethered vehicle in the HIL landing simulation can be extrapolated to verify that the landing state machine has been coded correctly onto the OBC. For example, in the Tensioning state of the landing state machine presented in Section 6.1.2, the OBC firmware issues a small climb rate reference thereby causing the vehicle to rise and pull the tether into tautness. The correct implementation of the Tensioning state in the OBC firmware can be verified by ensuring that the HIL simulation for the untethered vehicle exhibits a constant climb rate during the Tensioning phase as shown later in Figure 5.34b.

The above-mentioned HIL strategy sacrifices a small amount of insights that would have been gained through complete tethered HIL simulations in return for a manageable project scope. Regardless, the performance of control loops is still thoroughly investigated through non-linear SIL simulations.

4.4 Flight Test Strategy

A series of flight tests was undertaken in-order to systematically progress towards the ultimate goal of autonomously landing a tethered quad-rotor on a stationary platform.

A detailed account of all the flight tests performed is given in Chapter 8. This section briefly outlines the thinking behind the scheduling and progression of the flight tests as shown in Figure 4.4.

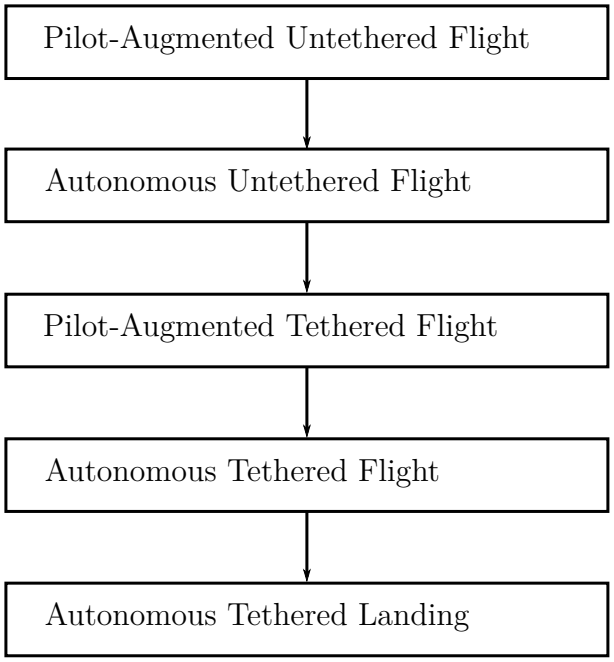

Figure 4.4: Flight test progression.

The rate loops are first validated through pilot-augmented untethered flights. As mentioned in Section 4.1, the rate loops are always armed. During pilot-augmented flight, the safety pilot steers the vehicle by issuing rate references and a virtual thrust command via the RC remote. This flight control mode verifies the stability of the vehicle and the performance of the rate loops at rejecting wind disturbances. Furthermore, sufficient rate loop damping is verified. This initial control mode also allows the safety pilot to set vehicle trim settings and to get a feel for the vehicle. It is important that the safety pilot be comfortable controlling the vehicle as he has to take control of the vehicle in emergency cases at any time throughout the practical flight test campaign. Iterative design and validation of the rate loops are conducted until satisfactory performance is achieved.

The next set of flight tests are designed to validate fully-autonomous flight of the untethered vehicle. This control mode involves arming the velocity controllers and issuing velocity step commands for a limited time before zeroing the velocity commands. Once satisfactory velocity response is achieved, the position controllers are armed and

position steps are issued. This control mode provides confidence in the capability of the velocity and position loops to stabilise the vehicle in the presence of wind disturbances.

Pilot-augmented tethered flight validates the capability of the rate loops to reject tether disturbances in addition to wind disturbances. This control mode also presents the safety pilot with an opportunity to get a feel for the tethered vehicle and determine suitable trim settings. This control mode poses the highest amount of risk. On the one hand, the safety pilot can easily lose control of the vehicle in the presence of significant tether tension. Even with extensive experience in RC control of miniature aircraft, this project is the first one in which the safety pilot has to control an aircraft attached to a taut tether. On the other hand, there is a risk of the tether becoming entangled in the vehicle's rotors if it is too slack. It is however imperative to implement this control mode, albeit risky, as the mode is used to take the vehicle from the runway into the air before autonomous tethered hovering or flight is armed.

Once the safety pilot can stabilise the tethered vehicle mid-air, fully-autonomous tethered hovering is armed. In this control mode, the vehicle tracks the tether feed-out point and hovers directly above the winch, keeping the tether in tension and vertical. Various techniques used to achieve autonomous tethered hovering are detailed in Chapter 8. This control mode verifies the stability of the vehicle in a tethered hover trim. The vertical dynamics of the taut tether are also verified.

Through the flight test progression described so far, confidence is gained to implement fully-autonomous tethered landing. Two winching strategies for bringing the quad-rotor from tethered hover onto the stationary platform are detailed in Chapter 6 and Chapter 7. With each control mode, the system is thoroughly validated through SIL simulations, HIL simulations where possible, and finally practical flight tests.

Chapter 5

Flight Control System Analysis and Design

This chapter presents the design of the different control loops of the flight control system suite. The complete non-linear mathematical model of the tethered quad-rotor was presented in Chapter 3. In this chapter, the non-linear model is used to obtain a linearised near-hover model of the untethered quad-rotor. The linearised model is formulated in terms of separate decoupled vertical, horizontal and yaw systems. Each decoupled system is controlled by successive control loops which are designed for disturbance rejection to cater for unmodelled tether dynamics and aerodynamic drag. The susceptibility of each control loop to tether and wind disturbances is taken into account when designing the control systems.

A detailed account of the flight control system architecture is given in Section 4.1. The layered nature of the control system opens up vast possibilities in terms of landing strategies. Two different but closely related landing strategies are proposed in Chapters 6 and 7. Chapter 6 presents a landing strategy based on a constant winching speed, and Chapter 7 presents a strategy based on a constant winching tension.

The vertical control system design is presented in Section 5.1 while the horizontal control system is detailed in Section 5.2. The horizontal control system consists of the longitudinal and lateral control systems. Due to the symmetry of the vehicle, the longitudinal and the lateral systems are identical. To avoid repetition, only the longitudinal control system design is presented. Section 5.3 details the design of the yaw control system.

The presentation of the control systems focusses on designing the controller gains using root locus and Bode plot techniques. Software-In-the-Loop (SIL) simulated step responses of the untethered vehicle and pole locations are discussed. Frequency domain characteristics like bandwidth, gain cross-over frequency, gain margin and phase margin are also used to quantify the performance of the control loops. For loops which are highly susceptible to disturbances, the disturbance rejection characteristics of the designed loops are investigated.

As mentioned in Section 4.3, Hardware-In-the-Loop (HIL) simulations are used to verify the performance of the flight control system in the presence of simulated sensor noise. For the autonomous landing system documented in this thesis, it is sufficient to investigate the effects of simulated sensor noise on the performance of the outermost control loops namely the altitude controller, the horizontal position controller and the yaw angle controller. To achieve this, outermost loop HIL simulation results for the untethered vehicle are presented and compared to SIL simulation results for the same loops on the untethered vehicle.

5.1 Vertical Control System

The vertical control system is designed to control the vertical translational motion of the vehicle. Owing to the layered successive loop architecture of the flight control system, the vertical control system can be issued with an acceleration reference, a velocity references or a position reference. Of the three decoupled systems, the vertical system has the highest susceptibility to tether weight and tether tension disturbances. The vertical system therefore needs dedicated control strategies to reject these disturbances.

The vertical control system consists of the normal specific acceleration (NSA) controller, the climb rate controller, and the altitude controller. A sampling rate of 50 Hz is adopted for the entire vertical control system. When the vehicle is in pilot-assisted flight, the pilot's RC remote commands are converted to a virtual thrust command which is in turn translated to individual rotor thrust commands. During autonomous flight, the virtual thrust command is generated by the NSA controller. Based on the vertical acceleration reference computed by the climb rate controller, the NSA controller computes a specific acceleration reference which it uses to indirectly control the vehicle's vertical acceleration. The climb rate controller's reference is issued by the altitude controller. In autonomous flight, altitude or climb rate steps can be commanded from the ground station.

5.1.1 Heave Dynamics

The heave plant is represented by the block diagram in Figure 5.1. The plant is described in terms of a commanded virtual thrust δT_R input and a specific acceleration (as measured by the accelerometer) C_B output. The instantaneous virtual thrust is related to the individual rotor thrusts through Equation 5.1. The commanded virtual thrust relates to the commanded individual rotor thrusts in a similar fashion, as shown in Equation 5.2.

Figure 5.1: The heave plant.

$$\delta T = T_1 + T_2 + T_3 + T_4 \tag{5.1}$$

$$\delta T_R = T_{R1} + T_{R2} + T_{R3} + T_{R4} \tag{5.2}$$

The instantaneous and commanded virtual thrusts are related by first order lag dynamics as shown in Equation 5.3.

$$\delta \dot{T} = -\frac{1}{\tau}\delta T + \frac{1}{\tau}\delta T_R \tag{5.3}$$

When the vehicle is rolled at an angle ϕ and pitched at an angle θ, Equation 5.4 gives the vehicle's upward vertical acceleration $\ddot{H}$.

$$\delta T\left(\cos\phi\cos\theta\right) - mg = m\ddot{H} \tag{5.4}$$

For small ϕ and small θ, Equation 5.4 can be approximated by Equation 5.5.

$$\delta T - mg \approx m\ddot{H} \tag{5.5}$$

The NSA controller detailed in Section 5.1.2 reads the vehicle's Z specific acceleration measurement C_B directly from the accelerometer. It is therefore convenient to perform vertical acceleration control indirectly through specific acceleration as measured by the onboard accelerometer. The vehicle's measured specific acceleration is related to the upward vertical acceleration and the acceleration due to gravity through

Equation 5.6. For a small roll angle ϕ and a small pitch angle θ, Equation 5.6 can be closely approximated by Equation 5.7.

$$C_B\left(\cos\phi\cos\theta\right) = \ddot{H} + g \tag{5.6}$$

$$C_B \approx \ddot{H} + g \tag{5.7}$$

In near-hover flight conditions, Equation 5.7 can be substituted into Equation 5.5 to obtain Equation 5.8.

$$\delta T \approx mC_B \tag{5.8}$$

Using Equation 5.8, Equation 5.3 can be written in terms of the specific acceleration as shown in Equation 5.9. Equation 5.9 is the state equation for the vertical system with specific gravity chosen as the state variable.

$$\left[\dot{C_B}\right] = \left[-\frac{1}{\tau}\right]\left[C_B\right] + \left[\frac{1}{\tau m}\right]\left[\delta T_R\right] \tag{5.9}$$

The specific acceleration is also chosen as the vertical system output resulting in Equation 5.10.

$$\begin{aligned} y &= C_B \\ &= \left[1\right]\left[C_B\right] \end{aligned} \tag{5.10}$$

The state variable model for the vertical system can be used to derive the vertical system transfer function model as detailed in Section B.2.2. Equation 5.11 is the transfer function model for the vertical system.

$$\begin{aligned} G_{heave}(s) &= \frac{C_B(s)}{\delta T_R(s)} \\ &= \frac{\dfrac{1}{m\tau}}{\left(s + \dfrac{1}{\tau}\right)} \end{aligned} \tag{5.11}$$

5.1.2 NSA Controller

The NSA controller is the inner-most loop of the vertical control system and controls the normal specific acceleration of the vehicle. Figure 5.2 shows the NSA control structure. The vehicle's vertical acceleration is controlled indirectly through the specific

acceleration as measured by the onboard accelerometer. With reference to Figure 5.2 and Equation 5.6, the vertical acceleration reference ($\ddot{H}_r$) is issued by the climb rate controller and then converted to a vertical specific acceleration reference by adding the gravitational acceleration. The result is a normal specific acceleration reference C_r. Thereafter, the normal specific acceleration reference is compensated to account for the vehicle's pitch and roll angles.

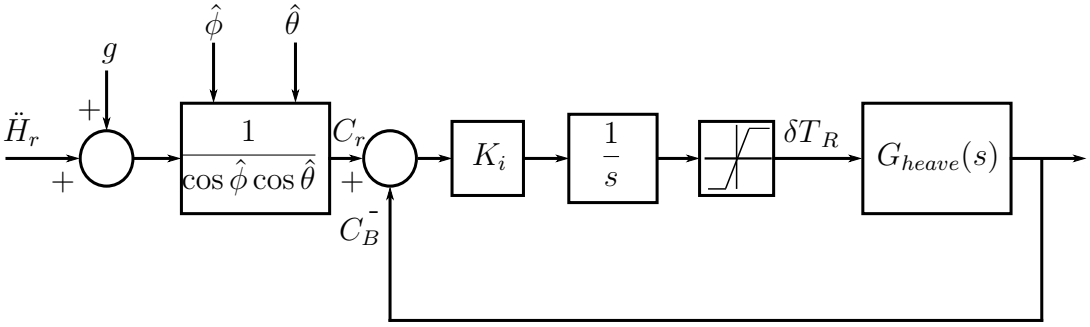

Figure 5.2: NSA control structure.

The NSA controller implements a pure integral control law in series with a constant gain, thereby giving the controller inherent low-pass filter characteristics. The need to filter high frequency noise arises from Ioppo's flight tests where mechanical vibrations and accelerometer high frequency measurement noise were observed [4]. Tether tensile forces predominantly affect the heave dynamics of the quad-rotor. The pure integral NSA control law also serves to reject these tether disturbance forces. For this project, the existing NSA controller will be analysed for disturbance rejection and bandwidth [4].

As shown in Figure 5.2, the NSA controller issues a virtual thrust command. The virtual thrust command is limited to be between 25 percent and 75 percent of the four rotors' combined thrust capacity. The upper thrust limit ensures that enough control effort is always available for the roll and pitch rate controllers to stabilise the vehicle. The lower thrust limit pegs the maximum descent rate of the vehicle in order to avoid hard landings during autonomous descent. Substituting a rotor time constant of $\tau = 0.05$ s and a quad-rotor mass of $m = 5.8$ kg as determined for the existing system, the heave plant transfer function is given by Equation 5.12 [4].

$$G_{heave}(s) = \frac{3.44}{s + 20} \tag{5.12}$$

The NSA system root locus is shown in Figure 5.3. The heave plant contributes a real pole at s = -20 and the NSA controller contributes an integrator. The closed-loop poles of NSA controller as designed by Ioppo are indicated on Figure 5.3 [4]. From root locus analysis it appears the NSA controller was designed for an optimal compromise between bandwidth and damping. For small gains prior to the root locus break-out points, the closed-loop bandwidth is very small. Beyond the break-out point, increasing the gain results in an increase in bandwidth and a reduction in damping. With an NSA controller gain of $K_i = 35$, the NSA closed-loop poles are placed at $s = -10 \pm j4.55$. The closed-loop poles have a damping ratio of $\zeta = 0.91$ and a natural frequency of $\omega_n = 10.6$ rad.s^{-1}.

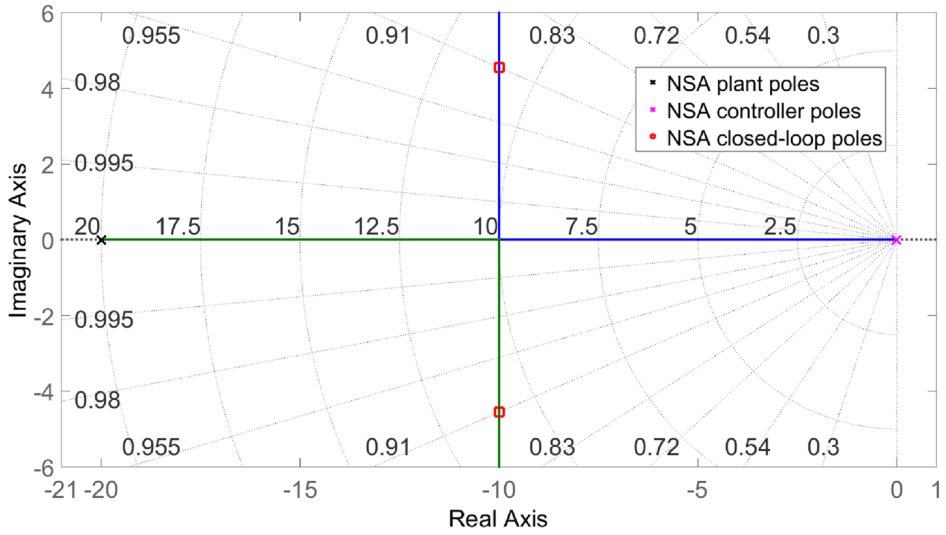

Figure 5.3: NSA root locus.

From the closed-loop pole locations shown in Figure 5.3, the NSA loop is expected to have a fast and well-damped response. Figure 5.4 shows the NSA closed-loop step response. A fast response with a rise time less than 1 second is observed. The non-linear and linear responses match very well. When a 6 N tether force disturbance is introduced along the Z_B-axis, the NSA loop rejects the disturbance and follows the reference vertical acceleration within 0.6 seconds. The NSA system is of type 1 due to the integrator contributed by the NSA controller. This means that as long as the actuators do not saturate, the tethered vehicle is able to track constant vertical acceleration references with zero steady-state error. A 6 N disturbance tether force was chosen as it equals the steady state tether tension in the implemented landing strategy as documented in Chapter 6.

The NSA controller can also be analysed in terms of frequency response using

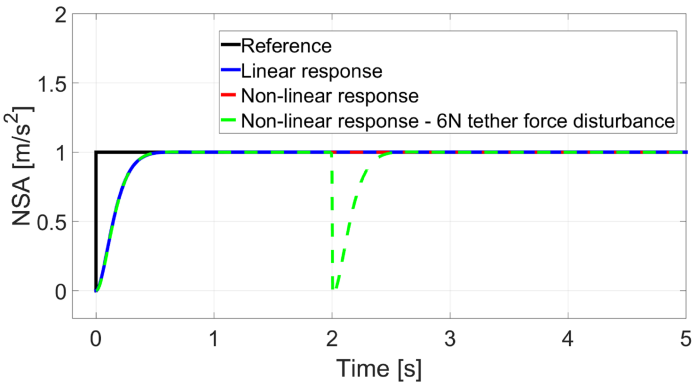

Figure 5.4: NSA step response.

Bode plot techniques. Figure 5.5a shows the magnitude plot of various components of the NSA system. The controller integrator introduces a -20dB/decade magnitude behaviour in the lower frequency region which reduces steady state errors and acts as a low-pass filter. The integrator on its own however reduces the relative stability of the system by shifting the phase response by -90 degrees. In root locus terms, the integrator tends to push the root locus branches towards the right half-plane.

The controller gain increases the gain cross-over frequency by shifting the magnitude plot by a constant. For well-damped systems, the gain cross-over frequency ω_c of the *open-loop system* is related to the bandwidth ω_{BW} of the *closed-loop system* through Equation 5.13. The NSA system has a gain cross over frequency of 5.8 rad.s^{-1} and closed-loop bandwidth of 8.05 rad.s^{-1}. The NSA Bode plots in Figures 5.5a and 5.5b show a gain margin of ∞ and a phase margin of 73.84 degrees, indicating a stable and well-damped loop.

$$\omega_c \leq \omega_{BW} \leq 2\omega_c \tag{5.13}$$

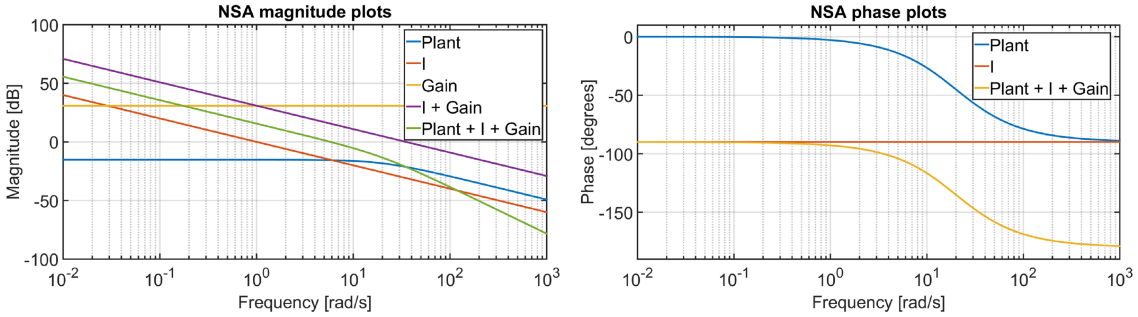

(a) NSA magnitude plot.

(b) NSA phase plot.

Figure 5.5: NSA Bode plots.

The analysis shows that the NSA loop designed by Ioppo possesses sufficient response time and disturbance rejection. For the landing strategy outlined in Section 6.1, the NSA controller is sufficient to reject anticipated tether disturbances well before the vehicle comes into close proximity to the landing target. The NSA closed-loop transfer function is given by Equation 5.14.

$$G_{C-cl}(s) = \frac{120.7}{s^2 + 20s + 120.7} \tag{5.14}$$

5.1.3 Climb Rate Controller

The climb rate controller controls the vehicle's climb rate $\dot{H}$ by issuing the appropriate vertical acceleration command $\ddot{H}_r$. As explained in Section 5.1.2, the vertical acceleration commands are converted to normal specific acceleration references and utilised by the NSA controller. Figure 5.6 shows the climb rate control structure. An estimate of the climb rate is obtained from the kinematic state estimator which utilises accelerometer and GPS raw measurements. Ioppo observed propagation delays between the GPS measured states and the accelerometer propagated states and modelled the delays using a Padé approximation [4]. In this project however, the delays are only modelled in HIL simulations. The control system is designed with inherent robustness for satisfactory performance even in the face of only a fairly accurate model.

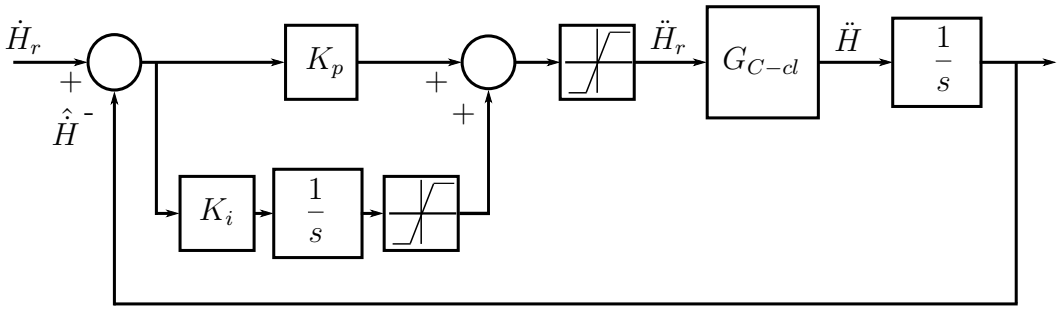

Figure 5.6: Climb rate control structure.

The climb rate root locus is shown in Figure 5.7. The climb rate plant possesses a high frequency complex pole pair from the NSA closed-loop system and a natural integrator arising from the relationship between climb rate and vertical acceleration. The climb rate PI controller contributes an additional integrator and a real zero. The climb rate closed-loop dynamics are dominated by the controller zero and the integrators. Figure 5.8 shows the dominant poles, zeroes and branches of the climb rate root locus.

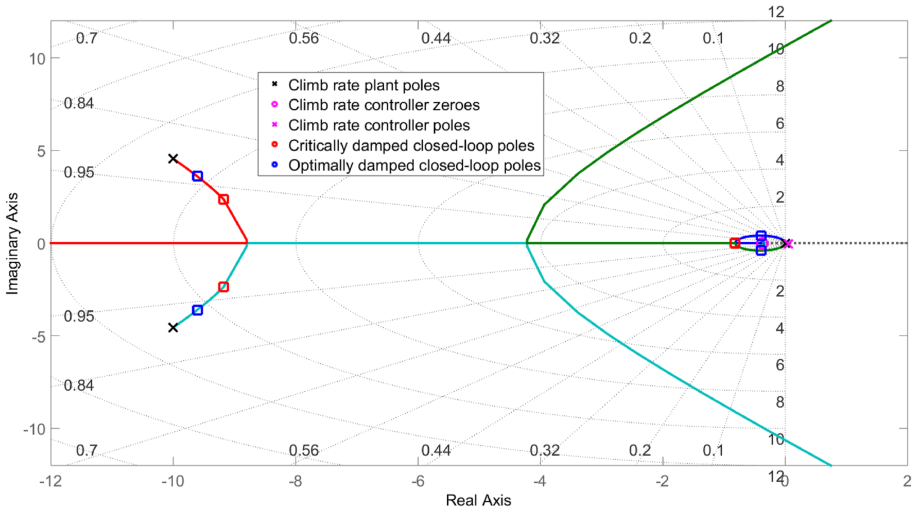

Figure 5.7: Climb rate root locus.

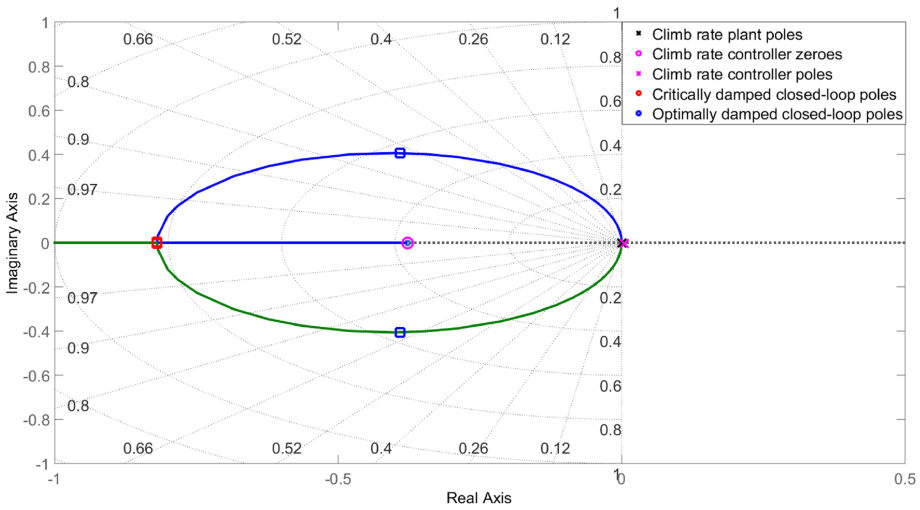

Figure 5.8: Dominant branches of climb rate root locus.

Based on the root locus shown in Figure 5.8, the initial goal was to design for optimally damped dominant closed-loop poles. The closed-loop pole locations required for an optimally damped closed-loop response are shown on Figure 5.8. With reference to Figure 5.8, it is clear that increasing the controller gain beyond optimal damping results in increased damping ratio and increased natural frequency. The controller was therefore adjusted to effect a critically damped closed-loop response through a proportional gain $K_p = 1.322$ and an integral gain $K_i = 0.5$. The critically damped climb rate system has a natural frequency of 0.81 rad.s^{-1}.

Figure 5.9 shows the climb rate closed-loop system step response. For the linear simulations, the optimally damped system exhibits more overshoot and more settling time than the critically damped system. This is expected because the critically damped system has a higher natural frequency and is more damped. The controller zero contributes to the overshoot in both the optimally damped and the critically damped systems. For the critically damped system, the non-linear and the linear simulations match very closely. The critically damped system was adopted for flight tests due its better damping ratio and rise time.

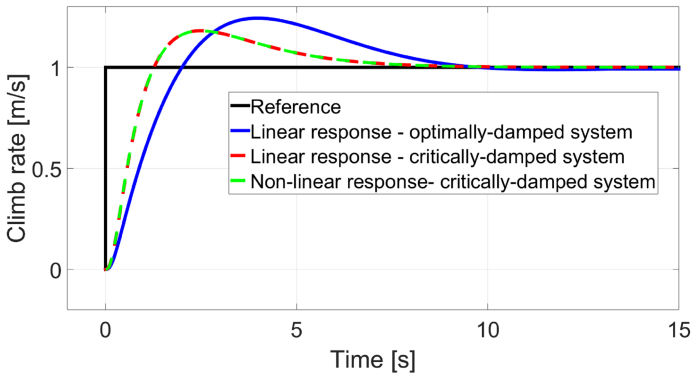

Figure 5.9: Climb rate closed-loop step response.

Figures 5.10a and 5.10b show the climb rate system magnitude and phase plots. The critically damped system has a higher cross-over frequency than the optimally damped system, reinforcing the fact that the critically damped system exhibits a faster response. Because of the two integrators, the climb rate system is of type 2 and can therefore track constant references and ramp references with zero steady state error.

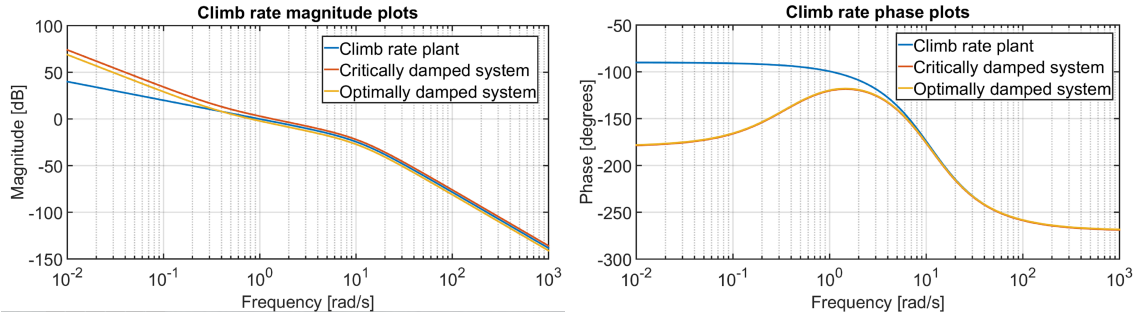

(a) Climb rate magnitude plot. (b) Climb rate phase plot.

Figure 5.10: Climb rate Bode plots.

Consistent with a type 2 system, the climb rate magnitude plot has a -40dB/decade low frequency slope. A 61.57 degrees phase margin, gain cross-over frequency of $\omega_c = 10.6$ rad.s^{-1} and a 17.37 dB gain margin can be observed from Figures 5.10a and 5.10b. The climb rate system has a bandwidth of 2.12 rad.s^{-1}. The climb rate system's bandwidth is roughly four times less than the NSA system bandwidth to ensure sufficient time-separation between the two loops. The climb rate closed-loop transfer function is given by Equation 5.15.

$$G_{\dot{H}-cl}(s) = \frac{159.7s + 60.36}{s^4 + 20s^3 + 120.7s^2 + 159.7s + 60.36} \tag{5.15}$$

5.1.4 Altitude Controller

Figure 5.11 shows the structure of the altitude controller which is the outer-most loop of the vertical control system. Altitude references are issued from the ground station. The altitude controller is a proportional controller and issues a climb rate reference. Prior quad-rotor work in the ESL utilised altitude measurements acquired from the kinematic state estimator [1]. However Ioppo showed that with the current UAV platform, GPS altitude measurements are less noisy and more reliable [4]. The altitude open-loop system possesses a natural integrator due to the relationship between altitude and climb rate. The altitude system is therefore of type 1, capable of tracking constant altitude references with zero steady-state error.

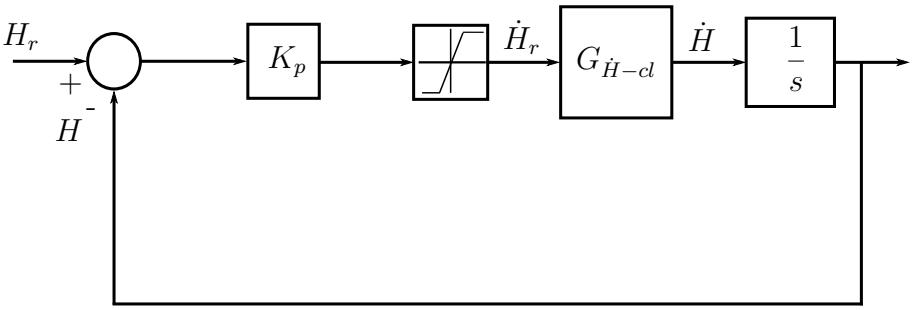

Figure 5.11: Altitude control structure.

The altitude system root locus is shown in Figure 5.12. The climb rate closed-loop system contributes a high frequency complex pole pair, a low frequency real pole and a real zero. An integrator arises from the natural climb rate-altitude relationship. The altitude closed-loop dynamics are dominated by the integrator, real pole and real zero as shown on the near-origin root locus in Figure 5.13.

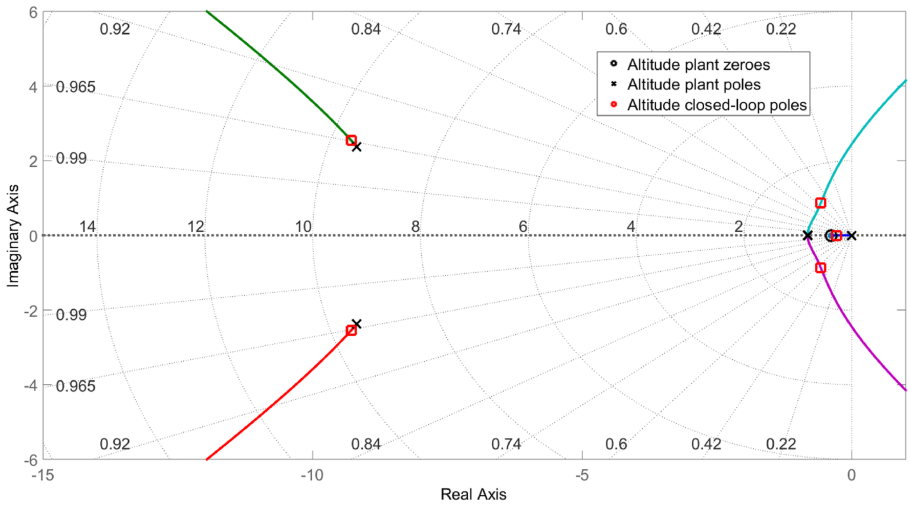

Figure 5.12: Altitude root locus.

The altitude controller was designed for a well-damped response with a gain margin of $GM \approx 70$ dB. With reference to Figure 5.13, increasing the controller gain excessively results in reduced damping and ultimately an unstable response when the closed-loop poles fall in the right half plane. A moderately low gain is therefore desirable. A moderately low gain also ensures a low altitude control bandwidth which is necessary to achieve acceptable timescale separation between the climb rate dynamics and the altitude dynamics.

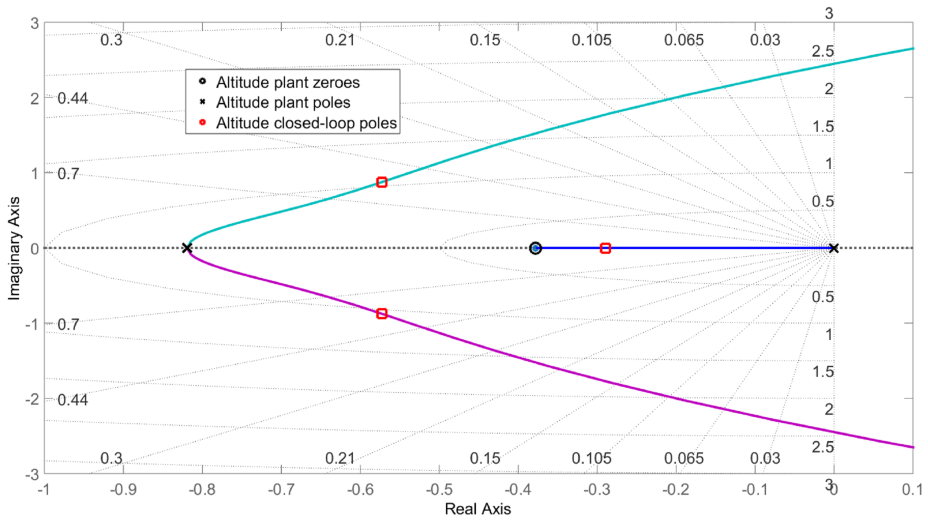

Figure 5.13: Near-origin root locus for the altitude system.

Figure 5.14 shows the altitude closed-loop step response with controller gain $K_p = 0.487$. Even though the real closed-loop pole is most dominant, the complex pole pair

also influences the altitude step response as seen by the slight oscillatory component superimposed on the otherwise first-order looking response. The open-loop zero is in close proximity to the dominant closed-loop poles and that contributes towards a step response with more overshoot. The altitude SIL simulation result in Figure 5.14a and the altitude HIL simulation result in Figure 5.14b show similar transient responses, namely a dominantly first-order response superimposed with a weak oscillatory component. The SIL simulation shows a rise time of $t_r \approx$ 4 seconds which is close to the HIL simulation's rise time of $t_r \approx$ 6 seconds. Figure 5.14b also shows the untethered vehicle rising at a constant climb rate of $\dot{H} =$ 0.2 m.s^{-1} when the Tensioning state of the landing state machine is activated.

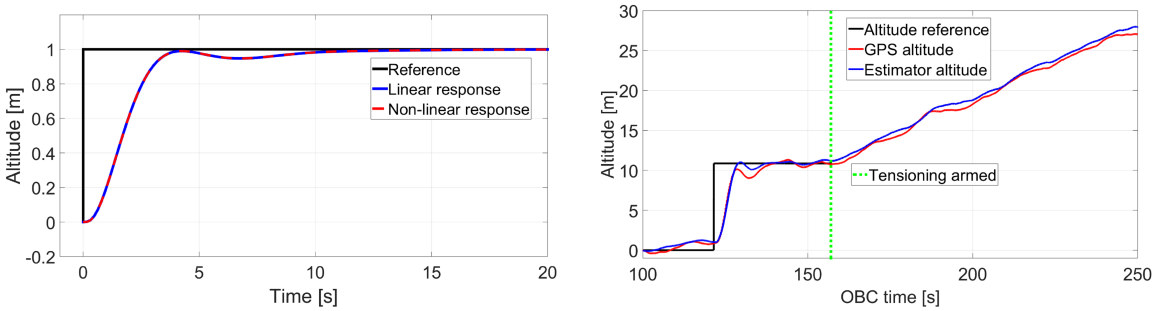

(a) Altitude SIL simulation step response. (b) Altitude HIL simulation step response.

Figure 5.14: Altitude controller step response.

Magnitude and phase plots of the altitude system are shown in Figures 5.15a and 5.15b respectively. The controller gain serves to increase the *open loop* gain cross-over frequency, which implies an increased *closed loop* bandwidth. The altitude system has a gain cross-over frequency of $\omega_c = 0.59$ rad.s^{-1} and a closed-loop bandwidth of $\omega_{BW} = 1$ rad.s^{-1}. A gain margin of $GM = 18.2$ dB and phase margin of $PM = 68.9$ degrees attest to a stable well-damped altitude loop.

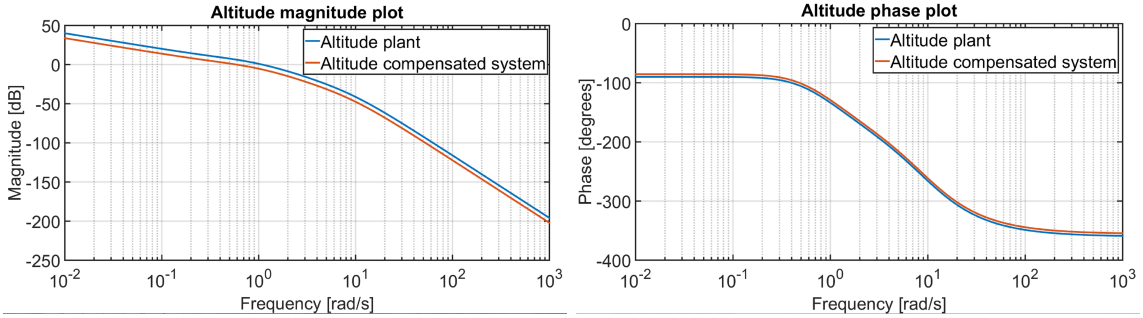

(a) Altitude magnitude plot. (b) Altitude phase plot.

Figure 5.15: Altitude Bode plots.

5.2 Horizontal Control System

The horizontal control system controls the longitudinal and lateral translation of the vehicle indirectly though the pitch and roll angles. The horizontal control system consists of pitch and roll rate controllers, pitch and roll angle controllers, horizontal velocity controllers ad horizontal position controllers. The longitudinal and lateral dynamics are identical, except for slight variation in the mass moment of inertia about the X and Y axes [4]. The pitch and roll rate controllers are the inner-most loops and are executed at a frequency of 100 Hz. The remainder of the loops run at 50 Hz. The slight difference in moments of inertia around the longitudinal and the lateral axes translates to a minor difference in inner rate loop control gains.

As mentioned in Chapter 4, the inner pitch and roll rate loops are always armed, regardless of whether the vehicle is flying under autonomous control or pilot-assisted flight. In pilot-assisted flight the rate safety pilot issues pitch and roll rate references through the RC remote while rate references are generated by the angle controllers in autonomous flight. In both cases, the rate loops generate virtual aileron and virtual elevator commands which are then converted to individual rotor thrust commands through a mixing matrix.

The rate loops, just like the entire control system suite, are designed based on a vehicle model that excludes the tether dynamics. However, the design incorporates strong disturbance rejection properties to counter the unmodelled tether disturbances. The pitch and roll rate loops are furnished with attitude rate measurements directly from the IMU and are instrumental to the overall stability of the vehicle. The rate loops must exhibit sufficient disturbance rejection to reject disturbances caused by wind, tether moments, non-uniformities in rotor displacement from the vehicle's centre and slight differences in rotor torque curves [4].

In addition to strong disturbance rejection characteristics the pitch and roll rate loops are also designed for high bandwidth. The bandwidth is designed to be high enough to allow satisfactory response times while low enough to not respond to high frequency noise from the IMU rate measurements. The outer angle, horizontal velocity and horizontal position controllers are available for utilisation by the autonomous flight algorithm or the safety pilot. In pilot-assisted flight, the RC remote inputs can be translated as pitch and roll angle references while the rate references are generated by the angle controllers. The layered architecture of the flight control system allows for this

flexibility in the interpretation of RC remote inputs by the safety pilot. In autonomous flight, velocity and position step commands can be issued from the ground station.

5.2.1 Pitch/Roll Dynamics

Due to symmetry of the quad-rotor UAV, the pitch and roll dynamics are identical. To avoid repetition, only the pitch dynamics will be presented. Figure 5.16 shows a representation of the pitch plant with virtual elevator command as input and the instantaneous pitch rate as output. Equation 5.16 shows the relationship between the instantaneous virtual elevator and the instantaneous rotor thrusts. The relationship between the commanded virtual elevator and the commanded rotor thrusts is given by Equation 5.17.

Figure 5.16: The pitch plant.

$$\delta E = d_m(T_1 - T_3) \tag{5.16}$$

$$\delta E_R = d_m(T_{R1} - T_{R3}) \tag{5.17}$$

The instantaneous and commanded virtual elevators are related by the first-order lag dynamics as shown in Equation 5.18.

$$\delta \dot{E} = -\frac{1}{\tau}\delta E + \frac{1}{\tau}\delta E_R \tag{5.18}$$

The virtual elevator is defined as the instantaneous pitching moment as shown by Equations 5.19 and 5.20. Equation 5.18 can therefore be re-written in terms of the pitching moment as shown in Equation 5.21.

$$M = \delta E \tag{5.19}$$

$$\dot{M} = \delta \dot{E} \tag{5.20}$$

$$\dot{M} = -\frac{1}{\tau}M + \frac{1}{\tau}\delta E_R \tag{5.21}$$

Equation 5.22 follows directly from Newton's second law of rotational motion around the vehicle's Y axis.

$$\dot{Q} = \frac{M}{I_{yy}} \tag{5.22}$$

The pitching moment M and the pitch rate Q are conveniently chosen as state variables for the pitch dynamics. Equations 5.21 and 5.22 can be combined into Equation 5.23 which is the state equation for the pitch system.

$$\begin{bmatrix} \dot{M} \\ \\ \dot{Q} \end{bmatrix} = \begin{bmatrix} -\frac{1}{\tau} & 0 \\ \\ \frac{1}{I_{yy}} & 0 \end{bmatrix} \begin{bmatrix} M \\ Q \end{bmatrix} + \begin{bmatrix} \frac{1}{\tau} \\ \\ 0 \end{bmatrix} \delta E_R \tag{5.23}$$

Equation 5.24 is the output equation, with the instantaneous pitch rate chosen as the output for the pitch system.

$$\begin{aligned} y &= Q \\ &= \begin{bmatrix} 0 & 1 \end{bmatrix} \begin{bmatrix} M \\ Q \end{bmatrix} \end{aligned} \tag{5.24}$$

To set the stage for control system design, it is convenient to formulate the pitch dynamics in the form of a transfer function according to Figure 5.16. Appendix B.2.3 details the procedure for converting the pitch system state equation in Equation 5.23 to the pitch system transfer function shown in Equation 5.25.

$$\begin{aligned} G_{pitch}(s) &= \frac{Q(s)}{\delta E_R(s)} \\ &= \frac{\frac{1}{I_{yy}\tau}}{s\left(s + \frac{1}{\tau}\right)} \end{aligned} \tag{5.25}$$

5.2.2 Pitch/Roll Rate Controllers

The roll and pitch rate controllers are the inner-most loops of the quad-rotor's horizontal control system. It was mentioned earlier that the vehicle's roll dynamics are identical to the pitch dynamics. The horizontal control system designed for the pitch dynamics can therefore be directly applied to the roll dynamics. Figure 5.17 shows the existing pitch rate control structure [4]. Pitch rate measurements are obtained directly

from the rate gyroscope. A non-zero trim values is added to the control signal to compensate for inaccuracies inherent in the rigid body model of the quad-rotor. The trim value is determined by the safety pilot as the trim setting where the vehicle can keep its pitch angle with RC transmitter's elevator control input at its resting position.

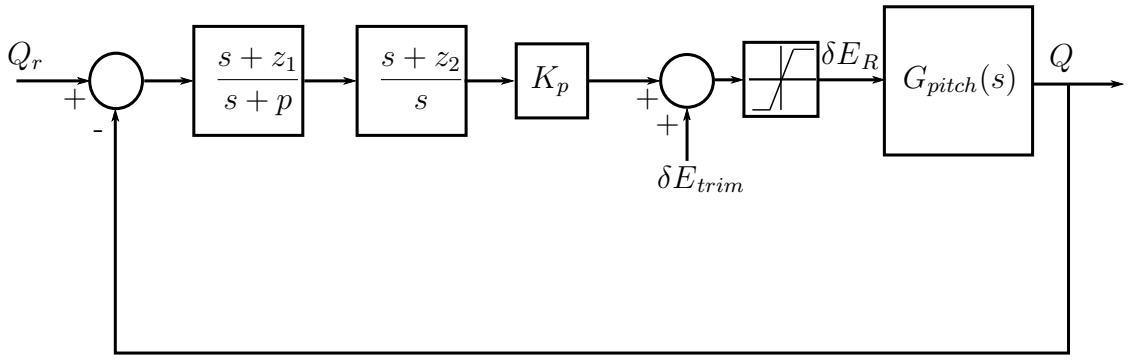

Figure 5.17: Pitch rate control structure.

By substituting $I_{yy} = 0.153$ kg.m^2 and $\tau = 0.05$ s into Equation 5.25, the yaw plant can described by Equation 5.26 [4].

$$G_{pitch}(s) = \frac{130}{s(s+20)} \tag{5.26}$$

The roll and pitch rate controllers are by far the most crucial control loops in stabilising the tethered quad-rotor UAV. The controllers directly issue virtual aileron and elevator commands which are practically the vehicles restoring moments. As the attitude restoring control loops, the controllers need to be designed for high bandwidth and sufficient damping. The roll and pitch rate loops are also susceptible to disturbances due to tether moments, aerodynamics drag and wind. Strong disturbance rejection properties therefore need to be incorporated in the design of these control loops.

The pitch rate control structure shown in Figure 5.17 is a special form of lead-lag compensator where the lag pole is an integrator. The existing pitch rate controller $D_q(s)$ is as captured in Equation 5.27[4]. The controller was designed for a high bandwidth of $\omega_{BW} \geq 10$ rad.s^{-1} [4].

$$D_q(s) = 17\frac{(s+10)}{(s+40)}\frac{(s+0.15)}{s} \tag{5.27}$$

The step response of the existing pitch rate system was found to possess some

overshoot as shown in Figure 5.18. The pitch rate controller was therefore redesigned for improved damping. Even before the procedure for redesign is presented, it can be observed from Figure 5.18 that the redesigned pitch rate controller results in a better damped response with no overshoot, but with the consequence of increasing settling time from $t_s \approx 0.25$ seconds to $t_s \approx 0.5$ seconds.

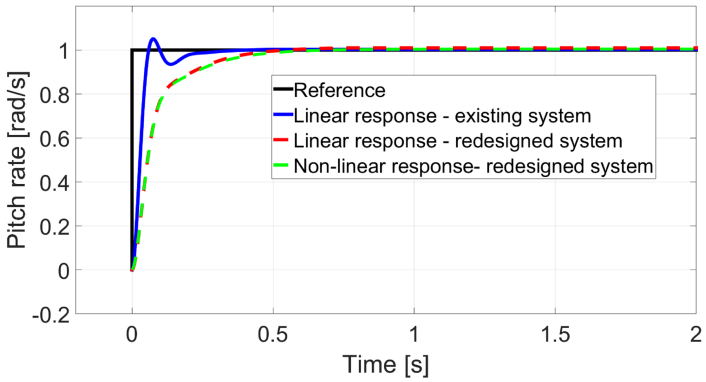

Figure 5.18: Pitch rate step response.

To understand the redesigned controller the pitch rate system root locus is shown in Figure 5.19. The pitch rate plant contributes an integrator and a real pole at $s =$ -20. The lead compensator contributes a real zero at $s =$ -10 and a real pole at $s =$ -40. Finally, the lag compensator has a real zero near the origin at $s =$ -0.05 and an integrator. A magnified view of the poles and zeroes near the origin is shown in Figure 5.20.

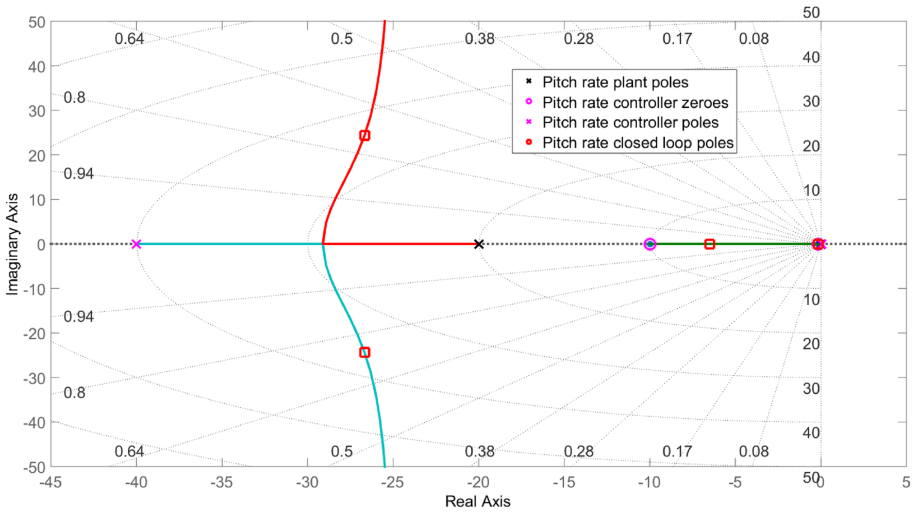

Figure 5.19: Pitch rate root locus.

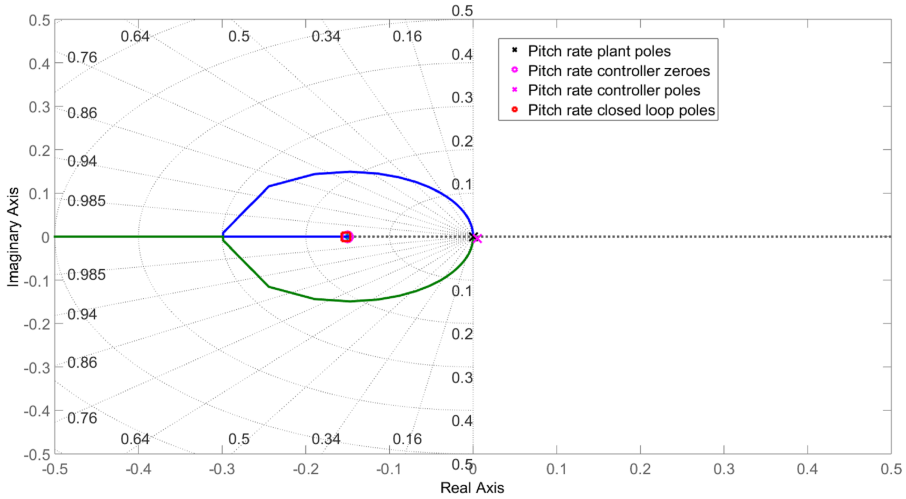

Figure 5.20: Near-origin pitch rate root locus.

One of the open-loop integrators arrives at the lag compensator zero at $s \approx$ -0.15 and the pole is almost cancelled, leaving only a weak residual. This weak integrator is however still an important part of the design and was incorporated for steady-state tracking [4]. Other than the residual of the afore-mentioned integrator, the pitch rate dynamics are influenced by the real pole and the complex pole pair whose closed-loop locations are determined by the controller gain. The real pole will always be well-damped, therefore the damping properties of the loop are mostly influenced by the closed-loop locations of the complex pole pair.

As seen from Figure 5.19, the damping ratio of the complex pole pair can be varied across a large range with little impact on their natural frequency. The redesign process therefore entailed designing the controller gain for a well-damped response with no overshoot without sacrificing significant bandwidth. With a redesigned controller gain of $K_p = 6.59$ the design goal was achieved as shown by the step responses in Figure 5.18.

Figures 5.21a and 5.21b show the Bode plots for the pitch rate plant and the pitch rate compensated system. One valuable feature of the pitch rate control structure is the use of lead compensation instead of a pure derivative thus alleviating the risk of amplification of high frequency noise from the gyroscope pitch rate measurements [4]. The lead compensator contributes a phase of $\phi_D \approx 27$ degrees at a gain cross over frequency of $\omega_c = 14.42$ rad.s^{-1}. The pitch rate closed-loop system bandwidth of $\omega_{BW} = 14.871$ rad.s^{-1} attests to a fast response while a phase margin of $PM = 89$ degrees indicates a well-damped loop. Because of the two integrators in its open loop, the pitch rate system is of type 2 and can therefore track ramp references with zero steady-state

error. As expected for a type 2 system, the magnitude plot in Figure 5.21a shows a -40 dB/decade low frequency slope.

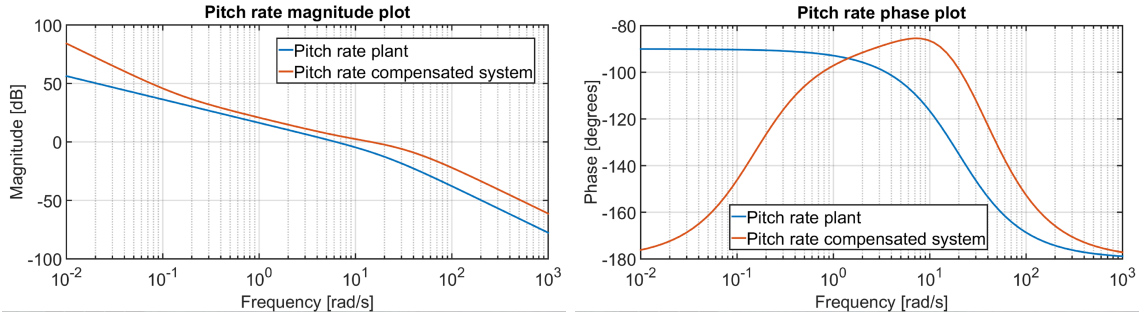

(a) Pitch rate magnitude plot. (b) Pitch rate phase plot.

Figure 5.21: Pitch rate Bode plots.

5.2.3 Pitch/Roll Angle Controllers

The pitch angle controller is a proportional controller designed to control the vehicle's pitch angle θ relative to the earth's horizon. The controller utilises an estimate of the vehicle's pitch angle from the kinematic state estimator. Roll and pitch angles are very difficult to measure directly on UAV platforms and are one of the reasons why state estimation has to be implemented for aerospace control systems [33]. The pitch angle control structure is shown in Figure 5.22. The plant includes a natural integrator due to the relationship between pitch rate and pitch angle.

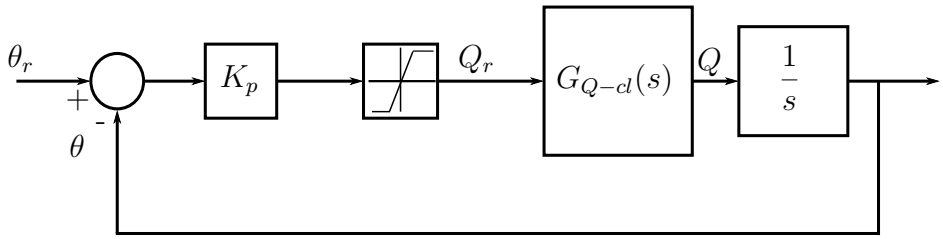

Figure 5.22: Pitch angle control structure.

The high bandwidth and strong disturbance rejection of the inner pitch rate controller is exploited, resulting in relaxed specifications for the pitch angle controller. The pitch angle controller was designed predominantly for bandwidth to achieve sufficient timescale separation between pitch rate dynamics and pitch angle dynamics. The design goal was to design the pitch angle bandwidth at approximately a quarter of the pitch rate bandwidth. A pitch angle bandwidth of $\omega_{BW} \approx 3.75$ rad.s^{-1} was therefore

desired.

Figures 5.23a and 5.23b show the pitch angle Bode plots. A controller gain of $K_p = 3.1$ is used to increase the gain cross-over frequency from $\omega_c = 1$ rad.s^{-1} to $\omega_c \approx 3$ rad.s^{-1}. A closed-loop bandwidth of $\omega_{BW} = 3.97$ rad.s^{-1} was achieved. The pitch angle loop is stable and well damped as indicated by its phase margin of $PM = 75$ degrees and gain margin of $GM = 22.1$ dB.

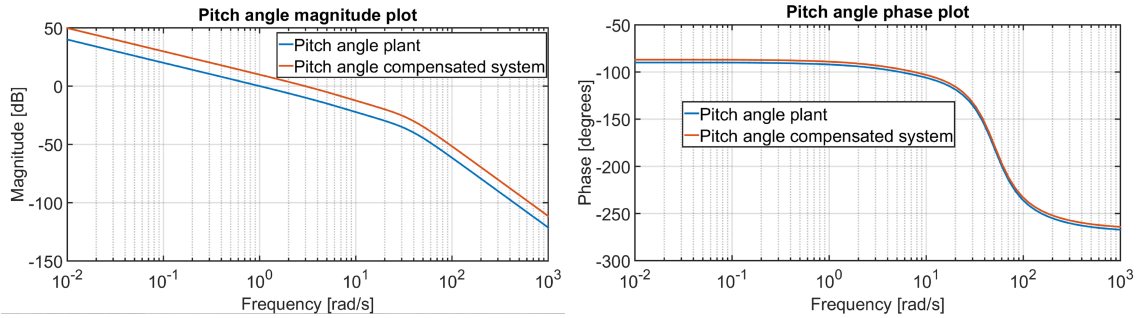

(a) Pitch angle magnitude plot. (b) Pitch angle phase plot.

Figure 5.23: Pitch angle Bode plots.

Figure 5.24 shows the pitch angle root locus while the near-origin portion of the root locus is shown in Figure 5.25. Figure 5.24 shows a complex pole pair, a real pole at $s \approx$ -5 and a lead compensator at $s =$ -10 contributed by the pitch rate closed-loop system. A pitch rate closed-loop pole and the pitch rate lag compensator zero can both be seen at $s \approx$ -0.15 in Figure 5.25. A natural integrator is also introduced by the natural relationship between pitch rate and pitch angle. The root locus in Figure 5.25 shows the natural integrator approaching the pitch rate lag compensator zero resulting in the pole being less dominant in the pitch angle closed-loop system.

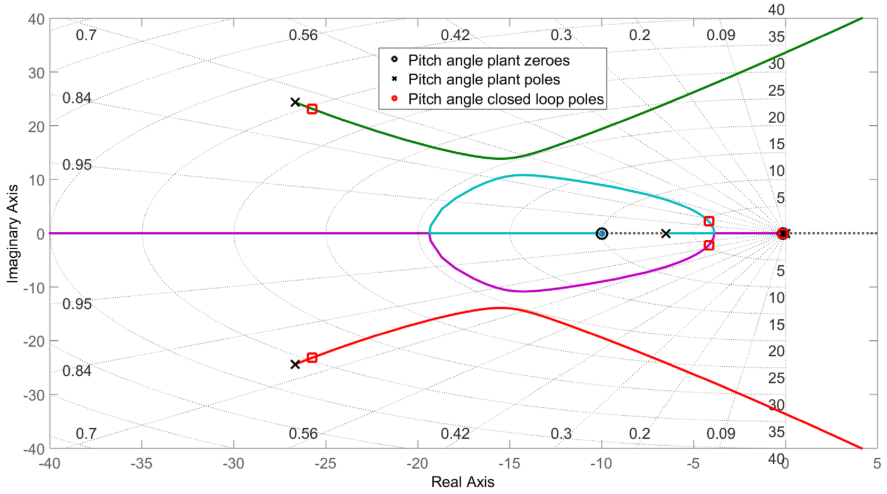

Figure 5.24: Pitch angle root locus.

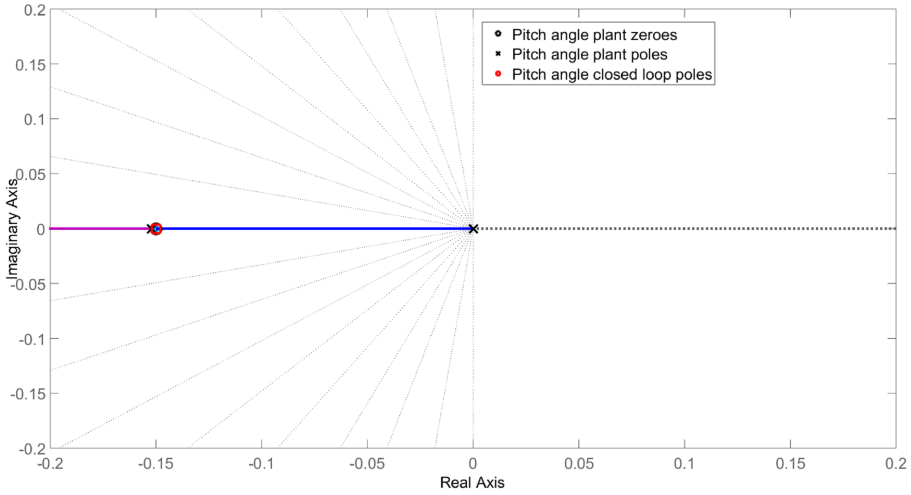

Figure 5.25: Near-origin pitch angle root locus.

The pitch rate closed-loop dynamics are influenced by two complex poles pairs as shown in Figure 5.24. Both pole pairs have good damping ratios of $\zeta \geq 0.7$. The linear and non-linear pitch angle step responses are shown in Figure 5.26. Due to aerodynamic drag, the non-linear simulation shows an overshoot and takes longer to settle than the linear simulation. The non-linear response still strives towards a zero steady state error since the pitch angle system is of type 1.

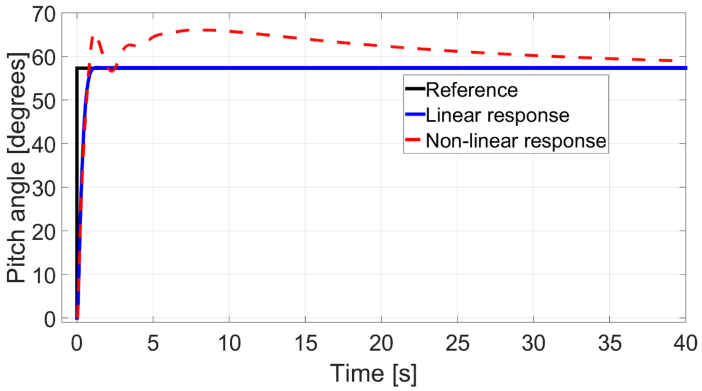

Figure 5.26: Pitch angle step response.

5.2.4 Horizontal Velocity Controllers

The velocity controllers are PI controllers designed to control the vehicle's longitudinal and lateral velocity by issuing pitch and roll angle commands. Figure 5.27 shows the horizontal velocity control structure[1]. The controller uses velocity estimates from the kinematic state estimator.

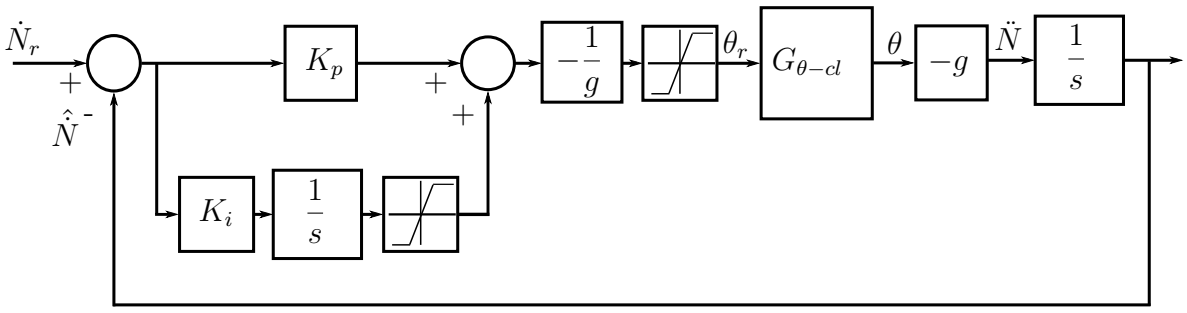

Figure 5.27: North horizontal velocity control structure.

The horizontal velocity controller was designed primarily for disturbance rejection and secondarily for bandwidth. The horizontal velocity plant is of type 1 due to the natural integrator in the open-loop system. The PI controller contributes an additional open-loop integrator rendering the system type 2 and therefore capable of tracking ramp velocity references with zero steady state error. The horizontal velocity magnitude plot in Figure 5.28a shows a -40 dB/decade low frequency slope which is typical for a type 2 system.

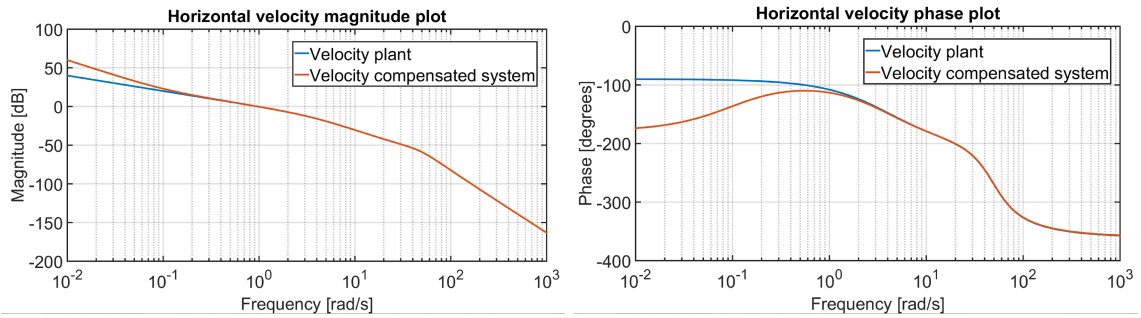

(a) Horizontal velocity magnitude plot. (b) Horizontal velocity phase plot

Figure 5.28: Horizontal velocity Bode plots.

As is common practice, the bandwidth of the velocity system was designed to be about a quarter of the pitch angle system bandwidth for sufficient timescale separation of the two loops. The pitch angle system has a bandwidth of $\omega_{BW} \approx 4$ rad.s^{-1}, therefore the velocity system was designed for a cross-over frequency of $\omega_c \approx 1$ rad.s^{-1}. The addition of the integrator to the velocity open-loop system introduces a 90 degrees phase lag, leaving the velocity system with an unacceptably low phase margin of $PM \approx 6$ degrees. A phase margin of $PM \geq 60$ degrees was specified for sufficient damping. The PI controller zero was therefore designed to contribute a phase lead of approximately 60 degrees at the desired cross-over frequency of $\omega_c = 1$ rad.s^{-1} as shown in Figure 5.28b. Finally, the PI controller gain is used to shift the magnitude plot so that the system attains the desired cross-over frequency.

With a PI controller gain of $K_p = 1$ and a controller zero placed at s = -0.1, a closed-loop bandwidth of $\omega_{BW} = 1.5$ rad.s^{-1} was achieved. The horizontal velocity system has a phase margin of $PM = 66.6$ degrees and a gain margin of $GM = 33.7$ dB indicating a well damped and stable loop.

Figure 5.29 shows the linear and non-linear step responses of the velocity system. The response of the non-linear system when a 3 m/s wind is introduced at time t = 20 seconds is also included. The response shows the velocity system rejecting the wind disturbance and restoring the vehicle to zero steady state error. A rise time of $t_r \approx 3$ seconds and an overshoot of $M_p \approx 10$ % can be observed in Figure 5.29.

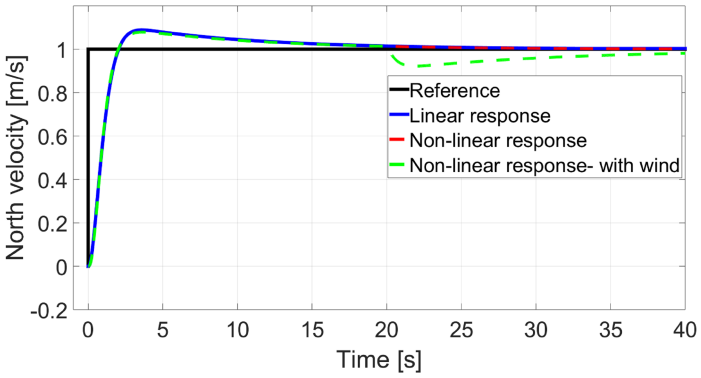

Figure 5.29: Horizontal velocity step response.

The velocity near-origin root locus in Figure 5.30 shows that two closed-loop poles approach the open-loop zeroes very closely and therefore do not dominate the velocity closed-loop response. The pitch rate lag compensator zero is located at s = -0.15 while the horizontal velocity controller zero is at s = -0.1. The velocity closed-loop dynamics are dominated by the over damped pole pair whose natural frequency of $\omega_n \approx 1.65$ rad.s^{-1} is approximately equal to the velocity system bandwidth of $\omega_{BW} = 1.5$ rad.s^{-1}. The horizontal velocity closed-loop system also consists of a real pole at $s \approx$ -7.85 and a complex pole pair with a natural frequency of $\omega_n \approx 50$ rad.s^{-1} as shown in Figure 5.31.

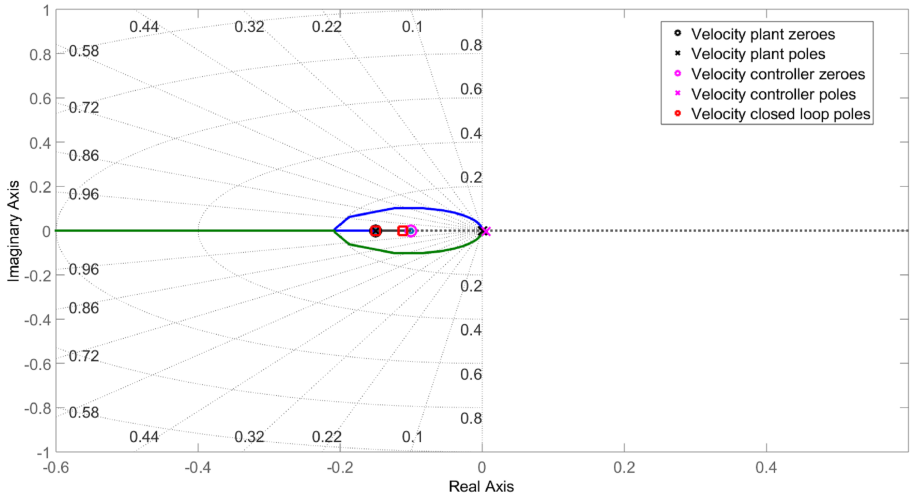

Figure 5.30: Near-origin horizontal velocity root locus.

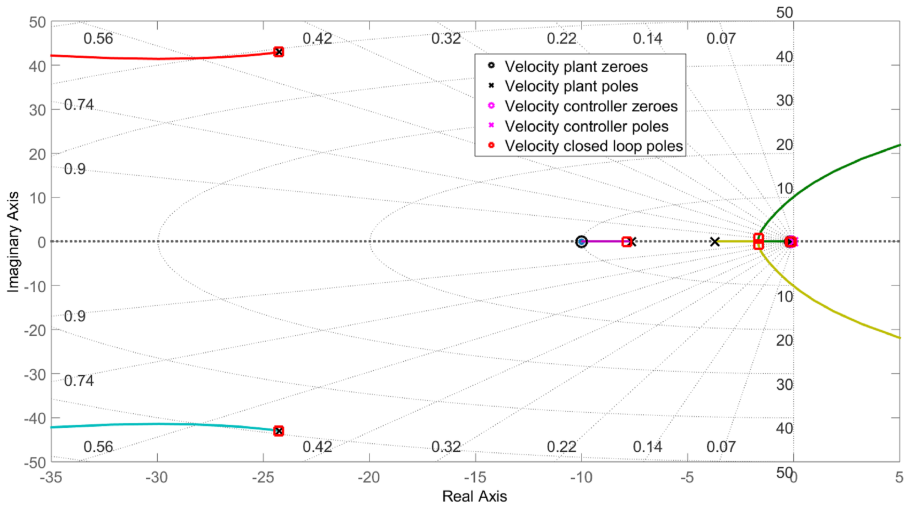

Figure 5.31: Horizontal velocity root locus.

5.2.5 Horizontal Position Controllers

The horizontal position controllers form the outermost loops of the horizontal control system. Figure 5.32 shows the structure of the position control system. Estimates of the horizontal position are obtained from the kinematic state estimator. The natural integrator emanating from the relationship between horizontal velocity and horizontal position provides disturbance rejection properties for the position loop. The position controller is a proportional controller designed for bandwidth to enforce sufficient timescale separation between velocity dynamics and position dynamics.

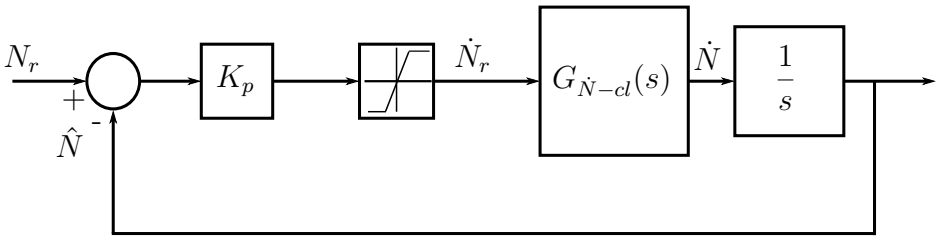

Figure 5.32: North position control structure.

With the horizontal velocity bandwidth being $\omega_{BW} \approx 1.5$ rad.s^{-1}, the position loop was designed for a cross-over frequency of $\omega_c \approx 0.4$ rad.s^{-1}. Figures 5.33a and 5.33b are the Bode plots for the horizontal position system. The uncompensated position system has a cross-over frequency of $\omega_c \approx 1.0$ rad.s^{-1} and a proportional gain of $K_p = 0.358$ shifts the position system to the desired cross-over frequency of $\omega_c = 0.4$ rad.s^{-1}. The position loop has a closed-loop bandwidth of $\omega_{BW=}$ 0.66 rad.s^{-1}. The position

loop is stable and well damped as indicated by its phase margin of $PM = 68$ degrees and gain margin of $GM = 17.3$ dB.

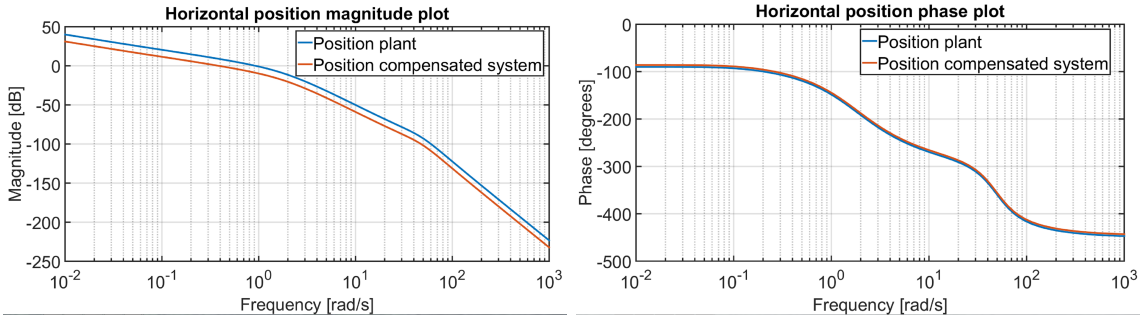

(a) Horizontal position magnitude plot.

(b) Horizontal position phase plot.

Figure 5.33: Horizontal position Bode plots.

The position closed-loop step response is shown in Figure 5.34. The SIL linear response agrees with the SIL non-linear response, both showing a rise time of $t_r \approx 5$ seconds and no overshoot. When a 3 m.s^{-1} disturbance wind is introduced at time $t = 20$ seconds, the system exhibits significant disturbance rejection properties. The wind disturbance displaces the vehicle's position by less than 14 % after which the system starts to restore the vehicle back to a zero steady-state error. The HIL simulated response in Figure 5.34b shows a well-damped response with a rise time of $t_r \approx 5$ seconds, similar to the SIL simulated response in Figure 5.34a.

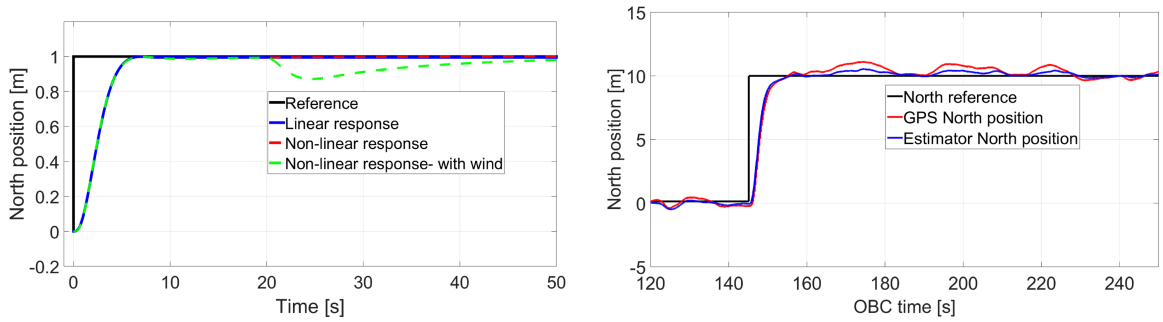

(a) Horizontal position SIL simulation step response.

(b) Horizontal position HIL simulation step response.

Figure 5.34: Horizontal position controller step response.

From the position system near-origin root locus shown in Figure 5.35, two closed-loop poles can be seen arriving at two open-loop zeros at $s = -0.15$ and $s = -0.1$. The open-loop zeroes emanate from the pitch rate lag compensator and the horizontal veloc-

ity PI controller respectively. A well damped complex pole pair at a natural frequency of $\omega_n \approx 0.78$ rad.s^{-1} and a real pole at $s \approx$ -2.14 dominate the position dynamics. The complete position system root locus in Figure 5.36 shows a real closed-loop pole at $s \leq$ -5 and a high frequency complex pole pair.

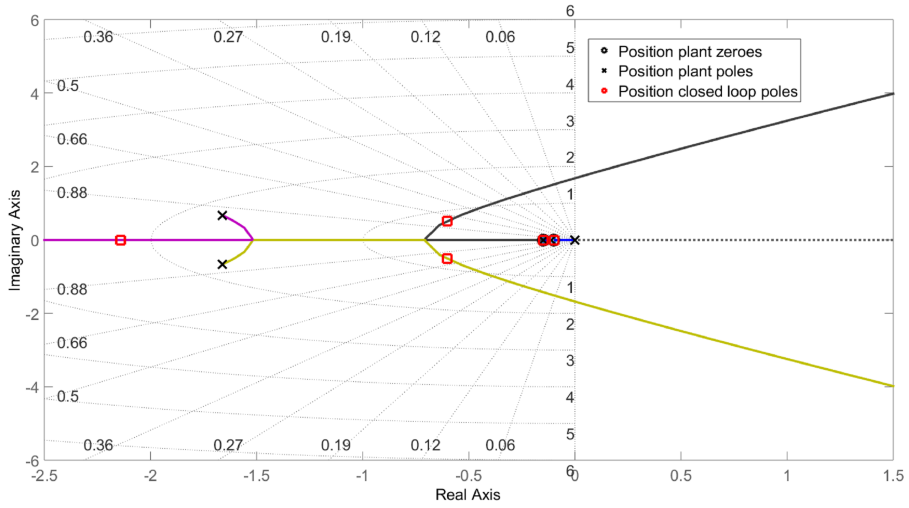

Figure 5.35: Near-origin horizontal position root locus.

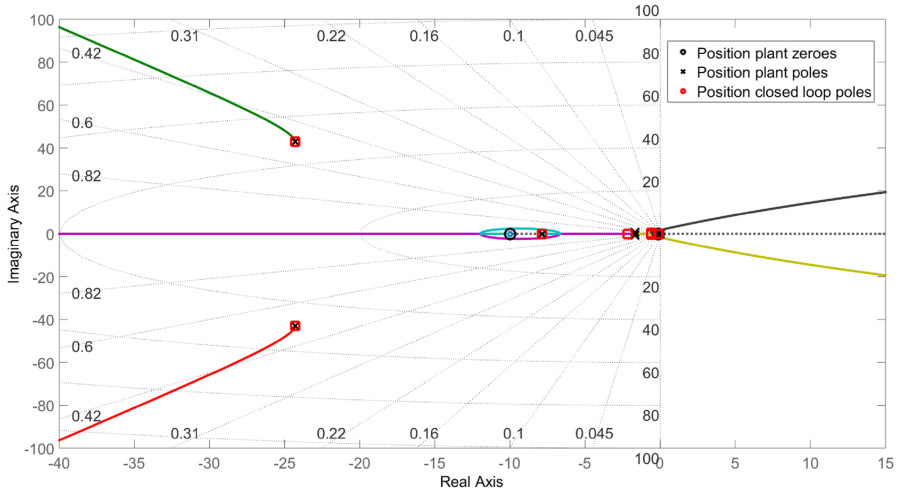

Figure 5.36: Horizontal position root locus.

By implementing successive loops from the innermost pitch rate system to the outermost position system, the horizontal control system is now of order eight. For such high-order systems, controller design using exclusively root locus techniques may not be straightforward as it becomes more subtle to determine which poles/zeroes may also significantly influence the closed-loop behaviour. It has been experienced in this

project that, as the system order increases, it becomes very important to support the root locus design techniques with frequency domain design techniques using Bode plots. The analysis of the horizontal position controller concludes the presentation of the horizontal control system design.

5.3 Yaw Control System

The yaw control system controls the quad-rotor's yaw and consists of the yaw rate controller and the yaw angle controller. Like the roll rate, pitch rate and NSA inner-most control loops, the yaw rate controller is executed at a frequency of 100 Hz on the OBC. The yaw angle control loop is executed at a frequency of 50 Hz.

The yaw dynamics are the quad-rotor's least responsive and most poorly actuated mode[4]. This is because the yaw dynamics are actuated indirectly through the drag moments induced on the rotor by rotor thrust. As explained in more detail in Section 5.3.1, the resultant drag torque is related to the rotor thrust through the drag to lift ratio scaling factor whose magnitude is generally small. Care must be taken to avoid aggressive yaw actuations or excessively high bandwidths in the yaw control system as the physical actuators can easily saturate, resulting in impaired responsiveness in the translational dynamics.

For this project it suffices to maintain a constant yaw angle throughout the landing procedure. This design ensures that the yaw dynamics settles before any aggressive translational and heave manoeuvres are executed.

In contrast to the quad-rotor vehicle's limited agility in yaw, the yaw dynamics are the least susceptible to disturbances. The vehicle's symmetry keeps the effects of wind disturbances on the yaw dynamics to a minimum. Furthermore, the swivel joints between the tether and the quad-rotor prevents a build up of torsional forces in the tether [4]. The mass moment of inertia of the quad-rotor around the body Z axis (I_{zz}) is also significantly larger than its X and Y axes counterparts. This further reduces the susceptibility of the vehicle's yaw dynamics to disturbances.

5.3.1 Yaw Dynamics

The vehicle's yaw dynamics are represented with the block diagram shown in Figure 5.37. The yaw plant has the virtual rudder command as input and the instantaneous yaw rate as output. Equation 5.16 shows the relationship between the instantaneous virtual rudder and the instantaneous rotor thrusts. The virtual rudder command possesses a similar relationship with the commanded rotor thrusts as shown in Equation 5.29.

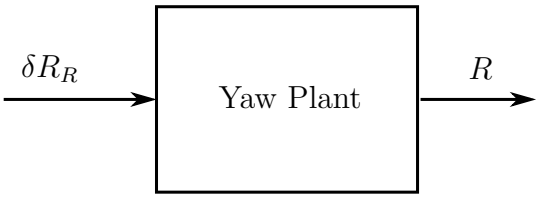

Figure 5.37: The yaw plant.

$$\delta R = \frac{-r_D}{R_{LD}}\left(-T_1 + T_2 - T_3 + T_4\right) \tag{5.28}$$

$$\delta R_R = \frac{-r_D}{R_{LD}}\left(-T_{R1} + T_{R2} - T_{R3} + T_{R4}\right) \tag{5.29}$$

With reference to the yaw plant representation shown in Figure 5.37, it is convenient to formulate the yaw dynamics into a state variable model with virtual rudder command δR_R as input and the instantaneous yaw rate R as output. Since the virtual rudder is obtained through a linear operator on the individual rotor thrusts, the instantaneous virtual rudder and the virtual rudder command are related by the lag dynamics shown in Equation 5.30.

$$\delta\dot{R} = -\frac{1}{\tau}\delta R + \frac{1}{\tau}\delta R_R \tag{5.30}$$

The instantaneous yawing moment N is chosen as a state variable. Since the instantaneous virtual rudder has been defined as being the instantaneous yawing moment, the expression for state variable N and its time rate of change $\dot{N}$ are given by Equations 5.31 and 5.32 respectively. With this definition of the instantaneous virtual rudder, Equation 5.30 can be re-written in terms of the yawing moment N as shown in Equation 5.33.

$$N = \delta R \tag{5.31}$$

$$\dot{N} = \delta\dot{R} \tag{5.32}$$

$$\dot{N} = -\frac{1}{\tau}N + \frac{1}{\tau}\delta R_R \tag{5.33}$$

The instantaneous yawing moment N is chosen as the second state variable. The application of Newton's law for rotational motion to the yaw dynamics yields Equation 5.34, where I_{zz} is the vehicle's mass moment of inertia around the body Z axis.

$$\dot{R} = \frac{N}{I_{zz}} \tag{5.34}$$

With the chosen state variables, the state equation for the yaw dynamics is as shown in Equation 5.35.

$$\begin{bmatrix} \dot{N} \\ \\ \dot{R} \end{bmatrix} = \begin{bmatrix} -\frac{1}{\tau} & 0 \\ \\ \frac{1}{I_{zz}} & 0 \end{bmatrix} \begin{bmatrix} N \\ \\ R \end{bmatrix} + \begin{bmatrix} \frac{1}{\tau} \\ 0 \end{bmatrix} \delta R_R \tag{5.35}$$

The instantaneous yaw rate R is chosen as the yaw system output. With the chosen state variables, Equation 5.36 is the output equation for the yaw system.

$$\begin{aligned} y &= R \\ &= \begin{bmatrix} 0 & 1 \end{bmatrix} \begin{bmatrix} N \\ R \end{bmatrix} \end{aligned} \tag{5.36}$$

The final step in specifying the yaw dynamics is to obtain the input-output equation in the form of a transfer function for the yaw plant, congruent to the scheme shown in Figure 5.37. Appendix B.2.4 details how the state matrix in Equation 5.35 can be used to obtain the desired transfer function as shown in Equation 5.37. The vehicle's yaw plant is represented by second-order dynamics with two poles, namely a natural integrator and a real pole at $s = -\frac{1}{\tau}$.

$$\begin{aligned} G_{yaw}(s) &= \frac{R(s)}{\delta R_R(s)} \\ &= \frac{\frac{1}{I_{zz}\tau}}{s\left(s + \frac{1}{\tau}\right)} \end{aligned} \tag{5.37}$$

5.3.2 Yaw Rate Controller

The yaw rate controller implements a PI control law and forms the inner-most loop of the yaw control system. The yaw rate control structure is shown in Figure 5.38. Yaw rate references are issued by the outer yaw angle controller and yaw rate measurements are obtained from the body z-axis gyroscope measurement. Integral control serves to reject tether and wind disturbances while proportional control is used to achieve desired bandwidth. Similar to the pitch rate controller, a non-zero trim value is added to the control signal. The trim value is determined by the safety pilot as the trim setting where the vehicle can keep its yaw angle with RC transmitter's rudder control input at its resting position.

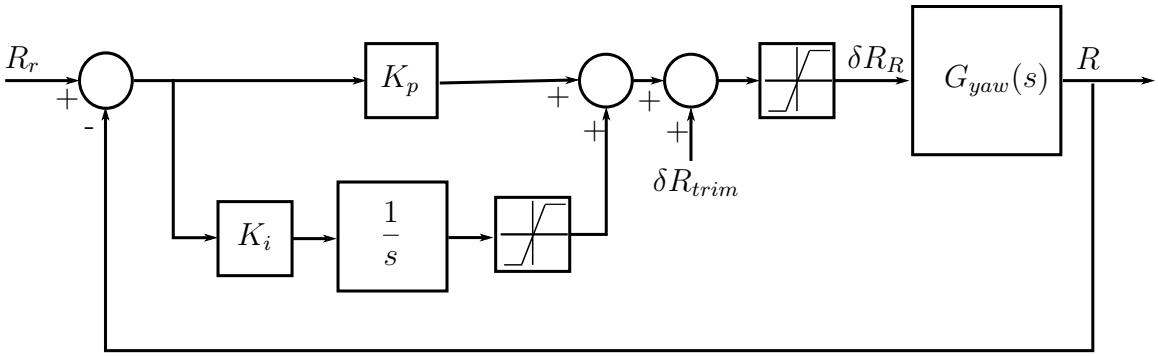

Figure 5.38: Yaw rate control structure.

By substituting $I_{zz} = 0.27$ kg.m^2 and $\tau = 0.05$ seconds into Equation 5.37, the yaw plant can described by Equation 5.38 [4].

$$G_{yaw}(s) = \frac{74}{s(s+20)} \tag{5.38}$$

Figure 5.39 shows the yaw rate root locus. The yaw plant contributes a high frequency real pole and an integrator. The yaw rate controller contributes an integrator and a real zero at s = -0.1. The yaw rate dynamics are dominated by the near-origin root locus shown in Figure 5.40. A real dominant closed-loop pole is placed at a natural frequency of $\omega_n = 1.95$ rad.s^{-1}. For near-optimally damped systems, the natural frequency, cross-over frequency and bandwidth are within the same order of magnitude.

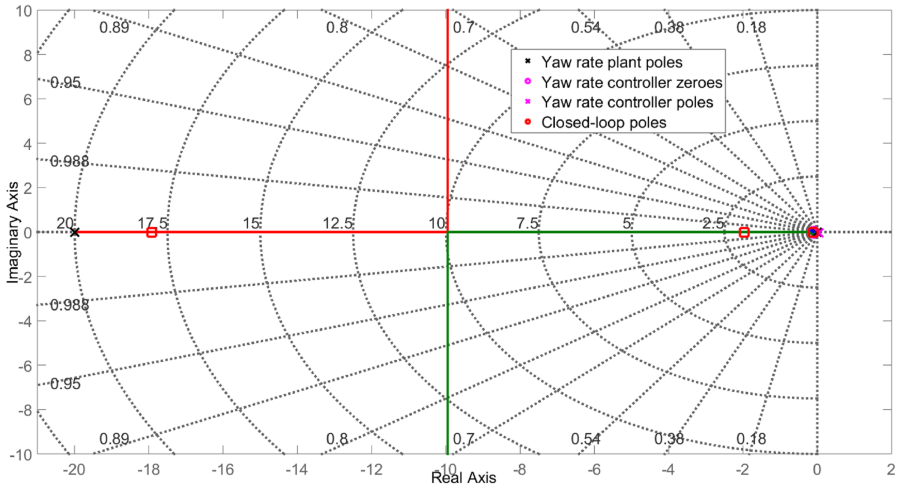

Figure 5.39: Complete yaw rate root locus.

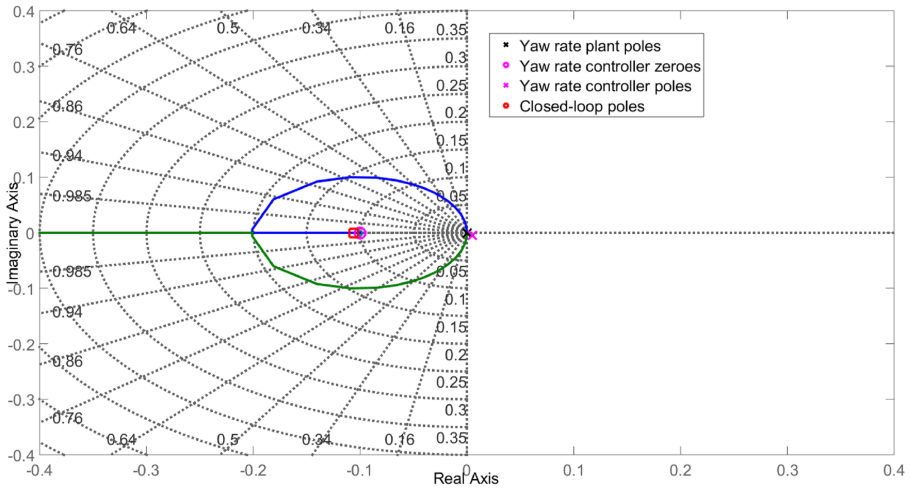

Figure 5.40: Near-origin yaw rate root locus.

Since the quad-rotor is poorly actuated in yaw, the yaw rate controller was designed for a low bandwidth in the region of $\omega_{BW} \approx 2$ rad.s^{-1}. With controller gains $K_p = 0.504$ and $K_i = 0.0504$, a closed-loop bandwidth of $\omega_{BW} = 2.16$ rad.s^{-1} was achieved. The yaw rate Bode plots in Figures 5.41a and 5.41b show a cross-over frequency of $\omega_c = 1.86$ rad.s^{-1} and a phase margin of $PM = 81.61$ degrees. By using a proportional gain less than unity in the design, the cross-over frequency was reduced from ≈ 4 rad.s^{-1} to the desired ≈ 2 rad.s^{-1}. Integral control serves to increase system type. The yaw rate system is type 2 as seen from the -40 dB/decade low frequency slope of the magnitude plot.

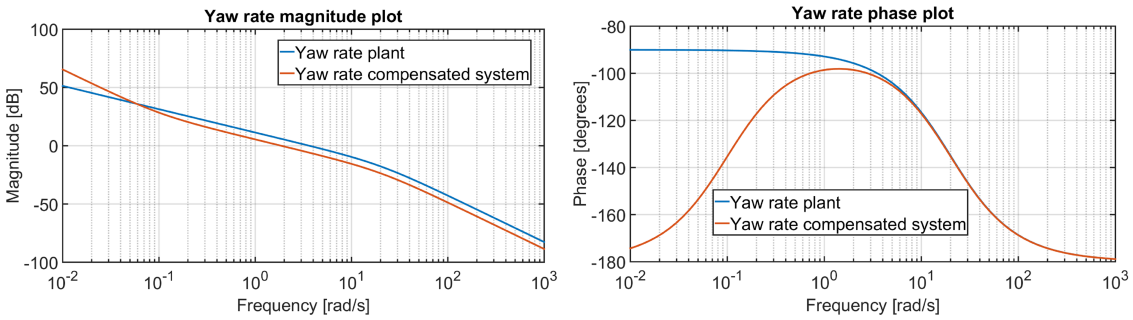

(a) Yaw rate magnitude plot. (b) Yaw rate phase plot.

Figure 5.41: Yaw rate Bode plots.

Figure 5.42 shows the linear and nonlinear step responses of the yaw rate system. The design results in a well-damped step response with a rise time of ≈ 2 seconds.

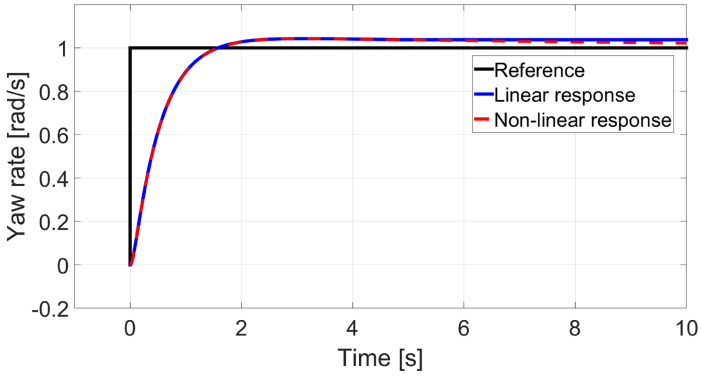

Figure 5.42: Yaw rate step response.

5.3.3 Yaw Angle Controller

The yaw angle controller is a proportional controller designed to control the UAV's yaw angle relative to North. From Equation 3.13 in Section 3.2.2.2, it is clear that the yaw dynamics of the vehicle are coupled to pitch and roll dynamics. Equation 5.39 is the last row of Equation 3.13 in which the coupling is evident.

$$\psi = Q \sin\phi \sec\theta + R \cos\phi \sec\theta \tag{5.39}$$

To compensate for the coupling between yaw and tilt dynamics, Möller implemented a two-part augmentation to the traditional proportional control architecture [1], [4]. The augmented yaw angle control scheme is shown in Figure 5.43. The first part of the augmentation involves gain scheduling where a scheduling gain is computed according to Equation 5.40 and the bounds in Equation 5.41 are applied. Simply stated, the gain scheduling effects softer control with an increase in the vehicle's roll/banking angle ϕ relative to its pitching angle θ. In addition to gain scheduling, feedback linearisation is performed as shown in Equations 5.42 and 5.43. Ioppo presents an in-depth analysis of this augmented scheme and a detailed derivation of how the scheme attempts to remove the non-linearity in the body axis angular rate R [4].

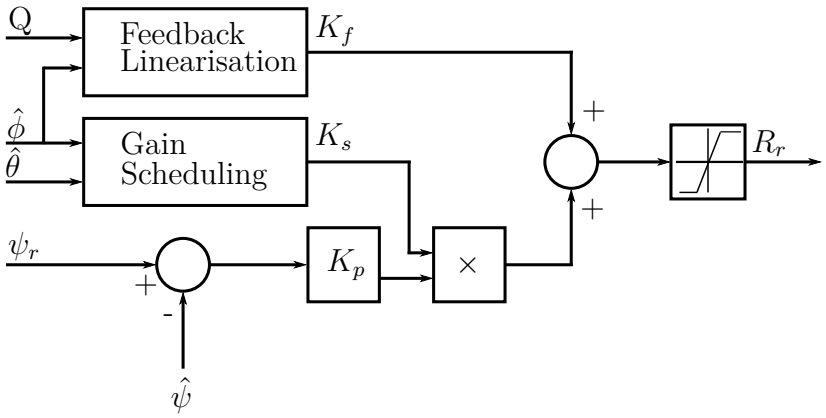

Figure 5.43: Yaw angle control structure.

$$K_s = \frac{\cos\left(\hat{\theta}\right)}{\cos\left(\hat{\phi}\right)} \tag{5.40}$$

$$0 \leq K_s \leq 1.1 \tag{5.41}$$

$$K_f = -\tan\left(\hat{\phi}\right)Q \tag{5.42}$$

$$-0.46 \leq K_f \leq 0.46 \tag{5.43}$$

For control system design, the linear model shown in Figure 5.44 was used. The yaw angle controller was designed for a well damped response with a phase margin $PM \geq 70$ degrees. To achieve sufficient timescale separation between the yaw rate dynamics and the yaw angle dynamics, the yaw angle controller was designed for a cross-over frequency which is ≈ 0.25 times that of the yaw rate controller. Due to the natural integrator relating yaw rate and yaw angle, the yaw angle system is of type 1 and thus can follow a constant reference with zero steady state error.

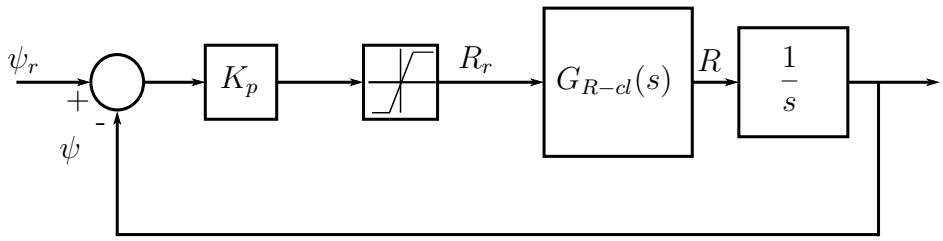

Figure 5.44: Yaw angle control structure used for design purposes.

Figures 5.45a and 5.45b show the yaw angle system Bode plots. With the yaw rate controller having a cross-over frequency $\omega_c \approx 2$ rad.s^{-1}, a yaw angle cross-over frequency of 0.5 rad.s^{-1} was achieved through the proportional gain $K_p = 0.48$. A phase margin of $PM = 75$ degrees and a gain margin of $GM = 39.2$ dB attest to a well damped and stable loop. A closed-loop bandwidth of $\omega_{BW} = 0.68$ rad.s^{-1} was also achieved.

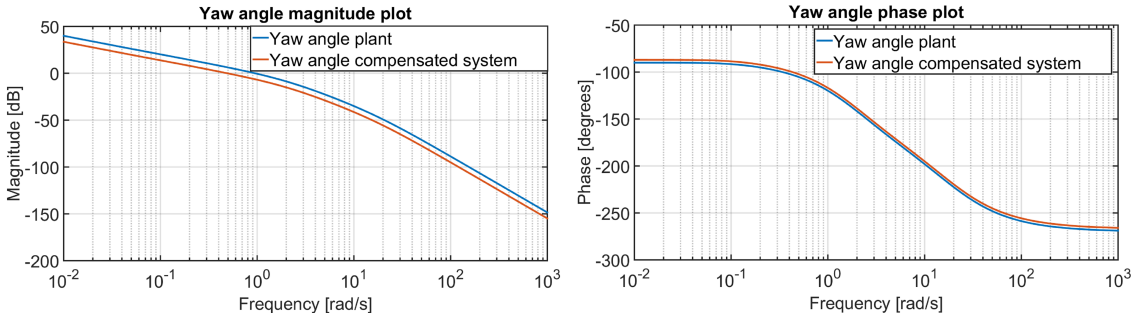

(a) Yaw angle magnitude plot. (b) Yaw angle phase plot.

Figure 5.45: Yaw angle Bode plots.

As shown by the yaw angle root locus in Figure 5.46, the yaw rate closed-loop system contributes three real poles and a zero. The zero almost cancels the pole closest to the origin at $s \approx$ -0.1. A natural integrator is introduced by the relationship between yaw rate and yaw angle. The near-origin root locus shown in Figure 5.47 shows the dominant branches of the yaw angle root locus. The closed-loop pole nearest to the origin is almost cancelled by the open-loop zero, leaving a dominant complex pole pair at a natural frequency of $\omega_n \approx$ 1 rad.s^{-1} and a damping ratio $\zeta \geq 0.9$.

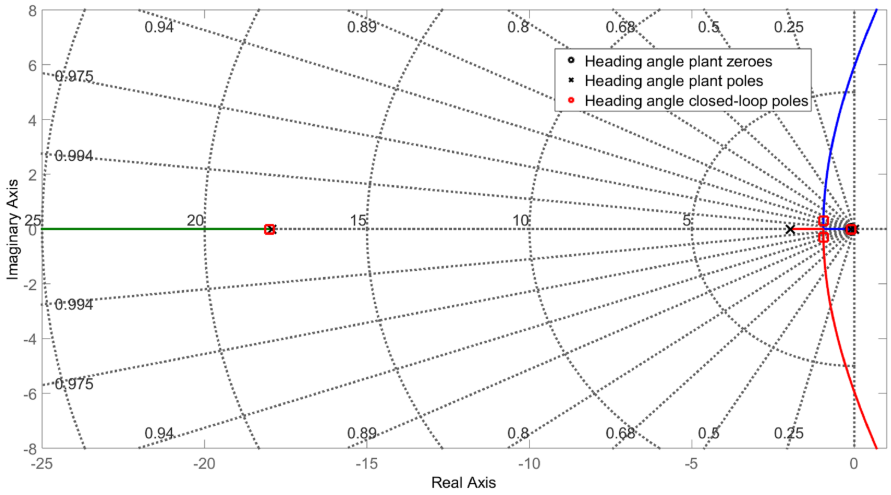

Figure 5.46: Complete yaw angle root locus.

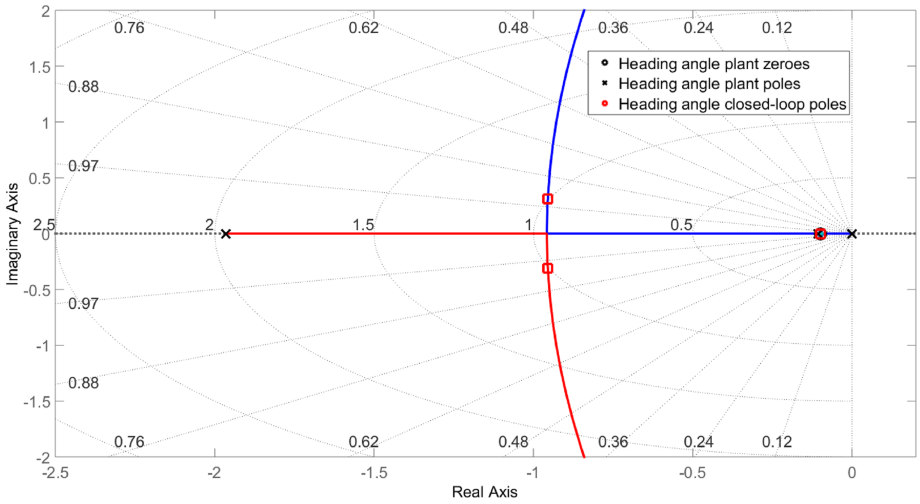

Figure 5.47: Near-origin yaw angle root locus.

SIL simulated responses for the yaw angle controller are shown in Figure 5.48a and HIL simulated responses for the yaw angle controller are shown in Figure 5.48b. The step responses attest to a well-damped system as seen by the absence of overshoot. The SIL simulation shows a rise time of $t_r \approx 4$ seconds while the HIL simulation exhibits a longer rise time of $t_r \approx 20$ seconds. These captured details of the yaw angle controller conclude the analysis of the yaw control system.

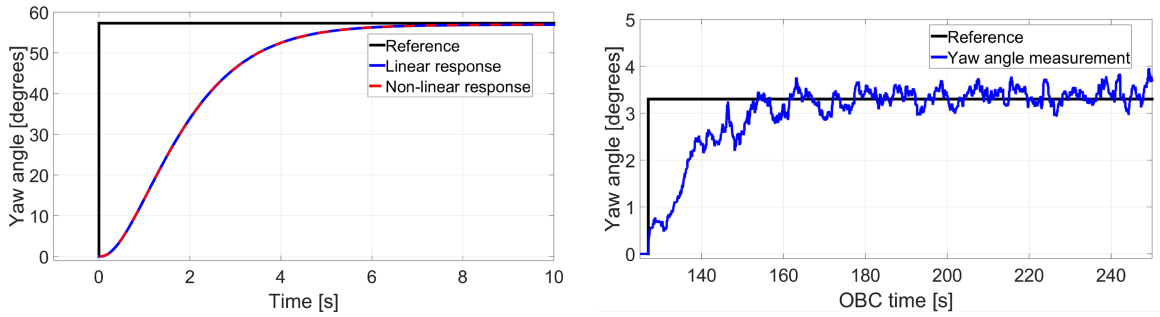

(a) Yaw angle SIL simulation step response. (b) Yaw angle HIL simulation step response.

Figure 5.48: Yaw angle controller step response.

5.4 Chapter Summary

The design and analysis of the flight control system was presented in this chapter. The control system is implemented using the successive loop closure technique. Each control loop implements a variation of PID control [4]. The non-linear model of the untethered quad-rotor presented in Chapter 3 was linearised about a hover static operating point and decoupled into separate vertical, horizontal, and yaw systems. Control systems were subsequently designed for each of the three systems, with each control system consisting of inner rate and angle loops, and outer velocity and position loops. The flight control system design was based on the model of the untethered vehicle with the design incorporating inherent disturbance rejection properties for sufficient rejection of tether and wind disturbances.

Vertical control system design was presented in Section 5.1. Section 5.1.1 detailed the decoupled heave dynamics of the untethered vehicle. The vertical control system consists of the NSA controller, the climb rate controller, and the altitude controller which were presented in Sections 5.1.2, 5.1.3 and 5.1.4 respectively. The NSA controller from the existing system was analysed and adopted while the climb rate and altitude controllers were redesigned [4].

Section 5.2 detailed the horizontal control system with the decoupled pitch/roll dynamics presented in Section 5.2.1. The pitch/roll rate and pitch/roll angle controllers were presented in Section 5.2.2 and 5.2.3 respectively. The horizontal velocity and horizontal position controllers are the outer loops of the horizontal control system and were presented in Sections 5.2.4 and5.2.5 respectively. The existing pitch rate controller gain was adjusted for improved damping while the remaining controllers was

redesigned [4].

The yaw control system consists of the yaw rate controller and the yaw angle controller which were presented in Sections 5.3.2 and 5.3.3. Prior to that, the dynamics of the decoupled yaw system were derived in Section 5.3.1. The entire yaw control system was redesigned. HIL simulation results for the altitude controller, horizontal velocity controller and yaw angle controller were also presented and compared to their corresponding SIL simulation results to verify the performance of the flight control system in the presence of simulated sensor noise.

Chapter 6

Constant Speed Winching Strategy

Having presented the flight control system design in Chapter 5, the next two chapters are dedicated to the description of the autonomous tethered landing strategies. A tethered landing strategy based on a constant winching speed is presented in this chapter. In Chapter 7, an alternative tethered landing strategy based on a constant tether tension will presented. The landing state machines in both chapters are adaptations to the state machine employed by Möller to demonstrate the autonomous landing of an untethered quad-rotor UAV on a translating platform [1].

A reduced-order model of the tether dynamics is derived and is linearised about a static operating point for various tether lengths. The linearised model is decoupled into a tethering angle model and a tethering radius model. The natural frequency and the damping ratio of the tethering angle dynamics are analysed as a function of horizontal velocity controller gain and also as a function of quasi-static tethering radius. The tethering radius dynamics are analysed as a function of tether stiffness and tether damping coefficient. The reduced-order tethering angle model and tethering radius model are validated using non-linear simulations.

6.1 Proposed Landing State Machine

The landing state machine shown in Figure 6.1 was designed to supervise the autonomous landing mission. The existence of out-of-envelope (OOE) at any instance during the execution of the landing state machine invokes the firmware emergency procedure as described in Section 6.1.1.The landing state machine assumes that the winch control system is designed to maintain a commanded constant winching speed. The winch speed control system is presented in Section 6.2.

6.1.1 Out-of-Envelope Conditions and Emergency Stop Procedures

Throughout the landing procedure, the tethered vehicle is monitored for out-of-envelope (OOE) conditions. For the purposes of this project, the vehicle is considered to be out of envelope if at least one of the conditions are present:

i. Safety pilot no longer comfortable controlling the vehicle in pilot-assisted flight.

ii. Tilt angle (roll or pitch) larger than 25 degrees in autonomous flight.

iii. Position error larger than 1 metre in autonomous flight.

In order to ensure the safety of the operators and the vehicle, the state machine is conservative and aborts the landing attempt once an out-of-envelope condition is detected. Every autonomous landing attempt is preceded by a pilot-assisted flight phase. If the vehicle is under the control of the safety pilot when out-of-envelope conditions occur, the safety pilot executes the safety pilot emergency procedure consisting of the following steps:

a. Detach the tether by flicking a switch on the RC transmitter.

b. Bring the vehicle to land on the runway.

If out-of-envelope conditions occur when the tethered UAV is in autonomous flight, the flight control firmware implements the autonomous emergency stop procedure with the following actions:

1. Detach the tether.

2. Arm all control loops.

3. Hold current horizontal position.

4. If altitude is more than 5 m, hold current altitude.

5. If altitude is less than 5 m, ascend to 5 m altitude.

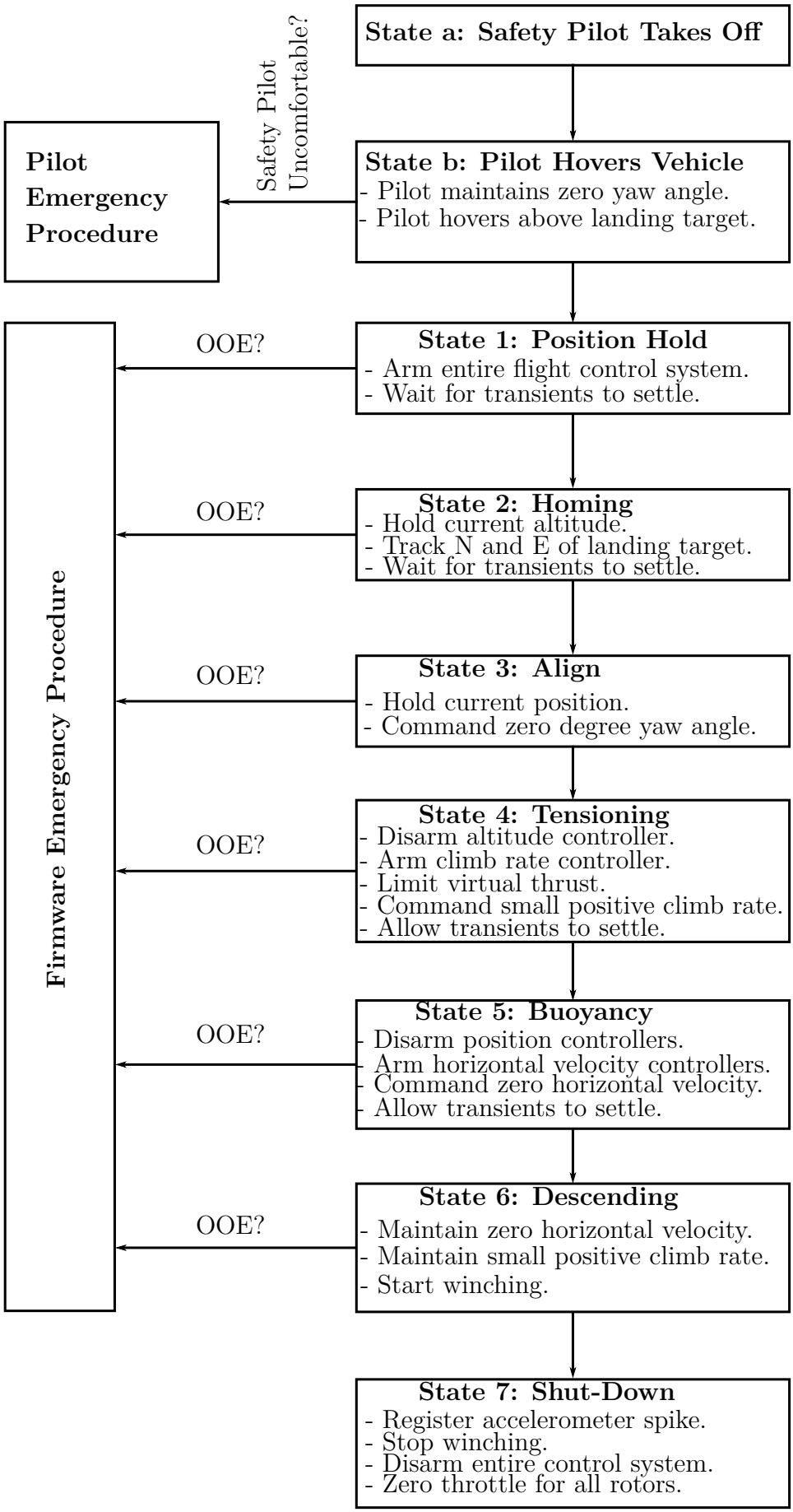

Figure 6.1: Constant speed landing state machine.

6.1.2 Description of Individual States

The logic implemented in each of the states shown in Figure 6.1 is explained in Sections 6.1.2.2 to 6.1.2.9. In each state carefully selected control loops are armed and strategic references are issued to the control system. The safety pilot can flick a switch and take over control of the vehicle at any stage of the autonomous flight should the vehicle respond in an unexpected fashion. Chapter 8 documents the dynamic response of the vehicle while executing each of the states.

6.1.2.1 State a: Safety Pilot Takes Off

The take-off phase of the flight is controlled completely by the safety pilot using an RC transmitter. The safety pilot uses the sticks on the transmitter to issue pitch/roll rate and yaw rate references as well as virtual thrust commands. The inner rate loops are always activated and in this phase they perform rate control using the references issued by the safety pilot. After take-off the safety pilot steers to a specified approximate horizontal position and altitude before he attempts to hover as outlined in Section 6.1.2.2.

6.1.2.2 State b: Safety Pilot Hovers Vehicle

After take-off, the safety pilot brings the tethered vehicle to a stable hover on a lack tether. Once stable hover has been achieved the ground station officer clicks a button on the ground station application. The ground station application in turn sends a signal to the vehicle over the RF link to trigger the Position Hold phase. The success of the Safety Pilot Hover phase depends on the ability of the safety pilot to control the tethered vehicle in tethered hover via the RC transmitter. If at any point the safety pilot feels uncomfortable controlling the tethered vehicle, the safety pilot executes the safety pilot emergency stop procedure.

6.1.2.3 State 1: Position Hold

Upon entering the Position Hold state, a timer is started and the tethered vehicle holds its current position. The current vehicle heading is maintained. If the timer expires without the occurrence of out-of-envelope conditions, the vehicles proceeds to the Homing phase of the landing state machine. In this state winching is not yet activated.

The success of the Position Hold state phase depends on the performance of the flight control system in tracking the vertical and horizontal positions while rejecting

wind and tether disturbances. The tether will inherently have some slack in this state since the pilot needs some slack to execute the Pilot-Assisted Hover. If out-of-envelope conditions are observed, the autonomous flight control firmware executes it emergency stop procedures and the landing attempt is aborted.

6.1.2.4 State 2: Homing

The expiration of the timer in the Position Hold state without the occurrence of out-of-envelope conditions indicates that the vehicle has settled and is holding position within the acceptable error margin. At the inception of the Homing state the horizontal position of the vehicle is commanded to match that of the landing target, whilst maintaining the current altitude and heading angle.

Once the vehicle's horizontal position approaches that of the landing target to within a specified margin, a timer is started. If the timer times out without the occurrence of out-of-envelope conditions, the vehicle proceeds to the Align state.

6.1.2.5 State 3: Align

The state machine is designed such that the quad-rotor maintains a constant heading angle while descending onto the landing target. When the system is implemented for landing on a translating deck, it would be practical for the quad-rotor's heading to track the deck's heading. For the purposes of landing on a stationary platform however, a zero heading angle was specified.

There is bound to be a non-zero heading angle during the transition from Pilot-Assisted Hover to Position-Hold phases. The heading angle which was left unaltered throughout the Position-Hold and Homing phases is now corrected in the Align phase. While maintaining horizontal position and altitude, a zero heading angle reference is issued.

As a general strategy, the vehicle may not be steered vertically or horizontally before the yaw angle response has settled as the quad-rotor is very poorly-actuated in yaw and requires excessive amounts of control effort to execute yawing manoeuvres. The Align phase terminates when the vehicle's heading angle error is smaller than a specified threshold value. The vehicle then proceeds to the next state of the landing state machine, namely the Tensioning state.

6.1.2.6 State 4: Tensioning

Upon entering the Tensioning state the altitude control is disarmed, leaving the climb rate controller as the outer-most loop in the vertical control system. Simultaneously, the virtual thrust issued by the inner-loop controllers is limited to a few newtons above hover thrust. These two actions cause the vehicle to slowly climb and tighten the tether until the tether tension balances the resultant upward thrust from the rotors.

During landing, the tether tension should be tight enough to prevent the tether from getting tangled into the rotors but slack enough to avoid excessive disturbances on the quad-rotor. The vehicle is allowed to settle before proceeding to the Buoyancy state.

6.1.2.7 State 5: Buoyancy

The Buoyancy state begins with the disarming of the horizontal position loop, leaving the horizontal velocity controller as the outer-most horizontal control loop. A zero velocity reference is issued. The tethered vehicle will then exhibit dynamics relating to horizontal velocity control as detailed in Sections 6.3.1 and6.3.3. The UAV is allowed to settle before winching is initiated in the Descending state.

6.1.2.8 State 6: Descending

The constant speed winch control system is activated at the inception of the descending state by pressing the **auto-wind** button on the winch keypad. As the quad-rotor's thrust limit is set lower than the winch's thrust capacity, the vehicle is pulled towards the landing target which is on the stationary platform.

6.1.2.9 State 7: Shut-Down

Touchdown causes an abrupt change in the vehicle's vertical acceleration. Similar to what was observed in previous landing projects, the abrupt change in vertical acceleration is indicated by an accelerometer measurement spike of magnitude $<$ -15 m.s^{-2} [1], [4]. The flight control firmware activates the Shut-Down phase when the accelerometer spike is registered.

Upon entering the Shut-Down state, all virtual thrust actuator commands are zeroed. The winch control system and the entire flight control system are disabled. For implementation safety, the safety pilot also zeroes the thrust command on the RC

transmitter and switches the vehicle control to safety pilot mode upon touch down. Thereafter, it is safe for the safety officer to approach the vehicle and turn motor batteries off.

6.2 Winch Speed Control System Design

The constant speed winching landing state machine presented in Section 6.1 assumes the existence of a winch speed controller. This section presents the design of the winch speed control system. We note that Chapter 7 will briefly investigate a constant tension strategy as an alternative approach to tethered landing. The design of a winching tension controller has been excluded from the scope of this project since the constant tension descent strategy has not been tested in practice. Furthermore, the design of a tension controller is readily available in the literature [36].

The control system presented in this section is based on the winch model presented in Appendix E and the corresponding model parameters determined in Appendix F. Based on the winch model presented in Appendix E, the winch speed control architecture is shown in Figure 6.2. The constant G_v is a conversion factor between duty cycle and armature voltage while G_w is a conversion factor, defined in Equation A.3, relating to the resolution of the rotary encoder in measuring angular speed. The winch speed controller is denoted $D_\omega(s)$.

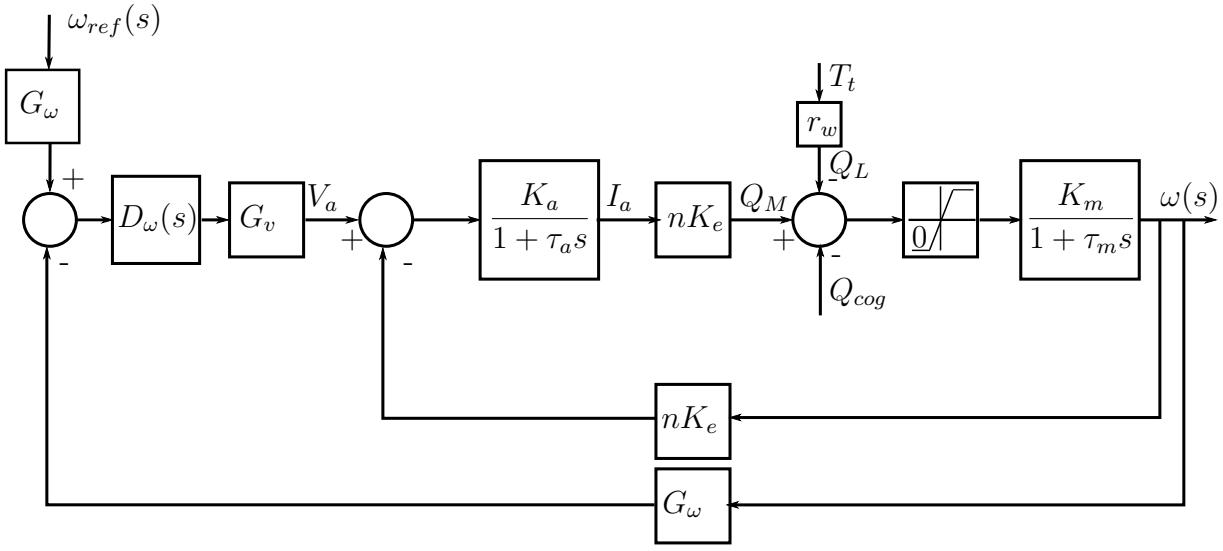

Figure 6.2: Control architecture for the speed control loop.

To simplify control system design, the DC geared motor parasitic feedback loop

shown in Figure 6.2 was ignored. Furthermore, the electrical time constant τ_a was also assumed to be zero since the electrical dynamics are significantly faster than the mechanical dynamics. A capacitor was placed across the geared DC motor terminals to filter commutation and measurement noise from the angular speed measurement. Neglecting the armature inductance, the time constant τ of the capacitor C and the armature resistance R_a can be approximated as $\tau \approx R_a C$. With a capacitor value of C = 1000 μF and an armature resistance of R_a = 1.2638 Ω as documented in Table F.7, the filter time constant is in the order of 1 ms. The filter dynamics are also ignored as they are significantly faster than the mechanical dynamics of the DC motor. Finally, friction is also ignored. With the aforementioned approximations in place, the resulting simplified control architecture is shown in Figure 6.3.

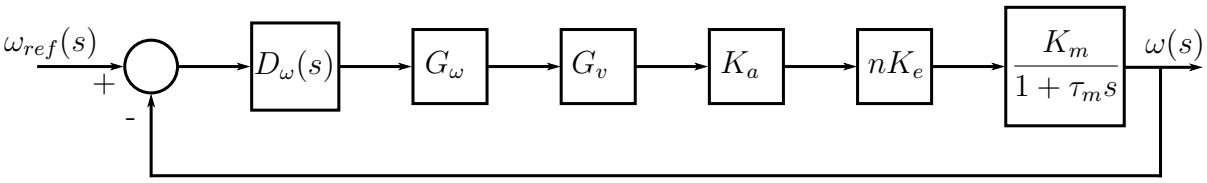

Figure 6.3: Simplified speed control loop architecture.

Based on the simplified model shown in Figure 6.3, the winch speed controller was designed for a well-damped response with a 2% settling time of 2 seconds. Figure 6.4 shows the winch speed root locus based on the simplified winch model. The mechanical dynamics contribute a plant pole at s = -0.25. The speed controller is a PI controller. The integral part was employed for steady-state tracking performance as well as for its low-pass characteristics in order to filter commutation and measurement noise. The PI controller zero at s = -1.04 pulls the root locus towards the left half-plane in order to achieve the desired speed of response. A controller gain K_p = 0.389 was designed for a critically damped response, corresponding to closed loop poles at $s \approx$ -1.9.

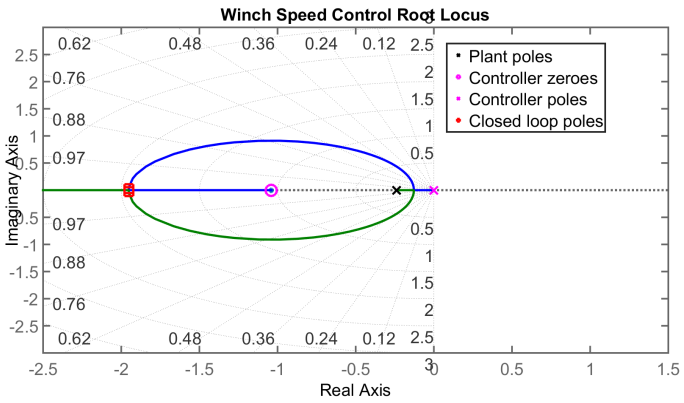

Figure 6.4: Winch speed control system root locus.

Figure 6.5 shows the step response of the winch speed system. The linear simulation based on the simplified model exhibits a settling time of less than 2 seconds as per design requirements albeit with an overshoot due to the PI controller zero. When simulated in a non-linear environment which includes the parasitic feedback loop, friction and the electrical time constant, the speed controller exhibits a more damped response with a much longer settling time $t_s \geq 15$ seconds. This is the consequence of neglecting parasitic feedback and friction during control system design.

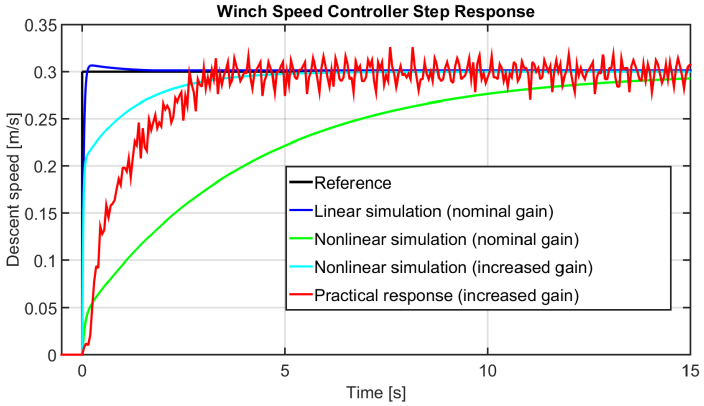

Figure 6.5: Winch speed controller step response.

The long settling time exhibited by the nominal controller gain was deemed unacceptable. While maintaining the PI controller zero at s = -1.04, the controller gain was iteratively increased and the corresponding non-linear step response was inspected. Figure 6.5 shows that for an increased controller gain of $K_p = 3$, the non-linear simulation yields a settling time of $t_s \approx 3$ seconds. For controller gains larger than 3, the non-linear simulated showed an almost instantaneous rise time which is understood to be practically impossible and only manifests in the simulation due to modelling inaccuracies. A 3 second settling time was accepted going forward.

Consistent with the non-linear simulation, the practical response with the increased controller gain exhibits a settling time of $t_s \approx 3$ seconds although a dead-band behaviour is evident in the practical response. The discrepancy between the non-linear and the practical responses could be due to inaccuracies in modelling winch friction, specifically stiction. Although significant measurement noise is visible in the practical response due to the choice of rotary sensor, the physical winch motion was sufficiently smooth to winch the quad-rotor during landing. The winch speed response exhibits zero steady-state error for step inputs.

6.3 Point-Mass Model Derivation

We recall from Section 1.3 that the secondary aim of this project is to analyse the dynamics of the tethered quad-rotor system. This section presents a point-mass model of the tethered system to facilitate the analysis of the system dynamics. The point-mass model is formulated to approximate the dynamics of the tethered vehicle during the Buoyancy state and the Descent state as shown in Figure 6.1.

During the Buoyancy and Descent phases, the vehicle's thrust is clamped at the set maximum thrust and the vehicle is in horizontal velocity control mode with zero velocity reference. The point-mass model is developed for no wind conditions to aid simplicity. Due to the small distance between the vehicle's CoG and the tether attachment point, the tether force's line of action is modelled as passing through the CoG. Since the flight control system controls horizontal velocity by issuing tilt angle references, the vehicle's tilt angle dynamics are inferred from the closed loop tilt angle dynamics and a zero velocity reference. The aforementioned approximations result in the point-mass model represented by the free body diagram shown in Figure 6.6.

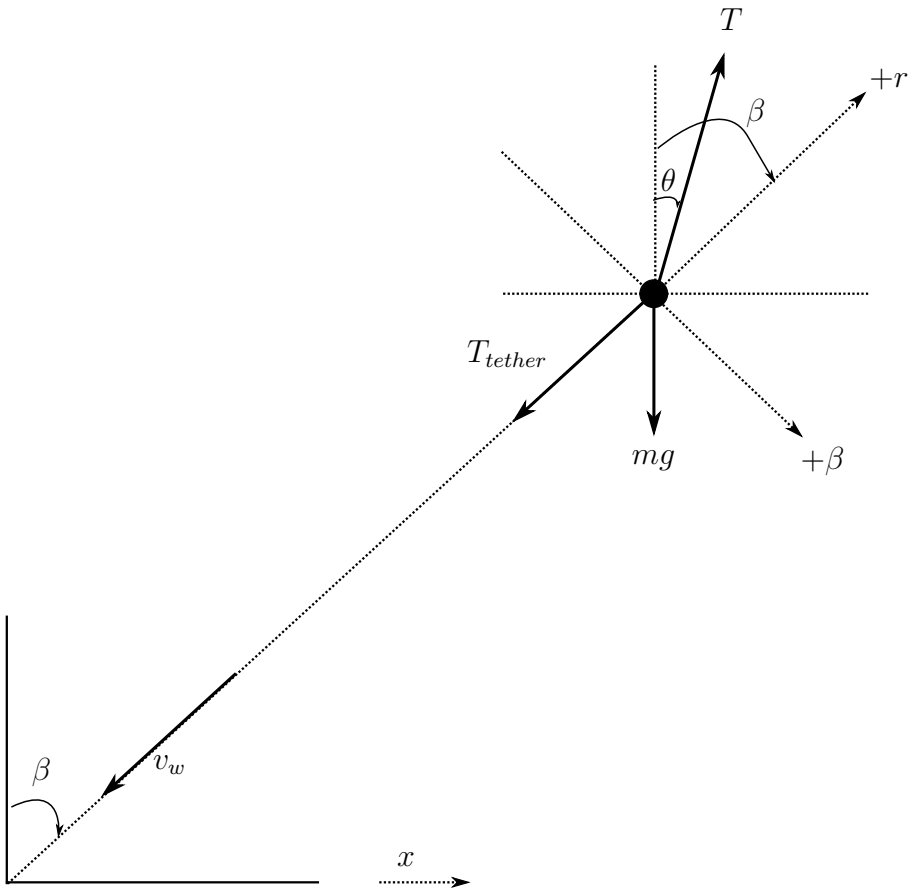

Figure 6.6: Tethered quad-rotor point-mass model.

The point-mass model is best analysed in a polar coordinate system comprised of a tethering angle β and a tethering radius r as shown in Figure 6.6. A model for the tethering angle dynamics is derived in Section 6.3.1, a model for the tether force is derived in Section 6.3.2, and a model for the tethering radius dynamics is derived in Section 6.3.3.

The derived system dynamics are linearised about a static operating point in Section 6.3.4. Lastly, linearised models for the tethering angle and the tethering radius dynamics are presented in Sections 6.3.5 and 6.3.7 respectively.

6.3.1 Tethering Angle Dynamics

The derivation of the tethering angle dynamics begins with expressions for the transverse acceleration a_β and the transverse velocity v_β as given by Equations 6.1 and 6.2. Equations 6.1 and 6.2 are standard expressions for the transverse acceleration and velocity in an (r, β) polar coordinate system [34].

$$a_\beta = r\ddot{\beta} + 2\dot{r}\dot{\beta} \tag{6.1}$$

$$v_\beta = r\dot{\beta} \tag{6.2}$$

Since the action line of the tether force is modelled as passing through the CoG, the rotational dynamics of the vehicle can no longer be modelled by Newton's law for rotational motion. Instead, the vehicle's tilt angle θ is modelled as being dependent only on the action of the horizontal velocity controller. The horizontal velocity controller presented in Section 5.2.4 implements the velocity control scheme shown in Figure 6.7. Given that the velocity controller is a PI controller, the horizontal velocity control law is given by Equation 6.3.

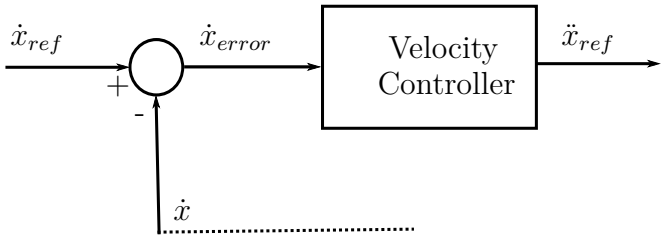

Figure 6.7: Quad-rotor horizontal velocity control law.

$$\ddot{x}_{ref} = K_i \int (\dot{x}_{ref} - \dot{x})dt + K_p(\dot{x}_{ref} - \dot{x}) \tag{6.3}$$

For small tethering angles, the horizontal velocity $\dot{x}$ is approximately equal to the transverse velocity v_β, and the horizontal velocity can therefore be written in terms of the tethering radius r and the tethering angle rate $\dot{\beta}$, as expressed in Equation 6.4 below.

$$\begin{aligned} \dot{x} &\approx v_\beta \\ &\approx r\dot{\beta} \end{aligned} \tag{6.4}$$

The approximation for horizontal velocity given in Equation 6.4 can be substituted into Equation 6.3 to yield Equation 6.5. With reference to the state machine shown in

Figure 6.1, a velocity reference of $\dot{x}_{ref} = 0$ is applicable.

$$\begin{aligned}\ddot{x}_{ref} &\approx K_i \int (0 - r\dot{\beta})dt + K_p(0 - r\dot{\beta}) \\ &\approx -K_i \int r\dot{\beta}dt - K_p r\dot{\beta} \\ &\approx -K_i r \int \dot{\beta}dt - K_p r\dot{\beta} \\ &\approx -K_i r\beta - K_p r\dot{\beta} \end{aligned} \tag{6.5}$$

As detailed in Section 5.2.4, the horizontal acceleration reference generated by the horizontal velocity controller is converted to a tilt angle reference using Equation 6.6. Equation 6.7 results from substituting Equation 6.5 into Equation 6.6.

$$\theta_{ref} \approx \frac{1}{g}\ddot{x}_{ref} \tag{6.6}$$

$$\approx \frac{r}{g}(-K_i\beta - K_p\dot{\beta}) \tag{6.7}$$

The closed-loop response of the roll/pitch angle controller designed in Section 5.2.3 is a dominantly first-order response with a time constant of $\tau_\theta = 0.35$ seconds and a zero steady-state tracking error. The relationship between the tilt angle reference and the instantaneous tilt angle can therefore be modelled by the first-order transfer function given by Equation 6.8 in the Laplace domain, and by the equivalent first-order differential equation given by Equation 6.9 in the time domain.

$$\frac{\theta(s)}{\theta_{ref}(s)} \approx \frac{1}{1 + s\tau_\theta} \tag{6.8}$$

$$\theta(t) \approx \theta_{ref}(t) - \tau_\theta\dot{\theta}(t) \tag{6.9}$$

Equation 6.7 can be substituted into Equation 6.9 to yield the expression for tilt angle as shown in Equation 6.10.

$$\theta \approx \frac{r}{g}(-K_i\beta - K_p\dot{\beta}) - \tau_\theta\dot{\theta} \tag{6.10}$$

With reference to Figure 6.6, the sum of forces in the β direction is given by Equation 6.11, where T is the total thrust.

$$F_\beta = mg\sin(\beta) - T\sin(\beta - \theta) \tag{6.11}$$

To conclude the derivation of tethering angle dynamics, the expression for transverse acceleration given in Equation 6.1 and the expression for the vehicle's tilt angle

given in Equation 6.10 are both substituted into Equation 6.11 to yield Equation 6.12. Equation 6.12 now represents a single expression for the tethering angle dynamics.

$$m(r\ddot{\beta} + 2\dot{r}\dot{\beta}) = mg\sin(\beta) - T\sin\left(\beta + \frac{r}{g}(K_i\beta + K_p\dot{\beta}) + \tau_\theta\dot{\theta}\right) \tag{6.12}$$

6.3.2 Tether Dynamics

This section seeks to establish a concise expression for the tether force in the point-mass model. The differential equations for the tether model were presented in Section 3.3.4 and are repeated in Equations 6.13 through to Equation 6.16 for convenience.

$$T_{tether} = k_t L_{ext} + b_t \dot{L}_{ext} \tag{6.13}$$

$$L_{ext} = r - L_t \tag{6.14}$$

$$L_t = L_{t0} - L_{wound} \tag{6.15}$$

$$L_{wound} = \int \frac{L_t}{L_{ext} + L_t} v_w dt \tag{6.16}$$

Equations 6.17 through to 6.19 are the time derivatives of Equations 6.14 through to 6.16 respectively, where T_{tether} is the tether force, k_t and b_t are the tether stiffness and damping coefficient respectively, L_{ext} is the instantaneous tether extension, L_t is the instantaneous tether length, L_{t0} is the initial tether length, L_{wound} is the unstretched length of wound tether, r is the winch radius and v_w is the linear winching speed.

$$\dot{L}_{ext} = \dot{r} - \dot{L}_t \tag{6.17}$$

$$\dot{L}_t = -\dot{L}_{wound} \tag{6.18}$$

$$\begin{aligned} \dot{L}_{wound} &= \frac{L_t}{L_{ext} + L_t} v_w \\ &= \frac{L_t}{r} v_w \end{aligned} \tag{6.19}$$

Substituting Equations 6.14 to 6.19 into Equation 6.13, the following expression is obtained for the tether force.

$$T_{tether} = k_t(r - L_t) + b_t\left(\dot{r} + \frac{L_t}{r} v_w\right) \tag{6.20}$$

6.3.3 Tethering Radius Dynamics

Equations 6.21 and 6.22 are the standard expressions of the radial acceleration a_r and the radial velocity v_r as a function of the tethering radius r and the tethering angle beta in polar coordinates [34].

$$a_r = \ddot{r} - r(\dot{\beta})^2 \tag{6.21}$$

$$v_r = \dot{r} \tag{6.22}$$

With reference to the free body diagram in Figure 6.6, the resultant force in the radial direction is given by Equation 6.23.

$$F_r = T\cos(\beta - \theta) - T_{tether} - mg\cos(\beta) \tag{6.23}$$

The acceleration expression in Equation 6.21 and the expression for tilt angle in Equation 6.10 can be substituted into Equation 6.23 to yield Equation 6.24. Equation 6.24 is Newton's law for the r dimension of the system and captures the tethering radius dynamics.

$$\begin{aligned} m(\ddot{r} - r(\dot{\beta})^2) = T\cos\left(\beta + \frac{r}{g}(K_i\beta + K_p\dot{\beta}) + \tau_\theta\dot{\theta}\right) - k_t(r - L_t) \\ - b_t\left(\dot{r} + \frac{L_t}{r}v_w\right) - mg\cos(\beta) \end{aligned} \tag{6.24}$$

6.3.4 Model Linearisation

Both the tethering angle dynamics derived in Section 6.3.1 and the tethered vehicle tethering radius dynamics presented in Section 6.3.3 are extremely non-linear partly because of the frequent occurrence of trigonometric functions cos and sin. In order to make use of available powerful state-space tools applicable exclusively to linear systems, the dynamics are linearised around a static operating point directly above the winch. For the linearised system, state variables are defined to be the deviations from the static point as given by Equation 6.25. Appendix C details the application of the Taylor Series approximation to linearise a model around a static operating point.

$$\Delta \mathbf{x} = \begin{bmatrix} \Delta\beta \\ \Delta\dot{\beta} \\ \Delta r \\ \Delta\dot{r} \end{bmatrix} \tag{6.25}$$

Following from the formulation in Appendix C, the state equation for the linearised system is given by Equation 6.26.

$$\begin{bmatrix} \Delta\dot{\beta} \\ \Delta\ddot{\beta} \\ \Delta\dot{r} \\ \Delta\ddot{r} \end{bmatrix} = \left.\begin{bmatrix} 0 & 1 & 0 & 0 \\ \frac{\partial F_1}{\partial\beta} & \frac{\partial F_1}{\partial\dot{\beta}} & \frac{\partial F_1}{\partial r} & \frac{\partial F_1}{\partial\dot{r}} \\ 0 & 0 & 0 & 1 \\ \frac{\partial F_2}{\partial\beta} & \frac{\partial F_2}{\partial\dot{\beta}} & \frac{\partial F_2}{\partial r} & \frac{\partial F_2}{\partial\dot{r}} \end{bmatrix}\right|_{(\mathbf{x}=\mathbf{x}_0, u=u_0)} \begin{bmatrix} \Delta\beta \\ \Delta\dot{\beta} \\ \Delta r \\ \Delta\dot{r} \end{bmatrix} + \left.\begin{bmatrix} 0 \\ \frac{\partial F_1}{\partial v_w} \\ 0 \\ \frac{\partial F_2}{\partial v_w} \end{bmatrix}\right|_{(\mathbf{x}=\mathbf{x}_0, u=u_0)} \Delta v_w \tag{6.26}$$

The functions F_1 and F_2 in Equation 6.26 are the second time derivatives of the system angle and system radius respectively. The function F_1 is defined in Equation 6.27 and follows directly from Equation 6.12. The partial derivatives with respect to F_1 are given by Equations 6.28 through to 6.32.

$$\begin{aligned} \ddot{\beta} &= F_1(\beta, \dot{\beta}, r, \dot{r}, v_w) \\ &= \frac{g\sin(\beta) - 2\dot{r}\dot{\beta}}{r} - \frac{T}{mr}\sin\left(\beta + \frac{r}{g}(K_i\beta + K_p\dot{\beta}) + \tau_\theta\dot{\theta}\right) \end{aligned} \tag{6.27}$$

$$\frac{\partial F_1}{\partial \beta} = \frac{g}{r}\cos(\beta) - \left(\frac{g + rK_i}{g}\right)\left(\frac{T}{mr}\right)\cos\left(\beta + \frac{r}{g}(K_i\beta + K_p\dot{\beta}) + \tau_\theta\dot{\theta}\right) \tag{6.28}$$

$$\frac{\partial F_1}{\partial \dot{\beta}} = -\frac{2\dot{r}}{r} - \left(\frac{K_p}{g}\right)\left(\frac{T}{m}\right)\cos\left(\beta + \frac{r}{g}(K_i\beta + K_p\dot{\beta}) + \tau_\theta\dot{\theta}\right) \tag{6.29}$$

$$\begin{aligned}\frac{\partial F_1}{\partial r} = {} & \frac{2\dot{r}\dot{\beta} - g\sin(\beta)}{r^2} + \frac{T}{mr^2}\sin\left(\beta + \frac{r}{g}(K_i\beta + K_p\dot{\beta}) + \tau_\theta\dot{\theta}\right) \\ & - \left(\frac{K_i\beta + K_p\dot{\beta}}{g}\right)\left(\frac{T}{mr}\right)\cos\left(\beta + \frac{r}{g}(K_i\beta + K_p\dot{\beta}) + \tau_\theta\dot{\theta}\right)\end{aligned} \tag{6.30}$$

$$\frac{\partial F_1}{\partial \dot{r}} = -\frac{2\dot{\beta}}{r} \tag{6.31}$$

$$\frac{\partial F_1}{\partial v_w} = 0 \tag{6.32}$$

Equation 6.33 and follows directly from Equation 6.24 and is the definition of F_2. The partial derivatives with respect to F_2 are given by Equations 6.34 through to 6.38.

$$\begin{aligned}\ddot{r} &= F_2(\beta, \dot{\beta}, r, \dot{r}, v_w) \\ &= r(\dot{\beta})^2 + \frac{T}{m}\cos\left(\beta + \frac{r}{g}(K_i\beta + K_p\dot{\beta}) + \tau_\theta\dot{\theta}\right) - \frac{k_t}{m}(r - L_t) \\ &\quad - \frac{b_t}{m}\left(\dot{r} + \frac{L_t}{r}v_w\right) - g\cos(\beta)\end{aligned} \tag{6.33}$$

$$\frac{\partial F_2}{\partial \beta} = -\left(\frac{g + rK_i}{g}\right)\left(\frac{T}{m}\right)\sin\left(\beta + \frac{r}{g}(K_i\beta + K_p\dot{\beta}) + \tau_\theta\dot{\theta}\right) + g\sin(\beta) \tag{6.34}$$

$$\frac{\partial F_2}{\partial \dot{\beta}} = 2r\dot{\beta} - \left(\frac{rK_p}{g}\right)\left(\frac{T}{m}\right)\sin\left(\beta + \frac{r}{g}(K_i\beta + K_p\dot{\beta}) + \tau_\theta\dot{\theta}\right) \tag{6.35}$$

$$\begin{aligned}\frac{\partial F_2}{\partial r} = {} & (\dot{\beta})^2 - \left(\frac{K_i\beta + K_p\dot{\beta}}{g}\right)\left(\frac{T}{m}\right)\sin\left(\beta + \frac{r}{g}(K_i\beta + K_p\dot{\beta}) + \tau_\theta\dot{\theta}\right) \\ & - \frac{k_t}{m} + \frac{b_t L_t v_w}{mr^2}\end{aligned} \tag{6.36}$$

$$\frac{\partial F_2}{\partial \dot{r}} = \frac{-b_t}{m} \tag{6.37}$$

$$\frac{\partial F_2}{\partial v_w} = -\frac{b_t L_t}{mr} \tag{6.38}$$

6.3.5 Decoupled Tethering Angle Model

Equation 6.26 describes the dynamics of the tethered quad-rotor UAV as a fourth order system with state variables related to both the tethering angle and tethering radius dimensions. At the static operating point the tethering angle and all time derivatives tend to zero. Moreover, the arguments of all sin() functions in Equations 6.27 through to 6.38 also tend to zero. Consequently, the partial derivatives $\frac{\partial F_1}{r}$, $\frac{\partial F_1}{\dot{r}}$, $\frac{\partial F_2}{\beta}$ and $\frac{\partial F_2}{\dot{\beta}}$ in Equations 6.30, 6.31, 6.34 and 6.35 all tend to zero at the static operating point. This allows the system dynamics to be decoupled into separate second order tethering angle and tethering radius systems.

The decoupled tethering angle dynamics are represented by the state equation in Equations 6.39 and 6.40. Equation 6.41 is the output equation for the tethering angle dynamics.

$$\begin{bmatrix} \Delta\dot{\beta} \\ \Delta\ddot{\beta} \end{bmatrix} = \left[\begin{matrix} 0 & 1 \\ \frac{\partial F_1}{\beta} & \frac{\partial F_1}{\dot{\beta}} \end{matrix}\right]\Bigg|_{(\mathbf{x}=\mathbf{x}_0,u=u_0)} \begin{bmatrix} \Delta\beta \\ \Delta\dot{\beta} \end{bmatrix} + \left[\begin{matrix} 0 \\ \frac{\partial F_1}{\partial v_w} \end{matrix}\right]\Bigg|_{(\mathbf{x}=\mathbf{x}_0,u=u_0)} \Delta v_w \tag{6.39}$$

$$= \begin{bmatrix} 0 & 1 \\ \left\{\frac{g}{r_0} - \left(\frac{g + gr_0K_i}{g}\right)\left(\frac{T}{mr_0}\right)\right\} & -\left\{\left(\frac{K_p}{g}\right)\left(\frac{T}{m}\right)\right\} \end{bmatrix} \begin{bmatrix} \Delta\beta \\ \Delta\dot{\beta} \end{bmatrix} + \begin{bmatrix} 0 \\ 0 \end{bmatrix} \Delta v_w \tag{6.40}$$

$$\Delta y_\beta = \begin{bmatrix} 1 & 0 \end{bmatrix} \begin{bmatrix} \Delta\beta \\ \Delta\dot{\beta} \end{bmatrix} + \begin{bmatrix} 0 \end{bmatrix} \Delta v_w \tag{6.41}$$

The poles of a general system expressed as a state variable model are the solutions of Equation 6.42 where *det* is the determinant operator, A is the state matrix and s is the Laplace variable. The system poles can be conveniently computed by passing the state and output matrices to the Matlab *pole()* function.

$$det\left[sI - A\right] = 0 \tag{6.42}$$

As seen in Equation 6.42, the system poles are a function only of the state matrix. With reference to Equation 6.40, the state equation is dependent on the values of the horizontal velocity controller gains K_p and K_i. The transfer function of the velocity PI controller is given in Equation 6.43. From Equation 6.43, the controller introduces a zero at $-\frac{K_i}{K_p}$ and an overall gain K_p.

$$\begin{aligned} G_v(s) &= K_p + \frac{K_i}{s} \\ &= K_p \left(\frac{s + \frac{K_i}{K_p}}{s} \right) \end{aligned} \tag{6.43}$$

6.3.6 Validation of Tethering Angle Model

This section seeks to validate the decoupled tethering angle model using non-linear simulations. As detailed in Section 6.3.5, the tethering angle system poles are dependent on the horizontal velocity controller gain and the tethering radius. The variation of tethering angle system poles with velocity controller gain is investigated in Section 6.3.6.1. Section 6.3.6.2 investigates the variation of tethering angle system poles as a function of tethering radius.

6.3.6.1 Variation of Tethering Angle System Poles with Velocity Controller Gain

To investigate the variation of the tethering angle system poles with respect to velocity controller gain, the controller gain K_p is iteratively varied in steps of 0.1 from 0 to 10. At each iteration the integral gain K_i is calculated so that the controller zero -$\frac{K_i}{K_p}$ is at $s = -0.1$ as designed in Section 5.2.4. Figure 6.8 shows the root locus of the tethering angle dynamics with a change in velocity controller gain at a constant radius of $r_0 = 10$ m and a total thrust T with a value 6 N above hover thrust.

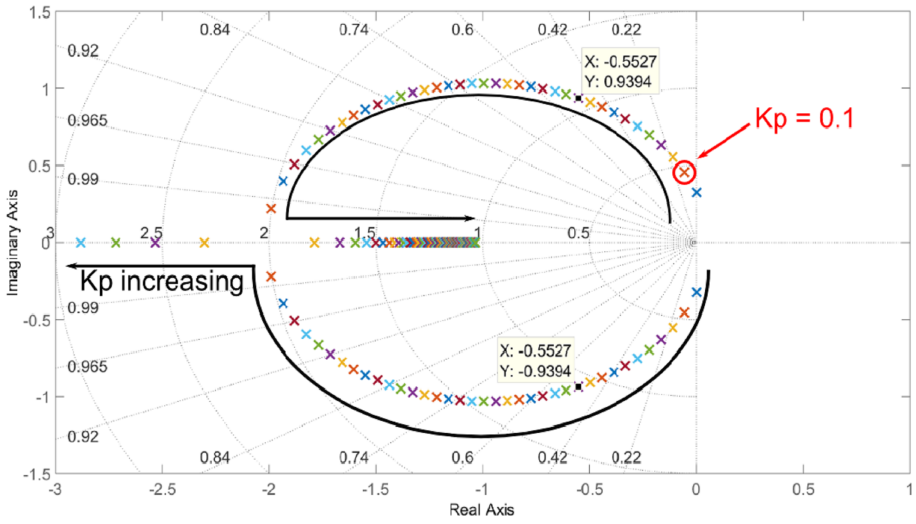

Figure 6.8: Root locus of tethering angle dynamics with a change in gain.

For a gain of zero, the tethering angle system poles are marginally stable corresponding to oscillations of the tethered vehicle around the equilibrium point with constant amplitude. As the controller gain is increased, the tethering angle dynamics become more damped with an increase in natural frequency. Proceeding further, the complex pole pair begins to become less damped whilst continue to increase in frequency. A continued increase in controller gain will result in the poles breaking in on the real axis. Thereafter one of the poles approaches a low-frequency asymptote on the real axis while the second pole tends to -∞ on the real axis.

To validate the tethering angle system model, a controller gain of $K_p = 0.1$ was chosen. The choice of controller gain places the tethering angle system poles at $s = -0.055 \pm j0.457$. This should result in a response with a natural frequency of 0.46 rad.s^{-1}, and a decay time constant of 18.2 seconds. With the selected gain, the tethered quad-rotor was initialised at an altitude of 10 m and North and East positions of 5 m. The Buoyancy state as detailed in Section 6.1.2.7 was activated at time $t = 1$ second. The non-linear simulation results are shown in Figure 6.9.

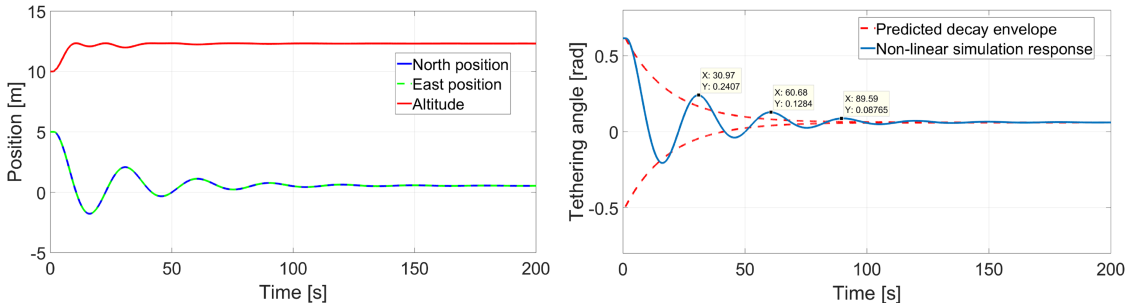

(a) Position responses.

(b) Tethering angle response.

Figure 6.9: Tethering angle response at 0.1 velocity controller gain.

Section B.3 details a method to predict the period of oscillation and the time constant of the exponential envelope for the tethering angle response. Figure 6.9b shows that for the selected controller gain of $K_p = 0.1$, the exponential envelope predicted by the point-mass model matches the envelope of the non-linear simulation closely. For the simulated case, the oscillation period of the non-linear response is approximately 30 seconds while the period predicted by the point-mass model is approximately 14 seconds. The prediction for the period of oscillation is not very accurate for this case even though it is within an order of magnitude of the simulation result. The inaccuracy stems from coupling between tethering radius and tethering angle dynamics and the assumption made in the point-mass model that the tether force 's line of action passes through the vehicle's CoG. The result suggests that the point-mass model determines the damping properties and the stability of the tethered vehicle with more accuracy than it determines the speed of the vehicle's response.

Going forward, an attempt was made to predict the tethering angle dynamics of the vehicle for the nominal velocity controller gain detailed in Section 5.2.4. The cursors in Figure 6.8 show the tethering angle dynamics poles corresponding to the controller gains implemented on the UAV as designed in Section 5.2.4. The poles are situated at a natural frequency of $\omega_n \approx 1.1$ rad.s^{-1} and a damping ratio of $\zeta \approx 0.5$.

Equation 6.44 infers a system's maximum overshoot from system pole's damping ratio while Equation 6.45 expresses the systems rise time from the pole's natural frequency [35].

$$M_p = e^{\left(\frac{-\pi\zeta}{\sqrt{1-\zeta^2}}\right)} \tag{6.44}$$

$$t_r \approx \frac{1.8}{\omega_n} \tag{6.45}$$

From Equations 6.44 and 6.45, the designed horizontal velocity controller gains are therefore expected to yield a moderately-damped tethering angle response with a maximum overshoot of $M_p = 16\ \%$ and a rise time of $t_r \approx 1.64$ seconds. The root locus in Figure 6.8 provides a design tool to ensure that the designed horizontal velocity controller gains result in an acceptably-damped and stable tethering angle response.

6.3.6.2 Variation of Tethering Angle Poles with Tethering Radius

This section discusses the variation of tethering angle system poles with tethering radius. Figure 6.10 shows the root locus of the tethering angle system with respect to tethering radius. With the velocity controller gains kept constant at the values designed in Section 5.2.4, the tethering radius was varied from 0.5 m to 50 m in increments of 0.5 m. The tethering angle system poles' real parts stay constant while the imaginary pole parts increase in magnitude with an increase in tethering radius.

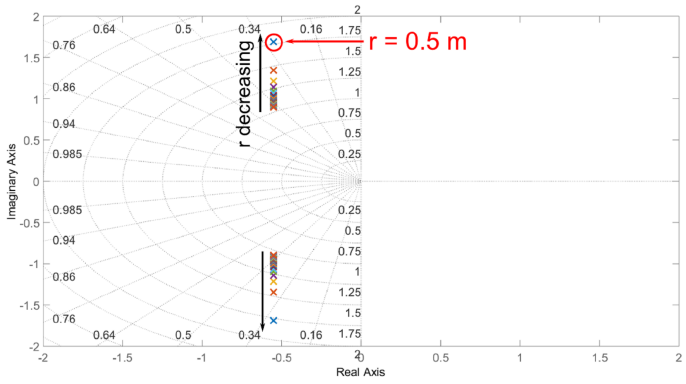

Figure 6.10: Root locus of tethering angle dynamics with respect to tethering radius.

As shown in Figure 6.10 the tethering angle system poles are always complex conjugates of each other for all possible values of tethering radius. Figure 6.11 is a plot of the natural frequency and damping ratio of the tethering angle system poles as the tethering radius is varied from 0.5 m to 50 m in increments of 0.5 m. An increase in natural frequency and a decrease in damping ratio is observed for very low tether radii. For radii larger than 4 m, the damping ratio rises very slowly while the natural frequency decreases very slowly with an increase in tether radius.

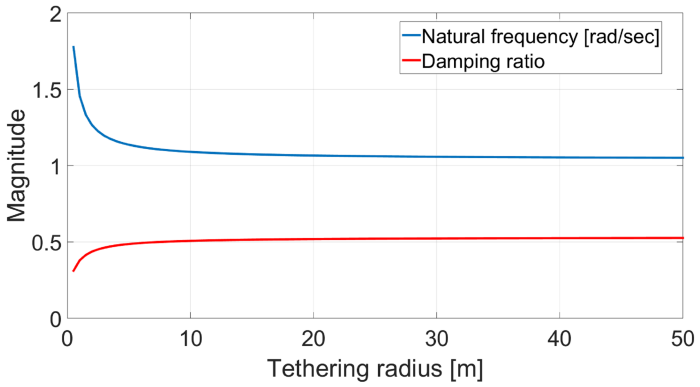

Figure 6.11: Variation of tethering angle system natural frequency and damping ratio with tethering radius.

To validate the variation of tethering angle system poles with variation in tethering radius, the tethered vehicle was initialised as an initial altitude of 0.5 m and North and East offsets of 0.1 m each. Due to the horizontal offsets being small, the initial tether radius is close to 0.5 m, corresponding to the poles located at $s = -0.5527 \pm j1.688$ as highlighted in Figure 6.10. The Buoyancy state was activated at time $t = 1$ second and the simulation results shown in Figure 6.12 were obtained. The non-linear vehicle response takes the form shown in Equation B.30. The simulated tethering angle response for this case matches the point-mass model response fairly well, albeit with a slightly faster settling time observed for the non-linear simulation.

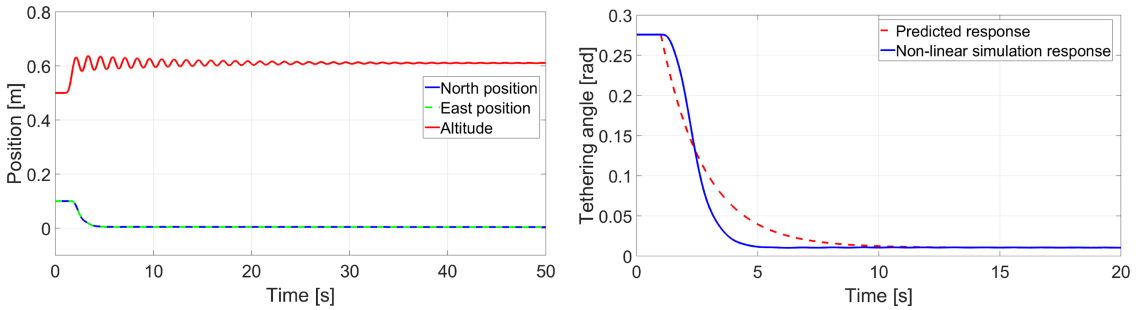

(a) Position responses.

(b) Tethering angle response.

Figure 6.12: Tethering angle response at 0.5 m tethering radius.

Based on the decrease in damping ratio at low altitudes as shown in Figure 6.11, the tethered vehicle is expected to exhibit a slight horizontal position drift as it enters the final 1 metre of its descent. At such a low altitude the chances of the vehicle missing the landing platform due to the drift are very low considering that the platform measures 2.4 m $\times$ 2.4 m. Moreover, the short tether length at such low altitude will tightly restrict the allowable lateral deviation of the vehicle, and coupled with the winching

action, the vehicle should be pulled towards the landing target (platform centre).

6.3.7 Decoupled Tethering Radius Model

The decoupled tethering radius dynamics are described by the state equation in Equations 6.46 and 6.47 and the output equation in Equation 6.48. Using the result in Equation B.3, the transfer function from winching speed to perturbations in the system radius is given by Equation 6.49.

$$\begin{bmatrix} \Delta\dot{r} \\ \Delta\ddot{r} \end{bmatrix} = \left.\begin{bmatrix} 0 & 1 \\ \dfrac{\partial F_2}{r} & \dfrac{\partial F_2}{\dot{r}} \end{bmatrix}\right|_{(\mathbf{x}=\mathbf{x}_0, u=u_0)} \begin{bmatrix} \Delta r \\ \Delta\dot{r} \end{bmatrix} + \left.\begin{bmatrix} 0 \\ \dfrac{\partial F_2}{\partial v_w} \end{bmatrix}\right|_{(\mathbf{x}=\mathbf{x}_0, u=u_0)} \Delta v_w \tag{6.46}$$

$$= \begin{bmatrix} 0 & 1 \\ -\dfrac{k_t}{m} & -\dfrac{b_t}{m} \end{bmatrix} \begin{bmatrix} \Delta r \\ \Delta\dot{r} \end{bmatrix} + \begin{bmatrix} 0 \\ -\dfrac{b_t L_{t0}}{m r_0} \end{bmatrix} \Delta v_w \tag{6.47}$$

$$\Delta y_r = \begin{bmatrix} 1 & 0 \end{bmatrix} \begin{bmatrix} \Delta r \\ \Delta\dot{r} \end{bmatrix} + \begin{bmatrix} 0 \end{bmatrix} \Delta v_w \tag{6.48}$$

$$\frac{\Delta r(s)}{\Delta v_w(s)} = \frac{-\dfrac{b_t L_{t0}}{m r_0}}{s\left(s + \dfrac{b_t}{m}\right) + \dfrac{k_t}{m}} \tag{6.49}$$

Equation 6.49 shows that the tethering radius poles are determined by the tether stiffness and the tether damping coefficient. The tethering radius pole locations for the tether parameters presented in Section F.2 are plotted in Figure 6.13. It should be recalled from Section F.2 that no effort was invested in accurately determining the numerical values of the tether stiffness and damping coefficient. The goal was to assign reasonable values that would still expose the basic dynamic behaviour of the system without agonising about parameter accuracy.

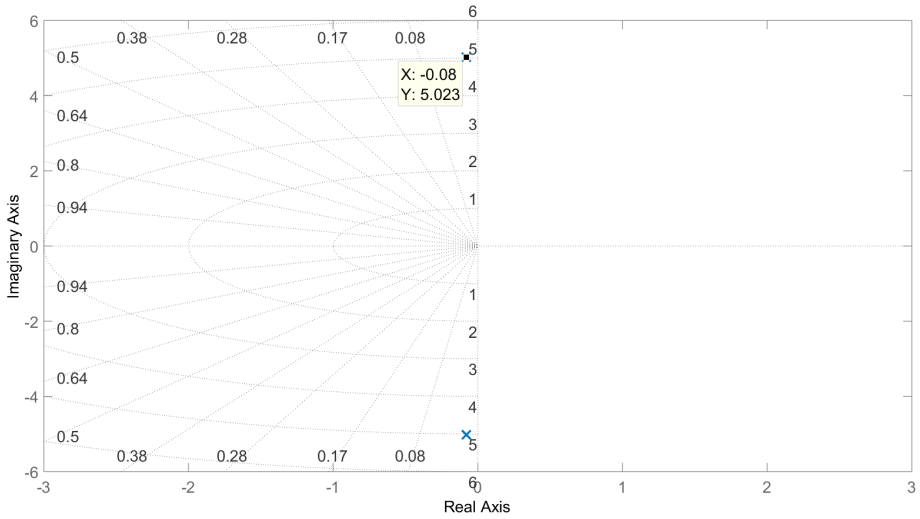

Figure 6.13: Tethering radius system poles.

Of the two decoupled systems, the tethering angle dynamics determine the overall system stability. With a significantly stiff tether capable of withstanding all possible tensile forces, it is intuitive to not expect any persistent or unstable oscillations in the tethering radius direction. We however proceed to show that the tethering radius dynamic poles lie on the left half-plane for all possible values of tether stiffness and damping coefficient.

Figure 6.13 shows the tethering radius system poles for the tether parameters stated in Section F.2. For the assumed tether parameters, the tethering radius system possesses a lightly damped complex pole pair. Our main goal in the tethering radius system analysis is to show that the tethering radius poles are always on the left half-plane for all valid values of each tether parameter.

6.3.8 Validation of Tethering Radius Model

As detailed in Section 6.3.7, the tethering radius system poles are dependent on the tether stiffness and the tether damping coefficient. The variation of tethering radius system poles with tether stiffness is investigated in Section 6.3.8.1. Section 6.3.8.2 investigates the variation of tethering radius system poles as a function of tether damping coefficient.

6.3.8.1 Variation of Tethering Radius Poles with Tether Stiffness

Figure 6.14 shows the tethering radius system poles as tether stiffness is varied from 10 to 1000 in steps of 10 with tether damping coefficient held constant at the nominal value. The stiffness of the steel core tether used is clearly in the order of hundreds therefore the analysis can be performed with a starting value of 10 without loss of generality. Figure 6.14 shows an increase in natural frequency and a decrease in damping as tether stiffness increases at constant damping coefficient. It is important to note that even though the tethering radius system damping deteriorates with and increase in tether stiffness, the system poles are always on the left half-plane indicating stability.

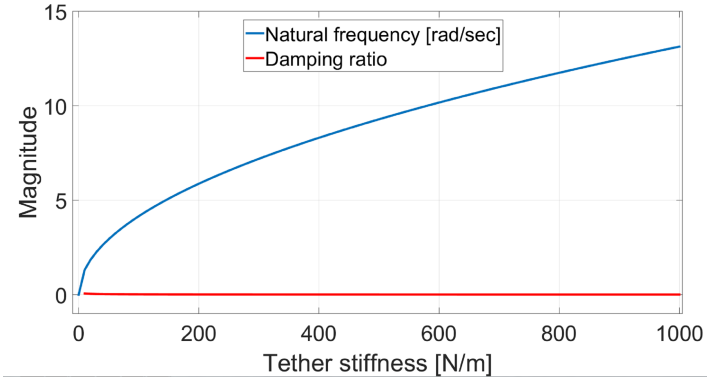

Figure 6.14: Variation of tethering radius natural frequency and damping ratio with tether stiffness.

To validate the variation of tethering radius system poles as a function of tether stiffness a non-linear simulation was performed with a tether stiffness of 100 N.m^{-1}. The natural frequency ω_n and the damping ratio ζ corresponding to a tether stiffness of 100 N.m^{-1} can be read off from Figure 6.14. The corresponding poles $s = -\sigma \pm j\omega_d$ can then be determined using Equations 6.50 and 6.51. For the simulated case, the poles are as $s = -0.08 \pm j4.152$.

$$\sigma = \zeta\omega_n \tag{6.50}$$

$$\omega_d = \omega_n\sqrt{1-\zeta^2} \tag{6.51}$$

The simulated tethering radius response is shown in Figure 6.15. The pole locations can be used to predict the period of oscillation and the time constant of the oscillation decay as presented in Section B.3. As seen from Figure 6.15b, the non-linear response's decay envelope is slightly faster than the predicted envelope. However, as shown in

Figure 6.15b the non-linear simulation response has an oscillation period of $T = 1.55$ seconds which is very close to the predicted oscillation period of $T = 1.51$ seconds. For this case, the point-mass model predicts the oscillation frequency of more accurately than it predicts the damping properties.

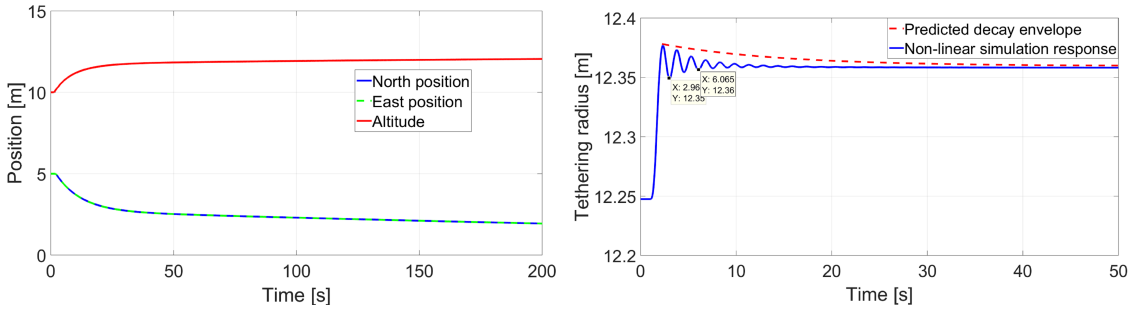

(a) Position responses. (b) Tethering radius response.

Figure 6.15: Tethering radius response with a tether stiffness of 100 N.m^{-1}.

6.3.8.2 Variation of Tethering Radius Poles with Tether Damping Coefficient

Figure 6.16 shows the tethering radius system pole locations when the tether damping coefficient is varied from from 0 to 200 in steps of 1 while the tether stiffness is kept constant to the value stated in Section F.2. For a zero damping coefficient the tethering radius system is marginally stable. This is expected since there the has to be some damping in order for any oscillations in the radial direction to eventually die down.

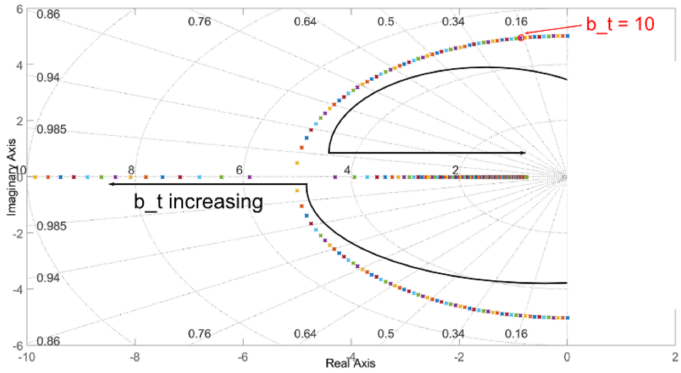

Figure 6.16: Tethering radius system root locus with respect to tether damping coefficient.

As the damping coefficient is increased the tethering radius system gains both damping and natural frequency. For a damping coefficient of 59, the tethering radius system becomes critically damped with both poles situated at $s \approx 5$ rad.s^{-1}. Further

increase in damping coefficient results in one recessive pole striving towards $s = -\infty$ while the dominant real pole moves to lower frequencies. The dominant pole has an asymptote at $s \approx$ -0.77.

To validate the variation of tethering radius system poles with respect to tether damping coefficient, a non-linear simulation was performed with a tether damping coefficient of $b_t =$ N.s/m while the the tether stiffness is at the nominal value. The chosen tether damping coefficient corresponds to tethering radius system poles at $s = -0.7759 \pm j4.964$ as highlighted in Figure 6.16. Following from Section B.3, the poles correspond to an oscillation period of $T = 1.256$ seconds. Figure 6.17b shows a period of $T = 1.195$ seconds for the non-linear response. The point-mass model therefore predicts the oscillation frequency very accurately for this simulated case. The non-linear simulation envelope decay also matches the predicted decay envelope closely.

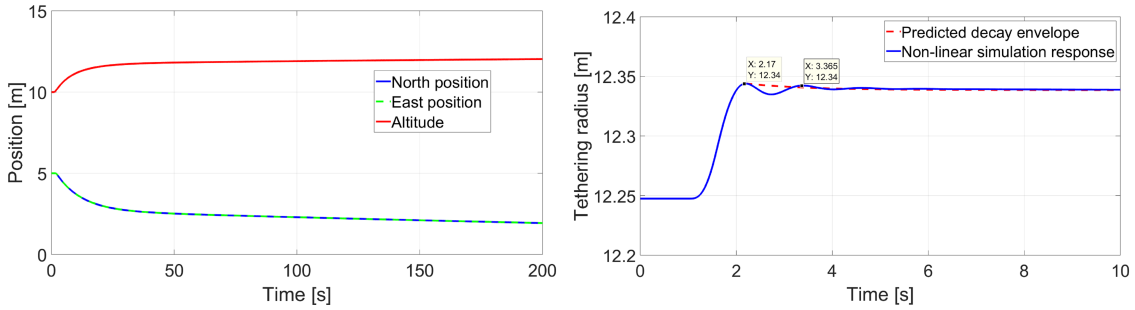

(a) Position responses.

(b) Tethering radius response.

Figure 6.17: Tethering radius dynamics with underdamped poles.

6.4 Simulated Landing

To cement the model validation presented in Sections 6.3.6 and 6.3.8, a complete autonomous landing of the tethered quad-rotor was simulated using the non-linear model presented in Chapter 3. Figure 6.18 shows the results of a simulated landing. The simulation kicks off with the tethered vehicle hovering under horizontal velocity control at an altitude of 10 metres above the landing target. A climb rate of 0.4 m.s^{-1} was is issued at time $t = 10$ seconds and causes the vehicle to execute the Tensioning phase of the landing procedure.

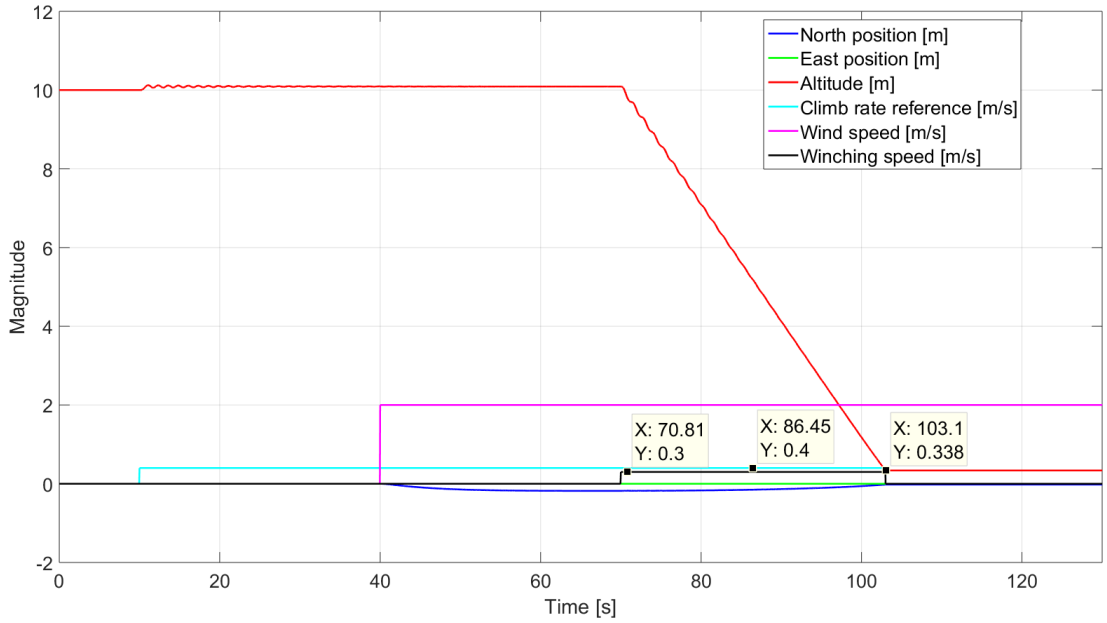

Figure 6.18: Simulated tensioning and landing.

Once in tension, the vehicle is allowed to settle, signifying the Buoyancy state. A 2 m.s^{-1} Northerly wind is introduced at time $t = 40$ seconds causing the vehicle to experiences a longitudinal position offset. In the presence of wind disturbance, the vehicle establishes a stable trim state with a North position offset of approximately -18 cm. The winch begins winching at a descent speed of 0.3 m.s^{-1} at time $t = 70$ seconds. During landing, the North position tends to zero and attains a value of just -2 cm upon touchdown. The East remains at zero throughout the simulation since there is no wind disturbance in the East direction. Winching is ceased upon touchdown and the rotors are shut down.

Equations 6.52 and 6.53 are used to convert the UAV's position from rectangular coordinates to polar coordinates. Figure 6.19 shows, among other things, the tethering angle β deduced from data shown in Figure 6.18. A plot of the pitch angle is also shown on Figure 6.19 to indicate that in addition to a very small position error, the tethered quad-rotor also touches down with an acceptably low tilt angle. It is very likely that the vehicle's legs will not touch down at the same time. A small landing position error and a small tilt angle ensures that once the first leg touches down, the weight of the vehicle and tether force will aid the stability of the vehicle as the remaining legs touch down.

$$r = \sqrt{N^2 + E^2 + H^2} \tag{6.52}$$

$$\beta = \sin^{-1}\left(\frac{\sqrt{N^2 + E^2}}{\sqrt{N^2 + E^2 + H^2}}\right)$$

$$= \sin^{-1}\left(\frac{\sqrt{N^2 + E^2}}{r}\right) \tag{6.53}$$

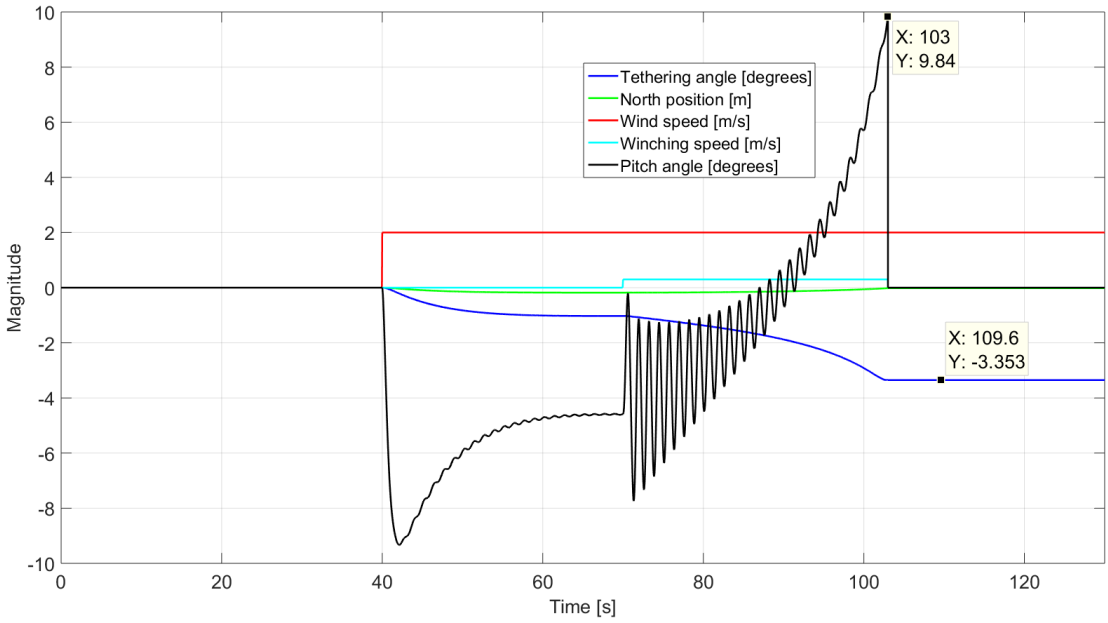

Figure 6.19: Plot of tethering angle during simulated landing.

Figure 6.19 is based on the same simulation data as Figure 6.18 and shows a relative drift in tethering angle as the vehicle approaches the platform. This agrees with the predicted deterioration of tethering angle damping at very low altitudes. The tethering angle upon touch-down is 3 degrees which is judged to be low. The non-zero tethering angle also agrees with a small position landing error. Pitch angle oscillations with an initial amplitude of about 4 degrees are triggered by the inception of winching. The oscillation amplitude however decreases exponentially and dies down before the vehicle touches down with a pitch angle of approximately 10 degrees. In summary, the point-mass model provides accurate insight into the tethering angle dynamics of the tethered UAV.

Figure 6.20 shows the system radius r extracted from the simulated landing data given in Figure 6.18. Oscillatory behaviour is observed in the radial direction both upon the issuing of a positive climb rate reference and also at the commencement of winching.

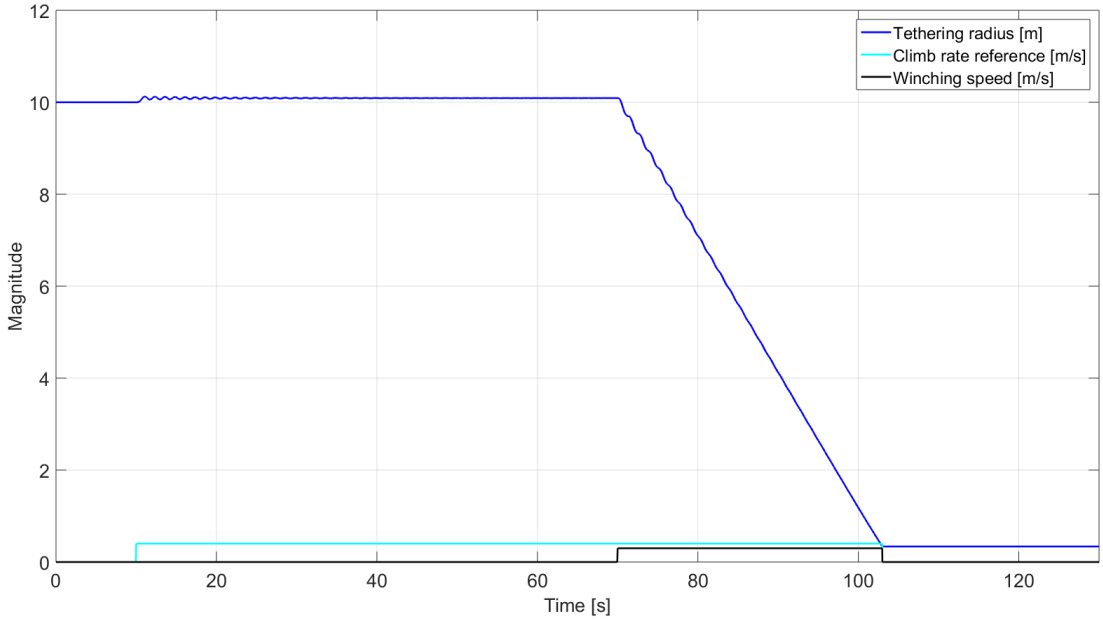

Figure 6.20: Plot of tethering radius during simulated landing.

Figure 6.21 shows a focused view of the tethering radius dynamics induced by the commencement of the Tensioning phase. The region bound by the cursors has 12 cycles within a time span of 15.08 seconds, yielding an average oscillation period of $T \approx 1.25$ seconds. From Figure 6.13, the tethering radius poles have an undamped natural frequency of $\omega_d = 5.023$ rad.s^{-1} and a real pole part magnitude of $\sigma = 0.08$. Applying Equation 6.54 to the tethering radius dynamics yields a predicted oscillation period of $T \approx 1.26$ seconds [35]. Equation 6.55 predicts a time constant of $\tau \approx 12.5$ seconds for the radial oscillations. As seen from Figure 6.21, the amplitude of oscillation decreases to below 63 % of the peak amplitude within 12.5 seconds from the introduction of the climb rate command. This agrees with the predicted time constant.

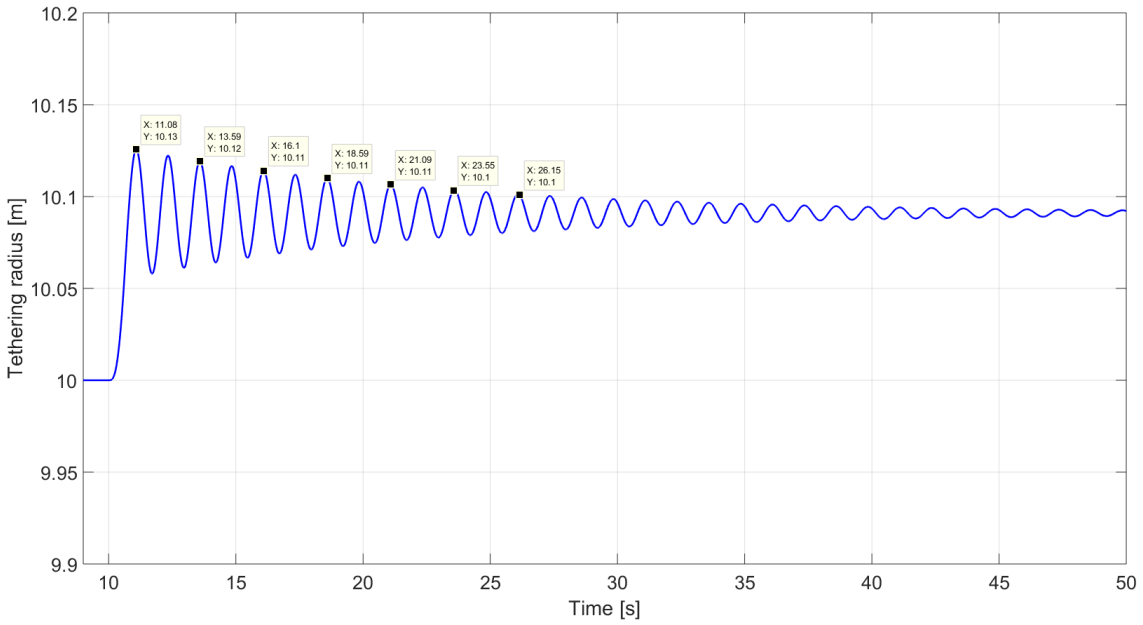

Figure 6.21: Magnified view of tethering radius during simulated tensioning.

$$
\begin{aligned}
T &= \frac{2\pi}{\omega_d} \\
&= \frac{2\pi}{5.023} \\
&\approx 1.26 \text{ s}
\end{aligned} \tag{6.54}
$$

$$
\begin{aligned}
\tau &= \frac{1}{\sigma} \\
&= \frac{1}{0.08} \\
&= 12.5 \text{ s}
\end{aligned} \tag{6.55}
$$

The observed oscillation frequency and time constant for the radial oscillations are close to the theoretical expectations captured in Equations 6.54 and 6.55. The non-linear simulated landing results reinforce the validation results presented in Sections 6.3.6 and 6.3.8 and builds confidence in the tethered landing system.

6.5 Chapter Summary

This chapter presented a proposed state machine for landing a tethered quad-rotor UAV on to a stationary platform. The state machine implements a constant speed winching landing strategy as presented in Section 6.1. Chapter 7 will present an al-

ternative state machine based on a constant tension winching strategy. A winch speed control system was presented in Section 6.2.

A point-mass simplified model for the tethered quad-rotor UAV system was presented in Section 6.3. The point-mass model was developed for no-wind conditions and assumes that the line of action for the tether force passes through the quad-rotor's COG. Based on these assumptions, the tethered quad-rotor dynamics were decoupled into separate tethering angle and tethering radius systems. The system poles derived from the decoupled point-mass models accurately predicted the non-linear dynamics of the tethered UAV system. Section 6.4 concluded the chapter with an analysis of a simulated landing of the tethered UAV.

Chapter 7

Constant Tension Winching Strategy

The state machine used in this project was presented in Chapter 6 and is based on a constant speed winching strategy. It is however still worthwhile to briefly explore an alternative landing strategy based on constant tension winching. In the literature, Lee demonstrated a tension control system for a spool [36]. Based on the work by Lee, it is possible to design a control system that controls tether tension indirectly through winch current.

In the constant winch speed strategy, the winch controls the descent rate of the quad-rotor, while the quad-rotor maintains the tether tension by commanding a small positive climb rate. In the constant winch tension strategy, the quad-rotor controls its own descent rate in the presence of the tether force disturbance, while the winch maintains the tether tension by commanding a constant motor current. The winch serves to control the tether tension to keep the disturbance experienced by the quad-rotor to manageable magnitudes as well as preventing the tether from becoming too slack and getting tangled into the rotors.

Section 7.1 details the proposed state machine for use with the constant tension landing strategy. A possible architecture for the winch tension control system is proposed in Section 7.2. Simulation results of waypoint navigation and step responses of the tethered vehicle under tension control are presented in Section 7.3 to validate the feasibility of the constant tension winching strategy.

7.1 Overview of Proposed Landing State Machine

The proposed landing state machine for the constant tension winching strategy is shown in Figure 7.1. The state machine is in fact the same as the constant speed state machine presented in Figure 6.1 except for different approaches to the Descent phase of the landing. The next two paragraphs outline the main differences between the constant speed and constant tension state machines.

The first difference between the constant speed and the constant tension landing strategies is that the constant tension state machine does not include the Tensioning state. As explained in Section 6.1.2.6, the Tensioning state in the constant speed strategy involves the limitation of the UAV thrust and the issuing of a small climb rate reference in order to tighten the tether in preparation for descent. For the constant tension however, the tether slack is taken up by the winch tension control system therefore a Tensioning state is not required. The bandwidth of the winch tension controller is designed to be much higher than the bandwidth of the quad-rotor's climb rate controller.

Moreover, the Tensioning state activates the climb rate control mode which is not used in the constant tension strategy as the vehicle is always in altitude control mode. Finally, in the constant tension strategy, the thrust commanded by the climb rate controller is not limited during the descent, because the quad-rotor needs sufficient control authority to reject the tether disturbances. (In the constant speed strategy, the thrust commanded by the climb rate controller is limited, to allow the downward force applied by the tether to overcome the upward force applied by the thrust.)

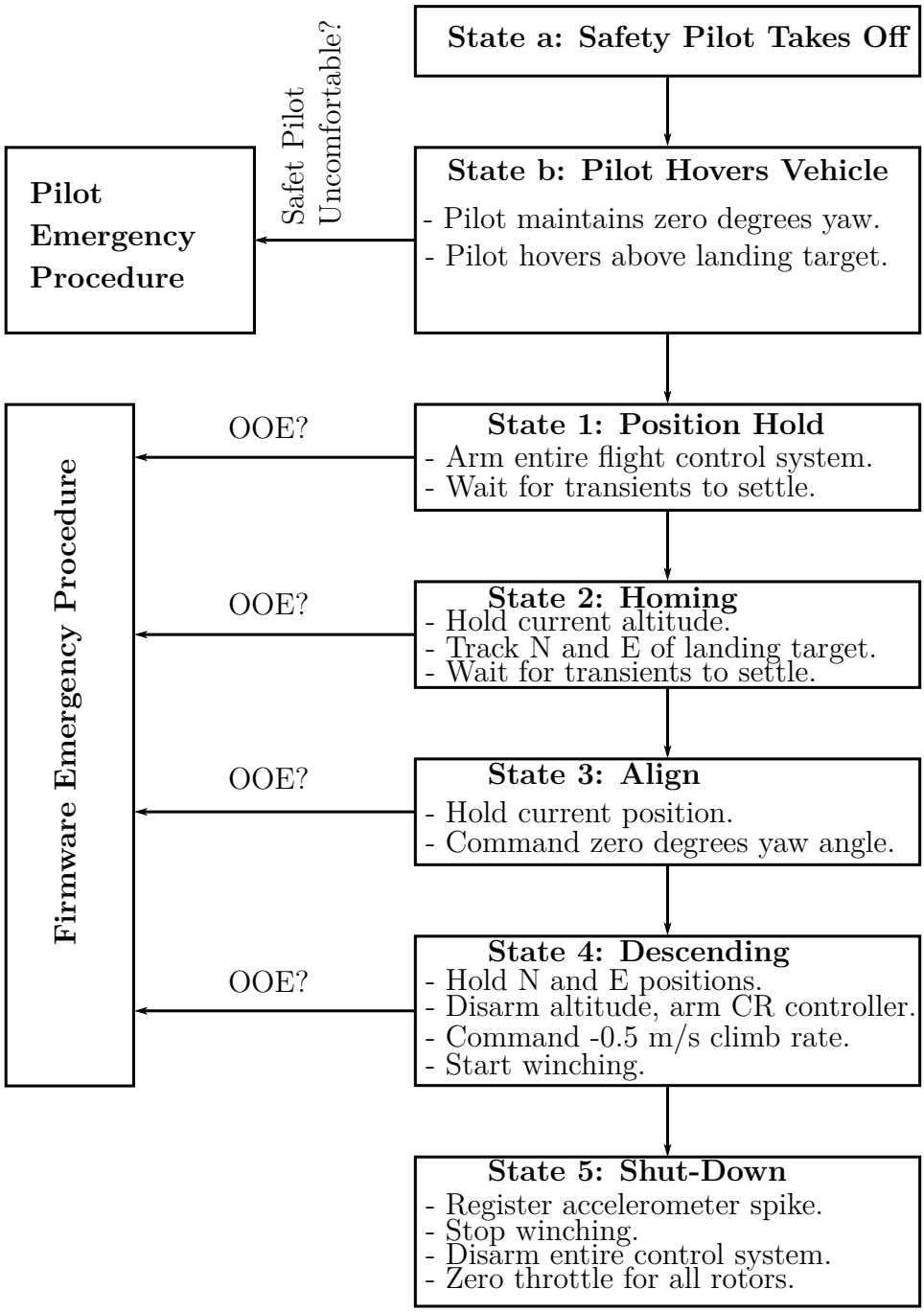

Figure 7.1: Constant tension landing state machine.

Another difference between the constant speed and constant tension strategies is that the constant tension strategy does not involve a Buoyancy state. From Section 6.1.2.7, the Buoyancy state involves the switching of horizontal control from position mode to velocity mode. The constant tension strategy implements horizontal position control therefore does not require a Buoyancy state.

7.2 Winch Tension Control System Architecture

The proposed control structure for the winch tension control system is shown in Figure 7.2. The control structure receives a reference tether tension T_{ref} and would be used with the constant tension landing state machine presented in Section 7.1.

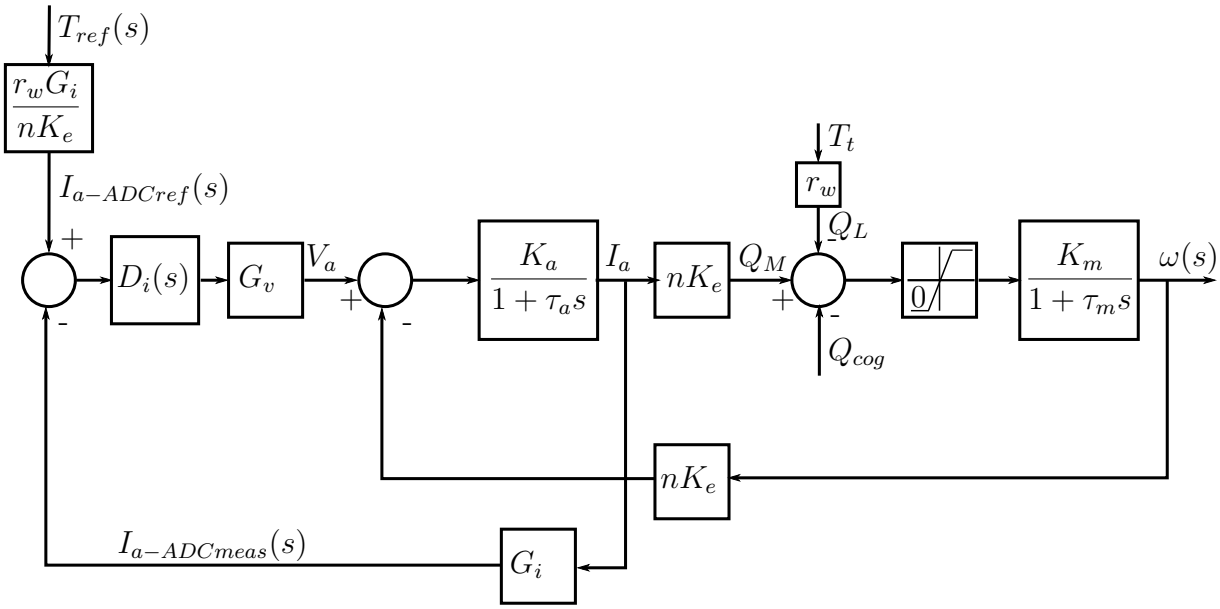

Figure 7.2: Control architecture for the tension control loop.

The winch tension control system aims to maintain a constant average tether tension T_t throughout the landing mission. It is important to realise that the control variable, i.e. the tether tension, does not form part of the open loop system but is instead a disturbance to the geared motor dynamics, with reference to Figure 7.2. A further design complication is that the system does not possess a sensor for direct tether tension measurement. The proposed control strategy controls the tether tension indirectly, through the armature current.

To understand the indirect tether tension control strategy, we consider a geared motor in steady-state, in the presence of a non-zero tether tension. From these steady-state conditions, an increase in tether tension will propagate through the mechanical dynamics and manifest as a decrease in angular speed ω. This decrease in angular speed propagates through the parasitic feedback loop and causes an increase in armature current I_a. With the tension controller shown in Figure 7.2 in place, this increase in armature current results in a decrease in commanded duty cycle hence a decrease in armature voltage V_a. The reduction in armature voltage then propagates through the electrical dynamics to bring the armature current down, closer to the reference current.

The control strategy therefore equips the winch to speed up and pick more tether slack when the tether becomes too slack and to slow down and release some tether tension when the tether becomes too tight.

Duty cycle is measured as a fraction of 255 units in the winch control firmware that runs on the Arduino Mega 2560 board. In the control system architecture shown in Figure 7.2, the tether tension reference is converted to an approximate mechanical torque reference through Equation 7.1, where Q_{Mref} is the reference mechanical torque, T_{Mref} is the reference tether tension and r_w is the radius of the winch drum.

$$Q_{Mref} = r_w T_{Mref} \tag{7.1}$$

The resulting torque reference is then converted to an equivalent armature current reference through Equation 7.2 where I_{aREF} is the reference armature current in amperes.

$$I_{aREF} = \frac{Q_{Mref}}{nK_e} \tag{7.2}$$

As mentioned in Section A.1, armature current is measured using a current transducer and an ADC unit with a measurement gain G_i. With this knowledge, the reference armature current in Amperes I_{aREF} is converted to ADC units $I_{aADC-ref}$ measured by the Arduino after analogue-to-digital conversion of current transducer measurements through Equation 7.3.

$$I_{aADC-ref} = G_i I_{aREF} \tag{7.3}$$

One of the reasons why the constant tension winching strategy was not used in practical flight tests is the roundabout manner in which tether tension is controlled through armature current. The fact that the variable to be controlled, i.e. the tether tension, takes the form of a disturbance signal according to Figure 7.2 makes it difficult to design the tension control system using well-understood design tools like root locus and Bode plots. Although a tension controller based on the proposed architecture has been successfully implemented in the literature [36], the controller gains were designed by trial and error. In contrast, the speed control system presented in Section 6.2 was designed using root locus techniques and the simulated step responses matched practical step responses closely.

The constant tension winching strategy is also likely to exhibit a rougher and more intermittent winching behaviour than the constant speed winching strategy. This postulation is made based on the fact that during the constant tension winching strategy, the winch control system does not actively attempt to maintain a constant descent speed. An autonomus landing is usually characterised by a constant descent speed, especially in the final few meters before touchdown [1]. The constant speed winching strategy is therefore expected to result in smoother winching behaviour albeit potentially at the expense of slight variations in tether tension. However, as long as the upward thrust applied by the quad-rotor is much less than the downward pull applied by the winch, the constant speed winching strategy is a smoother solution.

7.3 Validation of Constant Tension Winching Strategy

This section presents simulation results which were used to verify the capability of the flight control system to reject tether disturbances, and by extension the feasibility of the constant tension winching strategy. Section 7.3.1 discusses the navigation track results from simulated waypoint navigation in the presence of a tether disturbance. The step responses of the quad-rotor in the presence of a tether disturbance are discussed in Section 7.3.2.

7.3.1 Simulated Waypoint Navigation

Waypoint navigation was simulated in order to gain insights into the dynamics of the tethered vehicle under tension control. Waypoints were defined to encompass a 5 m $\times$ 5 m square. The tethered vehicle starts off at a 10 m altitude right above the landing target. The vehicle then proceeds to visit all the corners of the square, then back to the centre and finally drops its altitude from 10 m to 5 m as shown by the track in Figure 7.3.

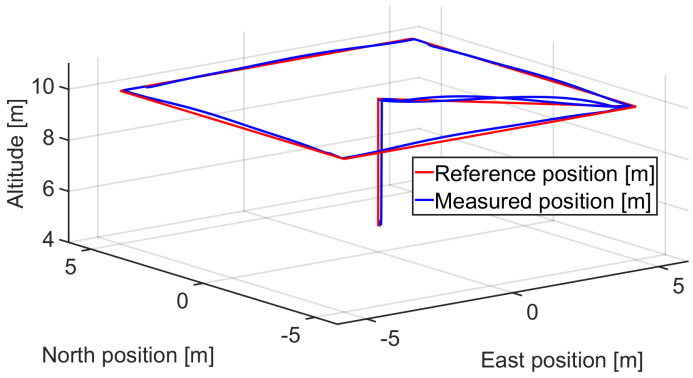

Figure 7.3: Three-dimensional navigation track for a tethered quad-rotor UAV.

Based on the approximately 6 N steady-state tether force observed in the constant speed strategy, a 6 N constant tether force was again adopted for the constant tension way-point navigation simulation. A constant 3 m.s^{-1} Northerly wind disturbance forms part of all simulations discussed in this chapter. The simulation was programmed such that once the UAV is within 10 cm of the target waypoint, the next waypoint is targeted. Figure 7.3 shows a three-dimensional plot of waypoint tracking performance of the tethered quad-rotor vehicle with constant tether tension. The quad-rotor remains stable and exhibits good tracking performance.

7.3.2 Time Response of the Tethered UAV under Tension Control

This section compares the response of the untethered quad-rotor to that of a tethered vehicle with a 6 N tether force, both in the presence of a 3 m.s^{-1} Northerly wind disturbance.

7.3.2.1 Altitude Response

Figure 7.4 shows the altitude response of the tethered vehicle alongside the untethered response which was presented in Section 5.1.4. The altitude responses were simulated at horizontal position offsets of 5 m from the winch both in the longitudinal and lateral directions. Both simulations incorporate a 3 m.s^{-1} Northerly wind disturbance and the tethered case refers to a simulated 6 N constant tether tension. The close match between the tethered and untethered responses validates the flight control system, which was designed based on an untethered vehicle model but with inherent capabilities to reject tether and wind disturbances.

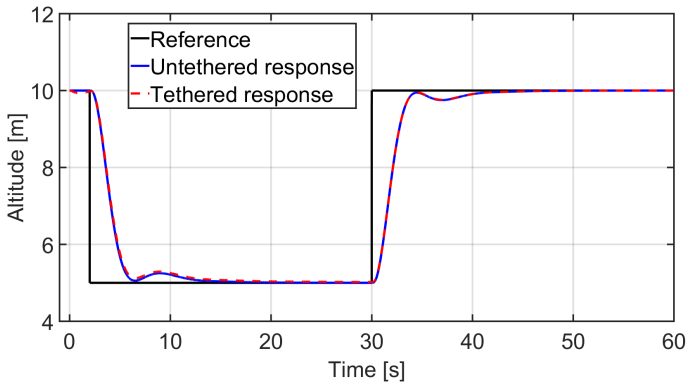

Figure 7.4: Untethered and tethered non-linear altitude responses.

7.3.2.2 Horizontal Position Response

The horizontal position responses of the tethered and the untethered vehicles at a constant altitude of 10 m are shown in Figure 7.5. The tethered horizontal position response matches the untethered response presented in Section 5.2.5 very closely. An increase in settling time is observed when the vehicle is translating away from the winch because the vehicle has to overcome a tether disturbance force pulling the vehicle towards the winch. The horizontal system damping is not diminished by the tether disturbance.

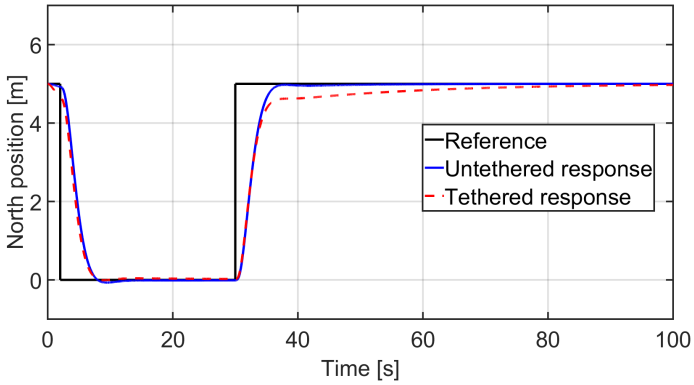

Figure 7.5: Untethered and tethered non-linear North position responses.

7.3.2.3 Yaw Angle Response

The tether has unnoticeable influence on the yaw angle response. Figure 7.6 shows the yaw angle responses for the tethered and the untethered systems. The swivel incorporated in the UAV-tether joint is free to rotate thereby minimising tether torsional forces [4].

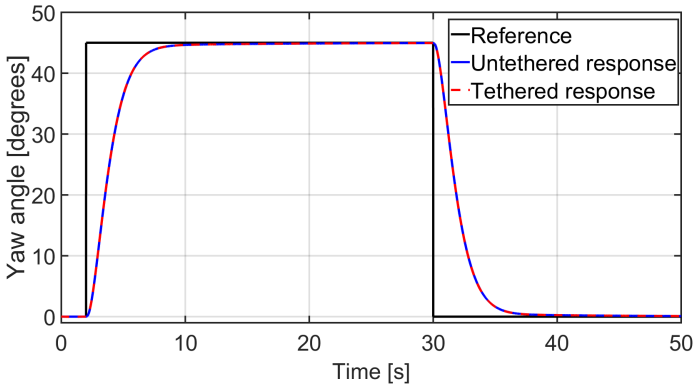

Figure 7.6: Untethered and tethered non-linear yaw angle responses

The analysis of the yaw angle response of the tethered and untethered systems concludes the constant tension system validation. The foregoing analysis suggests that a constant tension strategy is a valid alternative to the constant speed strategy adopted in this project.

7.4 Chapter Summary

This chapter explored a constant tension winching strategy as an alternative to the constant speed winching strategy presented in Chapter 6. A constant tension landing state machine was proposed in Section 7.1. A winch tension control system architecture was presented in Section 7.2. Simulation results were presented in Section 7.3 to validate the feasibility of the constant tension winching strategy. The constant tension winching strategy was not used for practical flight tests due to its susceptibility to intermittent winching behaviour. Furthermore, the constant speed winching strategy was preferred since the winch speed controller can be easily designed using well-understood techniques.

Chapter 8

Practical Flight Tests

This chapter outlines the practical flight test campaign which was undertaken to verify the tethered system design and to demonstrate an autonomous landing of the tethered quad-rotor UAV on a stationary platform. The flight test campaign was designed to incrementally build confidence by demonstrating untethered flight followed by tethered flights and finally tethered landings. A total of eleven flights were executed. Two of the flights were untethered while two complete landing flights were demonstrated. The remainder of the flights were tethered mock landings.

The untethered flights verify the flight control system on the actual vehicle in the presence of wind disturbances and unmodelled phenomena. Tethered flights proceed further to validate the dynamic behaviour of the tethered vehicle as predicted by the point-mass model developed in Chapter 6. The majority of the flights are mock landings, where the stages of the landing state machine in Figure 6.1 were incrementally explored to build insight and confidence while working towards complete autonomous landings.

All flight tests were conducted at the Helderberg Radio Flyers RC aircraft flying field, commonly known as HRF. The results from the untethered flights are discussed in Section 8.1 while tethered flight test results are presented in Section 8.2. Section 8.3 discusses the flight test results for a mock landing with reduced horizontal velocity controller gains. Flights were conducted in calm wind conditions of not more than 2 m.s^{-1}.

8.1 Untethered Flights

As mentioned earlier, a total of two untethered flight tests were conducted. We recall from Chapter 5 that the flight control system was designed based on an untethered vehicle model, with disturbance rejection characteristics incorporated in the design to reject disturbances introduced by the wind and the tether. The goal of the untethered flights was to validated the flight control system in the presence of unmodelled vehicle dynamics. Figure 8.1 shows the quad-rotor on the runway before take-off and mid-air during untethered flight.

(a) The untethered quad-rotor on the runway before take-off.

(b) The untethered quad-rotor moments after take-off.

Figure 8.1: The quad-rotor UAV in untethered flight.

The validation strategy for the untethered flights was to successively arm control loops, starting from the inner rate loops traversing outwards to the position loops. A similar strategy was adopted for validating the existing flight control system and an in-depth coverage of the validation strategy can be found in [4]. The landing mission is highly dependent on the performance of position controllers since the landing procedure begins with the tethered vehicle holding its current position, as discussed in Section 6.1. For this reason, focus is cast on validating untethered flight for stability and damping of the position and yaw angle response using the control system designed in this project.

Figure 8.2 shows the position and yaw angle step responses of the untethered vehicle. The untethered flight test begins with the safety pilot taking off and hovering at an altitude of approximately 15 m. Thereafter, the position and yaw angle control

loops are armed, leaving the quad-rotor under full autonomous control. Position and yaw angle step commands are then issued from the ground station. The safety pilot finally flicks a switch to revert to pilot-augmented flight and lands the vehicle.

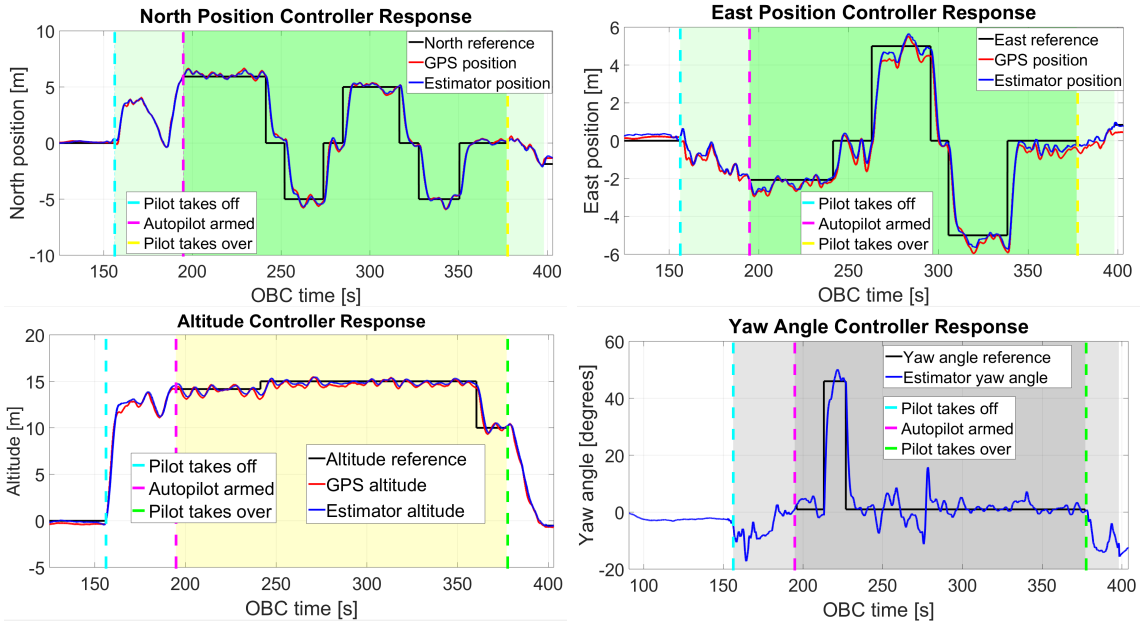

Figure 8.2: Position and yaw angle practical untethered responses.

As shown in Figure 8.2, the untethered vehicle exhibited stable well-damped responses in position, altitude and yaw angle. The satisfactory untethered response inspired confidence to proceed and attempt tethered flights.

8.2 Tethered Flights

A total of nine tethered flights were conducted, with seven being partial landings designed to incrementally explore specific aspects of the landing procedure and two being fully-fledged tethered landings. The two final fully-fledged tethered landings are a consolidation of all the mock landings therefore focus will be placed on the fully-fledged landings.

As mentioned earlier, the constant speed winching strategy was adopted for the practical tethered landings using the landing state machine shown in Figure 6.1. Two complete tethered landings were demonstrated. Landing 1 was conducted in calm conditions of little to no wind where Landing 2 was conducted in mild conditions with a wind speed slightly above 2 $\mathrm{m.s^{-1}}$. Besides the difference in atmospheric conditions,

the execution of both landings followed identical procedures.

To prepare for tethered flight, 10 m of tether is unwound from the winch and attached to the quad-rotor after which the quad-rotor is placed on the 2.4 m $\times$ 2.4 m stationary platform, right at the tether feed-out point. The kinematic state estimator is then initialised thereby specifying the tether feed-out point as the origin of the inertial coordinate system for the remainder of the flight. After estimator initialisation, the tethered vehicle is removed from the platform and placed on to the runway. The tether is neatly laid on the runway to avoid tangling into the vehicle upon take off.

The safety pilot takes off and brings the tethered vehicle to a pilot-augmented hover about 10 m right above the tether feed-out point which is also the landing target. Once the tethered vehicle is above the landing target, a command is sent from the ground station to arm all flight control loops. This ushers the Position Hold state in which the vehicle maintains its current position, altitude and yaw angle. Figure 8.3 shows the tethered vehicle in flight and on the platform moments after landing.

(a) The tethered quad-rotor during constant speed descent.

(b) The tethered quad-rotor on the platform, moments after touch-down.

Figure 8.3: The quad-rotor UAV in tethered flight.

The vehicle stays in the Position Hold state for a duration determined by a timer that is programmed on the On-Board Computer. Upon expiration of the timer, the Homing state ensures in which the vehicle tracks the horizontal position of the landing

target. Once the flight control system senses a horizontal position error less than a pre-programmed threshold, the Align state takes over and aligns the vehicle with North. Due to errors in position measurement as a result of GPS drift, the vehicle may not be directly above the landing target after homing and aligning. Small position step commands are issued from the ground station to inch the vehicle above the landing target.

Once the vehicle is directly above the landing target, a command is send from the ground station to begin the Tensioning state. The vehicle switches from altitude control to climb rate control with a small positive climb rate of 0.3 m.s^{-1} and simultaneously limits the available common thrust to 6 N above hover thrust. This causes the vehicle to maintain its horizontal position whilst ascending. A steady state condition is established in which the vehicle pulls on the tether with a tension determined by the thrust limit.

Once the transients of the Tensioning state have settled, the Buoyancy state is activated from the ground station. In this state, horizontal position control is disarmed and horizontal velocity control is armed with zero velocity reference. The tethered vehicle exhibits transients as approximated by the point-mass model derived in Section 6.3.5. Once the transients have settled, the Descent state is armed from the ground station and the winch starts winching with constant speed. Upon touch-down a spike in the Z accelerometer measurement is registered and the rotors are shut-down, marking the end of the flight test.

Figure 8.4 shows flight test results from Landing 1 and Landing 2 side by side. Additional practical landing data is presented in Appendix D. Landing 2 shows worsened horizontal position response during descent due to increased wind. However, there is no significant differences in altitude response indicating that the vertical control system is relatively immune to worsening wind conditions. Landing 2 shows a steady-state error in yaw angle.

Although the modelling conducted did not predict that wind would have an effect on yaw angle control, the foregoing results suggest so. Overall, the developed flight control system and landing state machine is sufficient for landing the tethered quadrotor in relatively calm conditions with wind speeds in the order of 2 m.s^{-1}.

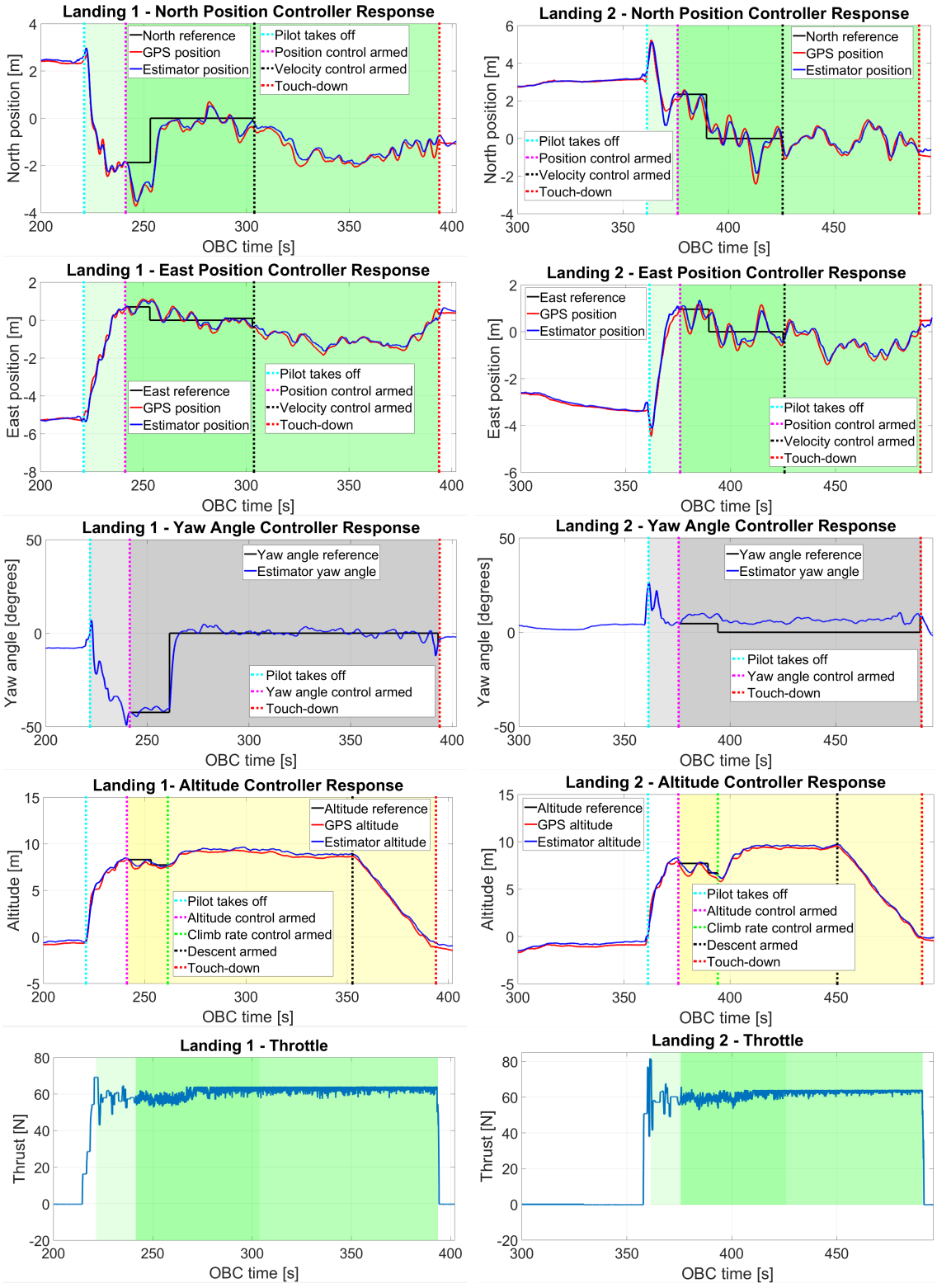

Figure 8.4: Tethered landing practical results.

8.3 Mock Landing with Reduced Velocity Gains

The formulation in Section 6.3.6.1 predicted that the damping of the tethering angle dynamics would be compromised at very low velocity controller gains. A mock landing was executed with a low velocity controller gain of $K_p = 0.2$ and the results are shown in Figures D.2a and D.2b. The response shows more horizontal position oscillations compared to the response of the vehicle with nominal horizontal controller gains shown in Figure 8.4. Figure 8.5 presents the data for the low gain flight in polar coordinates and clearly shows oscillations in tethering radius as predicted by the point-mass model.

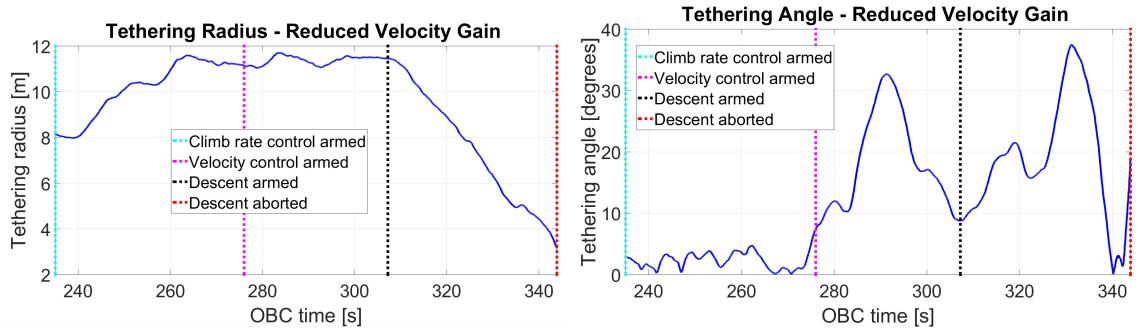

(a) Tethering radius.

(b) Tethering angle.

Figure 8.5: Tethering radius and tethering angle for practical flight with 0.2 velocity controller gain.

Chapter 9

Conclusion

This project extended the flight envelope of an existing tethered quad-rotor system to address the landing phase of tethered flight with a 10 m long tether. The existing flight control system was adapted for the task of landing onto a stationary platform. A winch system was also developed as part of the tethered UAV system. A winch speed controller was designed and validated through practical flight tests. A novel point-mass model was developed in order to predict the dynamic behaviour of the tethered quad-rotor during the landing phase of its flight. The dynamic behaviour of the tethered quad-rotor was determined in terms of poles of decoupled tethering radius and tethering angle systems.

Section 9.1 recaps the research objectives that have been set out in Chapter 1 and details the extent to which the research objectives have been achieved. The contributions of this research to the existing body of knowledge are presented in Section 9.2. Section 9.3 outlines some of the limitations that were taken into account in the execution of the project. Finally, recommendations for future research are given in Section 9.4.

9.1 Assessment of Research Objective Achievement

This sections sums up the main research results by examining the extent to which research objectives have been achieved. The achievement of the primary objective is assessed in Section 9.1.1 and an assessment on the achievement of the secondary objective is presented in Section 9.1.2.

9.1.1 Assessment of the Primary Objective

As mentioned in Section 1.3, the primary objective of this research is to design a tethered multi-rotor system and demonstrate the autonomous landing of a tethered quad-rotor UAV on a 2.4 m × 2.4 m stationary platform. This section evaluates the accomplishment of each of the primary research aims in order to assess whether the primary objective has been achieved. The primary aims listed in Section 1.3 are reproduced for convenience. Each aim is followed by a comment relating to its accomplishment.

(i) To analyse the existing flight control system and make necessary improvements for use during tethered landing:
The existing flight control system was analysed and adaptations were implemented to the control system as detailed in Chapter 5.

(ii) To design a winch system and a winch control system as part of the tethered landing system:
A winch system was designed as documented in Appendix A. Both the winch hardware and winch firmware were developed as new work in this project. A winch speed control system was designed as detailed in Section 6.2. The winch was successfully used to demonstrate two autonomous landings of the tethered quad-rotor on a stationary platform therefore this aim was achieved.

(iii) To design a strategy to autonomously land a tethered quad-rotor on a stationary platform:
A landing strategy based on constant winching speed was designed and presented in Section 6.1.

(iv) To demonstrate simulated autonomous landing of a tethered quad-rotor as a way of validating the flight control system and the landing strategy:
The designed flight control system was validated through non-linear simulation as presented in Section 6.4.

(v) To demonstrate autonomous landing of a tethered quad-rotor through practical flight tests:
The autonomous landing of a tethered quad-rotor on a stationary platform was demonstrated through practical flight tests. The results from the practical flight tests are

presented in Chapter 8. The developed classical PID flight control system and landing strategy proved to be robust and effective in addressing tethered multi-rotor landings in moderate wind conditions of up to 2 $m.s^{-1}$. However, deterioration in horizontal control was observed for wind speeds higher than 2 $m.s^{-1}$. The vertical control system exhibited significant immunity to worsening wind conditions.

The primary aims (i) to (v) have all been achieved. Aims (i) to (iv) serve to incrementally build confidence as the system is being designed while aim (v) is the fully-fledged demonstration of the system, whose successful execution amounts to the achievement of the primary research objective. By successfully demonstrating the autonomous landing of a tethered quad-rotor on a 2.4 m $\times$ 2.4 m stationary platform, the primary research objective was achieved.

9.1.2 Assessment of the Secondary Objective

As indicated in Section 1.3, the secondary objective of this research is to determine and validate the dynamics of a tethered multi-rotor UAV during the landing phase of its flight. The dynamics are to be presented in a form that is applicable not only to the particular vehicle used in this project, but to tethered multi-rotor UAVs in general. Each of the secondary aims is restated and followed with an assessment of its achievement.

(a) To formulate a simplified model of a tethered multi-rotor UAV, from which the dynamics of the vehicle during its landing phase can be obtained:
A point-mass model was developed as presented in Section 6.3. The point-mass model is sufficient to determine the dynamics of the tethered quad-rotor UAV as detailed in the discussion of secondary aim (b) which follows.

(b) To use the simplified model to determine the dynamics of a tethered multi-rotor UAV during its landing phase:
The dynamics of the tethered multi-rotor vehicle were determined in terms of system poles. Based on the point-mass model, a linearised model of the tethered quad-rotor was obtained as presented in Section 6.3.4. The linearised model was then decoupled in to a tethering angle system and a tethering radius system as presented in Sections 6.3.5 and 6.3.7 respectively. State-space models of the decoupled systems were used to determine the system poles.

(c) To validate the derived dynamics using data from simulated landings of the quad-rotor UAV used in this project:
Sections 6.3.6 and 6.3.8 show that the point-mass model fairly accurately predicts the dynamics of the tethered vehicle. Simulation data presented in these sections showed a high accuracy in the determination of system damping while moderate accuracy was achieved in the determination of system speed of response.

Having accomplished all the secondary research aims, the research by extension resulted in the achievement of the secondary objective. The state-space models for the decoupled tethering radius and tethering angle systems presented in Sections 6.3.5 and 6.3.7 are presented terms of the system parameters such as vehicle mass, horizontal velocity controller gain, tether stiffness, tether damping coefficient and initial tether length. For this reason, the point-mass model can be readily applied to determine the system poles of other multi-rotor vehicles with different inertial properties than the one used in this project.

9.2 Contributions

The research documented in this thesis contributed the following aspects to the existing body of knowledge:

1. Two strategies for executing the autonomous landing of tethered multi-rotors were developed. One strategy is based on constant winching tension, while the second strategy is based on constant winching speed.

2. A novel point-mass model of the tethered quad-rotor was developed and validated. The point-mass model accurately predicts the tethering angle dynamics and the tethering radius dynamics of the tethered vehicle during constant speed descent.

3. The constant winching speed strategy was demonstrated through two practical tethered landings.

9.3 Limitations

The following limitations were considered while conducting the research:

1. The number of practical flight tests had to be kept within reasonable limits since the execution of flight tests comes with transport costs and safety pilot hours. Safety

pilot availability also played a role since the safety pilot has other full-time commitments. As a result, only two complete autonomous tethered landings were demonstrated.

2. In order to keep the scope of the project to a manageable magnitude, Hardware-In-the-Loop (HIL) simulations were kept to a minimum. The tethered system was only simulated in Software-In-the-Loop (SIL) simulations. Results from HIL simulations of the untethered vehicle were used to verify that the landing state machine and flight control system have been coded correctly onto the On-Board Computer (OBC).

3. The tether model and the point-mass model developed for the landing phase of the quad-rotor flight assumes a taut tether. The project does not address the modelling of a slack tether or the modelling of the tethered quad-rotor on a slack tether.

9.4 Recommendations

There was a limited amount of time allocated to this research. Because of that, attention had to be given to the writing up of this thesis once the autonomous landing of the tethered quad-rotor was demonstrated through practical flights. The following aspects of the tethered system could not be attended to due to time constrains and are hereby recommended for future research:

1. A deterioration in horizontal control was observed for wind speeds above 2 m.s^{-1}, most likely due to unmodelled aerodynamic drag on the tether and unmodelled quad-rotor dynamics. There is room to improve the tether modelling to include aerodynamic drag. The flight control system could also be optimised for harsher atmospheric conditions. The flight tests were also limited to tether lengths of 10 m leaving room for control optimisation to cater for higher altitudes and longer tether lengths.

2. The point-mass model predicts worsening damping of the tethered vehicle at low altitudes. This deterioration in damping at low altitudes could have contributed to the drift in horizontal position that was observed just before touchdown in both tethered landings. The point-mass model however predicts that the damping ratio of the tethered response increases with an increase in horizontal velocity controller gain. Future research could investigate a gain-scheduling strategy where the horizontal velocity controller gain is increased at low altitudes to mitigate against the observed drift in horizontal position. The landing strategy could also include the modelling of ground effect and an attempt to mitigate against it.

3. Having demonstrated a sufficient strategy for landing a tethered multi-rotor on a stationary platform, the next logical step would be to expand the system to address tethered landing on a translating and finally a heaving platform in order to maximize the utility of the system. Thereafter, the dummy tether used in this project would have to be replaced by an optimally-designed powered tether to achieve the goal of persistent tethered flight.

4. The winch used in this project is bulky and is powered by laboratory power supplies. This prototype winch sufficed as a proof of concept as it was carefully positioned under the landing platform together with laboratory power supplies. A more compact winch design has to be developed together with a more convenient means of powering the winch electronics. The steel mesh platform used for this project also needs to be replaced by an optimally designed landing platform.

5. A quad-rotor configuration was used for this project. Redundancy can be effected by using more rotors like on the octocopter configuration [4]. That way, the vehicle can still be controlled even in the event of failure of one of its rotors.

Bibliography

[1] P.D.S. Moller. *Automated Landing of A Quadrotor on A Translating Platform.* Masters Thesis. Stellenbosch University, 2013.

[2] Drones Are Fun. *Batteries for UAV.* `http://dronesarefun.com/BatteriesForUAV.html`, 2015. [Online: accessed 2018-08-12].

[3] C.T. Le Roux. *Automated Landing of An Intelligent Unmanned Aerial Vehicle in Crosswind Conditions Using Total Energy Control.* Masters Thesis. Stellenbosch University, 2014.

[4] P.G. Ioppo. *The Design, Modelling and Control of an Autonomous tethered Multirotor UAV.* Masters Thesis. Stellenbosch University, 2016.

[5] S. Driessens and P.E.I. Pounds. *Towards a more efficient quadrotor configuration.* 2013 IEEE/RSJ International Conference on Intelligent Robots and Systems, Tokyo, 2013, pp 1386-1392.

[6] V.M. Martinez. *Modelling of the Flight Dynamics of a Quadrotor Helicopter.* Masters Thesis. Cranfield University, 2007.

[7] Y. Naidoo, R. Stopforth and G. Bright. *Quad-Rotor Unmanned Aerial Vehicle Helicopter Modelling Control.* International Journal of Advanced Robotic Systems, 2011.

[8] Forbes. *What Makes The Quadrotor Design So Great For Small Drones?* `http://www.forbes.com/sites/quora/2013/12/23/what-makes-the-quadcopter-design-so-great-for-small-drones/`, 2013. [Online: accessed 2014-03-04].

[9] Ellistair Innovative Airborne Solutions. *Tethered Drone Systems Flying All Day.* `https://elistair.com/`, 2018. [Online: accessed 2018-10-01].

[10] Broadfield Security Services. *TETHERED UAVS âĂŞ SAFE-T.* https://www.bssholland.com/product/tethered-uavs-safe-t/, 2018. [Online: accessed 2018-09-25].

[11] Veronte Products. *Tethred Multicopter Control.* https://products.embention.com/veronte/uav-autopilot/tethered-uav?___store=english, 2018. [Online: accessed 2018-10-06].

[12] ECA Group. *TETHERED MINI UAV FOR PERMANENT SURVEILLANCE.* https://www.ecagroup.com/en/solutions/tethered-mini-uav-permanent-surveillance, 2018. [Online: accessed 2018-16-01].

[13] P. Pounds, R. Mahony, and P. Corke. *Modelling and control of a large quadrotor robot.* Control Engineering Practice, vol. 18, no. 7, pp. 691-699, 2010.

[14] T. Nugent and J. Kare. *Laser power for UAVs.* Technical Report, Laser Motive, 2010.

[15] University of Southampton. *AETHER: Tethered UAV.* https://www.southampton.ac.uk/aerospace/research/aerospace/collaborationopportunities/aether_tethered_uav_vp.page, 2018. [Online: accessed 2018-10-05].

[16] Hoverfly. *Tether Powered Drones That Fly All Day.* https://hoverflytech.com/, 2018. [Online: accessed 2018-10-06].

[17] defenceWeb. *Tethered UAV launched in SA.* http://www.defenceweb.co.za/index.php?option=com_content&view=article&id=52045&catid=74&Itemid=30, 2018. [Online: accessed 2018-09-26].

[18] Skysapience. *The HoverMast Family.* http://www.skysapience.com/products/hovermast-family, 2012. [Online: accessed 2017-07-20].

[19] Cyphyworks. *The Persistent Aerial Reconnaissance and Communications (PARC) vehicle.* http://cyphyworks.com/parc/, 2014. [Online: accessed 2018-10-05].

[20] G. Carrillo, D. Lopez, A.E. Lozano and R.Pegard. *Modelling the Quad-Rotor Mini Rotorcraft.* In: Quad Rotorcraft Control. Advances in Industrial Control. Springer, London, 2013.

[21] S. Bouabdallah and R. Siegwart. *Full control of a quadrotor.* 2007 IEEE/RSJ International Conference on Intelligent Robots and Systems, San Diego, CA, 2007, pp. 153-158.

[22] J. Friis, E. Nielsen, R.F. Andersen, J. Bønding, A. Jochumsen, and A.F. Sørrensen. *Autonomous Landing on a Moving Platform.* AAU, 1st edition, 2009.

[23] M.A. Olivares-MeÌAndez, I.F. MondragoÌAn, P. Campoy and C. MartiÌAnez. *Fuzzy controller for UAV-landing task using 3D-position visual estimation.* International Conference on Fuzzy Systems, Barcelona, 2010, pp. 1-8.

[24] S. Saripalli, J.F. Montgomery and G.S. Sukhatme. *Visually guided landing of an unmanned aerial vehicle.* in IEEE Transactions on Robotics and Automation, vol. 19, no. 3, pp. 371-380, June 2003.

[25] S. Saripalli and G.S. Sukhatme. *Landing a Helicopter on a Moving Target.* Proceedings 2007 IEEE International Conference on Robotics and Automation, Roma, 2007, pp. 2030-2035.

[26] A.D. Swart. *Monocular Vision Assisted Autonomous Landing of a Helicopter on a Moving Deck.* Masters Thesis. Stellenbosch University, 2013.

[27] R.L. Maggot. *Fault-tolerant Flight Control for a Fixed-Wing Unmanned Aerial Vehicle with Partial Horizontal and Vertical Stabiliser Losses.* Masters Thesis. Stellenbosch University, 2016.

[28] G. Hugo. *Autonomous Landing of a Fixed-Wing Unmanned Aircraft with Partial Wing and Stabiliser Losses.* Masters Thesis. Stellenbosch University, 2017.

[29] A. De Bruin. *Accurate Autonomous Landing of a Fixed-Wing Unmanned Aircraft Under Crosswind Conditions.* Masters Thesis. Stellenbosch University, 2017.

[30] T-Motor. *Untitled.* `http://www.rctigermotor.com/html/2013/Navigator_0910/39.html`, 2017. [Online: accessed 2018-08-12].

[31] Dualsky Advanced Power Systems. *Air System.* `http://www.dualsky.com/Xpower_LiPos/`, 2017. [Online: accessed 2018-08-12].

[32] I.K. Peddle. *Autonomous Flight of a Model Aircraft.* Masters Thesis. Stellenbosch University, 2005.

[33] M.V. Cook. *Flight Dynamics Principles.* Elsevier Butterworth-Heinemann, 1997.

[34] R.C. Hibbeler. *Engineering Mechanics, Dynamics, In SI Units - 12th Edition.* Pearson Education Inc, 2010.

[35] G.F. Franklin and J.D. Powell and A. Emani-Neaini. *Feedback Control of Dynamic Systems - 6th Edition.* Pearson Education Inc, 2010.

[36] D.D. Lee. *Tethering System for Unmanned Aerial Vehicles.* `https://sunfest.seas.upenn.edu/wp-content/uploads/2018/07/13-Morales-report.pdf`, Hampton University, 2015. [Online: accessed 2018-12-02].

[37] D.G. Zill and W.S. Wright. *Advanced Engineering Mathematics - 4th Edition.* Jones and Bartlett Publishers, 2011.

[38] S.D. Umans. *Fitzgerald and Kingsley's Electric Machinery - 7th Edition.* McGraw-Hill, 2010.

[39] L. Zaccarian. *DC motors: dynamic model and control techniques.* `http://homepages.laas.fr/lzaccari/seminars/DCmotors.pdf`, 2015. [Online: accessed 2018-12-02].

[40] L. Rossouw. *Autonomous Flight of an Unmanned Helicopter.* Masters Thesis. Stellenbosch University, 2008.

[41] M.D. Schmidt. *Simulation and control of a quadrotor unmanned aerial vehicle.* Masters Thesis. University of Kentucky, 2011.

[42] A.M. de Jager. *The design and implementation of vision-based autonomous rotorcraft landing.* Masters Thesis. Stellenbosch University, 2011.

[43] N. Carstens. *Development of a Low-Cost, Low-Weight Flight Control System for an Electrically Powered Model Helicopter.* Masters Thesis. Stellenbosch University, 2005.

[44] S. Groenewald. *Development of a Rotary-Wing Test Bed for Autonomous Flight.* Masters Thesis. Stellenbosch University, 2005.

[45] W.J. Hough. *Autonomous Aerobatic Flight of a Fixed Wing Unmanned Aerial Vehicle.* Masters Thesis. Stellenbosch University, 2007.

[46] B.J. Visser. *Die Presisie Landing van 'n Onbemande Vliegtuig "The Precision Landing of an Unmanned Aircraft".* Masters Thesis. Stellenbosch University, 2008.

[47] C. van Schalkwyk. *Full State Control of a Fury X-Cell Unmanned Helicopter.* Masters Thesis. Stellenbosch University, 2008.

[48] S.G. Irwin. *Optimal estimation and sensor selection for autonomous landing of a helicopter on a ship deck.* Masters Thesis. Stellenbosch University, 2014.

[49] T. Bresciani. *Modelling, Identification and Control of a Quadrotor Helicopter.* Masters Thesis. Lund University, 2008.

[50] Machine Design. *Gear efficiency - Key to lower drive cost.* `http://machinedesign.com/mechanical-drives/gear-efficiency-key-lower-drive-cost`, 2016. [Online: accessed 2018-08-12].

[51] Wikipedia. *Makani Power.* `http://en.wikipedia.org/wiki/Makani_Power`, 2015. [Online: accessed 2018-12-02].

[52] So-Ryeok Oh, K. Pathak, S.K. Agrawal, H.R. Pota and M. Garrett.*Autonomous Helicopter Landing on a Moving Platform Using a Tether.* Proceedings of the 2005 IEEE International Conference on Robotics and Automation, Barcelona, Spain, 2005, pp. 3960-3965.

Appendix A

Winch System Design

This appendix details the design of the winch. Firstly, a systems level perspective is presented in Section A.1 on the various components of the winch and how they interact to produce the desired functionality. Thereafter, the selection of the winch drive motor is motivated and the limitations that come with the motor selection are discussed in Section A.2. Finally, the functionality of the winch as a complete subsystem is described in Section A.3.

A.1 System Integration

The major components of the winch system are the drive motor, the tether, the drum, the shaft, the keypad, an angle sensor (rotary encoder) and a current transducer. The tether winds around the drum and the shaft links the drive motor to the drum. Figure A.1 shows an annotated picture of the winch.

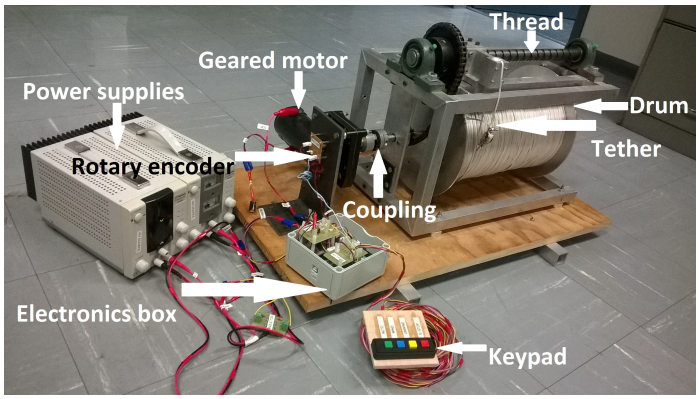

Figure A.1: Winch subsystem.

The PM 59 63 GB4 DC geared motor by Parvalux Electric Motors Ltd was selected to drive the winch. Section A.2 is devoted to explaining the calculations and considerations involved in the selection of the drive motor. The motor is powered by a DC power supply through a BB-VNH3SP30 H-bridge motor driver manufactured by OLIMEX.

An Arduino Mega 2560 board is included for the acquisition of sensor measurements and to execute the winch control algorithm. In order to implement a winching strategy, the angular speed and the torque exerted on the motor shaft must be measured. An approximation of the torque is obtained by measuring the current drawn by the motor. A LEM CAS-6 current transducer is placed in series with the DC motor to measure the current.

The transducer outputs 104 mV for every 1 Ampere of current while the Arduino Mega A/D converter measures 1024 ADC units for every 5 V of transducer voltage. Based on the foregoing relationships, the Arduino measures 64 ADC units per 3 Amperes of motor armature current and therefore measures armature current with a resolution of $R_i = \dfrac{3 \text{ Amperes}}{64 \text{ ADC units}} = 47$ mA. Equation A.1 shows a current transducer gain G_i which is useful if a current/tension controller similar to the one described in Section 7.2 is to be designed for the winch.

$$G_i = \frac{64}{3} \frac{\text{ADC units}}{\text{Amperes}} \tag{A.1}$$

Shaft angular speed is measured using an Austria Microsystems AS504B magnetic rotary encoder manufactured by Austria Microsystems. The rotary encoder outputs a digital output where 360 degrees correspond to 16384 units. The encoder therefore measures angles with a high theoretical resolution of $R_\theta = \dfrac{360 \text{ deg}}{16384 \text{ units}} = 0.022$ deg. Angular speed is calculated by measuring the change in angle per 10 ms. The sensor can therefore theoretically measure measure an angular speed corresponding to 1 unit per 10 ms. The theoretical angular speed measurement resolution is given by Equation A.2. The angular speed measurement gain given in Equation A.3 is applicable when designing winch speed control system.

$$R_\omega = \frac{\left(\frac{1 \text{ unit}}{16384 \text{ units}}\right) 360 \text{ deg}}{10 \text{ ms}} . \frac{1000 \text{ ms}}{1 \text{ s}}$$
$$= 2.20 \text{ deg.s}^{-1} \tag{A.2}$$
$$G_\omega = \frac{16384 \text{ units}}{200\pi \text{ rad.s}^{-1}} \tag{A.3}$$

For testing purposes, the winch is powered by two laboratory DC power supplies. A chain links the shaft to a thread. As the drum rotates, the thread also rotates thereby causing the tether feed-out point to translate horizontally. This allows even layering of the tether around the drum's circumference. Finally, a four-key keypad enables an operator to activate different modes of tether winding when necessary. Section A.3 discusses in more detail the different modes of tether winding.

A.2 Drive Motor Selection

The geared motor determines the torque and speed capabilities of the winch during the landing procedure. The motor selection process involved translating preliminary winch system specifications into drive motor specifications. It is convenient to refer to the simplified diagram of the winch system linked to the quad-rotor aircraft as shown in Figure A.2.

It is required that the motor be capable of driving the drum at a sufficient angular speed while simultaneously generating sufficient mechanical torque to overcome the opposing torque from the taut tether. The criteria for what qualifies as sufficient torque and angular speed depends on design decisions which will be addressed shortly. At the time of selecting the drive motor, the aircraft was still under construction and the eventual mass of the aircraft was estimated at 6 kg. A decision was made to design a winch system that can operate with a tether tension of up to 70 % of the aircraft weight. This decision placed the tether tension estimate at 40 N. The radius of the drum was measured as 0.12 m . The torque Q exerted on the shaft by the taut tether can be calculated as shown in Equation A.4.

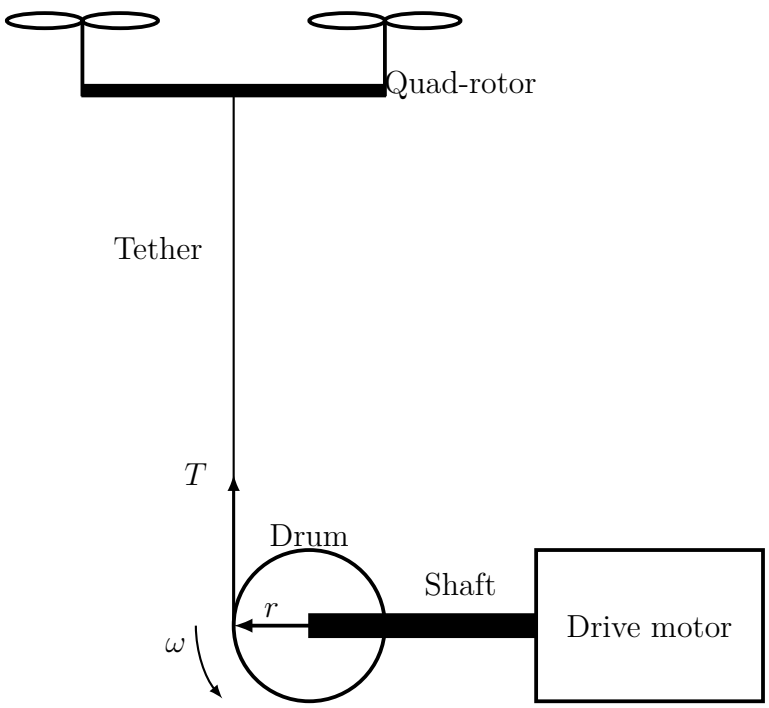

Figure A.2: Simplified diagram of winch and tethered quad-rotor.

$$\begin{aligned} Q &= T * r \\ &= 40 \text{ N} * 0.12 \text{ m} \\ &= 4.8 \text{ Nm} \end{aligned} \tag{A.4}$$

The calculation in Equation A.4 led to the torque specification of the drive motor being set to 5 Nm. To arrive at a speed specification for the drive motor, the literature was consulted for typical landing speeds. Möller demonstrated autonomous landing of a quad-rotor with an average descent rate of 0.5 m s^{-1} on touchdown [1]. Based on the literature, it was deduced that descent rates of between 0.5 m s^{-1} and 1 m s^{-1} are not unusual. Seeing that the descent rate of an aircraft is generally not constant during landing, an average descent rate of 0.8 m s^{-1} was assumed. The drum angular speed ω required to achieve a descent rate of 0.8 m s^{-1} is calculated in Equation A.5.

$$\begin{aligned}\omega &= \frac{v}{r} \\ &= \frac{0.8 \text{ m.s}^{-1}}{0.12 \text{ m}} \\ &= 6.6 \text{ rad.s}^{-1} \\ &= 64 \text{ rpm}\end{aligned} \tag{A.5}$$

Based on the calculation in Equation A.5, the drive motor speed specification was set to 64 rpm. Having set the speed and torque specifications, the minimum allowable power rating for the motor was approximated. The mechanical power delivered by a motor to the output shaft is given by:

$$\begin{aligned}P_{out} &= Q * \omega \\ &= 4.8 \text{ Nm} * 6.6 \text{ rad.s}^{-1} \\ &= 32 \text{ W}\end{aligned} \tag{A.6}$$

The motor experiences mechanical power losses due to friction on the motor shaft and windage, among other factors. Electrical power losses are also experienced in the rotor winding and brush resistance R_a. It was decided that due to the availability of DC power supplies, the selection be limited to geared DC motors with fairly low gear ratios. Assuming a DC motor with an efficiency η of 65%, the minimum power rating of the motor can be calculated as:

$$\begin{aligned}P_{rated} &= \frac{P_{out}}{\eta} \\ &= \frac{32 \text{ W}}{65\%} \\ &= 49.2 \text{ W}\end{aligned} \tag{A.7}$$

This concludes the derivation of speed, torque and power specifications for the drive motor. It is very unlikely that one would find a motor whose ratings are exactly the same as the derived specifications. In any case, the calculation of motor rated power requirements relies on the knowledge of motor efficiency, which can only be estimated roughly in the design phase. Compromises typically have to be made when purchasing a motor for use in a particular application. A balance should be struck such that the

purchased motor provides satisfactory performance without being overdesigned for the application. In this light, it was decided that a motor that just falls short of the speed specification would still be acceptable. The consequence of the shortfall would then be a reduction in aircraft descent rate during landing. On the other hand, the power and torque specifications were treated more strictly. A motor with a low torque rating runs the risk of stalling when the torque exerted by the taut tether exceeds the mechanical torque of the motor. The described situation would cause a zero angular speed on the drum and the objective of landing the tethered aircraft would not be achievable.

Based on this, a suitable motor would be one with torque and power ratings that are slightly higher than the derived specifications. The PM 50 63 GB4 permanent magnet geared DC motor, manufactured by Parvalux Electric Motors Ltd conforms to the selection criteria and was selected. The ratings of the motor are documented in Table A.1.

Motor Parameter	**Rated Value**
Rated voltage (V)	24
Rated current (A)	3.5
Rated power (W)	60
Gear ratio (n)	25
Rated speed without gearbox (rpm)	1500
Rated speed with gearbox (rpm)	60
Rated torque without gearbox (Nm)	0.24
Rated torque with gear box (Nm)	6
Measured mass with gear box (kg)	3.143

Table A.1: Ratings of the PM 50 63 GB4 permanent magnet DC motor.

A.3 Winch Subsystem Functionality

In this section we present the high level functionality of the winch subsystem as a complete unit. Section A.3.1 briefly describes the keypad which serves as the manual user interface. The operation of the winch is supervised by the winch state machine presented in Section A.3.2.

A.3.1 Winch User Interface

Manual user commands are given to the winch system through a four-button keypad shown in Figure A.3. The keypad has four buttons namely **e-stop**, **wind**, **unwind** and **auto-wind**. The keypad is functionally a series of contact switches where pressing a button short-circuits the corresponding switch to a common connection. Each button is wired to a digital input pin on the Arduino board and the common connection is wired to digital ground. The four buttons are used to trigger the IDLE, WIND, UNWIND and AUTO-WIND states of the state machine respectively. The state machine and its various states are explained in Section A.3.2.

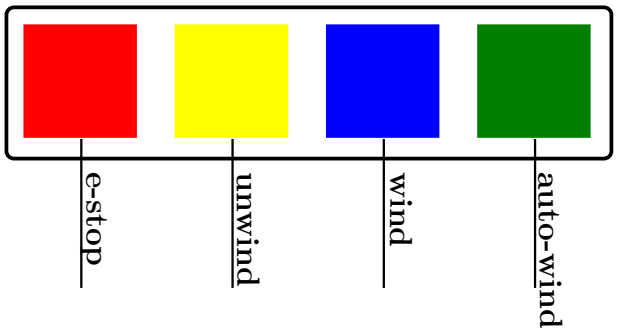

Figure A.3: Diagram of the winch keypad buttons.

A.3.2 Winch State Machine

The winch state machine is shown in Figure A.4. The winch starts off in the IDLE state upon power-up and thereafter can be made to transition to a different state by issuing commands through the keypad.

The IDLE state is activated by default upon power-up and holds the winch at a standstill. This is achieved by the winch control firmware writing a zero duty cycle command to the motor driver. The WIND state is triggered by pressing the **wind** button and persists *while* the button is pressed. In the WIND state the winch winds the tether in an open-loop fashion at a predefined speed by issuing a constant duty cycle to the motor driver. Releasing the **wind** button causes the winch to revert back to the IDLE state.

When the winch is in the UNWIND state it functions exactly the same as in the WIND state, save for a reversal in winding direction. The UNWIND state is active

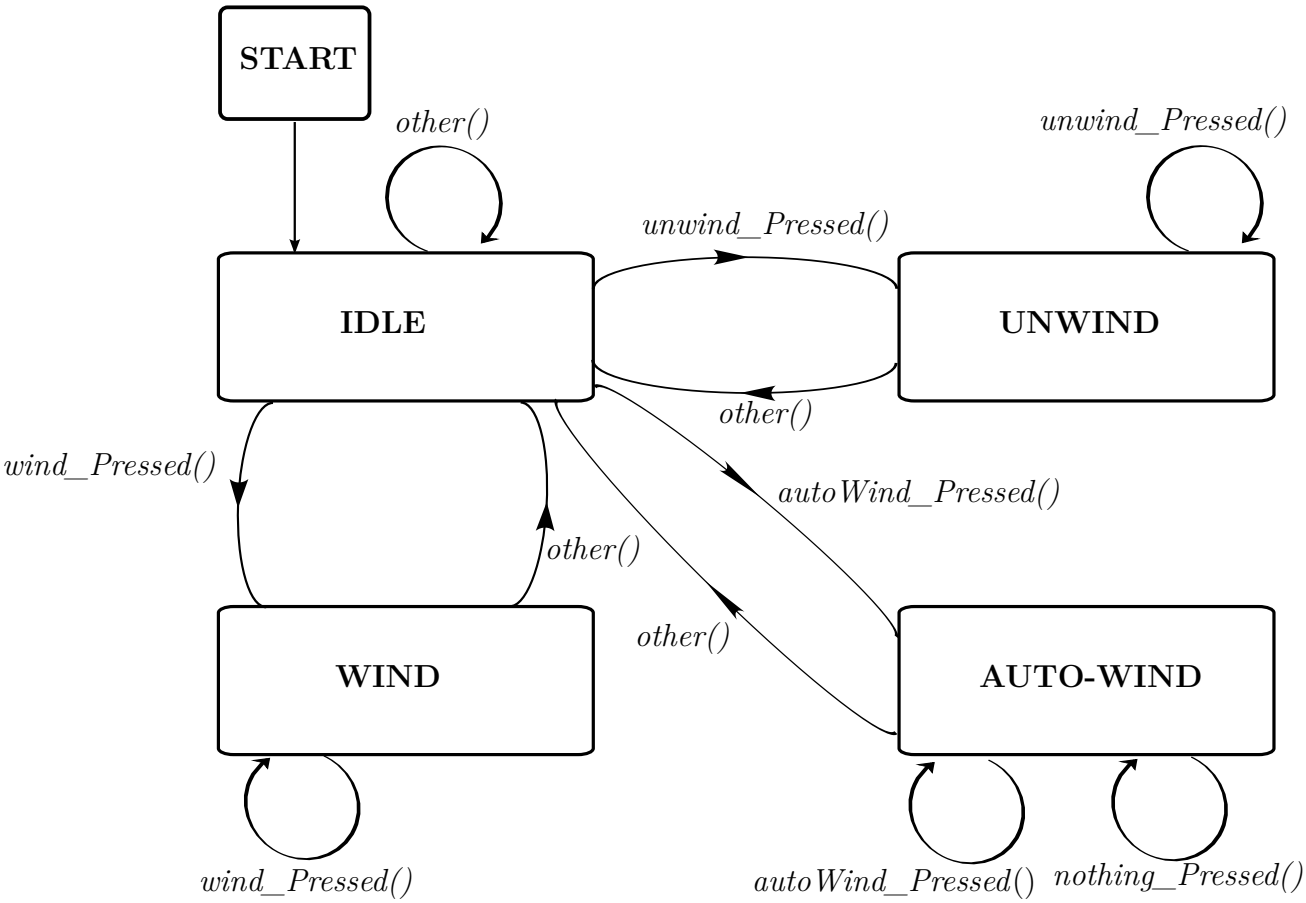

Figure A.4: Winch state machine.

while the **unwind** button is pressed. The WIND and UNWIND states are used to unwind the desired tether length before a flight.

In the AUTO-WIND state, the winch executes the speed control system presented in Section 6.2 to wind the tether at a constant speed. The AUTO-WIND state is triggered by pressing the **auto-wind** button on the keypad. The state remains active even after the button has been released, until a different button or button combination has been pressed. As shown in Figure A.4, either the **e-stop** button or any combination of two, three buttons or all four buttons can be pressed in case of emergency to revert the winch back to the IDLE state and abort winching.

A.4 Chapter Summary

This appendix presented the detailed design of the winch. The winch hardware and firmware were both developed as new work in this project to winch the tethered quadrotor during the autonomous landing of the UAV. Section A.1 briefly outlined the major components of the winch system and how they interact with each other. Thereafter the strategy used to select a motor for the purposes of driving the winch was detailed in Section A.2. The winch functionality was then explained in Section A.3. Specifically, the winch manual user interface was presented in Section A.3.1 and the winch state machine was explained in Section A.3.2.

Appendix B

Control System Design

This appendix presents derivations and results from control systems theory to support the flight control system design. Section B.1 presents the derivation of a system's closed loop transfer function from its open loop transfer function. The conversion of the heave, horizontal and yaw state variable system representations to a transfer functions is detailed in Section B.2.

B.1 Open Loop to Closed Loop Transfer Function Conversion

In this section, the closed loop transfer function is derived from the open loop transfer function for the general control system shown in Figure B.1.

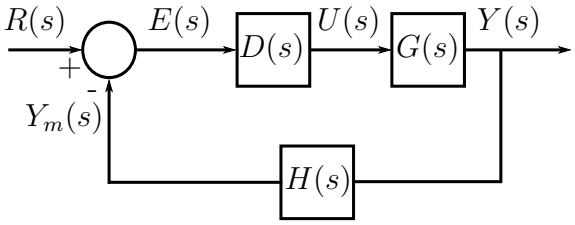

Figure B.1: General feedback control structure.

$$
\begin{aligned}
Y(s) &= D(s)G(s)E(s) \\
E(s) &= R(s) - Y_m(s) \\
Y_m(s) &= H(s)Y(s) \\
E(s) &= R(s) - H(s)Y(s) \\
Y(s) &= D(s)G(s)E(s) \\
Y(s) &= D(s)G(s)[R(s) - H(s)Y(s)] \\
Y(s) &= D(s)G(s)R(s) - D(s)G(s)H(s)Y(s) \\
Y(s)[1 + D(s)G(s)H(s)] &= R(s)[D(s)G(s)] \\
\frac{Y(s)}{R(s)} &= \frac{D(s)G(s)}{1 + D(s)G(s)H(s)}
\end{aligned}
$$

B.2 State Variable Model To Transfer Function Conversion

The conversion of a state variable system model into a transfer function is outlined in this section. Section B.2.1 presents the equations used to perform the conversion for a general state variable model. This general result is applied specifically to the heave dynamics in Section B.2.2 and to the pitch dynamics in Section B.2.3. Finally, the conversion of the yaw dynamics state variable model into a transfer function is presented in Section B.2.4.

B.2.1 General State Variable To Transfer Function Conversion

We consider a general SISO sytem with the state equation shown in Equation B.1 and the output equation shown in Equation B.2. The transfer function for the system is given be Equation B.3 [35].

$$\dot{\mathbf{x}} = \mathbf{A}\mathbf{x} + \mathbf{B}u \tag{B.1}$$

$$y = \mathbf{C}\mathbf{x} \tag{B.2}$$

$$\frac{Y(s)}{U(s)} = \mathbf{C}\left[s\mathbf{I} - \mathbf{A}\right]^{-1}\mathbf{B} \tag{B.3}$$

B.2.2 Heave Dynamics State Variable To Transfer Function

The heave dynamics of the quad-rotor UAV are captured by the state equation in Equation B.4 and the output equation in Equation B.5.

$$\left[\dot{C_B}\right] = \left[-\frac{1}{\tau}\right]\left[C_B\right] + \left[\frac{1}{\tau m}\right]\left[\delta T_R\right] \tag{B.4}$$

$$C = \left[1\right]\left[C_B\right] \tag{B.5}$$

The heave dynamics is a specific case of the general state variable model presented in Section B.2 in which the general matrices **A**, **B** and **C** are specified by Equations B.6, B.7 and B.8. The input and output for the heave system are defined by Equations B.9 and B.10 respectively.

$$\mathbf{A} = \left[-\frac{1}{\tau}\right] \tag{B.6}$$

$$\mathbf{B} = \left[\frac{1}{\tau m}\right] \tag{B.7}$$

$$\mathbf{C} = \left[1\right] \tag{B.8}$$

$$u = \delta T_R \tag{B.9}$$

$$y = C_B \tag{B.10}$$

The heave system transfer function with respect to the specified input and output can be derived as shown in Equations B.11.

$$\begin{aligned}\frac{C_B(s)}{\delta T_R(s)} &= \left[1\right]\left(\left[s\right] - \left[-\frac{1}{\tau}\right]\right)^{-1}\left[\frac{1}{\tau m}\right] \\ &= (1)\left(s + \frac{1}{\tau}\right)^{-1}\left(\frac{1}{\tau m}\right) \\ &= \frac{\frac{1}{\tau m}}{\left(s + \frac{1}{\tau}\right)}\end{aligned} \tag{B.11}$$

B.2.3 Horizontal Dynamics State Variable To Transfer Function

Equations B.12 and B.13 are the state and output equations for the pitch system of the vehicle.

$$\begin{bmatrix}\dot{M}\\ \dot{Q}\end{bmatrix} = \begin{bmatrix}-\frac{1}{\tau} & 0\\ \frac{1}{I_{yy}} & 0\end{bmatrix}\begin{bmatrix}M\\ Q\end{bmatrix} + \begin{bmatrix}\frac{1}{\tau}\\ 0\end{bmatrix}\delta E_R \tag{B.12}$$

$$Q = \begin{bmatrix}0 & 1\end{bmatrix}\begin{bmatrix}M\\ Q\end{bmatrix} \tag{B.13}$$

The pitch model is a specific case of the general state variable model presented in Section B.2 in which the general matrices **A**, **B** and **C** as defined by Equations B.14, B.15 and B.16 are applicable. The input and output for the pitch system are defined by Equations B.17 and B.18 respectively.

$$\mathbf{A} = \begin{bmatrix}-\frac{1}{\tau} & 0\\ \frac{1}{I_{yy}} & 0\end{bmatrix} \tag{B.14}$$

$$\mathbf{B} = \begin{bmatrix}\frac{1}{\tau}\\ 0\end{bmatrix} \tag{B.15}$$

$$\mathbf{C} = \begin{bmatrix}0 & 1\end{bmatrix} \tag{B.16}$$

$$u = \delta E_R \tag{B.17}$$

$$y = Q \tag{B.18}$$

Equations B.19 are a derivation of the transfer function model for the pitch system.

$$\begin{aligned}\frac{Q(s)}{\delta E_R(s)} &= \begin{bmatrix}0 & 1\end{bmatrix}\left(\begin{bmatrix}s & 0\\ 0 & s\end{bmatrix} - \begin{bmatrix}-\frac{1}{\tau} & 0\\ \frac{1}{I_{yy}} & 0\end{bmatrix}\right)^{-1}\begin{bmatrix}\frac{1}{\tau}\\ 0\end{bmatrix}\\ &= \begin{bmatrix}0 & 1\end{bmatrix}\left(\begin{bmatrix}s+\frac{1}{\tau} & 0\\ -\frac{1}{I_{yy}} & s\end{bmatrix}\right)^{-1}\begin{bmatrix}\frac{1}{\tau}\\ 0\end{bmatrix}\\ &= \begin{bmatrix}0 & 1\end{bmatrix}\left(\frac{1}{s\left(s+\frac{1}{\tau}\right)}\begin{bmatrix}s & 0\\ \frac{1}{I_{yy}} & s+\frac{1}{\tau}\end{bmatrix}\right)\begin{bmatrix}\frac{1}{\tau}\\ 0\end{bmatrix}\\ &= \frac{\frac{1}{\tau I_{yy}}}{s\left(s+\frac{1}{\tau}\right)}\end{aligned} \tag{B.19}$$

B.2.4 Yaw Dynamics State Variable To Transfer Function

The yaw system is identical in form to the pitch system. Equations B.20 and B.21 are the state and output equations for the yaw system.

$$\begin{bmatrix} \dot{N} \\ \dot{R} \end{bmatrix} = \begin{bmatrix} -\frac{1}{\tau} & 0 \\ \frac{1}{I_{zz}} & 0 \end{bmatrix} \begin{bmatrix} N \\ R \end{bmatrix} + \begin{bmatrix} \frac{1}{\tau} \\ 0 \end{bmatrix} \delta R_R \tag{B.20}$$

$$R = \begin{bmatrix} 0 & 1 \end{bmatrix} \begin{bmatrix} N \\ R \end{bmatrix} \tag{B.21}$$

Similar to the pitch system, the specific matrices characterising the yaw dynamics are given by Equations B.22, B.23 and B.24. The yaw system input and output are given by Equations B.25 and B.26 respectively.

$$\mathbf{A} = \begin{bmatrix} -\frac{1}{\tau} & 0 \\ \frac{1}{I_{zz}} & 0 \end{bmatrix} \tag{B.22}$$

$$\mathbf{B} = \begin{bmatrix} \frac{1}{\tau} \\ 0 \end{bmatrix} \tag{B.23}$$

$$\mathbf{C} = \begin{bmatrix} 0 & 1 \end{bmatrix} \tag{B.24}$$

$$u = \delta R_R \tag{B.25}$$

$$y = R \tag{B.26}$$

Equations B.27 show the derivation of the transfer model of the yaw system from

its state variable model respectively.

$$\begin{aligned}
\frac{R(s)}{\delta R_R(s)} &= \begin{bmatrix} 0 & 1 \end{bmatrix} \left(\begin{bmatrix} s & 0 \\ 0 & s \end{bmatrix} - \begin{bmatrix} -\frac{1}{\tau} & 0 \\ \frac{1}{I_{zz}} & 0 \end{bmatrix} \right)^{-1} \begin{bmatrix} \frac{1}{\tau} \\ 0 \end{bmatrix} \\
&= \begin{bmatrix} 0 & 1 \end{bmatrix} \left(\begin{bmatrix} s + \frac{1}{\tau} & 0 \\ -\frac{1}{I_{zz}} & s \end{bmatrix} \right)^{-1} \begin{bmatrix} \frac{1}{\tau} \\ 0 \end{bmatrix} \\
&= \begin{bmatrix} 0 & 1 \end{bmatrix} \left(\frac{1}{s\left(s + \frac{1}{\tau}\right)} \begin{bmatrix} s & 0 \\ \frac{1}{I_{zz}} & s + \frac{1}{\tau} \end{bmatrix} \right) \begin{bmatrix} \frac{1}{\tau} \\ 0 \end{bmatrix} \\
&= \frac{\frac{1}{\tau I_{zz}}}{s\left(s + \frac{1}{\tau}\right)}
\end{aligned} \tag{B.27}$$

B.3 System Poles to Dynamic Response

The step response of a second order system with an underdamped complex pole pair located at $s = -\sigma \pm j\omega_d$ is a sinusoid with a period of oscillation T given by Equation B.28 and an exponentially growing envelope with a time constant τ given by Equation B.29 [35].

$$T = \frac{2\pi}{\omega_d} \tag{B.28}$$

$$\tau = \frac{1}{\sigma} \tag{B.29}$$

The impulse response $y(t)$ of the system takes the form shown in Equation B.30, where K is a constant.

$$y(t) = Ke^{-\sigma t}\sin(\omega_d t) \tag{B.30}$$

For underdamped poles, the impulse response is a sinoid with an oscillation period given by Equation B.28. The amplitude of the sinusoid decays exponentially with a time constant given by Equation B.29.

Appendix C

Linearisation of Nonlinear Dynamics

This appendix outlines the linearisation of non-linear system dynamics about a static operating point. Firstly, the general theory for linearising a non-linear function about a static point is presented in Section C.1 [37]. Section C.2 extends the result of Section C.1 to express a set of non-linear dynamic equations in terms of a linearised state space model around a static operating point.

C.1 Taylor Series Approximation

Given y, a non-linear function of x as given by Equation C.1, the Taylor Series approximation allows y to be approximated by a linear function around a static operating point x_0 as given by Equation C.2 [37]. The right hand side of Equation C.2 can be approximated by its first two terms since the higher order terms are significantly small relative to the first two. Neglecting the higher order terms, Equation C.2 can be approximated by Equation C.3.

$$y = F(x) \tag{C.1}$$

$$y = F(x_0) + \left[\frac{dF}{dx}\bigg|_{x=x_0}\right](x - x_0) + \left[\frac{d^2F}{dx^2}\bigg|_{x=x_0}\right]\frac{(x - x_0)^2}{2!} + \dots \tag{C.2}$$

$$y \approx F(x_0) + \left[\frac{dF}{dx}\bigg|_{x=x_0}\right](x - x_0) \tag{C.3}$$

We can define perturbation variables around the static operating point as shown in Equations C.4 and C.5.

$$\Delta x = x - x_0 \tag{C.4}$$
$$\Delta y = y - y_0 \tag{C.5}$$
$$y_0 = F(x_0) \tag{C.6}$$

When expressed in terms of the perturbation variables, the approximation given in Equation C.3 can be written as a linear function as shown in Equation C.7.

$$\Delta y \approx \left[\left. \frac{dF}{dx} \right|_{x=x_0} \right] \Delta x \tag{C.7}$$

C.2 Derivation of Linearised State Space Model

The result captured in Equation C.7 can be extended to non-linear system dynamic equations [35]. Without loss of generality, we consider a system whose dynamics can be fully described in terms of the state vector in Equation C.8.

$$\mathbf{x} = \begin{bmatrix} x_1 \\ x_2 \\ x_3 \\ x_4 \end{bmatrix} \tag{C.8}$$

For the non-linear system under consideration, assume the time derivatives of the states are given by Equation set C.9 where F_1, F_2 F_3 and F_4 are non-linear functions of the state vector and the input.

$$\begin{aligned} \dot{x}_1(t) &= F_1 \{\mathbf{x}(t), u(t)\} \\ \dot{x}_2(t) &= F_2 \{\mathbf{x}(t), u(t)\} \\ \dot{x}_3(t) &= F_3 \{\mathbf{x}(t), u(t)\} \\ \dot{x}_4(t) &= F_4 \{\mathbf{x}(t), u(t)\} \\ y(t) &= g \{\mathbf{x}(t), u(t)\} \end{aligned} \tag{C.9}$$

We can define perturbation states around a static operating point as given by the set of Equations C.10.

$$\begin{aligned}
\Delta\mathbf{x} &= \mathbf{x} - \mathbf{x}_0 \\
\Delta\dot{\mathbf{x}} &= \dot{\mathbf{x}} - \dot{\mathbf{x}}_0 \\
\Delta y &= y - y_0 \\
\Delta u &= u - u_0
\end{aligned} \tag{C.10}$$

Following from the linear relationship in Equation C.7, the system perturbations from the static operating point can be represented by the state equation in Equation C.11 and the output equation in Equation C.12.

$$\Delta\dot{\mathbf{x}}(t) = \left[\begin{array}{cccc} \frac{\partial F_1}{\partial x_1} & \frac{\partial F_1}{\partial x_2} & \frac{\partial F_1}{\partial x_3} & \frac{\partial F_1}{\partial x_4} \\ \frac{\partial F_2}{\partial x_1} & \frac{\partial F_2}{\partial x_2} & \frac{\partial F_2}{\partial x_3} & \frac{\partial F_2}{\partial x_4} \\ \frac{\partial F_3}{\partial x_1} & \frac{\partial F_3}{\partial x_2} & \frac{\partial F_3}{\partial x_3} & \frac{\partial F_3}{\partial x_4} \\ \frac{\partial F_4}{\partial x_1} & \frac{\partial F_4}{\partial x_2} & \frac{\partial F_4}{\partial x_3} & \frac{\partial F_4}{\partial x_4} \end{array}\right]\Bigg|_{(\mathbf{x}=\mathbf{x}_0, u=u_0)} \Delta\mathbf{x}(t) + \left[\begin{array}{c} \frac{\partial F_1}{\partial u} \\ \frac{\partial F_2}{\partial u} \\ \frac{\partial F_3}{\partial u} \\ \frac{\partial F_4}{\partial u} \end{array}\right]\Bigg|_{(\mathbf{x}=\mathbf{x}_0, u=u_0)} \Delta u(t) \tag{C.11}$$

$$\Delta y(t) = \left[\begin{array}{cccc} \frac{\partial g}{\partial x_1} & \frac{\partial g}{\partial x_2} & \frac{\partial g}{\partial x_3} & \frac{\partial g}{\partial x_4} \end{array}\right]\Bigg|_{(\mathbf{x}=\mathbf{x}_0, u=u_0)} + \frac{\partial g}{\partial u}\Bigg|_{(\mathbf{x}=\mathbf{x}_0, u=u_0)} \Delta u(t) \tag{C.12}$$

It must be noted that Equations C.11 and C.12 are a technique to linearise the dynamics around a static operating point *provided* that such a static point exists. The equations themselves do not guarantee the existence of a static operating point [35]. It must be ensured that the static operating point does indeed exist before performing the linearisation.

Appendix D

Additional Flight Data

This appendix contains additional flight test data to support the data given in Chapter 8. Section D.1 shows horizontal velocity and climb rate data for the two tethered landings. Section D.2 contains flight data for the mock landing with a reduced horizontal controller gains.

D.1 Additional Landing Data

Figure D.1 shows velocity, climb rate and thrust data for the two tethered landings. The results presented in this section complement the position and heading angle flight data shown in Figure 8.4.

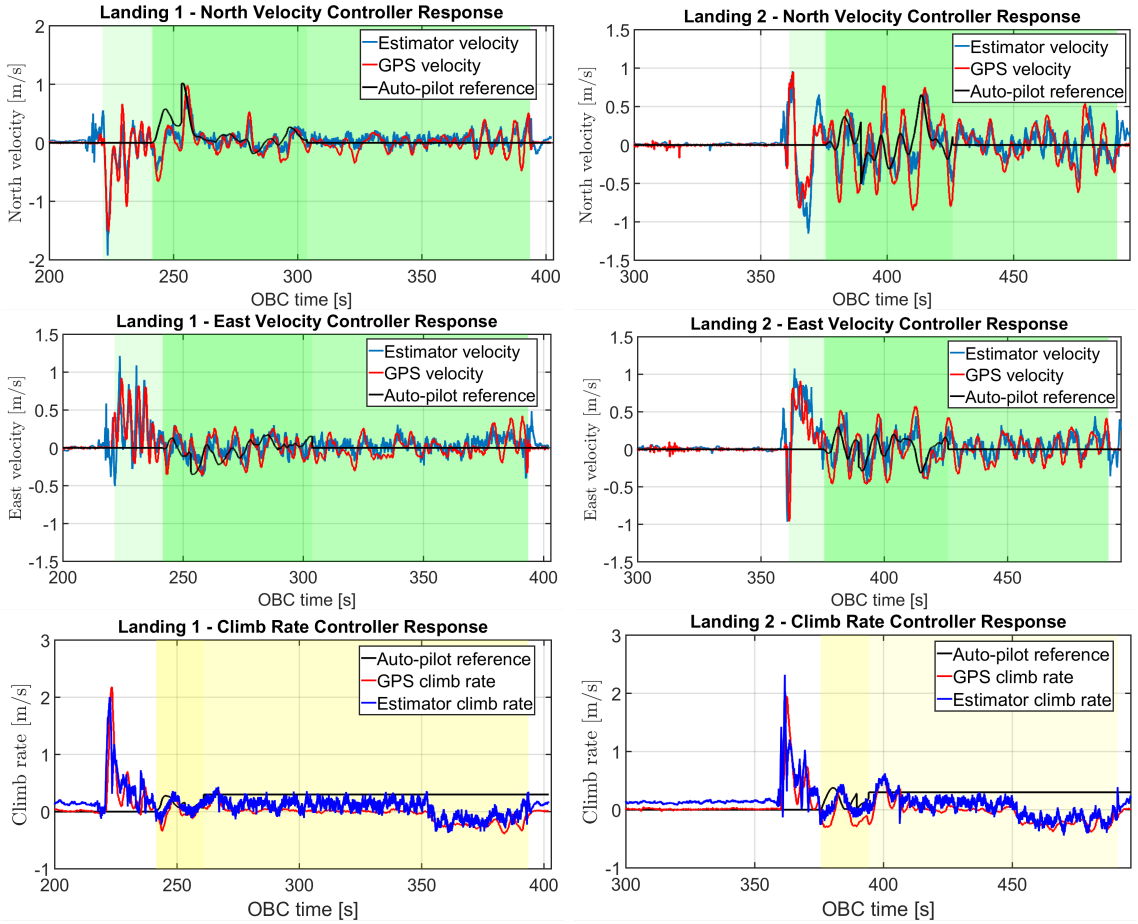

Figure D.1: Velocity and climb rate result for tethered landing.

D.2 Low Velocity Gain Flight Data

Figure D.2 shows flight data for the tethered mock-landing with a reduced horizontal controller gain of $K_p = 0.2$ as detailed in Section 8.3.

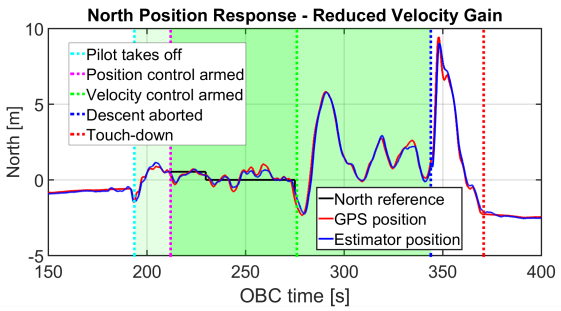

(a) North position response.

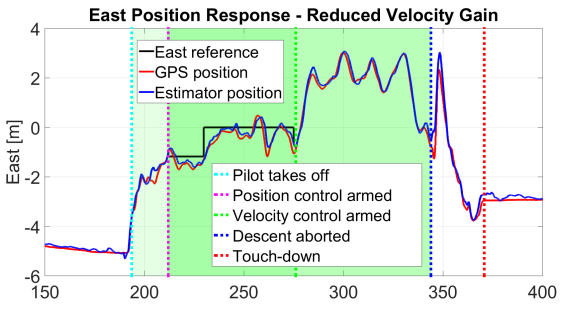

(b) East position response.

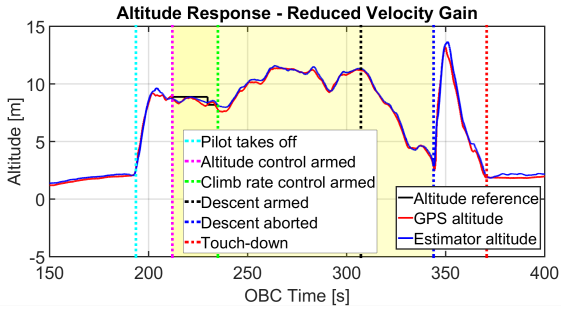

(c) Altitude response.

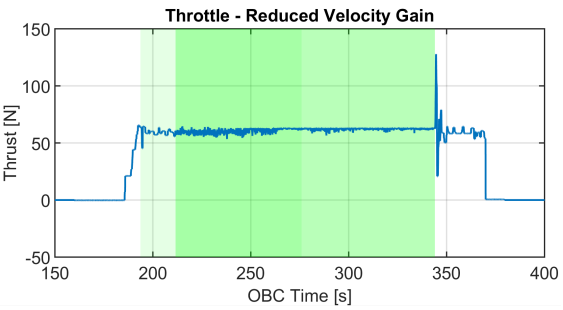

(d) Throttle measurement.

Figure D.2: Position and throttle plots for low gain descent.

Appendix E

Winch Modelling

This appendix presents the modelling of the permanent magnet geared DC motor used to drive the winch. The appendix focusses on the formulation of equations to capture the electro-mechanical properties of the permanent magnet DC motor. The formulated equations are then transformed into transfer functions to set the stage for control system design.

E.1 DC Motor Modelling

The dynamic equations of the permanent magnet DC geared motor are best explored by examining the ungeared motor first. Thereafter, the mechanical implications of the gearbox to the motor will be incorporated to complete the model. A DC motor consists of two main parts; a stationary stator and a rotor that rotates when sufficient current flows through its coils. The rotor coils that are connected to the motor terminals. The stator can either be furnished with a set of coils (field windings) or with permanent magnets to produce a stator magnetic field. In a permanent magnet DC motor, the stator magnetic field is produced by a set of permanent magnets.

The permanent magnet DC motor relies on the interaction between the stator magnetic field and rotor coil current to produce a force and thereby result in rotary motion. The rotating rotor extends to form a shaft which drives a mechanical load. The operation of DC motors has been studied extensively for many decades and is well-documented [38]. This section will focus on outlining the relationships between the electrical properties of the DC motor and its mechanical properties.

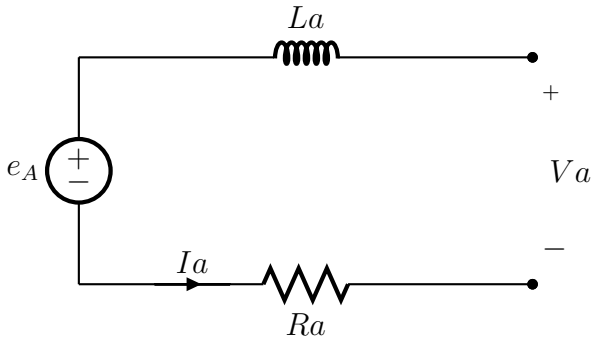

Figure E.1: Equivalent circuit for a DC motor armature winding.

The rotor winding is the armature and it connects to the motor terminals. Figure E.1 shows the equivalent circuit for the armature winding of a permanent magnet DC motor. The armature winding, commutator and brushes are represented by an inductance L_a in series with a resistance R_a. The spinning rotor induces a back electromotive force (EMF) whose polarity opposes that of the applied terminal voltage. As mentioned earlier, the stator magnetic field is supplied by a set of permanent magnets. Applying Kirchhoff's Voltage Law to the armature circuit in Figure E.1, Equation E.1 is obtained.

$$V_a(t) = L_a \frac{di_a(t)}{dt} + R_a i_a(t) + e_A \tag{E.1}$$

For control system design purposes, it is convenient to obtain the input-output relationship between the armature voltage and the armature current. Applying the Laplace Transform to Equation E.1 yields the desired transfer function, as depicted in Equation E.2.

$$\frac{I_a(s)}{V_a(s) - E_A(s)} = \frac{K_a}{1 + \tau_a s} \tag{E.2}$$

The quantities K_a and τ_a are defined as:

$$K_a = \frac{1}{R_a}$$
$$\tau_a = \frac{L_a}{R_a}$$

The relationship between the mechanical torque $Q_{M'}$ developed by the ungeared

DC motor and the armature current I_a is given by Equation E.3.

$$Q_{M'} = K_e i_a \tag{E.3}$$

K_e in Equation E.3 is a motor constant that takes into account, among other factors, the strength of the stator magnetic field and the number of turns in the armature winding. The back EMF e_A is related to the angular velocity of the rotor ω' through Equation E.4.

$$e_A = K_e \omega' \tag{E.4}$$

K_e in Equation E.4 is commonly know as the motor constant and is the same K_e in Equation E.3, provided both equations are written in SI units [38]. Equations E.2, E.3 and E.4 are commonly referred to as the electric equations of a DC motor [39]. A comprehensive derivation of the electrical equations is documented in [39]. To complete the dynamic modelling of the DC motor, the mechanical equations will be presented.

The physical phenomena contributing to the mechanical dynamics are the inertia of the motor and friction. Zaccarian modelled friction as a viscous friction for which the motion-opposing torque varies linearly with angular speed. A viscous friction model is sufficient for motors operating close to their rated speeds [39]. For this project however, a cogging friction model was appended to the viscous friction model. The resulting model utilises a cogging friction model while the geared motor is stationary and switches over to a viscous friction model once rotation begins. For now we focus on the viscous friction model as the motor will be in motion for the majority of the landing mission. The cogging friction affects the start up of the motor and will be addresses at the end of this section.

When the motor is rotating, the relationship between the mechanical torque developed and the angular speed of the rotor is as presented in Equation E.5.

$$Q_{M'}(t) - Q_{L'}(t) = J' \frac{d\omega'(t)}{dt} + F' \omega'(t) \tag{E.5}$$

The variables appearing in Equation E.5 are the mechanical torque developed by the ungeared motor $Q_{M'}$, the load torque exerted on the rotor shaft $Q_{L'}$, the rotor moment of inertia J', the angular speed of the rotor ω' and the coefficient of viscous

friction of the rotor F'. It is important to note the convention adopted when discussing mechanical properties. Symbols for the mechanical properties of the ungeared motor are primed. Mechanical properties of the gear-box will be superscripted with a 'G '. The properties of the geared motor will be represented by plain text symbols.

Taking the Laplace Transform of Equation E.5 yields the transfer function in Equation E.6.

$$\frac{\omega'(s)}{Q_{M'}(s) - Q_{L'}(s)} = \frac{K_{m'}(s)}{1 + \tau_{m'}s} \tag{E.6}$$

Where:

$$K_{m'} = \frac{1}{F'}$$
$$\tau_{m'} = \frac{J'}{F'}$$

Equation E.6 is the mechanical equation of a DC motor [39]. The electric equations and the mechanical equation together give full account of the dynamic behaviour of the permanent magnet DC motor as a machine that converts electrical energy into mechanical energy. The block diagram of a permanent magnet ungeared DC motor is shown in Figure E.2.

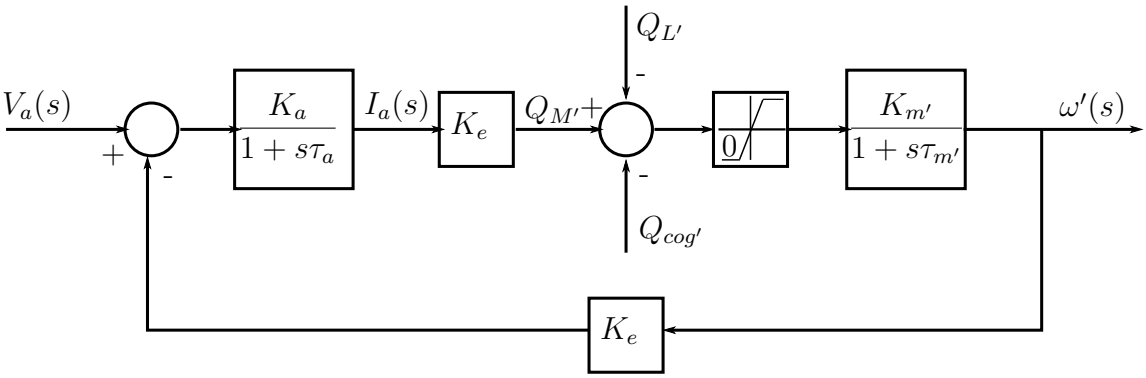

Figure E.2: Model of a permanent magnet DC motor.

E.2 Augmentation of the Gearbox Dynamics

Having outlined the equations for the permanent magnet ungeared DC motor, the effects of the gearbox are now considered. An in-depth coverage of geared systems is

beyond the scope of this project. It is sufficient to outline the effects of the gearbox on torque and angular speed. It is important to note that the gear box only affects the mechanical equations of a DC motor. The motor electrical equations remain unchanged. For a geared motor with gear ratio n, the mechanical power delivered to the rotor shaft is the same as the power delivered to the output shaft, neglecting frictional losses in the gear box. Equation E.7 demonstrates the equality in power delivered to the two shafts:

$$Q_{M'}\omega' = Q_M\omega \tag{E.7}$$

In Equation E.7, $Q_{M'}$ is the mechanical torque developed at the rotor shaft, Q_M is the mechanical torque developed at the output shaft, ω' is the angular speed of the rotor shaft and ω is the angular speed of the output shaft.

Traversing from the rotor shaft to the output shaft, the gear-box scales up the mechanical torque by a factor n whereas the angular speed is scaled down by a factor of n. This scaling effect of the gearbox is presented in Equations E.8 and E.9.

$$\omega = \frac{\omega'}{n} \tag{E.8}$$

$$Q_M = nQ_{M'} \tag{E.9}$$

Our goal is now to derive an equation based on Newton's law of rotational motion for the geared motor, similar to Equation E.5. The gearbox has a moment of inertia denoted by J^G. Adopting the viscous friction model, the gearbox has an associated coefficient of viscous friction F^G. It can be shown that the desired Newton's rotational law equation is as shown in Equation E.10 [39]. We highlight that the derivation of Equation E.10 does not add any insight to the subsequent system identification and/or control system design. For this reason, we adopt the equation as it is documented in [39] and skip its derivation.

$$Q_M(t) - Q_L(t) = (J^G + n^2J')\frac{d\omega(t)}{dt} + (F^G + n^2F')\omega(t) \tag{E.10}$$

Q_M in Equation E.10 is the torque exerted on the output shaft of the geared motor by the load. Equation E.10 takes the same form as Equation E.5. By comparing the two equations, it is apparent that the mechanical properties of the geared motor are a function of the mechanical properties of the ungeared motor and those of the gear-box. Specifically, the friction coefficient of the geared motor(F) and the mass moment of inertia of the geared motor(J) are given by Equations E.11 and E.12, respectively.

$$F = F^G + n^2 F' \tag{E.11}$$

$$J = J^G + n^2 J' \tag{E.12}$$

Taking the Laplace Transform of Equation E.10 yields Equation E.13.

$$\frac{\omega(s)}{Q_M(s) - Q_L(s)} = \frac{K_m}{1 + \tau_m s} \tag{E.13}$$

The quantities K_m and τ_m in Equation E.13 are defined as:

$$\begin{aligned} K_m &= \frac{1}{F^G + n^2 F'} \\ &= \frac{1}{F} \\ \tau_m &= \frac{J^G + n^2 J'}{F^G + n^2 F'} \\ &= \frac{J}{F} \end{aligned}$$

Equation E.13 is the mechanical equation of the geared motor. Together with the electrical equations in Equations E.2, E.3 and E.4, the mechanical equation encapsulates the dynamic behaviour of the permanent magnet geared DC motor. Figure E.3 shows the model of the geared DC motor in block diagram form. The origins of all the variables appearing in the model have been explained except for the cogging frictional torque Q_{cog}.

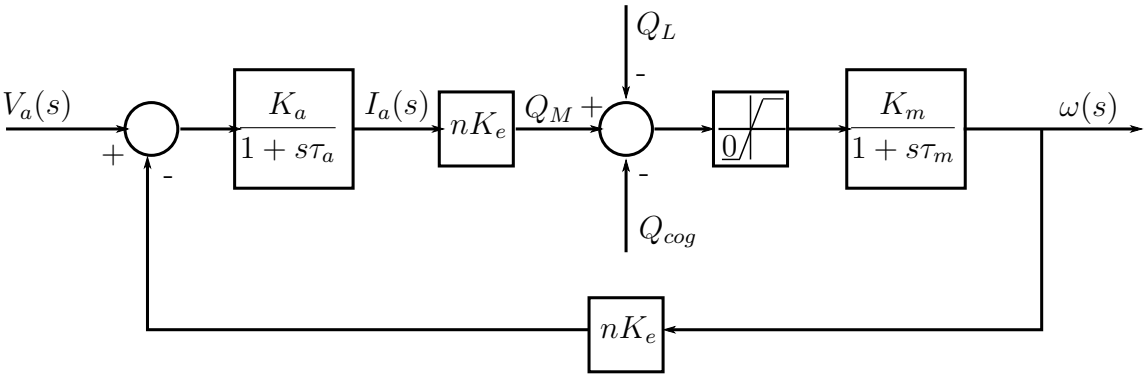

Figure E.3: Model of a permanent magnet geared DC motor.

E.3 Friction Profile Model

We conclude the modelling of the geared motor by explaining the friction profile model. As already mentioned, a cogging friction model is employed when the geared motor is not rotating while the viscous friction model takes over at the onset of rotation. The geared motor is operated at rated voltage throughout the project. When armature voltage is stepped from zero to rated voltage under no load conditions, rotation only occurs when the armature current rises above a threshold value I_{trans}. Once motion ensues, the armature current falls to a lower value I_{visc} and the angular speed rises to a steady state value ω_r. Figure E.4 shows the friction profile model developed. While the armature current rises from zero to a value I_{trans}, the cogging torque will be modelled as being equal to the mechanical torque as shown in Equation E.14.

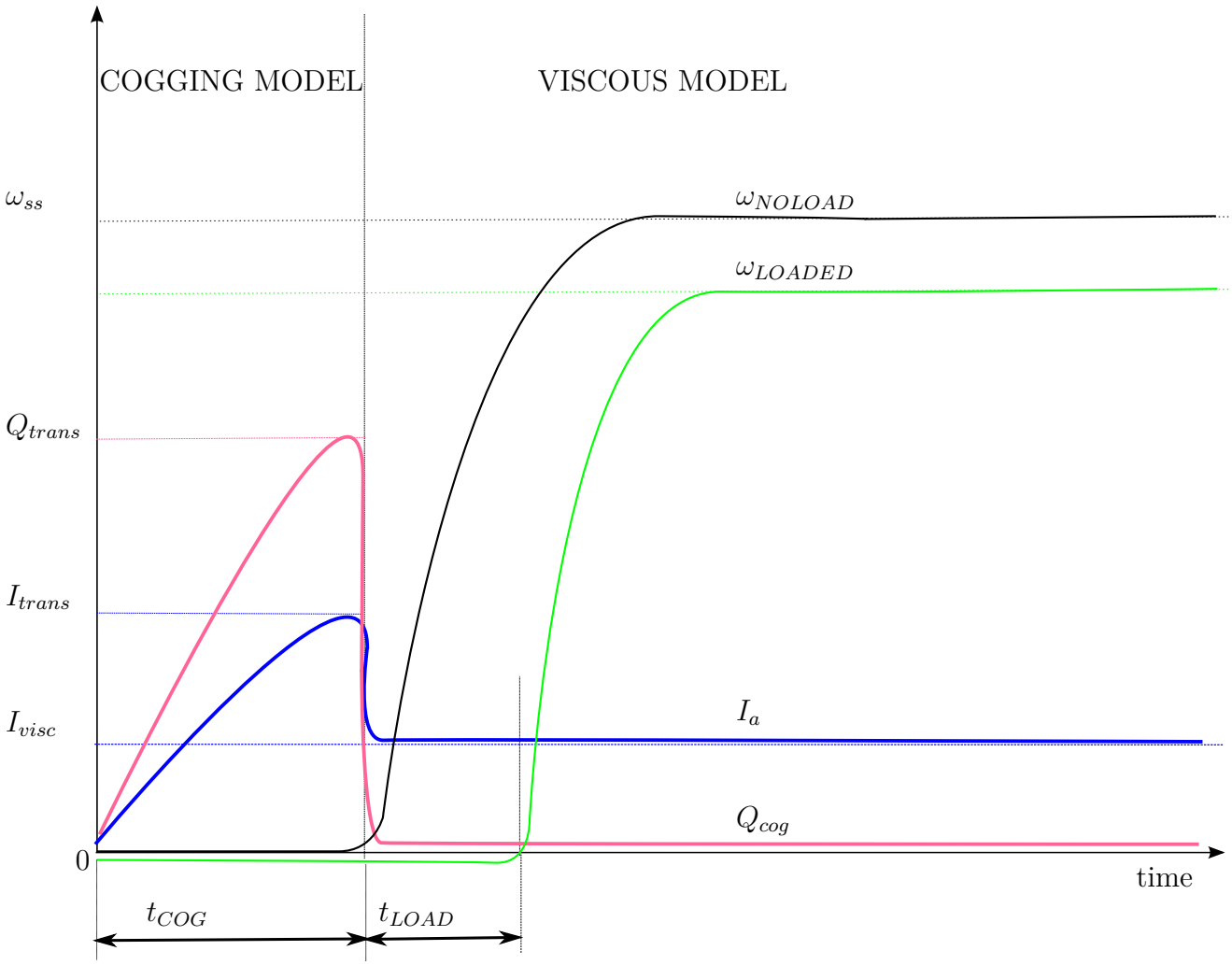

Figure E.4: Friction profile model for a permanent magnet geared DC motor.

$$\begin{aligned} Q_{cog} &= Q_M \\ &= nK_eI_a \end{aligned} \tag{E.14}$$

Once an armature current of I_{trans} is reached, the cogging torque is set to zero and the viscous friction model is activated and the armature current falls to a steady state value I_{visc}. The transition from a cogging friction model occurs when the cogging torque attains a value Q_{trans} given by Equation E.15. The time taken from the issuing of the armature voltage step and the commencement of rotation is denoted by t_{COG}. If the geared motor is unloaded, the angular speed will rise with a first order response as shown in Figure E.4. For a loaded motor however, a further dead time t_{LOAD} will manifest in the angular speed response. The input to the mechanical dynamics has a

zero lower limit to avoid modelling a negative torque. This scenario may result from the presence of a load torque while the cogging friction model is activated.

The flowchart in Figure E.5 shows the implementation of the friction profile model. With the dynamic modelling completed, a system identification campaign was embarked on to determine the numerical magnitudes of the variables contributing to the model. The system identification strategy is presented in Appendix F together with the approximation of tether stiffness and damping parameters. With the winch model in place, the stage is now set for winch control system design.

$$Q_{trans} = nK_eI_{trans} \tag{E.15}$$

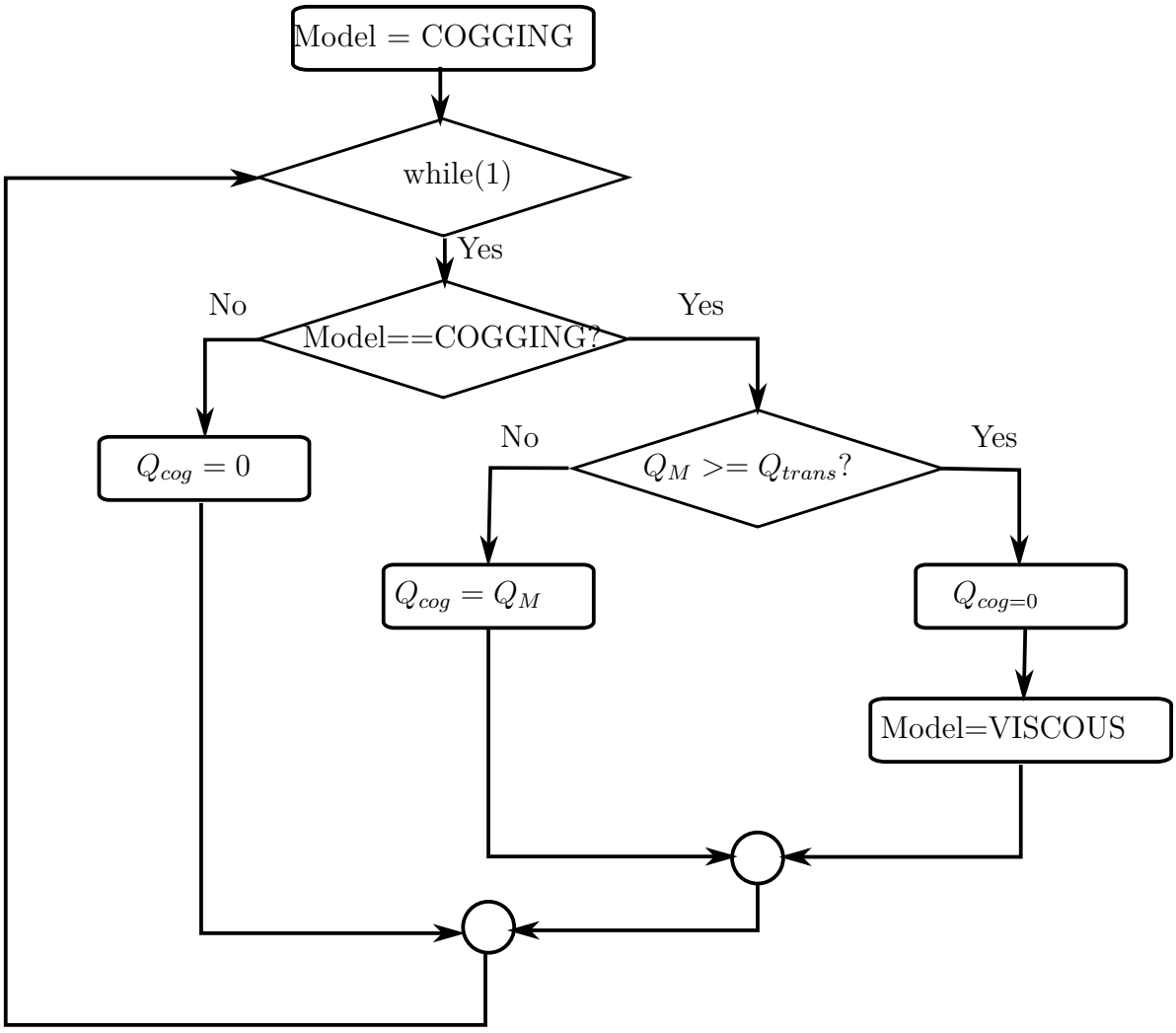

Figure E.5: Implementation of the friction profile model.

Appendix F

Winch and Tether Parameter Identification

This appendix outlines the procedure employed to obtain the parameters relating to the geared motor model as well as the tether. The experiments carried out to estimate the geared motor parameters are outlined in Section F.1. Section F.2 handles the estimation of tether stiffness and damping parameters.

F.1 Geared Motor System Identification

The block diagram representation of the geared motor model was presented in Appendix E and is reproduced in Figure F.1 for convenience. Complete system identification for the geared motor entails ascertaining the numerical values of n, R_a, L_a, K_a, K_e, K_m, τ_m, τ_a and Q_{cog}.

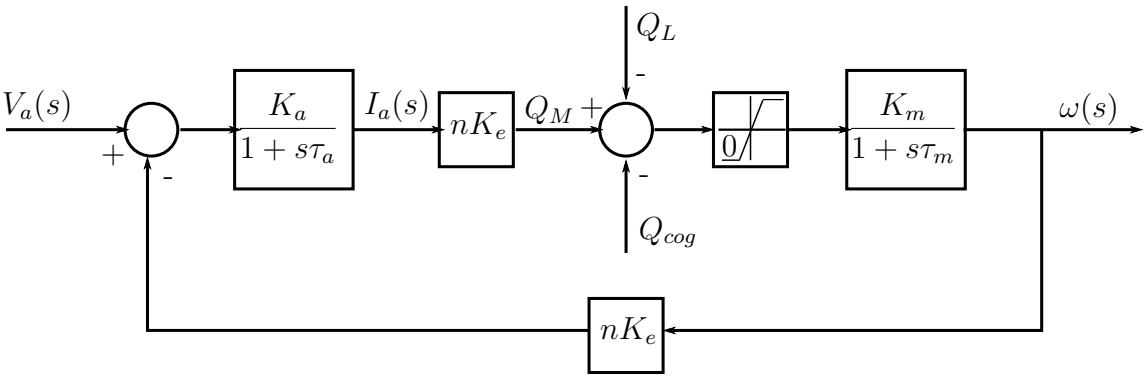

Figure F.1: Model of a permanent magnet geared DC motor.

Determination of the Gear Ratio n

The gear ratio n is supplied by the supplier of the geared motor and does not need to be determined experimentally. The value of n is supplied as 25.

Determination of the Armature Resistance R_a and Electrical Gain K_a

To determine the armature resistance, the gear-box and the motor were dismantled. The ungeared motor was then stalled using an iron lever and a small voltage was applied to the terminals. With the motor stalling, the rotor will have zero angular speed. According to Equation F.1, the back EMF produced by the rotor under stall conditions is zero. In steady state, the armature inductance can be approximated by a short circuit. With reference to Figure F.2, when the motor is stalling, the armature circuit reduces to a resistor R_a connected across the terminals of the motor.

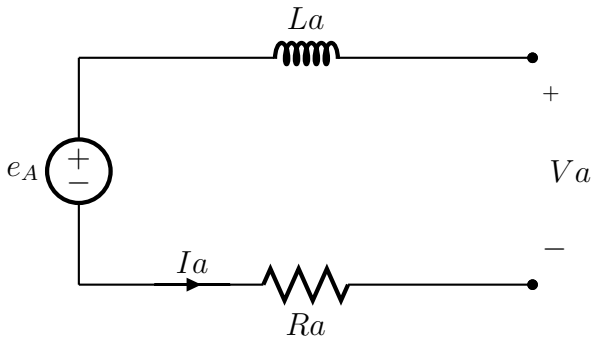

Figure F.2: Equivalent circuit for a DC motor armature winding.

$$e_A = K_e \omega' \tag{F.1}$$

The value of R_a is the quotient of terminal voltage V_a and the armature current I_a under stall conditions. Dismantling the gear-box from the motor made it easier to stall the motor in this experiment. For a given terminal voltage, the minimum opposing torque required on the output shaft to stall the geared motor is approximately n times more than the torque required to stall the motor on the rotor shaft with the gearbox dismantled. Small values values of V_a were used in the experiment, for two reasons.

Firstly, high values of V_a would produce a high current in the armature winding, resulting in overheating of the motor. Over heating alters the magnetic properties of the permanent magnets and leads to inaccurate measurements. Secondly, large terminal voltages produce large mechanical torques on the rotor shaft, thereby requiring large opposing torque on the rotor shaft to achieve stalling.

The stator magnetic field vector varies around the circumference of the stator. The stator magnetic fields can have an effect on the measured values of terminal voltage and armature current. The contact surface between the brushes and the commutator also varies with the rotor's rotational angle Θ relative to the stator. For the mentioned reasons, the steady state ratio $\frac{V_a}{I_a}$ was computed with the rotor stalled at different angles relative to the stator and the readings were averaged. Table F.1 shows the experimental values of I_a, V_a and R_a as measured on the stalled motor. The electrical gain was calculated from its definition as shown in Equation F.2.

$$\begin{aligned} K_a &= \frac{1}{R_a} \\ &= \frac{1}{1.2638\,\Omega} \\ &= 0.7912\,\Omega^{-1} \\ &= 0.7912\ \text{S} \end{aligned} \tag{F.2}$$

V_a**(V)**	Θ**(degrees)**	I_a**(A)**	**Calculated** $R_a(\Omega)$
1.30	0	1.033	1.2548
	45	1.030	1.2621
	90	1.026	1.2670
	135	1.030	1.2621
	180	1.029	1.2634
	225	1.028	1.2646
	270	1.029	1.2634
	315	1.024	1.2700
3.90	0	3.100	1.2580
	45	3.090	1.2620
	90	3.120	1.2500
	135	3.100	1.2580
	180	3.000	1.3000
	225	3.120	1.2500
	270	3.120	1.2500
	315	3.110	1.2540
R_a **average value** (Ω)			1.2638

Table F.1: Experimentally determined values of the armature resistance R_a.

Determination of the Armature Inductance L_a and the Electrical Time Constant τ_a

The experimental set up for the determination of the armature inductance and the electrical time constant is shown in Figure F.3. It is convenient to represent the circuit elements in the Laplace domain. The experiment requires the measurement of the time constant of the response of the armature current to a step in terminal voltage. A 1 Ω resistor R_i was connected in series with the armature circuit and a signal generator was connected to the motor terminals. With this set up the armature current can be measured by measuring the voltage across the 1 Ω resistor on the oscilloscope.

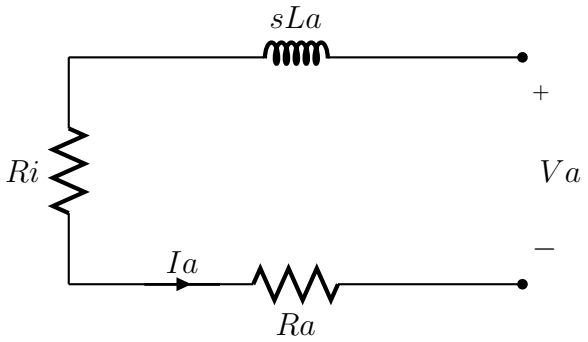

Figure F.3: Experimental set up for determining the electrical time constant.

With the gear-box dismantled and the motor stalling, the armature circuit was excited with a 1 kHz square wave. The time constant of the armature current response was measured as the time taken for the armature current to reach 63 % of its final value. This time constant will be denoted by $\tau_{a'}$ and is closely related to the electrical time constant which we seek to enumerate. Table F.2 shows the results obtained from the experiment.

Va_{peak}(mV)	Vi_{peak}(mV)	$63\% * Vi_{peak}$(mV)	$\tau_{a'}$(ms)
200	88.35	55.66	1.580

Table F.2: Experimentally determined time constant of the armature circuit.

With reference to Figure F.3, the total resistance R_t in the experimental set up is given by Equation F.3. Equation F.4 is a Kirchoff's Current Law (KCL) equation for the circuit shown in Figure F.3. Equation F.5 shows the transfer function from armature voltage to armature current as measured from the experimental set up, written in standard form to clearly show the measured time constant as indicated in Equation F.6. The armature inductance is the only unknown in Equation F.6. The armature inductance is calculated in Equation F.7. Finally, electrical time constant is calculated in Equation F.8 from its definition.

$$R_t = R_a + R_i \tag{F.3}$$

$$V_a(s) = I_a(s)[sL_a + R_t] \tag{F.4}$$

$$\frac{I_a(s)}{V_a(s)} = \frac{\frac{1}{R_t}}{s\frac{L_a}{R_t} + 1} \tag{F.5}$$

$$\tau_{a'} = \frac{L_a}{R_t} \tag{F.6}$$

$$\begin{aligned} L_a &= R_t \tau_{a'} \\ &= 2.2638\,\Omega * 1.580 \text{ ms} \\ &= 3.5768 \text{ mH} \end{aligned} \tag{F.7}$$

$$\begin{aligned} \tau_a &= \frac{L_a}{R_a} \\ &= \frac{3.5768 \text{ mH}}{1.2638\,\Omega} \\ &= 2.83 \text{ ms} \end{aligned} \tag{F.8}$$

Determination of the Motor Constant K_e

The motor constant K_e was calculated by measuring the angular velocity ω' of the rotor shaft and the armature current I_a produced by a specific armature voltage V_a in steady state. For large values of V_a, the magnitude of the mechanical developed torque is large enough that we can neglect frictional losses in the rotor. With reference to Figure F.2, a KVL equation can be written around the armature loop, having substituted e_A with $K_e\omega'$. The result is presented in Equation F.9.

$$K_e = \frac{Va - I_a R_a}{\omega'} \tag{F.9}$$

With the gearbox still dismantled from the motor, different values of armature voltage were applied to the motor terminal and measurements of ω' and I_a were recorded. With these measurements, the value of K_e was calculated using Equation F.9. The results of the experiment are recorded in Table F.3.

V_a(V)	ω'(rad/s)	I_a(A)	Calculated K_e(V.s/rad)
20.07	161.64	0.250	0.12220
21.13	169.16	0.252	0.12300
22.04	177.06	0.249	0.12268
23.01	185.76	0.249	0.12180
24.05	194.70	0.252	1.12190
Average value of K_e			0.12232

Table F.3: Experimentally determined value of Ke.

The motor constant can alternatively be obtained by examining the Performance Characteristic Graph of a motor. In that case, the no load speed of the motor is read from the Performance Characteristic Graph and divided by the the rated voltage to give an approximation for the motor constant. The data sheet of the geared motor used does not contain a Performance Characteristic Graph. However, Umans states that the motor constant can be approximated by dividing the motor rated voltage by the rated speed [38]. This approach was adopted to find a rough approximation of the motor constant and compare it with the value obtain through system identification techniques. The approximated motor constant $K_{e'}$ is shown in Equation F.10. The approximation is close to the value documented in Table F.3. The approximation therefore inspires confidence in the identified value.

$$\begin{aligned} K_{e'} &\approx \frac{V_{rated}}{\omega_{rated}} \\ &\approx \frac{24 \text{ Volts}}{1500 \text{ r.p.m}} \\ &\approx \frac{24 \text{ Volts}}{50\,\pi \text{ rad/sec}} \\ &\approx 0.153 \frac{\text{Volts}}{\text{rad/sec}} \end{aligned} \tag{F.10}$$

Determination of the Mechanical Gain K_m

At this stage the electrical properties of the motor are known. To determine the mechanical properties of the geared motor, the gearbox was fitted to the motor and the drum was coupled to the geared motor through the Oldham couplings. With reference to Figure F.1, the transfer function from armature voltage to output angular speed is given in by Equation F.11.

$$\begin{aligned}\frac{\omega(s)}{V_a(s)} &= \frac{\dfrac{nK_eK_aK_m}{(1+\tau_a s)(1+\tau_m s)}}{1+\dfrac{(nK_e)^2K_aK_m}{(1+\tau_a s)(1+\tau_m s)}} \\ &= \frac{nK_eK_aK_m}{(1+\tau_a s)(1+\tau_m s)+(nK_e)^2K_aK_m}\end{aligned} \tag{F.11}$$

It is importance to note that in writing Equation F.11, friction and load torque have been neglected. Equation F.11 can be re-written to make $\omega(s)$ the subject of the formula, as shown in Equation F.12. In the experiment, the relationship between a *constant* terminal voltage and the output angular speed will be recorded. For a constant terminal voltage, we can make the substitution shown in Equation F.13, where V_m is a constant armature voltage and s is the Laplace variable. Making the substitution and applying the Final Value Theorem to Equation F.12 yields Equation F.14.

$$\omega(s) = \frac{nV_a(s)K_eK_aK_m}{(1+\tau_a s)(1+\tau_m s)+(nK_e)^2K_aK_m} \tag{F.12}$$

$$V_a(s) = \frac{V_m}{s} \tag{F.13}$$

$$\begin{aligned}\omega_{ss} &= \lim_{s\to 0} s\frac{V_m}{s}\frac{nK_eK_aK_m}{(1+\tau_a s)(1+\tau_m s)+(nK_e)^2K_aK_m} \\ &= \frac{nV_mK_eK_aK_m}{1+(nK_e)^2K_aK_m}\end{aligned} \tag{F.14}$$

Equation F.15 is a re-arrangement of Equation F.14 in which K_m has been made the subject of the formula. To obtain K_m, a constant armature voltage V_m is measured and applied to the geared motor terminals. The steady state output angular speed ω_{ss} is then measured. A high armature voltage close to the motor voltage rating was used to mitigate against inaccuracies introduced by neglecting frictional losses. Table F.4 shows the measured values of armature voltage and angular rate and the calculated mechanical gain.

$$K_m = \frac{\omega_{ss}}{nV_m K_e K_a - \omega_{ss}(nKe)^2 K_a} \tag{F.15}$$

V_m(V)	ω_{ss}(rad/s)	Calculated K_m(V.s/rad)
20.06	6.42	6.1897
21.00	6.72	6.1538
22.06	7.08	7.1283
23.10	7.45	9.6495
24.07	7.68	5.4185
Average value of K_m		6.9080

Table F.4: Experimentally determined value of K_m.

Determination of the Mechanical Time Constant τ_m

To determine the mechanical time constant of the geared motor, a voltage step of 24 V was applied to the terminals of the geared motor. With the terminal voltage close to the motor rated voltage, friction and load torque can be neglected. The time constant from applied terminal voltage to output angular speed was measured. We denote this time constant with $\tau_{m'}$. Due to friction and inertia of the geared motor and drum, the mechanical dynamics of the geared motor will be at least an order of magnitude slower than the electrical dynamics. From this fact, we can neglect the electrical time constant in Equation F.11 to obtain Equation F.16.

$$\begin{aligned}
\frac{\omega(s)}{V_a(s)} &\approx \frac{nK_eK_aK_m}{(1+\tau_m s)+(nK_e)^2K_aK_m} \\
&\approx \frac{nK_eK_aK_m}{\tau_m s+[1+(nK_e)^2K_aK_m]} \\
&\approx \frac{\frac{nK_eK_aK_m}{1+(nK_e)^2K_aK_m}}{1+s\frac{\tau_m}{1+(nK_e)^2K_aK_m}}
\end{aligned} \tag{F.16}$$

Equation F.16 is in the form of a standard first order transfer function whose time constant is given by Equation F.17. With $\tau_{m'}$ measured in the experiment, τ_m remains the only unknown variable in Equation F.17. The mechanical time constant is presented

in Equation F.18.

$$\tau_{m'} = \frac{\tau_m}{1 + (nK_e)^2 K_a K_m)} \tag{F.17}$$

$$\begin{aligned} \tau_m &= \tau_{m'}[1 + (nK_e)^2 K_a K_m] \\ &= 0.08[1 + (25 * 1.2232)^2 * 0.7912 * 6.9080] \\ &= 4.17 \text{ sec} \end{aligned} \tag{F.18}$$

Determination of the Cogging Torque Profile Q_{cog}

The friction developed in Appendix E is reproduced in Figure F.4 for convenience.

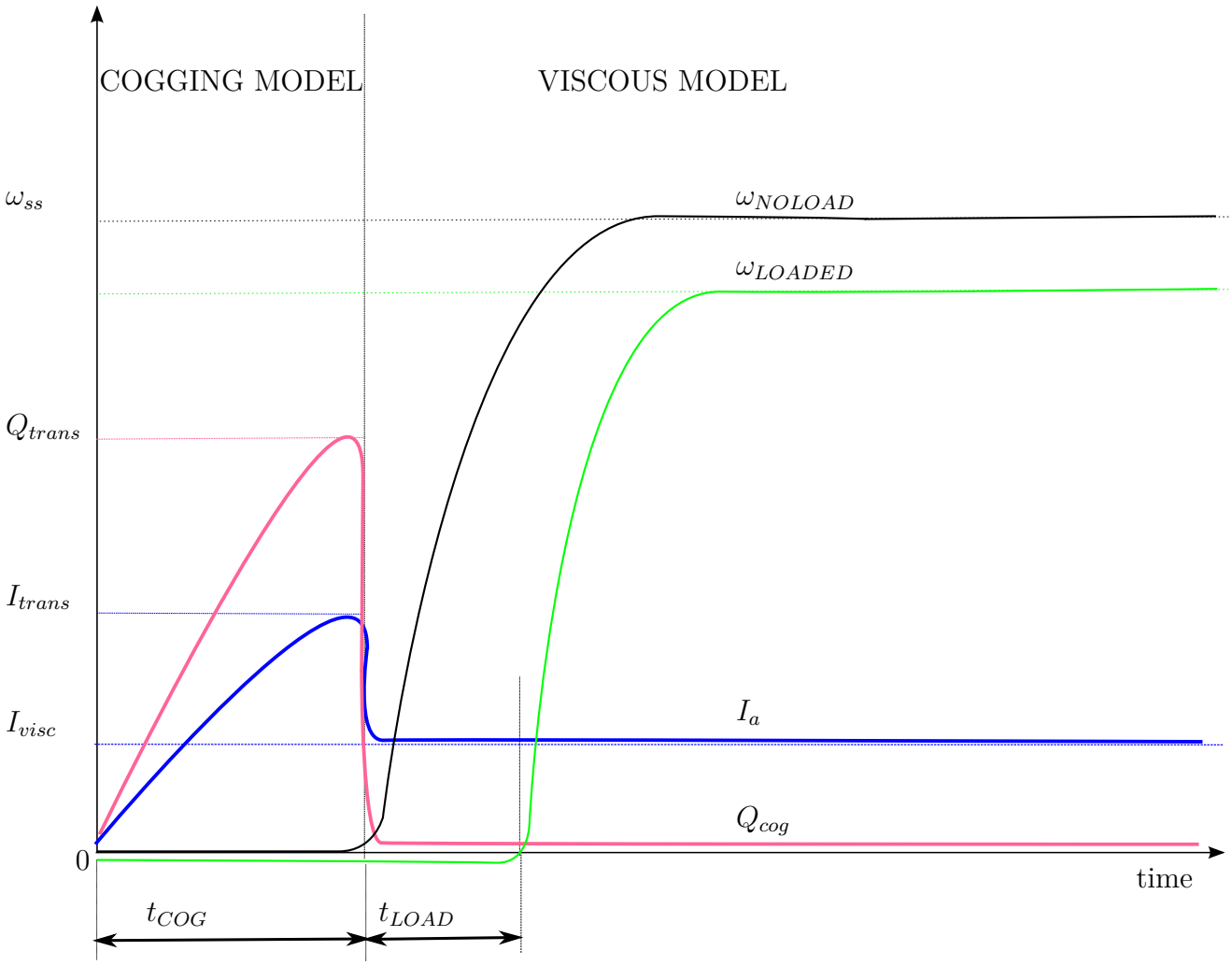

Figure F.4: Friction model profile for the geared motor.

To characterise the cogging friction profile we need to quantify the mechanical torque right at the commencement of rotation Q_{trans}. Due to the linear relationship between armature current and mechanical torque as seen in Figure F.1, the desired mechanical torque can be calculated from a measurement of the armature current at the commencement of rotation as shown in Equation F.19. To measure I_{trans}, a DC power supply is connected across the terminals of the geared motor in series with an ammeter. The current setting on the DC power supply is slowly tuned up until rotation ensues. The ammeter reading is taken as the motor begins to rotate. Values of measured armature current and calculated mechanical torque at commencemence of rotatio are recorded in Table F.5.

$$Q_{trans} = nK_e I_{trans} \tag{F.19}$$

Parameter	Value
I_{trans}	0.630 A
Q_{trans}	1.927 Nm

Table F.5: Experimentally determined values of I_{trans} and Q_{trans}

Determination of the Armature Current of the Unloaded Geared Motor at Rated Voltage I_{visc}

It should be noted that I_{visc} is not a model parameter but rather it is the steady state value of armature current when the geared motor is driven at rated voltage under no load conditions. The value of I_{visc} can however be used to validate the values of K_e and K_a obtained from the system identification campaign. I_{visc} can be measured by taking the steady state current reading of an ammeter placed in series with the geared motor while rated voltage is applied to the motor terminals. From the block diagram shown in Figure F.1, the value of I_{visc} is given by Equation F.20 where ω_r is the steady state value of angular speed at rated voltage. ω_r can be obtained directly from the last row of readings tabulated in Table F.4.

$$I_{visc} = [V_{rated} - nK_e\omega_r]K_a \tag{F.20}$$

The measured value of I_{visc} is documented in Table F.6 alongside the value obtained

by applying Equation F.20. The calculated value is within 4 % of the measured value. Because the calculation utilises the values K_e and K_a as given by Equation F.20, the measurement inspires confidence in the accuracy of K_e and K_a obtained through system identification.

Measured Value (A)	Calculated Value (A)
0.377	0.393

Table F.6: Measured and calculated values of armature current at rated voltage.

F.2 Tether Parameter Approximation

The tether force model presented in Section 3.3.4.2 requires that the tether stiffness k_t and the tether damping coefficient b_t be quantified. As already outlined in Section 3.3.4.2, the transfer function from applied tether tension T_{tether} to tether extension L_{ext} is given by Equation F.21.

$$\frac{L_{ext}(s)}{T_{tether}(s)} = \frac{\frac{1}{k_t}}{1 + s\left(\frac{b_t}{k_t}\right)} \tag{F.21}$$

Experimental determination of the tether stiffness and damping coefficient would involve a series of tether loading experiments requiring accurate displacement measurements. Seeing the tether used for the project has a steel core, the stiffness values that would be obtained from the experiments would be very high since steel has a very high material stiffness. A high stiffness values implies a very fast time constant in Equation F.21. In simulating fast dynamics with such a fast time constant, the Matlab/Simulink sampling frequency may be too small to accurately simulate the dynamics. On the other hand, increasing the Matlab/Simulink sampling frequency too much will drastically slow the simulation time.

Luckily, we do not necessarily need to accurately quantify the tether parameters. We only need to model the tether as being *very stiff* with *very fast dynamics*. To ensure the tether dynamics are modelled as fast, the $\frac{b_t}{k_t}$ time constant in Equation F.21 was designed to be at least 10 times the bandwidth of the fastest control loop. The pitch rate loop has the fastest bandwidth of $\omega_{BW} \approx 14$ rad/sec therefore the time constant

was designed as $\frac{b_t}{k_t} \leq \frac{1}{140}$. Fixing the damping coefficient at $b_t \approx 1$ for simplicity, the condition for the tether stiffness becomes $k_t \geq 140$.

With the initial approximations for b_t and k_t, the steady state gain of the transfer function in Equation F.21 is shown in Equation F.22.

$$\begin{aligned} \frac{1}{k_t} &= \frac{1}{140} \\ &\approx 0.007 \end{aligned} \tag{F.22}$$

The physical interpretation of the steady state gain is that for every 1 N tensile force exerted on the tether the tether will experience a steady state extension of 7 mm from its original length. In other words, the tether will experience a 7 cm extension per 1 kg tensile load. Based on the actual properties of steel, this steady state gain exaggerates the elasticity of steel. As mentioned earlier however, we can still gain an understanding of the system dynamics even with not so accurate tether parameters as long the conditions in Equations F.23 and F.24 are satisfied.

$$b_t \approx 1 \tag{F.23}$$

$$k_t \approx 140 \tag{F.24}$$

By adjusting k_t up, a smaller and more realistic steady state gain can be realised. However, this also results in a faster time constant. A trade off has to be found between representing the stiffness accurately and keeping the time constant slow enough for simulation in Matlab/Simulink. To obtain a more accurate time constant, the damping coefficient b_t can be adjusted down. If the value of b_t is too small, the time constant becomes too fast for the Matlab/Simulink environment to accurately simulate tether dynamics. Based on the foregoing motivation, a tether stiffness of $k_t = 146.4$ N/m and a damping coefficient of $b_t = 0.928$ N.s/m were arrived at. This appendix concludes with a tabulation of all the winch and tether parameters as shown in Table F.7.

Parameter	Symbol	Value
Armature resistance	R_a	1.2638 Ω
Armature inductance	L_a	3.5768 mH
Electrical gain	K_a	0.7912 S
Electrical time constant	τ_a	2.8300 ms
Motor constant	K_e	0.1223 V.s/rad
Gear ratio	n	25
Mass moment of inertia	J	0.6036 rad/V
Coefficient of viscous friction	F	0.1448 rad/(V.s)
Maximum cogging torque	Q_{trans}	1.9270 Nm
Mechanical gain	K_m	6.9080 V.s/rad
Mechanical time constant	τ_m	4.17 s
Tether stiffness	k_t	146.4 N/m
Tether damping coefficient	b_t	0.928 N.s/m

Table F.7: Summary of winch and tether parameters.